Department of

Earth and Environmental Sciences

PhD program Chemical, Geological and Environmental Sciences
Cycle XXXVI

Curriculum in Geological Sciences

ANALYSIS OF DEFORMATION AND STRESS REGIMES ASSOCIATED WITH DIKE EMPLACEMENT

Surname   Corti   Name Noemi

Registration number   776427

Tutor: Prof. Andrea Marco ZANCHI

Supervisor: Prof. Alessandro TIBALDI

Co-Supervisor: Prof. Fabio Luca BONALI

Coordinator: Prof. Marco Giovanni MALUSÀ

ACADEMIC YEAR   2022/2023

Acknowledgments

I want to acknowledge my supervisor, Prof. Alessandro Tibaldi, for his support during these three years. His guidance and meaningful advice stimulated me through all the stages of my research and in the writing of this thesis. I would also like to thank my co-supervisor, Prof. Fabio Luca Bonali, who supported and helped me during all these years through his useful comments and suggestions. I would like to thank both of them for teaching me new skills, and for giving me the opportunity to conduct this research.

I would also like to give a special thanks to the reviewers of this thesis, Prof. Valerio Acocella and Prof. Thomas Walter, for their availability to examine and improve this work.

Also, I would like to thank Dr. Kyriaki Drymoni and Dr. Elena Russo, for the stimulating discussions and their collaboration, both in the field and in the office, as well as for helping me with numerical modeling. I kindly thank Dr. Emanuela De Beni and Massimo Cantarero, for their significant collaboration in the field and for the drone surveys on Mt. Etna. Furthermore, I thank Prof. Agust Gudmundsson, Dr. Marco Neri, and Prof. Federico Pasquaré Mariotto, for their useful suggestions that helped me to improve my work, thanks to their scientific expertise.

During my PhD, I had the opportunity to spend three months at the University of Iceland, and I would like to thank all the people I met and worked with during this experience. A special thanks goes to Prof. Halldor Geirsson and his research group, who gave me the chance to approach new techniques and methodologies, and to broaden my scientific knowledge.

I would also like to express my gratitude to my colleagues and friends Martina and Sofia, as well as the already cited Sandy and Elena. I have learned a lot from each of them and I have enjoyed all the time in the office with them.

Finally, I would like to give a special thanks to my parents, my family, and all my friends, for always being with me and encouraging me through these years. Your constant support helped me to reach this important goal.

Abstract

During eruptive events, magma propagates vertically towards the surface through magma-filled fractures, referred to as dikes. However, in most cases dikes arrest in the crust, not leading to an eruption. In shallow settings, dike emplacement causes a concentration of tensile and shear stresses in the host rock, which can lead to brittle deformation at the topographic surface, with the formation of tension fractures and normal faults, often creating a graben. In the last decades, analytical, analogue and numerical models have been designed to analyze the relation between magma emplacement and dike-induced surface deformation, but mostly with an elastic half-space, homogeneous and isotropic, without taking into account the layering of the crust. Realistic field data should be considered to overcome this limitation, to avoid errors in the reconstruction of dike geometry.

For this reason, in this project I integrated realistic structural data with numerical modeling. Study areas are located on Mt. Etna (Italy), along the 1928 and 1971 eruptive fissures, and in SW Iceland, along the Younger Stampar eruptive fissure. These case studies were all affected by shallow dike emplacement. On Mt. Etna, this led to brittle surface deformation, which is nowadays still visible in plan view and, for the 1971 case study, also in section view. The main aim is to investigate the parameters that *i)* promote or inhibit dike-induced brittle deformation at the surface, *ii)* control the geometry of dike-induced graben faults, and *iii)* favor dike arrest at shallow depths.

To collect new structural data, I integrated classical fieldwork with remote sensing analyses, thanks to high-resolution 2D and 3D models derived from drone-collected images and historical aerial photographs through Structure from Motion (SfM) techniques. All these data were then used as inputs for Finite Element Method (FEM) numerical modeling using the software COMSOL Multiphysics®, running sensitivity analyses to understand which parameters affect dike-induced surface deformation and dike propagation.

This thesis confirms the role of dike overpressure and inclination on its propagation and on dike-induced stresses. Furthermore, it points out the effects of layering on the formation of stress barriers and on the distribution of dike-induced stresses, with stiffer materials that concentrate stresses and softer materials that suppress them. Shear stress distribution in the

host rock also suggests that softer layers favor the formation of narrow grabens, whereas stiffer layers promote wider grabens. The role of topography is also investigated, confirming its influence on dike propagation path and on the geometry of graben faults. Finally, this thesis highlights the impact of lateral compression due to nearby previous intrusions, which can favor dike arrest and the absence of surface deformation. This result also validates conceptual models by previous authors, regarding the geometry of dike-induced grabens at slow and fast spreading ridges.

List of contents

1. Introduction

1.1 Aims and objectives

During volcanic eruptions, magma is transported up to the surface through magma-filled fractures, referred to as vertical dikes or inclined sheets, which propagate perpendicular to the minimum and parallel to the maximum principal compressive stresses (Anderson, 1951). These dikes (or sheets) are driven mainly by their internal magmatic overpressure (Delaney et al., 1986; Gudmundsson, 2011a, 2020; Acocella, 2021). However, in most cases dikes arrest during their vertical propagation in the crust, thus not leading to an eruption (Figs. 1A-B) (Rubin, 1992; Gudmundsson et al., 1999; Gudmundsson and Brenner, 2001; Gudmundsson, 2003; Calais et al., 2008; Pallister et al., 2010; Nobile et al., 2012; Rivalta et al., 2015; Townsend et al., 2017). The majority of dikes arrest at contacts between layers characterized by different mechanical properties, or they become deflected into sills (Gudmundsson, 1986a; Parsons et al., 1992; Kavanagh et al., 2006; Rivalta et al., 2005; Thomson, 2007; Menand, 2008; Tibaldi and Pasquaré Mariotto, 2008; Gudmundsson, 2011a, 2011b; Maccaferri et al., 2011; Drymoni et al., 2020).

In shallow settings, dike emplacement causes a concentration of tensile (σ_3) and shear (τ) stresses in the host rock (Gudmundsson, 2003; Bazargan and Gudmundsson, 2019, 2020), that can lead to brittle deformation above the dike tip and at the topographic surface, generating tension fractures (e.g., Anderson, 1951; Rubin and Pollard, 1987) and normal faults, often creating a graben (Figs. 1C-D) (e.g., Mastin and Pollard, 1988; Rubin and Pollard, 1988). Over the past decades, several dike intrusions have led to surface deformation, generating, or reactivating normal faults and tension fractures at the surface, along both slow and fast spreading boundaries (Chadwick and Embley, 1998; Acocella and Trippanera, 2016, and references therein). Graben formation was observed recently in Iceland during the Krafla rifting episode in 1975-1984 (Sigurdsson, 1980; Rubin, 1992) and the Bardarbunga eruption in 2014 (Hjartardóttir et al., 2016; Ruch et al., 2016). Tension fractures and faults formation following dike intrusions was also observed on volcanic edifices during eruptive events, like Kilauea (Pollard et al., 1983), Cumbre Vieja (Walter et al., 2023), and Mt. Etna

(Murray and Pullen, 1984; Acocella and Neri, 2003; Billi et al., 2003; Bonaccorso et al., 2011; Falsaperla and Neri, 2015).
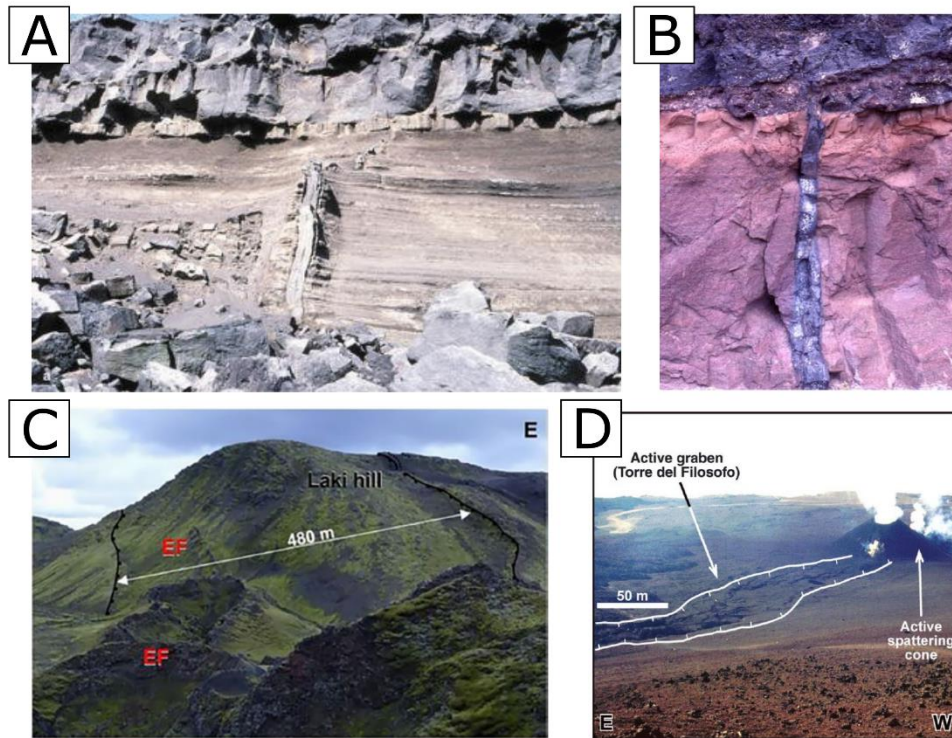
Fig. 1. Examples of arrested dikes (A) in the SW of Iceland and (B) in Tenerife (from Gudmundsson and Brenner, 2004). Examples of grabens formed (C) in Iceland during the Laki eruption (from Acocella and Trippanera, 2016) and (D) during the 2001 Mt. Etna eruption (from Billi et al., 2003).

Studies on dike-induced surface deformation have been increasing during the past decades, due to their importance for volcanic hazard assessment. Analytical (Isida, 1955), analogue (Mastin and Pollard, 1988; Trippanera et al., 2015a; Xu et al., 2016) and numerical (Pollard et al., 1983; Rubin and Pollard, 1988) models have been used to analyze the relation between dike properties and surface deformation, to infer the depth and shape of the dike. Regarding the relation between the depth of the dike tip and the width of the graben, the so-called "graben rule" derived from Pollard et al. (1983) is widely used in the literature, suggesting that dike-induced grabens have a width equal to about twice the depth of the dike top (e.g.,

Rubin, 1992; Hjartardóttir et al., 2016; Al Shehri and Gudmundsson, 2018). However, recently some authors suggested that this relation is more complicated than this (Magee and Jackson, 2021). Furthermore, many cases of arrested dikes are not associated with brittle deformation at the surface (Gudmundsson, 2003). All the above cited models, in fact, only considered an elastic half-space, both homogeneous and isotropic, without considering the heterogeneity of the crust. Numerical modeling integrated with realistic field data can be used to overcome this limitation, which can lead to errors in the reconstruction of dike geometry (Al Shehri and Gudmundsson, 2018; Bazargan and Gudmundsson, 2019, 2020; Clunes et al., 2023).

Therefore, my project is developed with a multidisciplinary approach consisting in the integration of field structural data with numerical modeling. Data are collected in two different areas: Mt. Etna Volcano in Sicily, Italy, and the Reykjanes Peninsula in the southwest of Iceland. Regarding the geodynamic setting of the areas, the basement of Mt. Etna is characterized by compression, whereas extension is dominant locally on the volcanic edifice due to the seaward slipping of the eastern flank; in Iceland, an extensional setting is present because of its location along the mid-oceanic ridge. Both areas are characterized by the presence of outcropping dikes and brittle surface deformation associated to dike intrusions in historical times. Specifically, on Mt. Etna my project will focus along two ENE-trending eruptive fissures on the eastern flank of the volcano, formed during the eruptions of 1928 and 1971. Flank eruptions, related to the lateral propagation of dikes, represent one the most dangerous volcanic processes on Mt. Etna. In 1928, the lava flow generated by the eruption destroyed the village of Mascali, causing damages to primary infrastructures (Branca et al., 2017). The lateral propagation of the dike generated deformation at the surface, with the formation of grabens and half-grabens, tension fractures, volcanic vents, and eruptive fissures. For this case, the scenarios that could have led to the formation of these different structures were investigated. During the 1971 eruption, the lateral propagation of the dike formed an asymmetric graben that is still visible in section along the northern wall of the Valle del Bove (VdB), a huge depression located on the eastern flank of Mt. Etna (Calvari et al., 2004). Since dike-induced grabens are usually studied in plan view (e.g., Ruch et al., 2016; Trippanera et al., 2019), this represents an exceptional case to study a dike-induced graben in section view, to describe the geometry of the faults, and analyze its relationship with dike-induced stresses in the host rock. Finally, in SW Iceland, I focused on

two exposed dikes associated with the "Younger Stampar" eruption (1210-1240 AD, Sæmundsson et al., 2016) and the related crater row. This area is interesting for two main reasons: understanding what affected the propagation of the dikes, resulting in one arrested and one feeder dike, and why there was no formation of faults or tension fractures at the surface, even if the non-feeder dike arrested at a very shallow depth (5 m below the surface).

My research project aims at collecting new structural measurements in these areas, related to dike-induced brittle deformation at the surface, and along outcropping dikes. These new data are successively integrated with numerical modeling. Therefore, the main goal of this work is contributing to the following volcanotectonics main issues: *i)* which parameters can favor, or inhibit, dike-induced brittle deformation at the surface? *ii)* which factors control the geometry of dike-induced graben faults? *iii)* what can favor dike arrest? Furthermore, this thesis will provide new structural data related to the geometry (vertical offset, width, and length) of dike-induced grabens. These will enhance the records of values from the literature that, up to now, are not abundant.

1.2 Thesis structure

This PhD thesis will start with a general explanation of the used methodologies (Chapter 2). Then, a description of the geological settings of all the studied areas, on Mt. Etna and in Iceland will follow (Chapter 3). After that, every case study will be presented in a dedicated chapter, with the specific materials and methods, the results and discussion related to each of them (Chapter 4, 5, 6). Finally, a general discussion (Chapter 7) and the conclusions (Chapter 8) considering all the case studies will follow.

2. General Methodologies

To reach the scientific goals, in this thesis I used a multidisciplinary approach, with the collection of new structural data subsequently integrated with numerical modeling. For all the case studies, this workflow was followed: *i)* historical aerial photographs were used to reconstruct orthomosaics and Digital Surface Models (DSMs) through Structure from Motion (SfM) techniques, to preliminary identify the structures present in the study area; ii) these structures were validated and new structural data were collected through field surveys, and thanks to 2D and 3D models derived from Unmanned Aerial Vehicles (UAVs)-collected images, also using the immersive Virtual Reality (VR); iii) all these structural data were then integrated with Finite Element Method (FEM) numerical modeling using the software COMSOL Multiphysics®, to carry out sensitivity analyses aimed at understanding how different parameters affect surface deformation and dike propagation.

Regarding my contribution in performing each methodology: I collected and elaborated field data for the three case studies with a support by Prof. Alessandro Tibaldi, Prof. Fabio Luca Bonali, Dr. Elena Russo, and Prof. Federico Pasquaré Mariotto. Furthermore, for all the case studies I collected structural data on SfM-derived models, which were reconstructed with the help of Prof. Fabio Luca Bonali. Finally, for numerical modeling, I developed the models for the Stampar and 1971 fissure case studies, in collaboration with Dr. Kyriaki Drymoni, Dr. Elena Russo, and Prof. Fabio Luca Bonali.

In this chapter, I present a general introduction on how field surveys were conducted, and on the SfM photogrammetric techniques, the immersive VR, and numerical modeling. The detailed materials and methods used for each case study will be explained in the specific chapters.

2.1 Field survey

During field surveys, structures previously identified on historical aerial photos were validated. Structures were classified as normal faults when they presented a vertical displacement, or as tension fractures when there was no vertical offset. When a continuous

scarp was not observable due to sediment coverage, the classification was made based on the topography. When fractures were characterized by the presence of spatter lavas, lava flows or scoriae deposits, they were classified as eruptive fissures, differently from dry fractures that did not present signs of eruption. In the field, the new structures related with the studied diking events (1928 and 1971 events on Mt. Etna, and Younger Stampar event in Iceland) were distinguished from the older ones, since the latter were more filled with sediments and vegetation, whereas the former showed a lower degree of sediment infilling and only young vegetation. Fault scarps were observed in detail to recognize signs of reactivation, such as different degrees of erosion or different distributions of vegetation.

Along the structures, quantitative data were collected at specific sites, called structural stations. Regarding tension fractures, the strike, amount of opening and opening direction were measured, when possible, using compass and laser rangefinder. Opening directions were collected only when piercing points were visible on both sides of the fracture, measuring the strike of the line connecting them. For eruptive fissures, the strike and the opening were measured. Finally, along normal faults, strike, dip, dip angle, and vertical offsets were collected, using a tape for offsets < 2 m, and with a laser rangefinder in case of higher offsets. When possible, the location of each measurement was set with one high-resolution GPS, using one Emlid Reach RS+ receiver as a rover with a Real-Time Kinematic (RTK) correction and reaching a centimeter accuracy. Locations were referred to the WGS84 datum.

Due to the hard logistic conditions of the study areas, structural data were collected also on 2D, and 3D models derived by photogrammetric techniques, as will be explained in detail in the next Section 2.2.

2.2 Structure-from-Motion photogrammetry and Virtual Reality

Structure-from-Motion (SfM) techniques applied to geological studies represent a powerful tool to collect a great amount of data, allowing to overcome some limitations of classical fieldwork. Often, geological sites are characterized by difficult logistic conditions, or the studied areas are too big to be covered only by fieldwork. For these reasons, the application

of SfM on remote-sensing derived images has increased over the last decades. For this PhD thesis, field-collected measurements were integrated with data from historical aerial photographs and UAV-collected pictures. The general SfM workflow is presented in this chapter, whereas the detailed materials and settings used for each case study will be presented separately in the specific chapters.

2.2.1 SfM applied to UAV-collected photographs

UAVs have become popular for remote sensing analyses in geological sciences due to the advantages that they offer compared to satellite images, giving the possibility to *i)* choose data acquisition and time; *ii)* adjust flight height to obtain a higher spatial resolution; *iii)* repeat more flights according to what is needed; *iv)* produce 3D models of the surveyed area thanks to the incorporated RGB camera; *v)* survey vertical cliffs; *vi)* acquire data with relatively low costs. Because of these characteristics, in the last few years UAVs have been used also in volcanic areas (Fig. 2A) and during volcanic eruptions to study surface deformation (Müller et al., 2017; Darmawan et al., 2018; De Beni et al., 2019; Bonali et al., 2019, 2020; Walter et al., 2018, 2020a; Tibaldi et al., 2021), to investigate the distribution of hydrothermal vents (Walter et al., 2020b), and to analyze features of lava flows (Favalli et al., 2018).

Several types of UAVs can be used for geological purposes, including balloons, multi-rotor (Fig. 2B), fixed-wing (Fig. 2C), and hybrid ones (Fig. 2D). The latter allows to switch between flights as a fixed-wing aircraft and as a multi-rotor one. Balloons do not need fuel or batteries, but they cannot be remotely controlled. For this thesis, all the studied areas were surveyed using commercial quadcopters, because they are easy to be transported in the field with batteries, they can fly at very low heights guaranteeing a high resolution, and they are simple to be piloted (Fig. 2A). These advantages make them useful in difficult logistic terrains, like volcanic areas (e.g., Bonali et al., 2019, 2020).
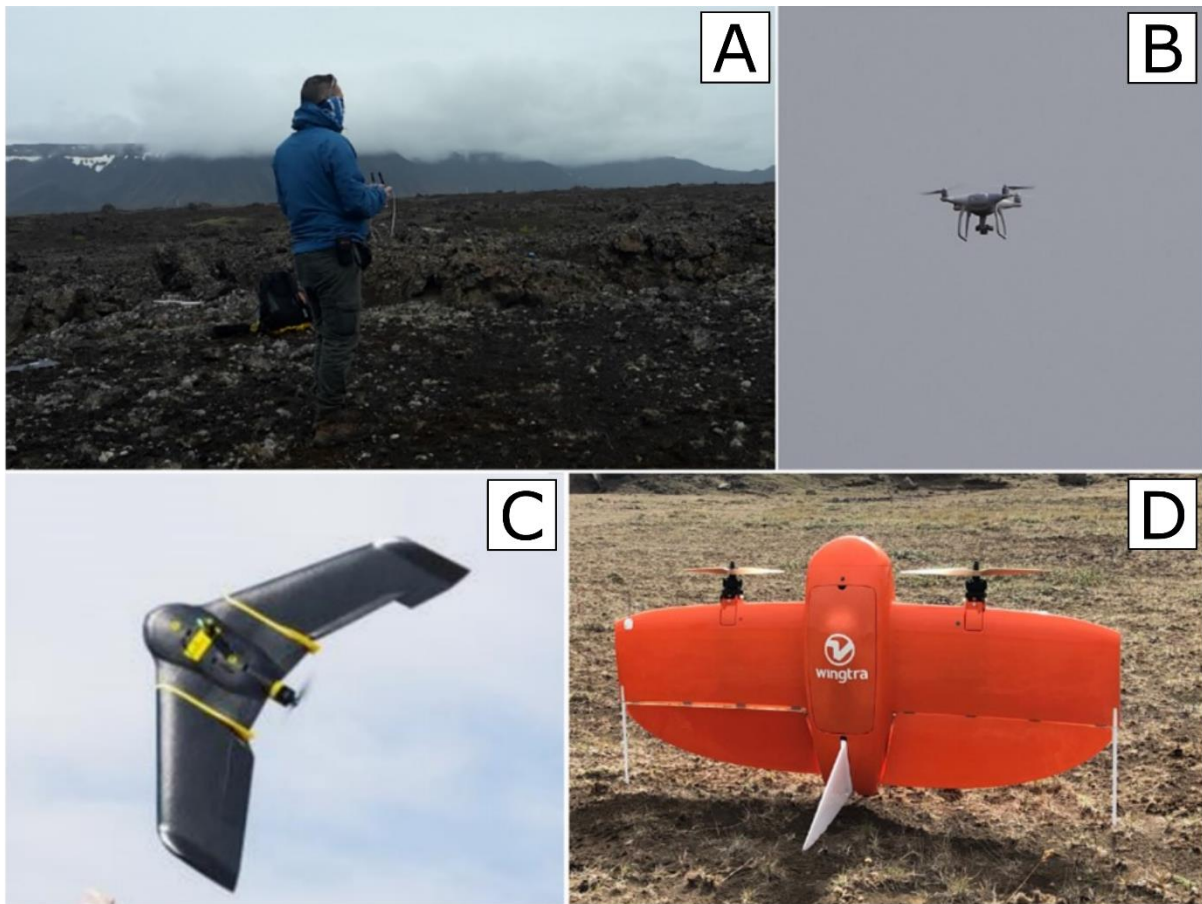
Fig. 2. (A) Pilot at work with a quadcopter. Examples of (B) a commercial UAV quadcopter, (C) a fixed-wing UAV, and (D) a hybrid UAV (Bonali et al., 2021a).

Starting from UAV-collected photos, Digital Surface Models (DSMs) and orthomosaics can be reconstructed through SfM techniques. To obtain them, the workflow from Bonali et al. (2021a), presented in Figure 3A, was followed for all the case studies. Part I of the workflow is dedicated to data collection, including photos and Ground Control Points (GCPs), whereas Part II is devoted to data processing to reconstruct the models.

Regarding Part I, the first step consists in the definition of the area to be surveyed. This can be planned with the help of a specific software, the DJI Ground Station Pro (https://www.dji.com/ground-station-pro), also considering wind conditions. The overlap between the photo should also be defined, considering that the greater is the overlap, the better will be the alignment of the photos and the quality of the resulting orthomosaics (Gerloni et al., 2018; Bonali et al., 2019; Krokos et al., 2019; Antoniou et al., 2019). To scale

and reference the resulting models, at least 4 GCPs should be selected near the corners of the area, and at least one in the central part to reduce the "doming" effect (e.g., James and Robson, 2012; Turner et al., 2012; Westoby et al., 2012; James et al., 2017). To locate GCPs, well visible artificial markers can be used, as well as natural and ecological targets (Figs. 3B-C-D) to save time during the survey. Natural targets can be visible stones, lava flow borders or piercing points along fractures (Fig. 3B). As ecological targets, pieces of bread can be used (Fig. 3D). In general, GCPs should be clearly visible in the photos, and they should have a shape that allows a high accuracy, with a maximum size of 5-10 cm. For my project, GCPs were surveyed in a Real-Time Kinematic (RTK) configuration, using one Emlid Reach RS+ receiver as a rover. The rover was linked to the closest available NTRIP network, used as reference station. When the network was not available, I applied a Post-Processed Kinematic (PPK) correction through the RTKLIB software (http://www.rtklib.com/), using the raw RINEX data, registered by the rover, and the RINEX data of the nearest base station. In both cases, the accuracy is in the order of centimeters. All the altitude values of the GCPs were then corrected according to the geoid model (https://geographiclib.sourceforge.io/cgi-bin/GeoidEval), to obtain the orthometric height for the models.

Part II of the workflow (Fig. 3A) is focused on data processing to reconstruct the models, obtaining DSMs and orthomosaics as final products. In this work, the software Agisoft Metashape (http://www.agisoft.com/) was used for the processing. This commercial SfM software is widely used in the scientific community due to its user-friendly interface, the intuitive workflow and the high quality of the point clouds (Benassi et al., 2017; Burns and Delparte, 2017; Cook, 2017). The software automatically identifies matching features in different photos and aligns them, first considering only measured camera locations (Reference preselection mode). After the alignment, the photos with a quality value < 0.5 were excluded from the processing, following the suggestions of the Agisoft user manual (Agisoft LLC, 2018). The software also automatically detects the focal length and the photo dimensions, using them to calibrate the intrinsic parameters of the camera, namely the distortion coefficients and the principal point coordinates. After that, GCPs were added in all photos, to scale and georeference the model, optimize the extrinsic parameters (estimated camera locations and orientations) and improve the accuracy of the final models. As explained before, using the RTK/PPK configuration allows to obtain an accuracy in the order

of centimeters (Ouédraogo et al., 2014; Ruzgienė et al., 2015; Chandler and Buckley, 2016; Tonkin and Midgley, 2016).
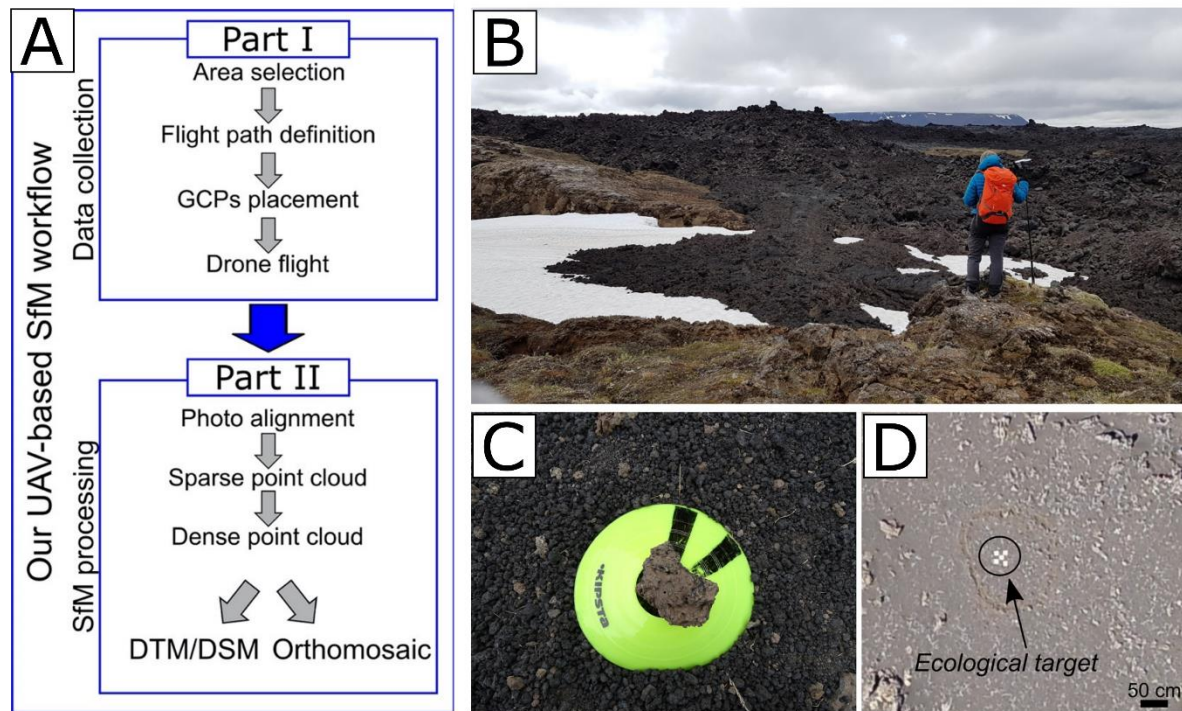
Fig. 3. (A) Overall workflow used in this thesis to generate DSMs and orthomosaics from UAV-collected pictures, using the SfM software Agisoft Metashape. Examples of GCPs on (B) a natural target collected by an operator, (C) an artificial target and (D) an ecological target (modified after Bonali et al., 2021a).

Subsequently, the photos were realigned, with the creation of a sparse cloud (Fig. 4A). After that, a dense point cloud (Fig. 4B) was reconstructed from the sparse cloud, and the mesh was generated. Finally, the DSMs were obtained from the dense cloud to obtain a better resolution, and they were georeferenced in the WGS84 – geographic coordinates reference system. The orthomosaics were eventually generated considering the DSM as surface, with the same reference system (further details in Stal et al., 2012; Westoby et al., 2012).
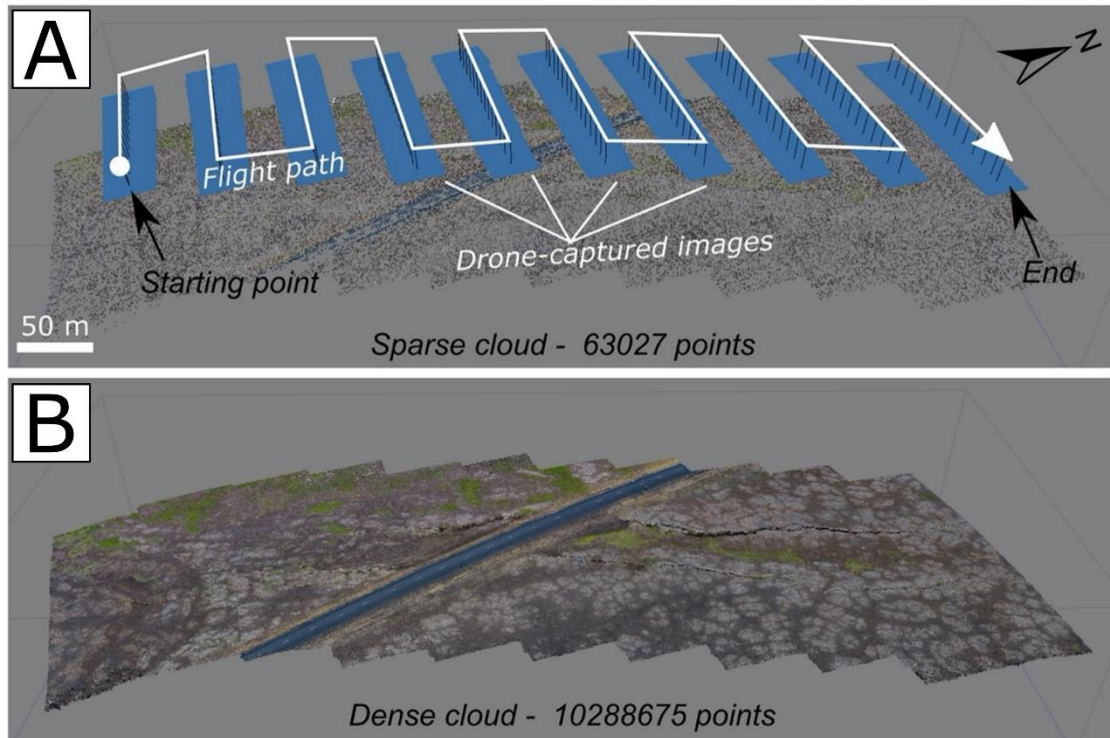
Fig. 4. Examples of a (A) sparse and (B) dense cloud generated by the SfM software. Computed camera positions are represented as blue rectangles, black lines show the pitch angle and camera orientation (modified after Bonali et al., 2021a).

2.2.2 SfM applied to historical aerial photographs

In some cases, historical datasets are needed to analyze long-term deformation in a specific area, and UAV-collected pictures cannot provide them. The SfM technology allows to process also historical aerial photographs, to obtain orthomosaics, DSMs and 3D models with a relatively high resolution, according to the initial resolution of the input images (Grottoli et al., 2020). Historical aerial photographs have been used in the last few years in different fields of geosciences, to study glacial surfaces (Micheletti et al., 2015; Mertes et al., 2017; Mölg and Bolch, 2017), landscape evolution (Gomez et al., 2015; Mertes et al., 2017; Modica et al., 2017; Sevara et al., 2018), and coastal and riverine environments (Aguilar et al., 2013; Redweik et al., 2016; Bakker and Lane, 2017; Warrick et al., 2017; Carvalho et al., 2020).

For this thesis, the historical images were processed with Agisoft Metashape, following a workflow similar to the one used for UAV-collected pictures (Fig. 3A). For Mt. Etna, photos

were bought from the Istituto Geografico Militare (https://www.igmi.org/) at a resolution of 2400 dpi, in a TIFF image format, whereas for Iceland, the photos were downloaded for free from the National Land Survey of Iceland website (https://www.lmi.is/).

As explained for the UAV-collected pictures, the software automatically aligns the photos recognizing common features in different images, that should have been collected with a high degree of overlap, generally 60-80% (Schonberger and Frahm, 2016; Bonali et al., 2019). Subsequently, a dense point cloud was reconstructed from the sparse point cloud. The quality of the alignment and of the elaboration of the dense point cloud was chosen after several attempts, to select the best compromise between good-quality results and relatively short processing time. After the creation of the dense clouds, the latter were georeferenced, using elements of known coordinates (X, Y, Z) as GCPs. These were derived from existing databases, like topographic maps, georeferenced aerial photos, or Google Earth. Finally, the DSMs were reconstructed from the dense cloud, and the orthomosaics were generated using the DSMs as surface, as explained for the UAV-collected pictures.

In this project, the models derived from historical aerial photographs were useful for preliminary analyses, to plan more detailed surveys of the study area, and to compare images prior and after a specific event (e.g., volcanic eruptions).

2.2.3 Immersive Virtual Reality

To overcome the difficult logistic conditions characterizing some outcrops, the use of Virtual Reality (VR) applications have increased in Earth Sciences in the last few years, both for research and education purposes (Bonali et al., 2021b). VR can be classified as non-immersive and fully immersive experiences (Choi et al., 2016). Simple 3D visualizations and 3D models displayed on computer or mobile devices screens are referred to as non-immersive VR, whereas immersive VR allows the users to perceive themselves as physically present in a virtual world, by surrounding them with images (Granshaw and Duggan-Haas, 2012; Trexler et al., 2018; Zhao et al., 2019). This approach is based on photogrammetric techniques, and it provides the users with several virtual geological landscapes, called virtual outcrops or geosites (Krokos et al., 2019; Pasquaré Mariotto and Bonali, 2021). In this thesis,

I used the software tailored by Tibaldi et al. (2020a), developed in the framework of two research and innovation projects: the Italian Argo3D (https://argo3d.unimib.it/) and the EU Erasmus + 3DTeLC (http://3dtelc.lmv.uca.fr/) Projects. This software is based on technologies that are commonly used in entertainment applications, including modern game engines (Unity, https://unity.com/) combined with Virtual Reality devices (Oculus Rift, https://www.oculus.com/).

The workflow is summarized in Figure 5. Through Part I of the workflow, a high-resolution 3D Digital Outcrop Model (DOM) was created, starting from UAV surveys or historical aerial photos. The input photographs were processed following the SfM workflow presented in Section 2.2.1. The resulting DOM is called also Virtual Outcrop (VO) (Xu et al., 1999; Tavani et al., 2014) and can be studied in first person with an immersive experience. From the SfM processing with Agisoft Metashape, a 3D Tiled Model was reconstructed using the dense cloud as source data and was exported in OBJ format (Wavefront Object File). The resolution and the accuracy of the resulting DOM is based on the quality of the SfM processing, the quantity of used GCPs, flight height and camera resolution (Westoby et al., 2012; Bonali et al., 2019).

After that, this file was then imported and managed in the Unity game engine, in order to replicate a real-world reference system (Part II of the workflow in Fig. 5, Krokos et al., 2019). At this point, an invisible object called "collider" was assigned to the mesh, and the scene was georeferenced and scaled according to the SfM-derived information, defining the scene dimensions (in meters) and the geographic coordinates, including the altitude. Finally, the use of Unity Levels of Details (LODs) methodology was suggested by Tibaldi et al. (2020a), to reduce the details visible when the model is far from the camera.

Once the 3D VR scene is set, the user can select the navigation mode between the "walk mode", the "drone mode" and the "plane mode". In the first case, the user walks on a "solid ground surface", moving around within the virtual scene. In the other two modes, the user can fly over the area to have a different view of the outcrop, also analyzing sites that cannot usually be reached in the field (e.g., high vertical cliffs). The software by Tibaldi et al. (2020a) also includes several tools, which allow the users to collect quantitative and qualitative data as if they were in the field. Besides, the angle of view can be changed, to take measurements with the better possible perspective. The different tools allow to: assess geographic

coordinates; select point features; map polygons and lines; measure areas; measure the attitude of an object; measure length and thickness and reconstruct topographic profiles. Finally, specific tools allow to take notes as well as photographs of the DOM.
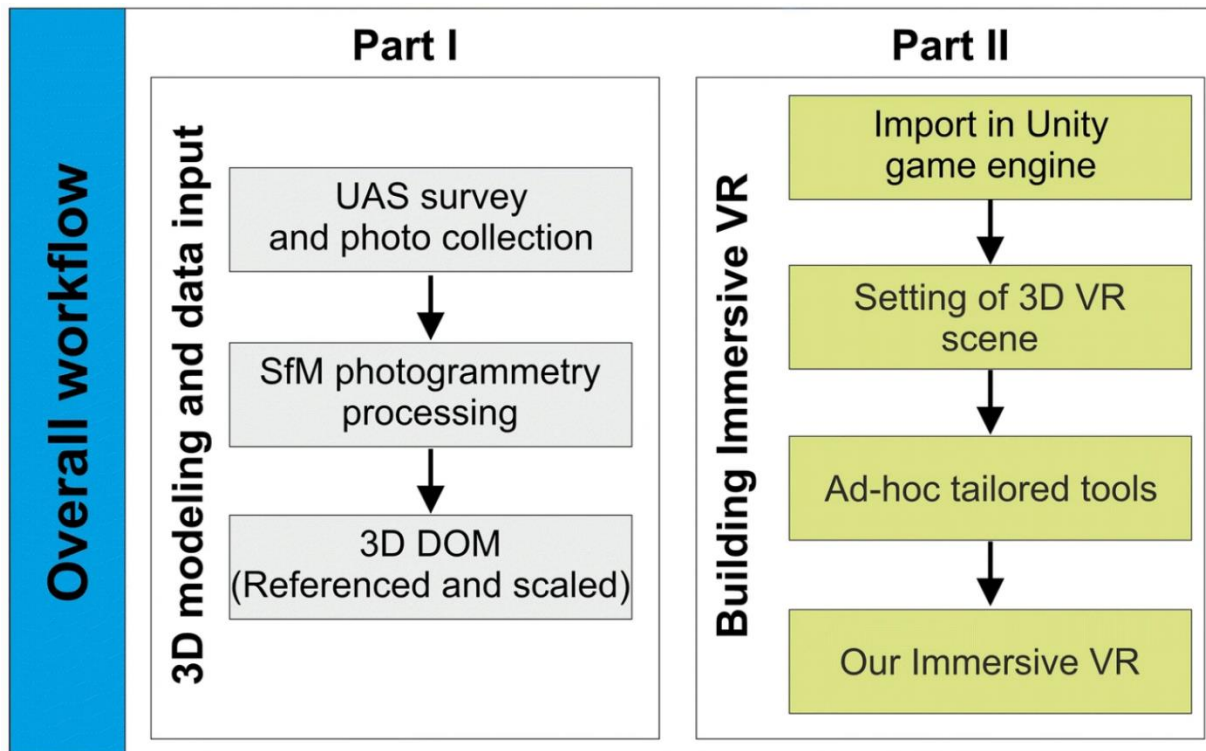
Fig. 5. Workflow to create a 3D DOM and build the immersive VR (from Tibaldi et al., 2020a).

2.3 Numerical modeling with COMSOL Multiphysics®

Numerical models were run using the FEM software COMSOL Multiphysics® (v. 5.6 and 6.1), specifically using the Structural Mechanics module in 2D (xy plane). For all the case studies of this thesis, numerical models are based on structural and on lithostratigraphic data, previously collected in the field or on SfM-derived models.

The examined crustal segment was always assumed with a linear elastic behavior (Gudmundsson, 2011a). To reproduce heterogeneities in the crust, the domain was divided in different layers, characterized by different mechanical properties. Values of Young's modulus (E), Poisson's ratio (ν) and density (ρ) were assigned to each layer according to

24

values commonly found in the literature. For all the case studies, Poisson's ratio was considered constant and equal to 0.25 for all the layers (Babiker and Gudmundsson, 2004), whereas density values were considered equal to 2600 kg/m^3 for lava deposits, and 2000-2300 kg/m^3 for more compliant deposits, like tuffs or scoriae (Gudmundsson, 2011a). Stiffness (E) was selected from the most common values found in the literature for *in situ* Young's moduli of volcanic rocks, which are lower than E values of intact rocks. *In situ* E values are typically between 10 and 40 GPa for basement rocks (Gudmundsson, 2020), and between 1 and 15 GPa for the shallow crust (Ray et al., 2007; Becerril et al., 2013). Finally, pyroclastic deposits have lower values of stiffness, as much as 0.001 GPa (Heap et al., 2020). For the 1971 fissure case study, I calculated the *in situ* E value of the lava layers starting from E values of intact rocks of Mt. Etna and scaling the average of these values according to the GSI (Geological Strength Index) of the studied outcrop (as suggested by Heap et al., 2020). The selected E values for each case study will be presented in detail in the dedicated chapters.

COMSOL Multiphysics® allows to investigate the distribution and orientation of stresses and strains at the dike tip and in the host rock, according to imposed user-defined boundary conditions. In all the models, the dike was designed as an elliptical cavity driven by internal overpressure (P_0). Values of overpressures were varied in the range 1-20 MPa, accordingly to values used by Becerril et al. (2013) and Drymoni et al. (2020). The dike was placed in the central part of the domain, to exclude edge effects from the results' interpretations. All the models were fastened at the bottom edge to avoid rigid-body rotation and translation (Geyer and Gottsmann, 2010; Browning et al., 2021), whereas the upper surface was free to simulate the Earth's surface (Bazargan and Gudmundsson, 2019). Besides the dike overpressure, other boundary conditions were added, to simulate extensional or compressional stress fields, as pressures on the model's lateral edges. In each case study, these boundary loads (or some of them) were varied, together with the host rock mechanical properties, to investigate the role of these parameters on dike-induced stresses. The sensitivity analyses conducted for each case study will be presented and explained in more detail in the dedicated chapters.

The distribution and the orientation of dike-induced stresses, based on the above-presented parameters, enable to assess both the probability of fracturing (Al Shehri and Gudmundsson, 2018; Bazargan and Gudmundsson, 2019) and the likelihood of dike arrest or propagation (Drymoni et al., 2020). For a Mode I fracture to form, the tensile stress should be at least equal to the tensile strength (T_0) of the host rock (Gudmundsson, 2011a). According to laboratory experiments, tensile strength of intact basalt samples is around 5 MPa (Graue et al., 2011; Perras and Diederichs, 2014). However, the *in situ* tensile strength obtained from hydraulic fracture experiments is commonly between 0.5 and 6 MPa, with a maximum value of 9 MPa measured at a depth of about 9 km in a drill hole in Germany (Amadei and Stephansson, 1997), and most typical values between 2 and 4 MPa, already used in previous numerical models (Al Shehri and Gudmundsson, 2018; Bazargan and Gudmundsson, 2019). With regards to volcanic areas and rocks, hydrofracturing measurements by Haimson and Rummel (1982) showed values between 1 and 6 MPa for the uppermost part of the Icelandic crust (depth < 200 m), with an average value of 2.8 MPa, and a standard deviation of 1.5 MPa. According to Schultz (1995), basaltic rock masses with weakening effects, like columnar joints, have an even lower tensile strength, between 0.1 and 2.5 MPa. For fault formation, or for a pre-existing fracture to slip, the von Mises shear stress concentration should be at least equal to the shear strength of the host rock, which is commonly about twice the tensile strength (Haimson and Rummel, 1982; Schultz, 1995).

Considering this, the following properties were plotted in the models to investigate the distribution of dike-induced stresses at the dike tip and in the host rock:

- Tensile stress, plotted as a color scale in the background for all the case studies;
- Absolute shear stress (component of the von Mises shear stress on the xy plane), plotted as contours for the 1928 fissure and Stampar case studies;
- Von Mises shear stress, plotted as a color scale in the background for the 1971 fissure case study.

To analyze dike-induced deformation at the surface, the following properties were also plotted as 1D graphs for the 1928 fissure and Stampar case studies:

- Tensile stress;

- Von Mises shear stress.

Regarding magma path, the vertical propagation of a dike can occur if σ_1 is vertical, whereas if σ_1 becomes horizontal the dike arrests, or is deflected into a sill, due to the presence of a stress barrier (Anderson, 1951; Gretener, 1969; Gudmundsson, 1986a). The orientation of σ_1 and σ_3 (maximum and minimum compressive stress, respectively) also determines the likely arrangement of a fault plane (e.g., Anderson, 1905; Hafner, 1951; Ramsay and Lisle, 2000; Fossen, 2016). Therefore, to understand the orientation of principal stresses, σ_1 and σ_3 orientations were also plotted as arrow surfaces. This allows to assess the probability for a dike to propagate/arrest (for the 1928 fissure and Stampar case studies) and the likely arrangement of the faults (for the 1971 fissure case study).

3. Geological setting

3.1 Mt. Etna and ENE Rift

Mt. Etna is a large basaltic composite stratovolcano, located in a compressional environment at the border between the African and European plates (Lanzafame et al., 1997; Cocina et al., 1997, 1998) (Fig. 6A). It formed during the last 500 ka in eastern Sicily, during four different phases of eruptive activity: the Basal Tholeiitic (500-330 ka), Timpe (220-110 ka), Valle del Bove (110-60 ka) and Stratovolcano (60 ka-present) phases (Branca et al., 2011a; Barreca et al., 2018).

Regional compression in the area is related to a horizontal σ_1 oriented N-S to NNW-SSE, which produces WSW-ENE trending reverse faults and NW-SE strike-slip faults (Villani et al., 2020). More to the east, there is the presence of transtensional and reverse faults offshore, associated with the interaction with the Ionian microplate (Gambino et al., 2022) (Fig. 6A). Within Mt. Etna, this regional stress field is replaced by a more local active stress field, affected also by magmatic and gravity forces. Indeed, the whole eastern flank of the volcano is unstable, producing sliding of the flank towards the sea. This local stress field, with an E-W to WNW-ESE horizontal σ_3, produces the formation of several faults affecting the northeast, east and southeast sectors of the volcano (De Guidi et al., 2018; Carnemolla et al., 2023), like the left-lateral strike-slip Pernicana Fault in the north (Kieffer, 1985; Neri et al., 1991; Borgia et al., 1992; McGuire and Saunders, 1993) (Fig. 6B). The sliding rate is 2 cm/yr, or higher during episodes of flank slip acceleration (Groppelli and Tibaldi, 1999; Tibaldi and Groppelli, 2002; Palano et al., 2009), and it is accompanied by complex internal deformation and active faulting along the flank margins.

Mt. Etna presents a constantly open central conduit, which feeds five summit central craters, named Northeast Crater (formed in 1911), Voragine (1945), Bocca Nuova (1968), Southeast Crater (1971), and New Southeast Crater (2007), causing summit eruptions (Fig. 6B). Volcanic activity occurs also on volcanic flanks, along radial fissures fed by shallow dikes (depth of 1-3 km) propagating laterally from the central conduit (Acocella and Neri, 2009). These fissures are distributed along three main rift zones: the W rift, the S rift, and the NE rift (Cappello et al., 2012). On the eastern flank of the volcano, a wide depression with an amphitheater

shape, known as Valle del Bove (VdB), is evident. For my project, I focused on an area located to the NE of the northern escarpment of the VdB (Fig. 6B), which is constituted of volcanic deposits of the Valle del Bove phase. Above these deposits, the thick succession of the Ellittico volcano is composed of lava flows alternated with pyroclastic deposits, emplaced between about 60 and 15 ka. The most recent activity (< 15 ka), related to the Mongibello volcano, covers most of the area and determines the morphology of the actual Etna volcano (Branca et al., 2011a, b). In this area, the eruptive fissures of the Mongibello are spatially concentrated along two main weakness zones, along which magma rises generating flank eruptions: the NE Rift and another ENE-trending alignment, named ENE Rift (Kieffer, 1975, 1985; Lo Giudice et al., 1982; McGuire and Pullen, 1989; Patanè et al., 2011; Azzaro et al., 2012; Cappello et al., 2012) (Fig. 6B).
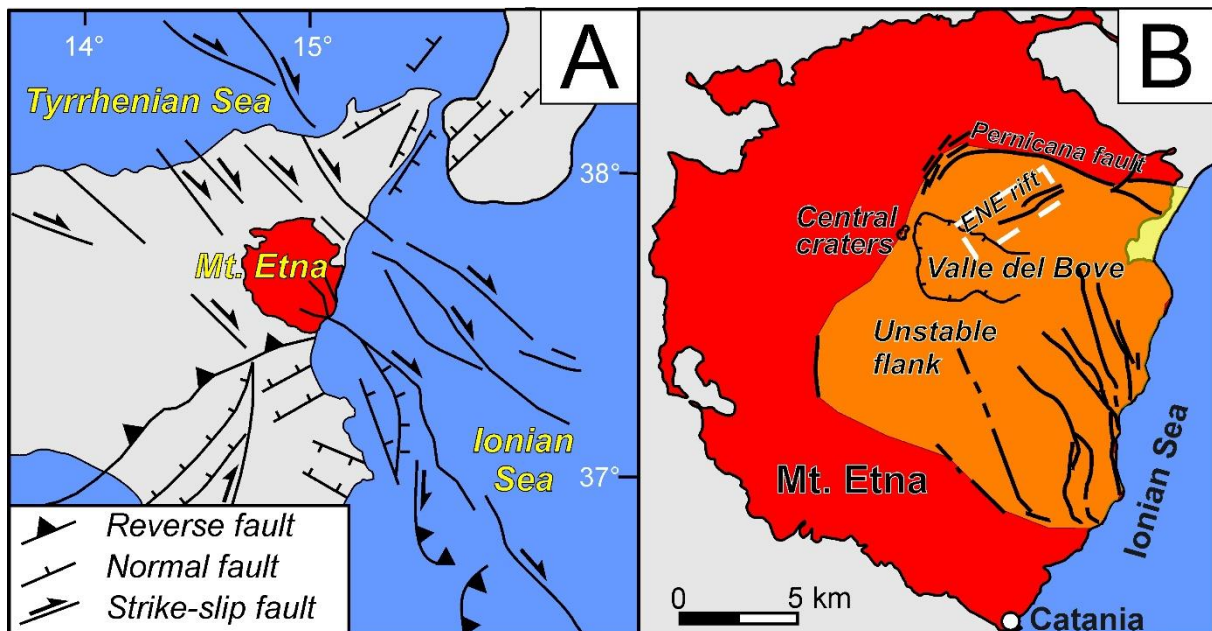
Fig. 6. (A) Map showing the geodynamic setting of Mt. Etna (Coordinate Reference System: WGS 84 – Geographic coordinates), and (B) main structures of Mt. Etna, modified after Villani et al. (2020). The offshore faults in (A) are from Gambino et al. (2022). The white dashed box in (B) marks the location of the ENE Rift zone (Drymoni et al., 2023).

The ENE Rift is located along the northern shoulder of the VdB, and it is composed of a swarm of dry and eruptive fissures striking from N70°E to N90°E, at an elevation of about

2300-1600 m a.s.l. (Azzaro et al., 2012). The first eruptive fissures of the ENE Rift formed during flank eruptions occurring between 15 ka and 3.9 ka (Branca et al., 2011a). In the last 2500 years, the ENE Rift was affected by the eruptions of Mt. Rinatu, dated 1000 ± 50 AD, and Scorciavacca, dated 1020 ± 40, and by eruptions dated 1865, 1928, 1971 and 1979 AD (Branca et al., 2011a). My case studies are focused on two of the most recent eruptions, the 1928 and the 1971 events.

3.1.1 1928 Eruptive Fissure

The 1928 fissure eruption generated a swarm of fractures and eruptive vents extending from the northern edge of the VdB to the west, up to the Ripe della Naca faults to the east (Fig. 7). The eruption started on November 2nd, after an intense explosive activity at the NE crater (Branca et al., 2017). The first segment of the eruptive fissure was 450 m long and formed at 2600 m a.s.l. (UF in Fig. 7), producing a short, 0.45 km-long lava flow in less than one hour. A second segment opened on November 3rd more to the east, at Serra delle Concazze, with a length of 3.2 km between 2300 m and 1560 m a.s.l., forming a lava flow that destroyed the woods nearby, reaching a distance of 3.8 km (MF in Fig. 7). The third and last segment opened more to the east on November 4th, at a lower altitude (1200 m a.s.l.), at the Ripe della Naca faults (LF in Fig. 7). The development in time of these eruptive fissures, from west to east, clearly indicates a propagation in the same direction of the feeder dike. The lava flow emitted from the last segment (LF) advanced fast along the Pietrafucile-Vallonazzo stream gully, with a velocity of 0.46 km/h, reaching the village of Mascali and destroying it on November 6th. On the following days, the advance of the lava flow caused the interruption of all the communication routes between the cities of Catania and Messina, destroying 716 ha of productive land and eight industrial plants, and resulting in about 5000 people homeless. Finally, on November 19th, lava emission ended, after having generated a 9.4 km-long overall flow, which reached an elevation of 25 m a.s.l. and destroyed a few houses in the village of Carrabba. As a result of these 17 days of activity, a total volume of 52.9 ± 5.2 × 10^6 m^3 of lava was erupted, with an average effusion rate of 38.5 m^3/s (Branca et al., 2017). This eruption has been the only event, after 1669, that destroyed a village in the Etna region, involving the northeastern flank and the opening of a fissure system.
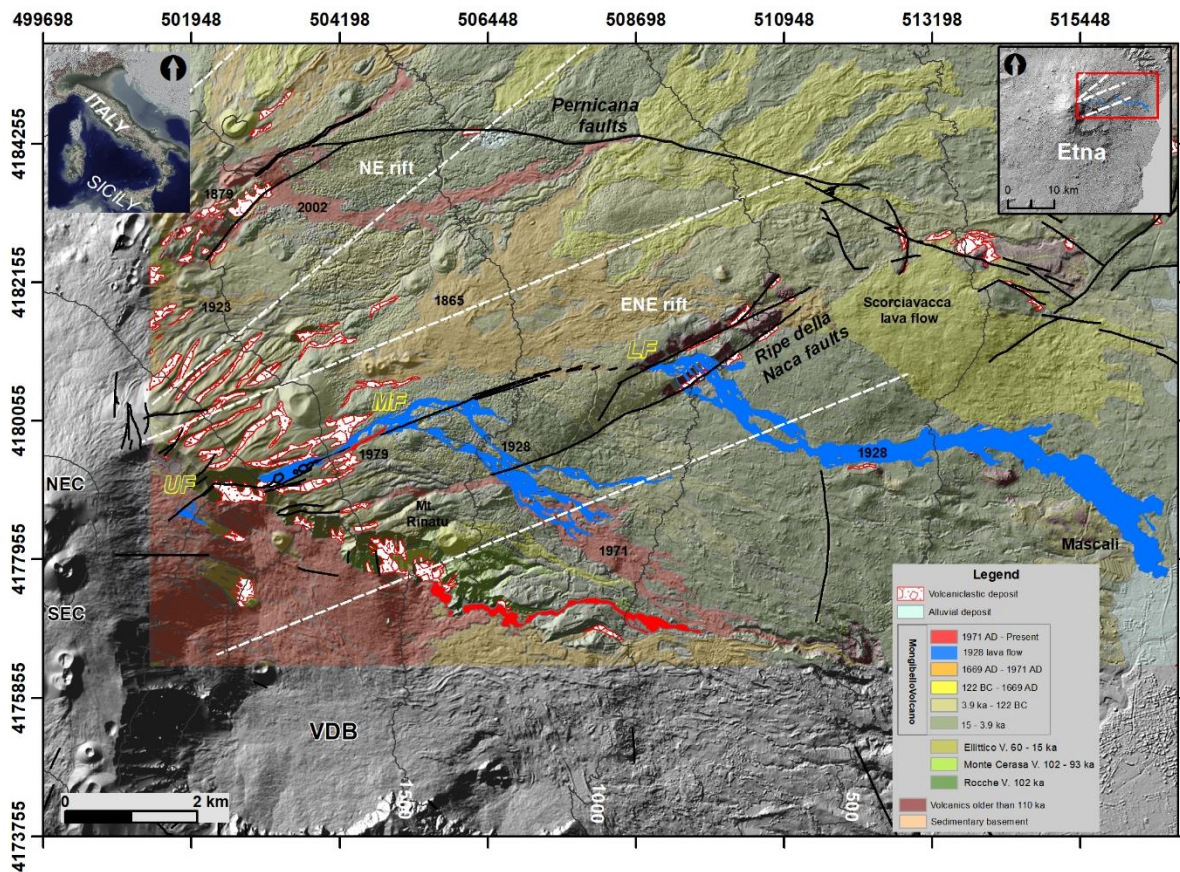
Fig. 7. Geological map of the area affected by the 1928 eruption. The shaded DEM on the background is from http://geodb.ct.ingv.it/geoportale. The two insets show the location of Mt. Etna and the study area. The white dashed lines delimit the NE Rift and the ENE Rift. The numbers specify the age of flank eruptions. Black lines indicate the main faults (after Azzaro et al., 2012). Coordinate Reference System: WGS 84 - UTM zone 33N. UF: Upper Fracture, MF: Middle Fracture, and LF: Lower Fracture are the segments of the 1928 fracture swarm. Contour lines every 500 m were extracted from the 2005 DEM by Gwinner et al. (2006). VDB: Valle Del Bove, SEC: Southeast Crater, NEC: Northeast Crater (Tibaldi et al., 2022).

3.1.2 1971 Eruptive Fissure

The 1971 eruption developed in two stages, first between April 5th and May 6th, and later between May 7th and June 12th (Branca et al., 2021). During the first stage, four WNW-ESE to N-S-trending eruptive fissures formed at an elevation of about 3000 m a.s.l., near to the southern and eastern sectors of the summit craters (Fig. 8). After May 7th, a fissure system

with a WSW-ENE orientation opened from about 2900 m a.s.l. to 2300 m a.s.l., with the formation of five eruptive vents that emitted lava flowing in the VdB (Fig. 8). During this eruption (May 17th), a new pit crater formed on the SE flank of the summit craters, at about 3000 m a.s.l. In the following years, this crater became the most active within the summit craters of Mt. Etna, and it was called SE crater (Romano et al., 1981). On May 11th/12th, the eastward propagation of the dike intersected the northern wall of the VdB at Serra delle Concazze, generating two eruptive fissures at 1840 and 1800 m a.s.l., at Serracozzo. These fissures were characterized by effusive activity only, with lava that flowed for 7 km, before stopping at about 600 m a.s.l. (Fig. 8) (Branca et al., 2021).
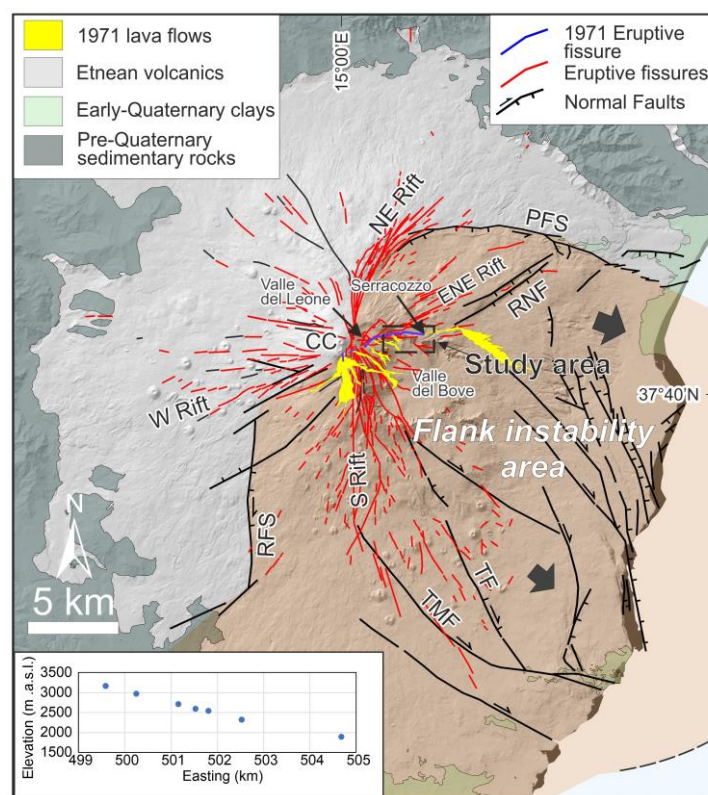
Fig. 8. Map of the main volcanotectonic structures of Mt. Etna, with the 1971 eruptive fissures and lava flows highlighted. Arrows indicate the direction of the flank-instability displacement. The black box indicates the study area. CC: central craters; RNF: Ripe della Naca normal faults; PFS, Pernicana fault system; RFS, Ragalna fault system; TF, Trecastagni fault; TMF, Tremestieri fault (modified after Neri et al., 2011; Branca et al., 2011a, 2021). Coordinate Reference System: WGS84 - Geographic coordinates. In the inset, the elevation of the 1971 vents relative to the Easting is shown (modified after Bonali et al., submitted).

In my project, I focused in the area located in correspondence of the northern escarpment of the VdB, and immediately to the NE (Fig. 8). Here, the eastward propagation of the feeder dike caused the formation of a graben, still well visible in section along the VdB wall (Fig. 9A). In the study area, products related to the Ellittico (60-15 ka) and Mongibello (< 15 ka) volcanoes are exposed and are nowadays covered by meters of recent pyroclastic fall deposits (Branca et al., 2011a, b). The detailed stratigraphy of the northern VdB wall in the study area is shown in Figure 9B.
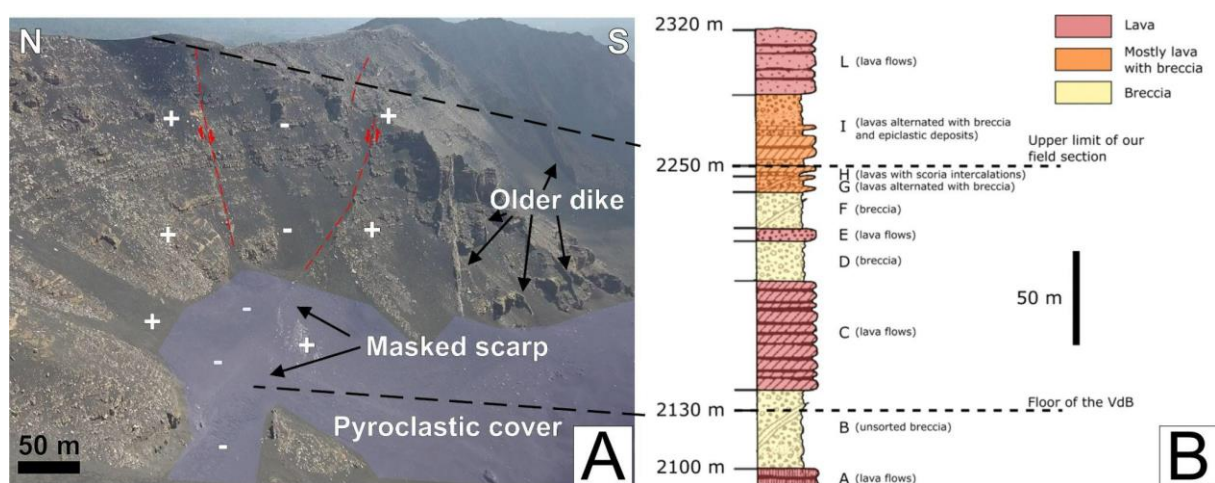
Fig. 9. (A) Dike-induced graben in section view, photo collected with UAV survey. Normal faults are shown in red with the direction of movement, and the downthrown block is highlighted with the negative symbol. Nowadays, pyroclastic deposits cover the scarps in the VdB. (B) Stratigraphic column of the studied outcrop along the northern wall of the VdB, after Branca et al. (2011a). A-I: subunits of the Serra delle Concazze Formation - Ellittico Volcano (60–15 ka). L: Pietracannone formation - Mongibello Volcano (last 15 ka). The units have been summarized according to their mechanical properties, as will be explained in detail in Chapter 5 (modified after Bonali et al., submitted).

3.2 Iceland

Iceland is located along the Mid-Atlantic Ridge, at the boundary between the North American and Eurasian plates, and above the Iceland hotspot, centered beneath the

Vatnajökull icecap (Jacoby and Gudmundsson, 2007; Thordarson and Höskuldsson, 2014). It represents a very peculiar site from a geological point of view, being the result of the combination of mid-oceanic ridge and hotspot volcanism. Due to this combination of magmatism, Iceland represents the only emerged part of the Mid-Atlantic ridge, rising more than 3000 m above the surrounding sea floor (Thordarson and Höskuldsson, 2014). The oceanic crust forming the island is very young, with the oldest rocks dated 14-15 Ma found in western and eastern Iceland (Sigmundsson and Sæmundsson, 2008).

The presence of the Mid-Atlantic Ridge is evident on land through active volcanic zones (or rift zones) that cut the island from SW to NE. The main volcanic zones present in Iceland are shown in Figure 10: the Western and Eastern Volcanic Zones (WVZ and EVZ), the Reykjanes Peninsula Ridge (RPR), and the Northern Volcanic Zone (NVZ) (Einarsson, 2008). These volcanic zones are 20-50 km wide, and are in turn composed of several volcanic systems, which include fissure swarms. Nowadays, there are 30 active volcanic systems, with about 40 extinct ones that have been identified and located (Gudmundsson, 2000) (Fig. 10). Fissure swarms are composed of eruptive fissures, tension fractures and normal faults extending from central volcanoes (Tryggvason, 1973; Sæmundsson, 1978; Hjartardóttir and Einarsson, 2015), representing the result of deformation due to tectonic and magmatic activity. Transform faults, called fracture zones, connect the volcanic zones, and represent the most seismically active regions of Iceland (Fig. 10) (Einarsson, 2008). In the North, most of the seismicity is concentrated along the Tjornes Fracture Zone (TFZ), which includes the Grímsey Oblique Rift (GOR), the Húsavík-Flatey Zone (HFZ) and the Dalvík Zone (DZ), and connects the NVZ to the offshore Kolbeinsey Ridge (Einarsson, 1991; Magnúsdóttir and Brandsdóttir, 2011). In the South, the EVZ and RPR are linked by the South Iceland Seismic Zone (SISZ) (Fig. 10).

In Iceland, the average spreading rate is 2 cm/yr (DeMets et al., 1994), but this is episodic along each volcanic system. Structures along fissure swarms are mainly activated during rifting episodes, when magma propagates through dikes, inducing tension fractures and faults and, if it reaches the surface, eruptive fissures (Sæmundsson, 1978; Sigmundsson, 2006). The plate boundary is also clearly defined by the earthquakes epicenters, visible in Figure 10.
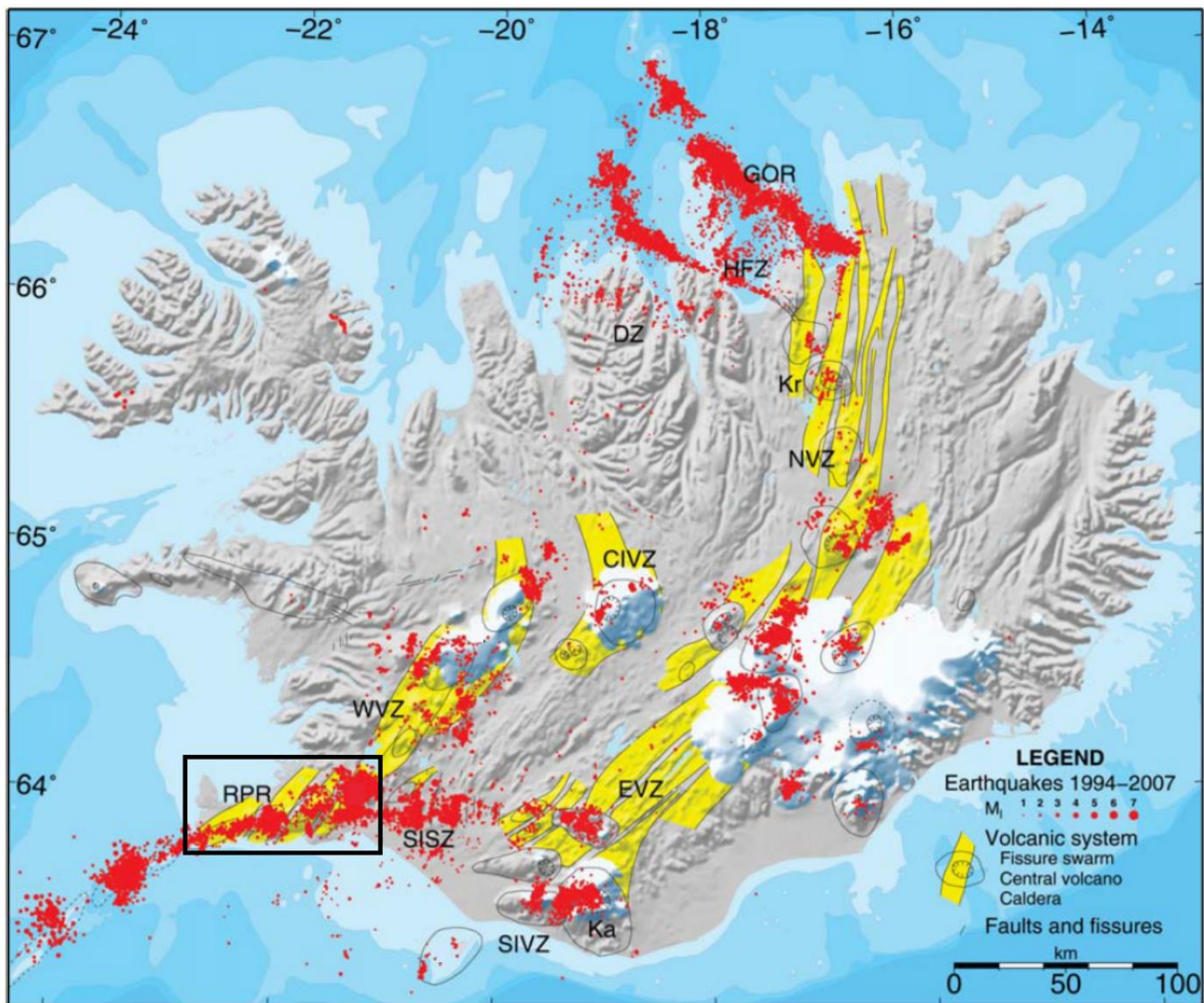
Fig. 10. Map showing the volcanic zones and the volcanic systems of Iceland, and earthquakes epicenters between 1994-2007. The black box indicates the location of Figure 11. RPR: Reykjanes Peninsula Rift, WVZ: Western Volcanic Zone, SISZ: South Iceland Seismic Zone, SIVZ: South Iceland Volcanic Zone, EVZ: Eastern Volcanic Zone, CIVZ: Central Iceland Volcanic Zone, NVZ: Northern Volcanic Zone, GOR: Grímsey Oblique Rift, HFZ: Húsavík-Flatey Zone, DZ: Dalvík Zone. Coordinate Reference System: WGS84 - Geographic coordinates (modified after Einarsson, 2008).

During historical time, 20-25 eruptions for century have occurred in Iceland, with different styles of eruption (Thordarson and Larsen, 2007). The eruptions that produced the largest lava flows were the Laki eruption in 1783-1784 AD and the Katla (Ka in Fig. 10) eruption in 934 AD. However, the magmatic activity in Iceland is not reflected only by volcanic eruptions,

but also by intrusive episodes that occur in the crust. Seismicity and crustal deformation studies show that the intrusion of magma towards the shallow levels of the crust is episodic, with an alternation of inflation and deflation periods (e.g., Sigmundsson, 2006; Sturkell et al., 2006; Ducrocq et al., 2021). In most cases, no eruption at the surface occurs, and magma is emplaced at various depths in the crust (Pedersen and Sigmundsson, 2006). The first instrumentally recorded rifting episode took place in the Krafla Fissure Swarm (NVZ) between 1975-1984 and was related to continuous inflow of magma towards a magma chamber at a depth of 3-7 km (Tryggvason, 1994; Brandsdóttir et al., 1997). During the episode, the formation of tension fractures and normal faults associated with dike intrusions was observed (Sigurdsson, 1980; Opheim and Gudmundsson, 1989; Rubin, 1992).

In my project, I focused on an area located in the Reykjanes Peninsula Ridge, in the southwest, that will be presented in the following subsection.

3.2.1 Reykjanes Peninsula Ridge and Stampar crater row

In Iceland, the Reykjanes Peninsula Ridge (RPR) represents the southernmost segment of the Mid-Atlantic Ridge, characterized by a high obliquity respect to the spreading direction. This peculiarity causes the coexistence of volcanism and strong earthquakes in the Reykjanes Peninsula, combination that is uncommon in the rest of the island (Einarsson, 2008). The trend of the RPR is ENE, with a direction of N70°E, whereas the spreading direction has been calculated as N101°E in this area (DeMets et al., 1994). Along the RPR, four volcanic systems have been identified. These volcanic systems affect an area characterized by a strong volcanic and geothermal activity and are, from west to east, Reykjanes, Krísuvík, Brennisteinsfjöll and Hengill Volcanic Systems (Einarsson and Sæmundsson, 1987). They include fissure swarms, which are in turn composed of eruptive fissures, normal faults and tension fractures (Fig. 11). On the peninsula, rifting episodes associated with volcanism occur every 800-1000 years, affecting different volcanic systems at intervals of 100-200 years. Fissural volcanism became dominant in the RP starting from 14,500 yr BP (Sæmundsson et al., 2020), with alignments of scoria and spatter cones identifying the eruptive fissures. These have an average strike of N40°E, parallel to the orientation of the fissure swarms (Clifton and Schlische, 2003) (Fig. 11).

Before the 2021-2023 Fagradalsfjall eruption, the last episode in the RP occurred between 700 and 1240 AD, with fissure eruptions with the same NE-trending orientation (Sæmundsson et al., 2016, 2020).
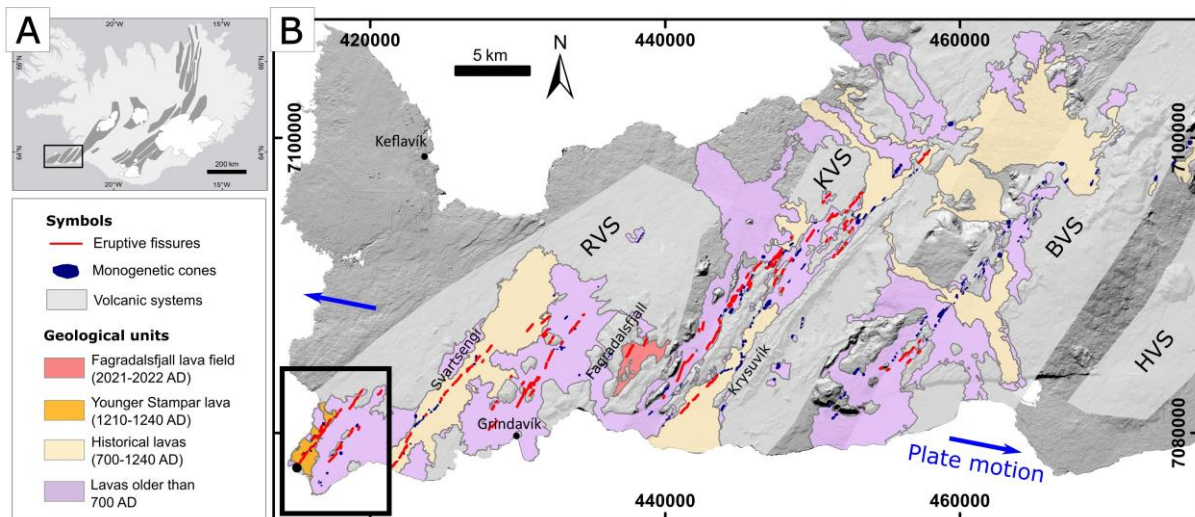
Fig. 11. (A) Inset showing the main volcanic zones of Iceland (from Einarsson, 2008), coordinate Reference System: WGS84 - Geographic coordinates. (B) Map showing the volcanic systems of the Reykjanes Peninsula (after Einarsson and Sæmundsson, 1987) and historical and prehistoric lava fields (from Sæmundsson et al., 2016), including the Younger Stampar and the 2021-2022 Fagradalsfjall lava flows (from https://geovis.hi.is/). Coordinate Reference System: WGS 84 - UTM zone 27N. RVS: Reykjanes, KVS: Krísuvík, BVS: Brennisteinsfjöll, HVS: Hengill Volcanic System. Blue arrows show the plate motion direction (N101°E, from DeMets et al., 2010). The DEM in the background is the 2-m resolution Arctic DEM (https://www.pgc.umn.edu/data/arcticdem/). Location of the study area is indicated by the black box. The black dot indicates the location of the studied outcrop (Corti et al., 2023).

The case study area is located in the Reykjanes Fissure Swarm (RFS), in the Reykjanes Volcanic System (RVS). The RFS is 45 km long, of which 30 km on land, and 5-6 km wide (Sæmundsson et al., 2020). Eruptive activity along this fissure swarm is characterized by hydrovolcanic activity offshore and effusive activity on land, as occurred during the Younger Stampar eruption, in the early 13th century (Sigurgeirsson, 1995). This was the youngest of

37

three "Stampar" eruptions, occurred in the last 4000 years (Sigurgeirsson, 1992). The oldest one is dated 3500-4000 yr BP, and today its products are visible only in three small outcrops. The other two eruptions are called "Older" and "Younger Stampar", dated 2000 yr BP and 13th century, respectively, and their crater rows are clearly visible on land, with a length of 7 and 4 km, respectively (Fig. 12A).

This work is focused especially on the Younger Stampar eruption, which occurred during the Reykjanes Fires (1210-1240 AD, Sæmundsson et al., 2016). The eruption started offshore, with the formation of two tuff cones due to surtseyan eruptions (Sigurgeirsson, 1995). These craters have been mostly eroded by the sea, but the remains of the younger of the two cones, called Karl, are still visible from the cliff (Fig. 12A), forming a 50-m tall pillar. After this first offshore phase, the eruption started on land with a Hawaiian type of eruption. Subaerial activity formed a NE-SW trending 4-km-long eruptive fissure characterized by an alignment of scoria and spatter cones (Sigurgeirsson, 1995), highlighted in Figures 12A-B.
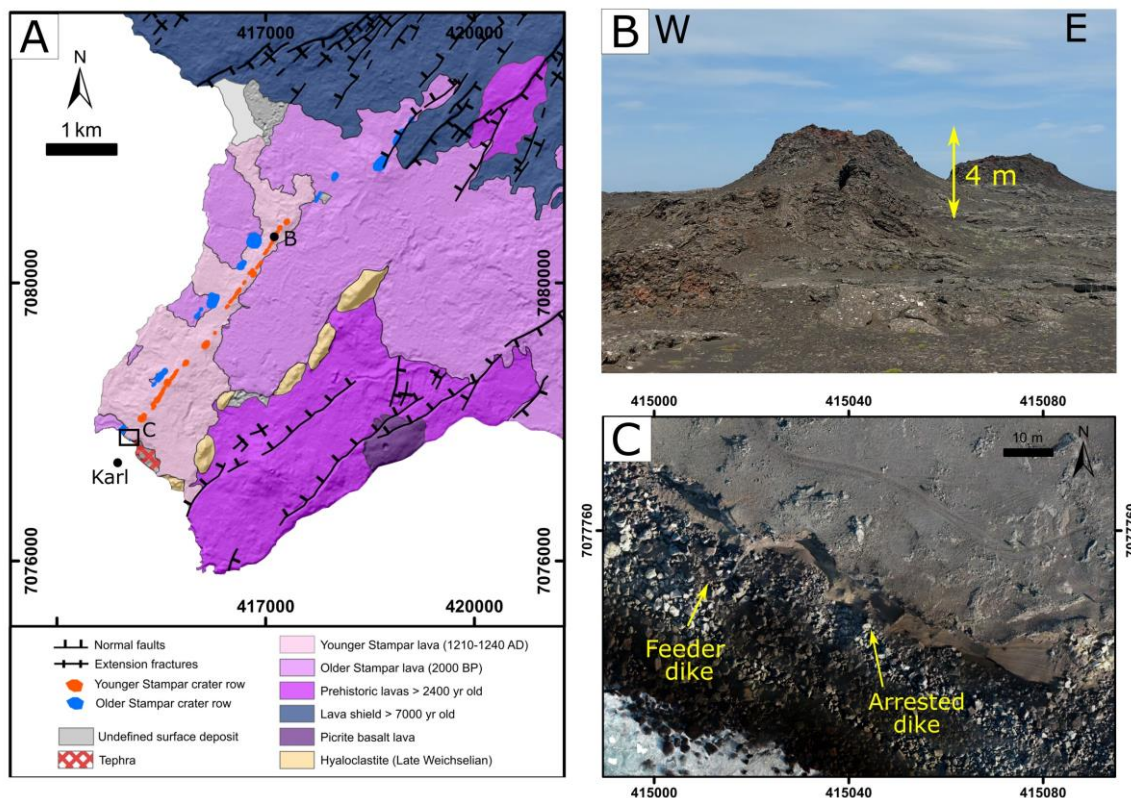
Fig. 12. (A) Geological-structural map of the area affected by the Older and Younger Stampar eruptions, modified after Sæmundsson et al. (2016) with the help of historical aerial

photographs. The crater rows associated with these eruptions and the location of the Karl crater cone are highlighted. Coordinate Reference System: WGS 84 - UTM zone 27N. (B) Aligned scoria and spatter cones of the Younger Stampar crater row (location in Fig. 12A). (C) Plan view of the dikes outcropping along the cliff on a high-resolution orthomosaic (location in Fig. 12A). Coordinate Reference System: WGS 84 - UTM zone 27N (Corti et al., 2023).

Along the cliff, two dikes related to the eruption are exposed. One of them is clearly arrested, whereas the other one, located at a distance of just 30 m to the NW, fed the upper part of the Younger Stampar lava flow (Gudmundsson, 2017) (Figs. 12C and 13). As highlighted in the literature, the former cuts through a soft tuff layer, constituted by tephra deposits from the Karl crater cone, dated 1211 AD using tephrochronology, ^{14}C dating, and written sources (Sigurgeirsson, 1995; Sæmundsson et al., 2020), but it arrests when it meets the Younger Stampar lava flow only few meters below the surface (Gudmundsson, 2017). The latter feeds the Younger Stampar lava flow and is suggested by Gudmundsson (2017) to have intruded before the arrested dike. The feeder dike is visible up to the center of the Younger Stampar lava flow, suggesting that probably it fed the upper part of it and the main part of the Younger Stampar volcanic fissure, whereas the lower part of the lava flow was erupted before from the Karl crater cone (Gudmundsson, 2017).
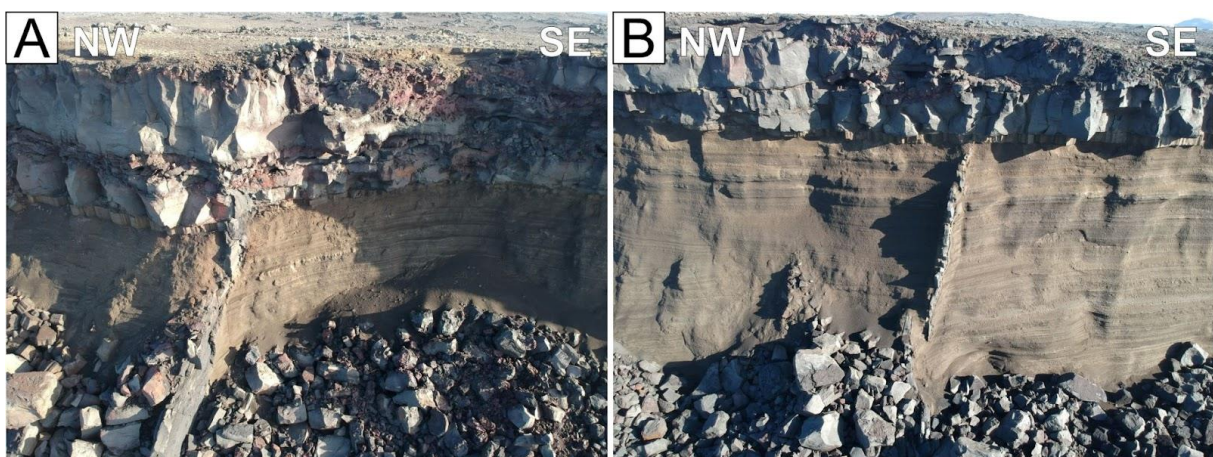
Fig. 13. UAV-captured pictures showing (A) the feeder and (B) the arrested dikes. Locations of the two dikes are shown in Figure 12C (Corti et al., 2023).

4. Case study 1 – 1928 Fissure (Mt. Etna)

4.1 Introduction to the case study

In shallow settings, the propagating dike causes a concentration of tensile (σ_3) and shear (τ) stress at its tip and in the host rock (Gudmundsson, 2011a), which can lead to deformation of the topographic surface, with upwarping, tension fractures, normal faults and grabens (e.g., Rubin and Pollard, 1988; Acocella and Trippanera, 2016). The geometry of these structures depends on geometric characteristics of the dike, layering of the host rock and topographic effects (e.g., Acocella et al., 2006, 2009; Battaglia et al., 2011; Abdelmalak et al., 2012; Trippanera et al., 2014, 2015a; Guldstrand et al., 2017; Gudmundsson, 2020; Tibaldi et al., 2020b). Studies on dike-induced surface deformation have increased in the last years, but more field observations and realistic data regarding surface deformation, dike geometry and host rock stratigraphy are needed to better understand the relation between dike intrusions and deformation at the surface.

This case study focuses on the structures associated with the eruptive event occurred at Mt. Etna (Italy) in 1928 AD (Duncan et al., 1996; Branca et al., 2017). The eastward propagation of a dike caused the opening of three eruptive fissures (Fig. 7), and the formation of various kinds of structures, such as grabens, half-grabens, dry tension fractures and volcanic vents. Field- and remote sensing-collected structural data and lithostratigraphic observations were integrated with FEM numerical models to investigate the geometrical and mechanical conditions that could have determined the formation of the observed structures at the surface. Sensitivity tests were performed to observe the effect on surface deformation of dike overpressure and attitude, host rock properties, layer thickness and stratigraphic sequence.

The results of this case study have been published in two papers; the first one shows the collected structural data (Tibaldi et al., 2022), whereas the other is more focused on numerical modeling (Drymoni et al., 2023). I actively participated in the fieldwork and in the quantitative structural data collection. Numerical models were designed by Dr. Kyriaki Drymoni and Dr. Elena Russo.

4.2 Specific materials and methodology

4.2.1. Analysis of historical aerial photographs and field surveys

To recognize and map all the structures associated with the propagating dike, I used historical aerial photographs collected in 1932, 1954 and 1955. As explained in detail in Chapter 2, the photos were bought from the Istituto Geografico Militare (IGM, https://www.igmi.org/) and were processed to obtain georeferenced orthomosaics and DSMs of the study area. Comparing photos from different years, all the structures were mapped and classified, separating the ones associated with the 1928 eruption from the ones formed during later eruptions in the same area (1971 and 1979 AD). In GIS environment (ArcMap v. 10.8.1), through the "Linear Directional Mean" tool, it was possible to collect the strike, length, and the coordinate (X, Y) of the midpoint of each structure, which are presented in Appendix 1, Table A1.1.

After this step, I performed a detailed field survey along the entire length of the 1928 fissure, to validate the classification made on the historical aerial photographs and collect quantitative and qualitative structural measurements. Structures were classified as normal faults (Fig. 14A), tension fractures (Fig. 14B) and eruptive fissures (Fig. 14C), using the method described in Section 2.1. Furthermore, the structures associated with the 1928 eruption were distinguished from those generated by earlier events. To do that, the stratigraphic relation between the structures and the 1928 products was considered, classifying as previous structures the ones that were clearly covered by the 1928 lava flows. Moreover, in the field the pre-1928 structures were filled with sediments and vegetation, whereas the 1928 structures showed a lower degree of sediment infilling and only young vegetation. Fault scarps were observed in detail to recognize signs of reactivation, such as different degrees of erosion or different distributions of vegetation, finding no evidence. Finally, historical papers that describe the 1928 eruption and report the new fractures were considered (Imbò, 1928; Ponte, 1928, 1929; Friedlander, 1929).
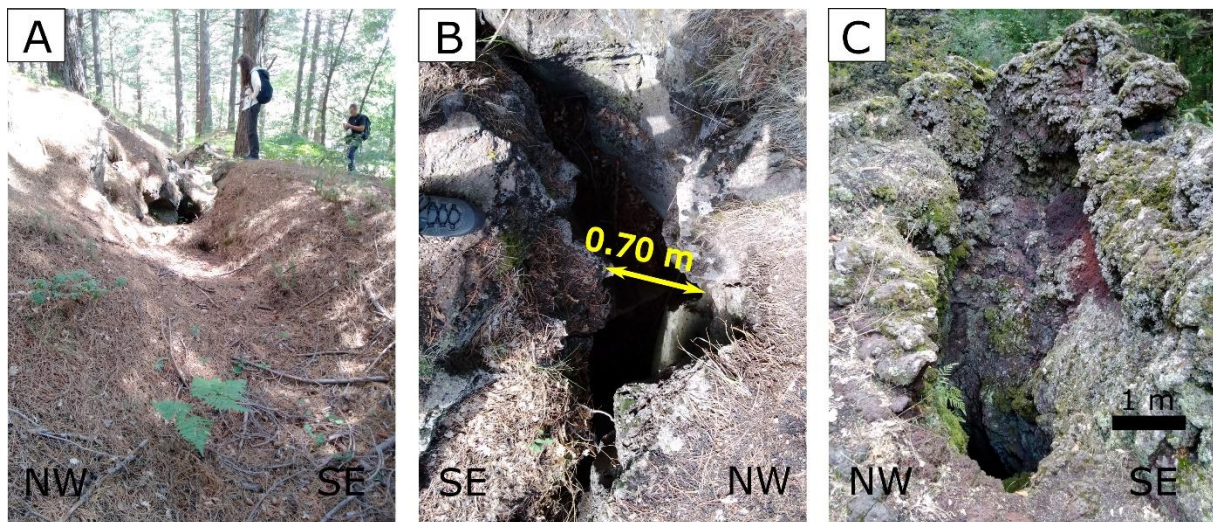
Fig. 14. Examples of (A) a SE-dipping normal fault, (B) a dry tension fracture and (C) an eruptive fissure with spatter lava deposits, surveyed in the field (Tibaldi et al., 2022).

In the field, structural data were collected at 439 structural stations. Each measurement was collected with RTK-GPS accuracy (2 cm) and was referred to the WGS84 datum. In each site, strike, opening direction and opening amount of tension fractures were measured, as well as the vertical offset and attitude (dip and dip direction) of normal faults. Opening directions were calculated only when piercing points were visible on both sides of the fracture (Fig. 14B). Vertical offset of faults was measured using a tape for offsets < 2 m, and with a laser rangefinder for offsets > 2 m, with an uncertainty of 0.10 m and 0.20 m, respectively. All the quantitative structural measurements collected in the field at the structural stations are presented in Appendix 1, Table A1.2.

4.2.2. Setup of models

As explained in Chapter 2, the collected structural data were used as inputs for 2D FEM numerical models, through the software COMSOL Multiphysics (v. 5.6), to understand the conditions that could have caused the formation of the observed structures at the surface. Specifically, the role of dike overpressure and attitude, host rock properties, layer thickness and stratigraphic sequence was investigated. The dike was created as an elliptical cavity, with

a thickness of 0.5 m and an overpressure of P_0 = 1-20 MPa (Becerril et al., 2013), propagating through an elastic layered host rock.

For the sensitivity analyses, the setup was designed in a 50 x 50 m square box, discretizing the domain using very fine triangular meshing, with a minimum element quality of 0.4534 m and 1100 boundary triangular elements. The models were fastened in the two bottom corners with fixed constraints to avoid rigid-body rotation and translation (Geyer and Gottsmann, 2010; Browning et al., 2021) (Fig. 15).

The stratigraphy replicated the one observed in the field (Fig. 15) at an altitude of ~1600 m a.s.l., and was composed of:

- two comparatively stiff lava layers with a thickness of 1 m and 0.2 m, as measured in the field; $E_{CS, CS2}$ = 7-10 GPa, ρ = 2600 kg/m^3, v = 0.25.
- a tuff layer intercalated between the two comparatively stiff lavas, with a measured field thickness of 1 m; E_T = 1-5 GPa, ρ = 2000 kg/m^3, v = 0.25.
- a stiff lava layer constituting the host rock in the model setups; E_S = 7-30 GPa, ρ = 2600 kg/m^3, v = 0.25.

To analyze stress concentration around the dike tip and at the surface, tensile stress (σ_3) magnitude was plotted as color scale in the background, while absolute shear stress (τ, component of the von Mises shear stress on xy plane) concentration was plotted as line contours. Finally, σ_1 and σ_3 (maximum and minimum compressive stress, respectively) orientations were plotted as arrow surfaces, to observe the potential formation of stress barriers.

The following parameters were first varied to observe their influence on stress distribution and orientation: dike overpressure in the range 1-20 MPa, layer thickness within the range 0.1-1 m, stiffness of the layers within a range of 1-30 GPa, stratigraphic sequence, and dike inclination (0-10°) (Fig. 15). Subsequently, more sensitivity analyses were run considering also the presence of a scoria layer (E = 0.5 GPa, ρ = 2000 kg/m^3, v = 0.25) at the top and at the bottom of the stratigraphy, to investigate the effect of very soft pyroclastic layers in the sequence. For these last models, two scenarios were tested in terms of boundary loads: one with an overpressure of 1 MPa and an extension of 2 MPa, and the other with an

overpressure of 5 MPa and an extension of 0.5 MPa. Local extension was added to analyze the effect of active faults that exist near to the study area, like the Pernicana Fault at the NE tip of the rift, which is characterized by a slip rate of 2.7 cm/yr during the Late Pleistocene-Holocene (Tibaldi and Groppelli, 2002). GPS values are also consistent with this value (Palano et al., 2009). However, GPS vectors indicate a decrease of the flank slipping from NE to SW (Bonforte et al., 2007; Palano et al., 2009; Palano, 2016). For this reason, a scenario with a 0.5 MPa extension was also considered for the western part of the 1928 fissure.
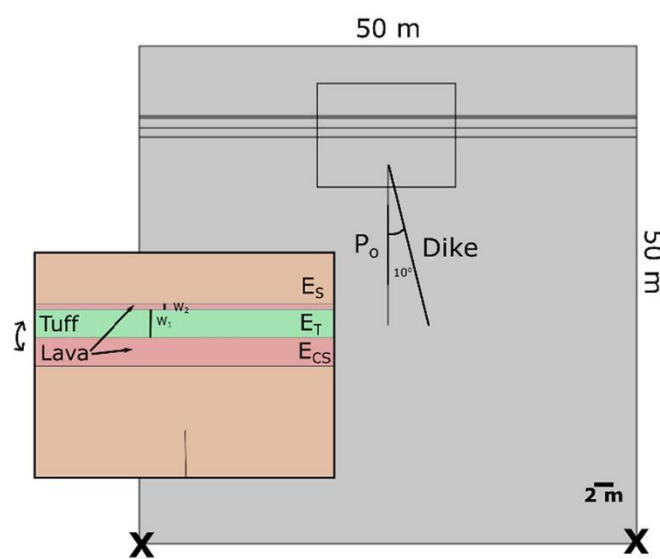
Fig. 15. Numerical model setup for sensitivity analyses. The dike is driven by internal overpressure (P_0) and was tested with different dip angles. The crosses at the two bottom corners indicate fixed constraints. Layers with different mechanical properties are represented with different colors (green for tuff, red for comparatively stiff lava flow and orange for the host rock) (Tibaldi et al., 2022).

Besides running sensitivity analyses, two different computational domains were designed to represent two different sectors of the 1928 fissure: the westernmost part of the 1928 fissure (called "Sector 1" in the next Section 4.3.1), and an easternmost site ("Sector 3" in the next Section 4.3.1). As will be explained in detail later, both sectors are characterized by the

presence of a graben formed during the 1928 eruption, a large one (385 m wide) in the western site, and a narrower one (about 70 m wide) more to the east.

For the western site, the stratigraphy was derived from a stratigraphic log from Branca et al. (2011a), located along the northern escarpment of the Valle del Bove, between 2100 and 2330 m a.s.l. The stratigraphic sequence here includes two formations, Serra delle Concazze and Pietracannone, that are in turn divided into several volcanic units (A-L) (Fig. 16A). From bottom to top, we find:

A) Porphyritic lava flows (10 m thick);

B) Brecciated layers, crossed by the 1971 and 1986-87 eruptive fissures (40 m thick);

C) Subaphyric lava flows (55 m thick);

D) Scoriaceous breccia deposits (20 m thick);

E) Compact subaphyric lava flows (5 m thick);

F) Scoriaceous breccia deposits (19 m thick);

G) Sequence of lavas and breccias (6 m thick);

H) Sequence of thin lava flows intercalated with scoriae deposits (5 m thick);

I) Sequence of epiclastic and scoriaceous breccia deposits with lava units (40 m thick);

L) Lava flows (30 m thick).

In the numerical models setup (Fig. 16B), the host rock material was at the bottom of the stratigraphy, characterized by a constant stiffness of 30 GPa. For stiffer materials, like lavas and lavas with intercalation of breccia, stiffness values of 10 GPa and 7 GPa were used, respectively. For softer materials, such as tuffs, breccia with minor lava intercalations, breccia and scoria, values of 5 GPa, 3 GPa, 1 GPa and 0.5 GPa were assigned, respectively. Poisson's ratio was 0.25 for all the materials, with density of 2600 kg/m^3 for stiff deposits and 2300 kg/m^3 for soft pyroclastic deposits (Babiker and Gudmundsson, 2004; Gudmundsson, 2012).

The dike was modeled at each contact (C), to observe the effect of stiffness contrasts both for the western (C_{W1}-C_{W6}) and the eastern (C_{E1}-C_{E3}) site (Fig. 16B). Mechanical contrasts are defined as the dimensional ratio, namely the E value of the upper layer divided by the E value of the lower layer (Kavanagh et al., 2006; Drymoni et al., 2020). For the western site, the contacts are the following, from the bottom to the top:

C_{W1} = L/HR = 10/30 = 0.3

C_{W2} = B/L = 1/10 = 0.1

C_{W3} = L/B = 10/1 = 10

C_{W4} = MB/L = 3/10 = 0.3

C_{W5} = ML/MB = 7/3 = 2.3

C_{W6} = L/ML = 10/7 = 1.42

For the eastern site, the stratigraphy is the one observed in the field that was used also for the sensitivity analyses (Fig. 16B). Contacts from the bottom to the top are the following:

C_{E1} = L/HR = 0.3

C_{E2} = T/L = 5/10 = 0.5

C_{E3} = L/T = 10/5 = 2
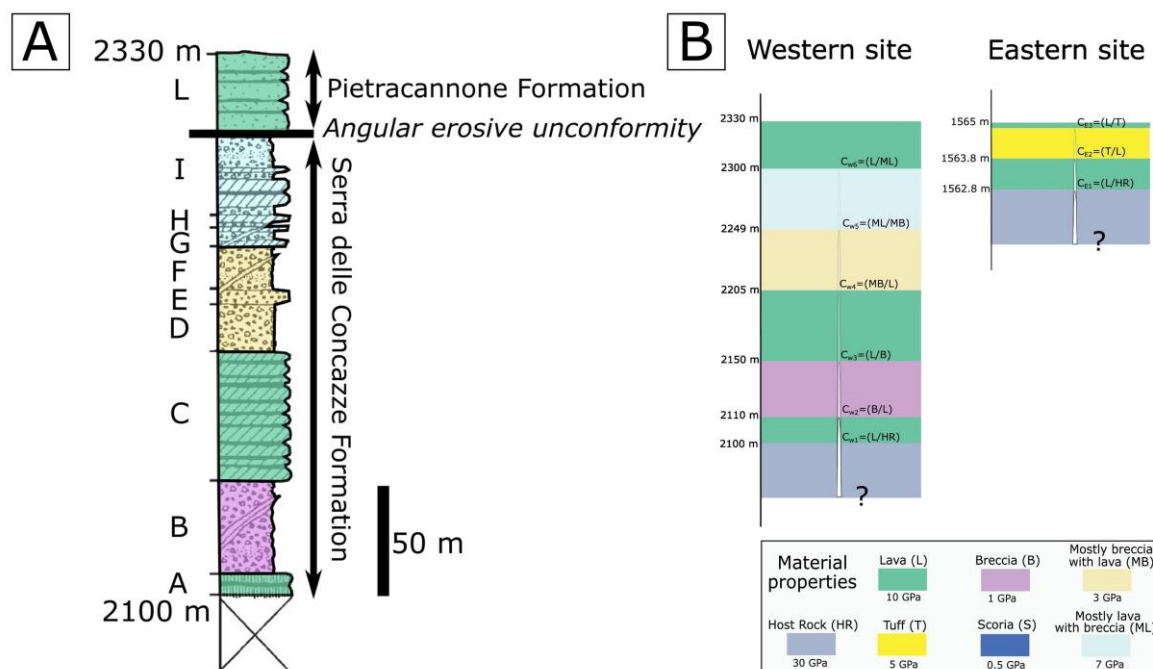
Fig. 16. (A) Detailed stratigraphic column of Sector 1 (defined also as "western site"), from Branca et al. (2011a), simplified based on mechanical properties of the layers for the numerical modeling setup. (B) Field-based setups of numerical models, with realistic properties based on Gudmundsson (2011a). Western site stratigraphy is based on (A), whereas the eastern site on field observations. C_{W1}-C_{W6} are the mechanical contacts of the western site, C_{E1}-C_{E3} of the eastern site (modified after Drymoni et al., 2023).

It is worth noting that the two sites differ in layer thickness of one order of magnitude, so, although the values of stiffness are the same, the ratios represent mechanical contrasts at different scales. With COMSOL Multiphysics (v5.6), two different computational domains were designed, 2330 x 2330 m for the western and 50 x 50 m for the eastern site, due to the different size of the layers in the two sectors (Fig. 16B). The domains have been discretized with an extremely fine triangular meshing, with a minimum element size of 0.0466 m for the western site and 0.001 m for the eastern site.

The dike overpressure ranges 1-10 MPa, consistently with previous studies (Gudmundsson, 2011a, 2012; Drymoni et al., 2020). The local extensional stress field (F_{ext}) ranges 0.5-2 MPa to reflect the existence of active faults, as already explained above. Based on GPS vectors, which indicate a decrease of the flank slipping from NE to SW (Bonforte et al., 2007; Palano et al., 2009; Palano, 2016), an extension of 2 MPa was applied for this case study, whereas only 0.5 MPa of extension were applied for the western site.

4.3 Results

4.3.1. Surface deformation

Through remote sensing analysis and field surveys, 159 structures were recognized along the 1928 fissure, and were classified as: 1928 eruptive vents (11 out of 159 - 7%) and previous eruptive vents (8 – 5%), eruptive fissure walls (33 – 21%), normal faults (29 – 18%), dry tension fractures associated with the 1928 event (38 – 24%), older structures (36 – 23%), and sinkholes (4 – 2%), as can be seen in Figure 17F.

The linear structures that were identified (136 in total, including eruptive fissures and dry tension fractures, normal faults and pre-1928 structures) mostly present an ENE-WSW direction, with a peak between N60-70°E (Fig. 17A), an average of N69.1°E and a standard deviation (SD) of 8.3°. This trend can be observed also in all the subsets, as can be seen in Figures 17B-C-D-E. Eruptive fissures show a peak between N60-70°E, with an average of N65.8°E and a SD of 7.1° (Fig. 17B). Normal faults present a peak in the interval N60-70°E, with an average of N72.3°E and a SD of 9.6° (Fig. 17C), whereas dry tension fractures show a peak between N70-80°E, with an average of N70.8°E and a SD of 6.4° (Fig. 17D). Finally,

structures generated by previous events show the same trend, with most values in the interval N60-70°E, an average of N67.6°E and a SD of 8.4° (Fig. 17E). Furthermore, quantitatively structural measurements were collected at 439 sites (Fig. 17G), as explained in the previous Section 4.2.1. All the collected measurements are listed in Appendix 1, Tables A1.1 and A1.2.
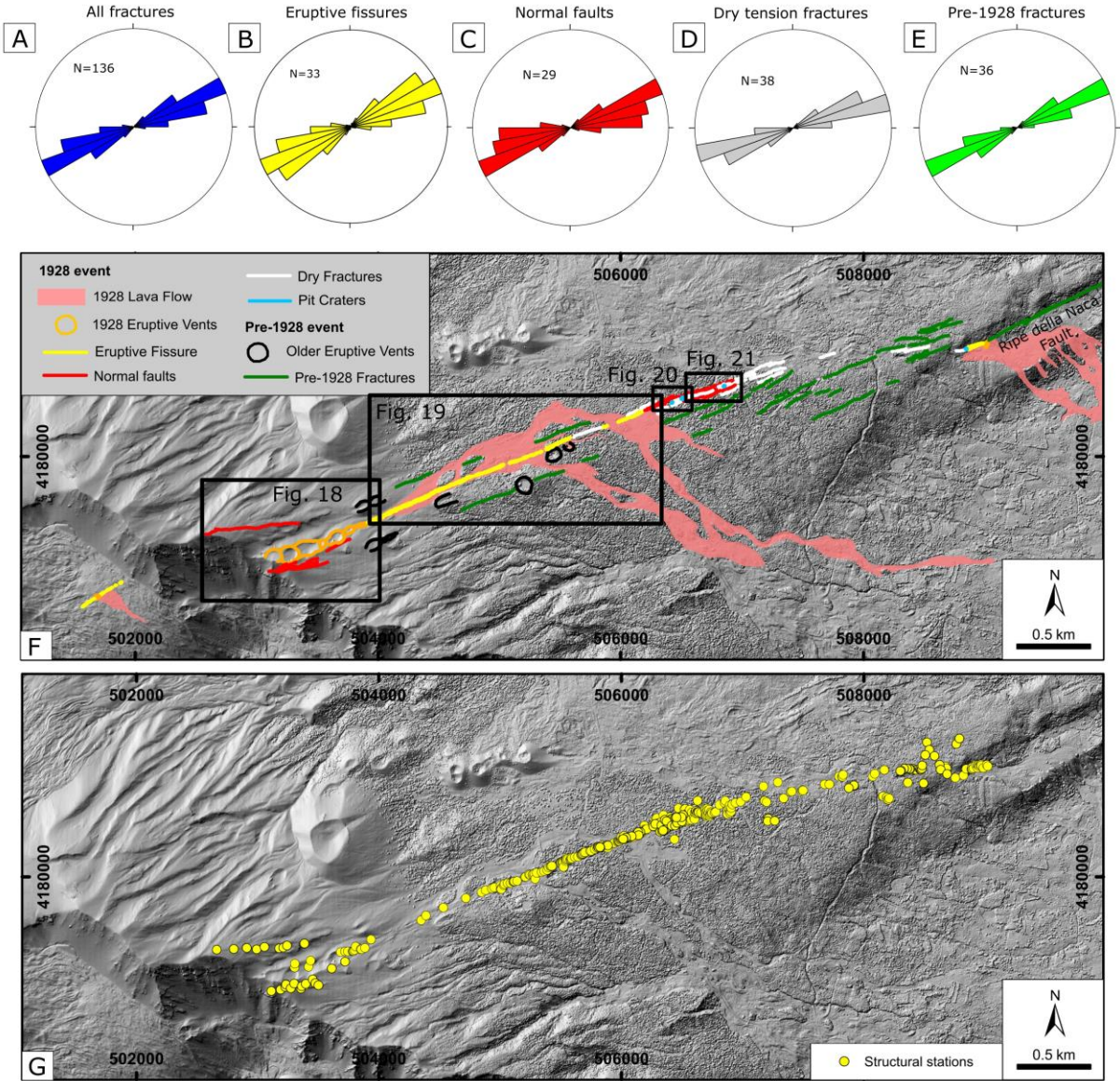
Fig. 17. Rose diagrams showing the strike of (A) the complete set of fractures, (B) eruptive fissures, (C) normal faults, (D) dry tension fractures and (E) pre-1928 fractures. (F) Structural map with the location of the different surface deformation settings, shown more in detail in

48

Field observations and the classification of the structures revealed four different settings of surface deformation (Fig. 17F), from the west to the east:

1) A sequence of eight eruptive vents with an ENE-WSW alignment, surrounded by a 385-m-wide graben with vertical offsets up to 10 m;

2) A single eruptive fissure, with ramparts of limited height indicating a minor Strombolian activity compared to sector 1, without the formation of a graben;

3) A 74-m-wide half-graben with offset values up to 1.2 m, followed by a 68-m-wide graben with offset values ranging from 0.3 m to 3.5 m, without evidence of eruption;

4) Lower vents aligned along the pre-existing Ripe della Naca Fault.

All these different settings will be described in greater detail in the following sections.

4.3.1.1. Sector 1: volcanic vents and graben

In the westernmost and more elevated sector of the 1928 fissure, an alignment of eight volcanic vents can be observed, with an average direction of elongation of N67°E, coherent with the general trend of the 1928 fissure (Figs. 18A-C). These vents are surrounded by normal faults with converging dips, which form a 385-m-wide graben (Fig. 18A). The width of the graben is constant through its length, along which the elevation decreases from 2300 to 2160 m a.s.l. for the southern fault, and from 2590 to 2220 m a.s.l. for the northern fault. These faults show an E-W strike, with vertical offsets values up to 10 m along the southern side of the graben. However, it must be considered that these scarps are now covered by younger volcanic deposits, as can be observed in Figure 18B, that make the measurements more difficult causing an underestimation of the true value of displacement. Moving to the east, from 2160 to 2100 m a.s.l., a single fault is observed south of the vents, with a 0.5-m offset (Fig. 18A).

Along the southern side of the graben, more faults are visible, whereas in the northern side one single fault is present, with offset values ranging between 1 and 3 m. The aerial photos

of 1932 collected by IGM confirmed that these structures were not associated to post-1928 events (such as the events of 1950, 1971 and 1979, which affected the same area on the eastern flank of Mt Etna).
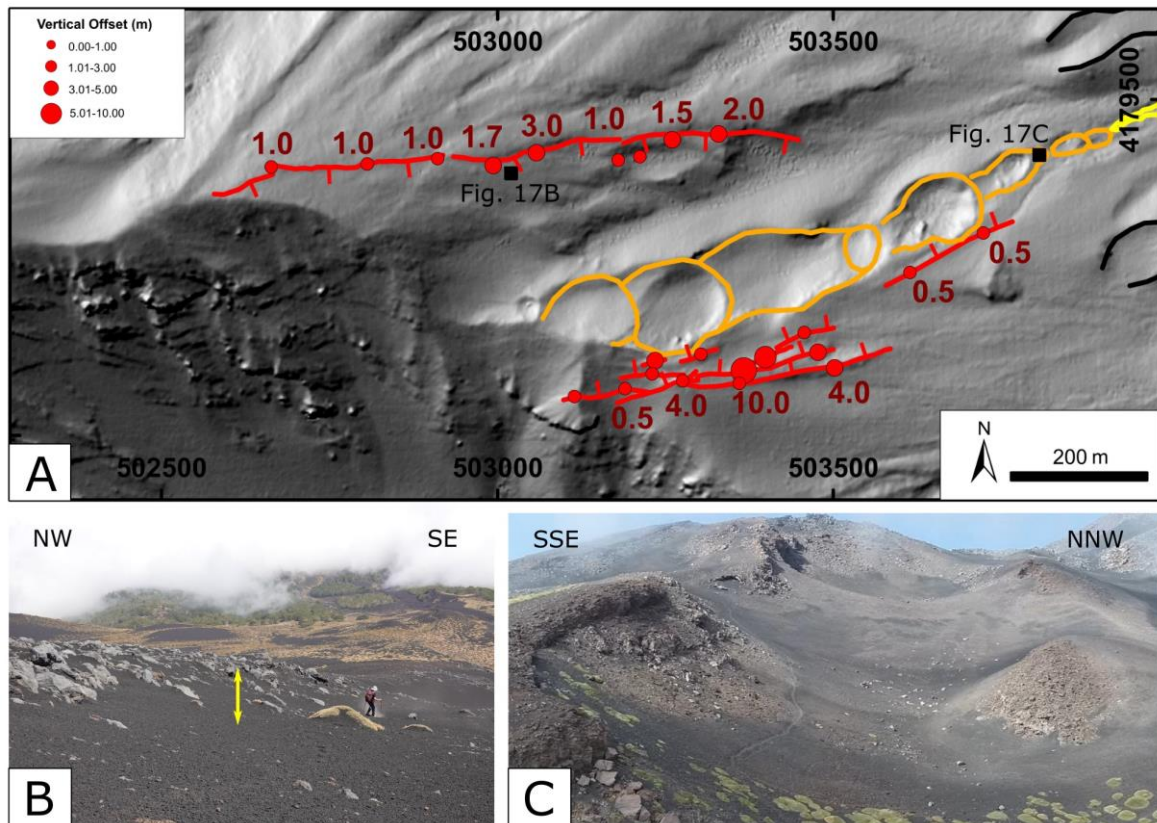
Fig. 18. (A) Map showing in detail Sector 1, where volcanic vents surrounded by a graben can be observed. For the legend of the structures and location of this figure see Figure 17F. Coordinate Reference System: WGS 84 - UTM zone 33N. (B) and (C) show the S-dipping normal fault and the volcanic vents, respectively. The yellow arrow in (B) indicates the vertical offset (Tibaldi et al., 2022).

4.3.1.2. Sector 2: single eruptive fissure

More to the east, at an altitude of ~2080 m a.s.l., volcanic vents are not visible anymore, whereas a single eruptive fissure can be observed, indicating a minor Strombolian activity. Moving eastward, this fissure appears continuously for 2.5 km up to an altitude of ~1600 m

a.s.l., where it suddenly disappears, and finally emerges again in correspondence of the lower vents (~1150 m a.s.l.), almost 3 km to the east.

In this sector, differently from Sector 1, there are no evidence of normal faults on both sides of the fissure. Both to the NW and to the SE of the eruptive fissure, only fractures associated to pre-1928 events were recognized, without traces of vertical displacement (Fig. 19A). In the northeastern part of this sector, the uprise of the dike up to the surface caused several collapses, forming a series of sinkholes, aligned and elongated in the same direction of the dike (Figs. 19B-C). In the easternmost sinkhole, a shallow stratigraphic sequence composed of two lava units intercalated with a tuff deposit is visible, which was used for numerical modeling (as explained in Section 4.2.2).
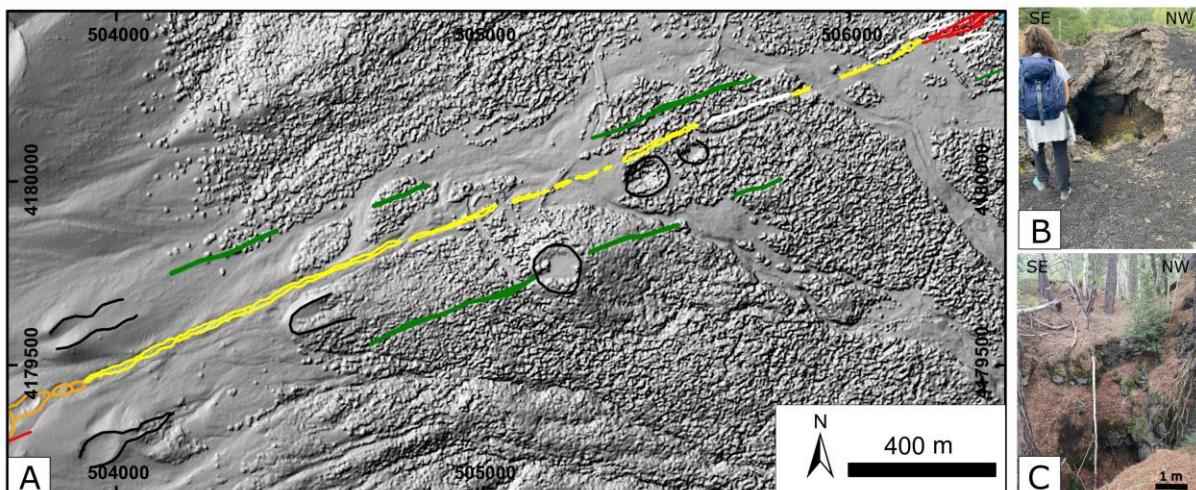
Fig. 19. (A) Map showing in detail Sector 2, where surface deformation is characterized by a single eruptive fissure without evidence of normal faults at its sides. For legend and location of this figure see Figure 17F. Coordinate Reference System: WGS 84 - UTM zone 33N. (B) and (C) show examples of the eruptive fissure and of a sinkhole (Tibaldi et al., 2022).

4.3.1.3 Sector 3: half-graben and symmetric graben without eruption

At ~1600 m a.s.l., the eruptive fissure disappears, and only surface deformation associated with dike emplacement below the surface is observed, without evidence of eruption.

51

The western part of this sector is characterized by the presence of a 74-m-wide half-graben, shown in detail in Figure 20A. The SE-dipping normal faults at the northern side of the half-graben (Fig. 20D) show offsets ranging from 0.3 to 1.2 m, whereas only dry tension fractures are visible along the southern side, without any evidence of vertical offset (Fig. 20E). Along the tension fractures, the maximum amount of opening is 3 m, with an average of 1.1 m and a SD of 0.8 m. In 12 sites, opening direction was also measured, obtaining an average value of N161.2°E and a SD of 12.4°, with a peak between N160-180°E. Considering the local strike measured in the same sites, we obtained an average of N68.9°E and a SD of 6.3°, with a peak in the interval N60-70°E, indicating a small right-lateral component of motion of 2.3° (Fig. 20B). Specifically, 6 sites are characterized by pure extension (lateral component < 5°), 5 by right-lateral component of motion and only 1 by a left-lateral component of motion. In the graph in Figure 20C, opening direction values are related to the local strike, showing that a clockwise rotation of the former corresponds also to a clockwise rotation of the latter. Finally, some sinkholes in the middle of the half-graben can be observed (Fig. 20A).
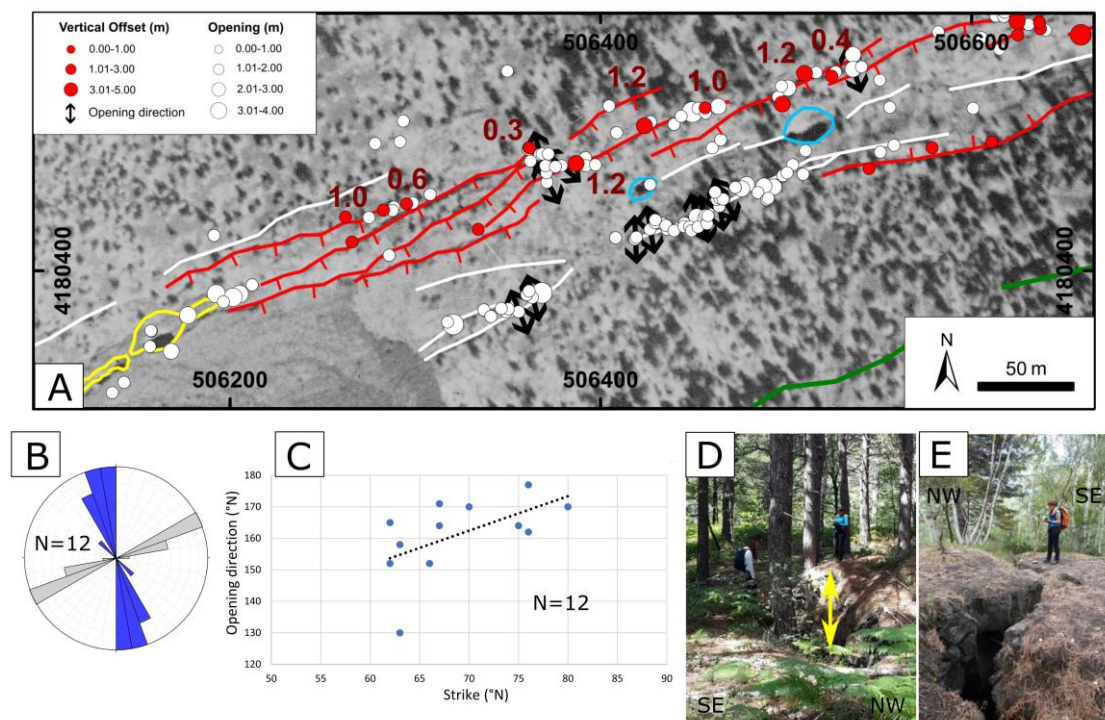
Fig. 20. (A) Map showing in detail the western part of Sector 3, where a half-graben without evidence of eruption is observed. Black arrows represent the opening direction, whereas the numbers the vertical offset (in meters) at the structural stations. For legend of the structures

and location of this figure see Figure 17F. Coordinate Reference System: WGS 84 - UTM zone 33N. (B) Rose diagram showing the local strike (in grey) and the opening direction (in blue). (C) Graph showing the relation between the local strike and the opening direction. (D) and (E) show a SE-dipping normal fault, with the yellow arrow highlighting the vertical offset, and a dry tension fracture, respectively (Tibaldi et al., 2022).

In the eastern part of this sector, the half-graben suddenly becomes a 68-m-wide symmetric graben, with vertical offset on both its sides (Figs. 21B-C). Again, the dike did not arrive up to the surface, with no evidence of eruption. Vertical offsets range between 0.3 and 3.5 m, with a maximum cumulated value of offset of 4 m along the northern side of the graben, where SE-dipping normal faults are present (Fig. 21A-C). In the middle of the graben, tension fractures were detected, but opening directions could not be measured because piercing points were not visible. Regarding the amount of opening, the maximum detected value was 2.7 m, but most of the values were < 1 m (Fig. 21A).
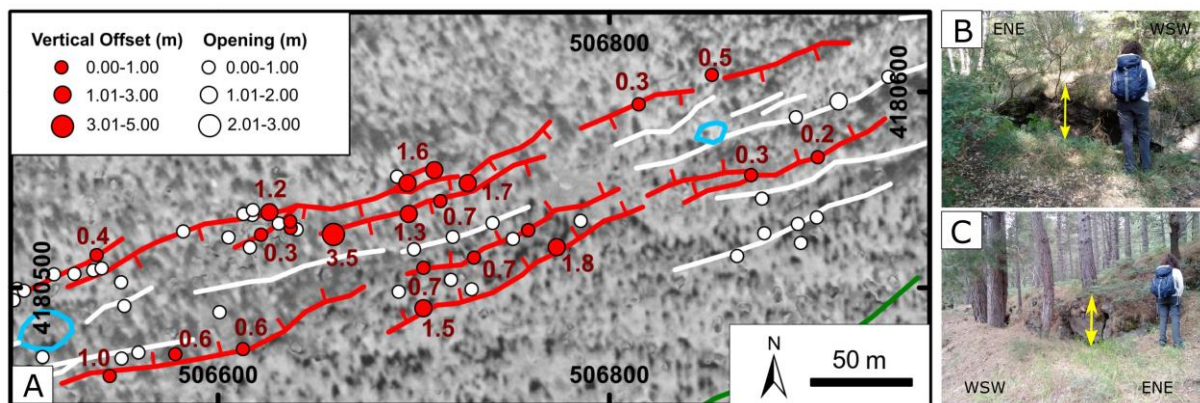
Fig. 21. (A) Map showing in detail the eastern part of Sector 3, where a graben without evidence of eruption is observed. The numbers indicate the vertical offset (in meters) at the structural stations. For legend of the structures and location of this figure see Figure 17F. Coordinate Reference System: WGS 84 - UTM zone 33N. (B) and (C) show a NW-dipping and SE-dipping normal fault, respectively, with the yellow arrows highlighting the vertical offset (Tibaldi et al., 2022).

4.3.1.4 Sector 4: lower vents along Ripe della Naca faults

This sector is the easternmost part of the 1928 fissure and is connected to Sector 3 by dry fractures with a right-stepping geometry (Fig. 17F). Here, aligned sinkholes are observed, with small pyroclastic cones forming a series of aligned vents. These vents show craters elongated N65°-74°E and aligned in an ENE-WSW direction, which generated the lava flow that destroyed the Mascali village. These vents are located at the foot of the upper escarpment of the Ripe della Naca faults, which intersect with the 1928 fissure in this area. The Ripe della Naca faults are composed of two main scarps, dipping towards SSE with a strike of about N70°E. The northern scarp shows a height of 90-130 m, whereas the southern one is about 110-125 m high.

4.3.2. Numerical models

The main goal of numerical models was to investigate the parameters that could have affected surface deformation along the 1928 fissure, as well as the propagation path of the dike.

4.3.2.1. Sensitivity analyses

First, sensitivity analyses were run, with the setup presented in Figure 15. Initially, a vertical dike was modeled as propagating in the observed stratigraphy, with overpressure increasing from 1 MPa (Fig. 22A), to 10 MPa (Fig. 22B) and finally 20 MPa (Fig. 22C). The host rock has a stiffness of 30 GPa, whereas the two comparatively stiff lava flows have E = 7 GPa, and the tuff E = 1 GPa. The dike is modeled at the contact between the tuff (above) and the lower lava layer (below), that represents a soft/stiff mechanical contrast. When the overpressure is equal to 1 MPa (Fig. 22A), tensile stress concentrates in the stiffer lava layer, with values in the range 0.5-5 MPa. Absolute shear stress is very low (2 MPa at most) and is concentrated only around the dike tip, without approaching the surface. Above the dike tip, at the contact between the lava and the tuff layer, a 90° rotation of stresses is observed, with the formation of a stress barrier. If overpressure increases to 10 MPa (Fig. 22B), tensile stress still

concentrates in the lava layers, but reaches higher values of magnitude, up to 10 MPa. Again, a 90° rotation of principal stresses is observed at the contact between the lava and the tuff layer, suggesting an arrest of the dike. Absolute shear stress is distributed closer to the surface, reaching higher magnitudes than the previous case. The presence of the tuff layer suppresses the shear stress concentration, but at the same time it favors its distribution towards the surface, with the contours that are steeper than the ones in stiffer layers. Finally, with an overpressure of 20 MPa (Fig. 22C), the absolute shear stress contours become closer to the surface, with values up to 8 MPa in the upper layer. Also in this case, it is possible to observe a steeper pattern of shear stress contours in the tuff compared to the lavas. Regarding tensile stress, it concentrates in the stiffer layers, and especially in the upper stiff lava layer, where it reaches magnitudes of 10 MPa. At the contact between the lava and the tuff, a 90° rotation of principal stresses is still observed, indicating the presence of a stress barrier. In all cases, stress distributions (both tensile and shear) are symmetrical above the dike tip and in the host rock (Figs. 22A-B-C).
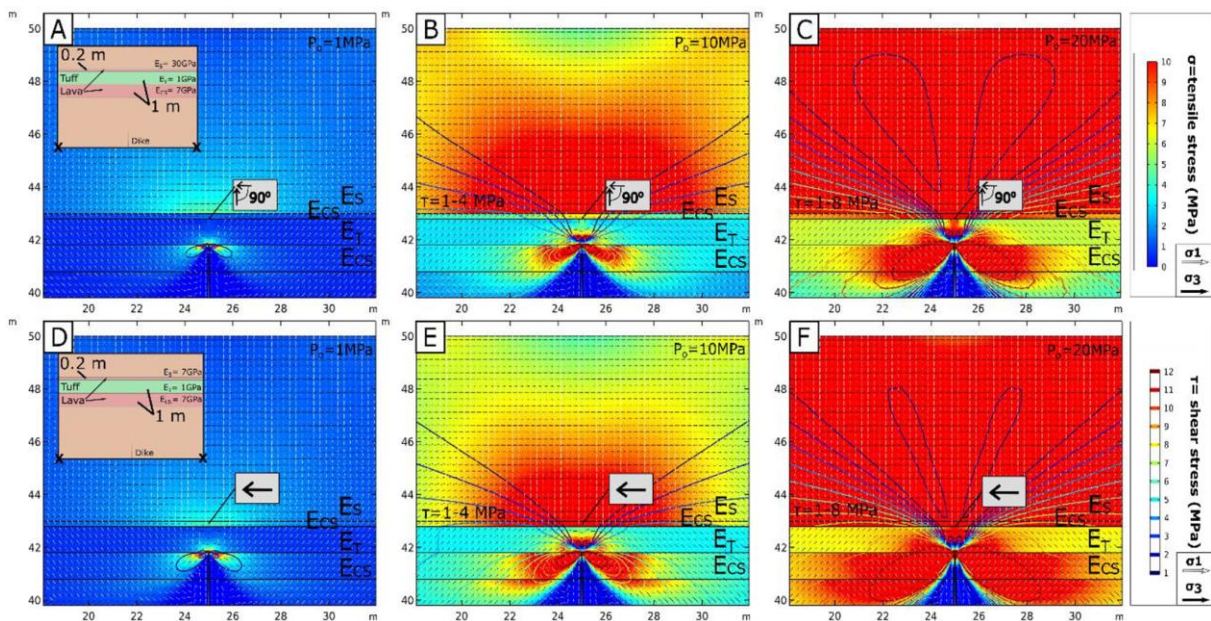
Fig. 22. Numerical models showing a vertical dike intruding in a layered host rock. Layering properties are denoted in the insets. Tensile stress (σ_3) is represented as a color scale bar, and the absolute shear stress (τ, component of the von Mises shear stress on xy plane) as contours. The orientations of σ_1 and σ_3 are shown with white and black arrows, respectively.

Dike overpressure is equal to 1 MPa (A-D), 10 MPa (B-E) and 20 MPa (C-F) (Tibaldi et al., 2022).

To understand how the stiffness of the top layer affects stresses distribution, in Figures 22D-E-F the Young's modulus of the top lava layer was changed to 7 GPa. Again, stresses tend to concentrate in the stiffer layers, with higher magnitudes in the case of higher overpressure (up to 10 MPa for tensile stress and 8 MPa for the absolute shear stress) (Fig. 22F). However, the orientation of principal stresses is affected by this variation of stiffness, showing no rotation of σ_1 and σ_3, and suggesting a vertical propagation of the dike.

In Figures 23A-B-C, the thickness of the tuff layer was decreased of one order of magnitude, up to 0.1 m. With an overpressure of 1 MPa (Fig. 23A), an 80° rotation of principal stresses is still observable, indicating a possible dike deflection. Increasing the overpressure to 10 MPa (Fig. 23B) and 20 MPa (Fig. 23C), the concentration of stresses increases in the top layer, with tensile stress reaching 10 MPa, and shear stress that is symmetric above the dike tip and reaches values of 7 and 12 MPa, respectively. In both cases, no rotation of stresses is observed, suggesting a vertical propagation of the dike.

In the next models, the tuff layer was completely removed from the stratigraphy, alternating lavas with $E_{CS, CS2}$ = 7-10 GPa (Figs. 23D-E-F). In this case, with 1 MPa of overpressure the principal stresses show a 90° rotation, indicating the arrest of the dike, but stresses concentrations are not high enough in the top layers to allow fracturing and faulting (Fig. 23D). When the overpressure increases to 10 MPa (Fig. 23E), there is an increase of magnitude of tensile and absolute shear stresses, with the latter that distributes higher and wider above the tip, compared to the case with a thin tuff layer in the sequence (Fig. 23B). If the overpressure is equal to 20 MPa (Fig. 23F), tensile stress concentration becomes higher both at the tip of the dike and closer to the surface. Both tensile and absolute shear stress distributions are wider than the case with the tuff layer in the stratigraphy (Fig. 23C). Both in the case of 10 and 20 MPa of overpressure, principal stresses rotate of 80°, suggesting a deflection of the dike (Figs. 23E-F).
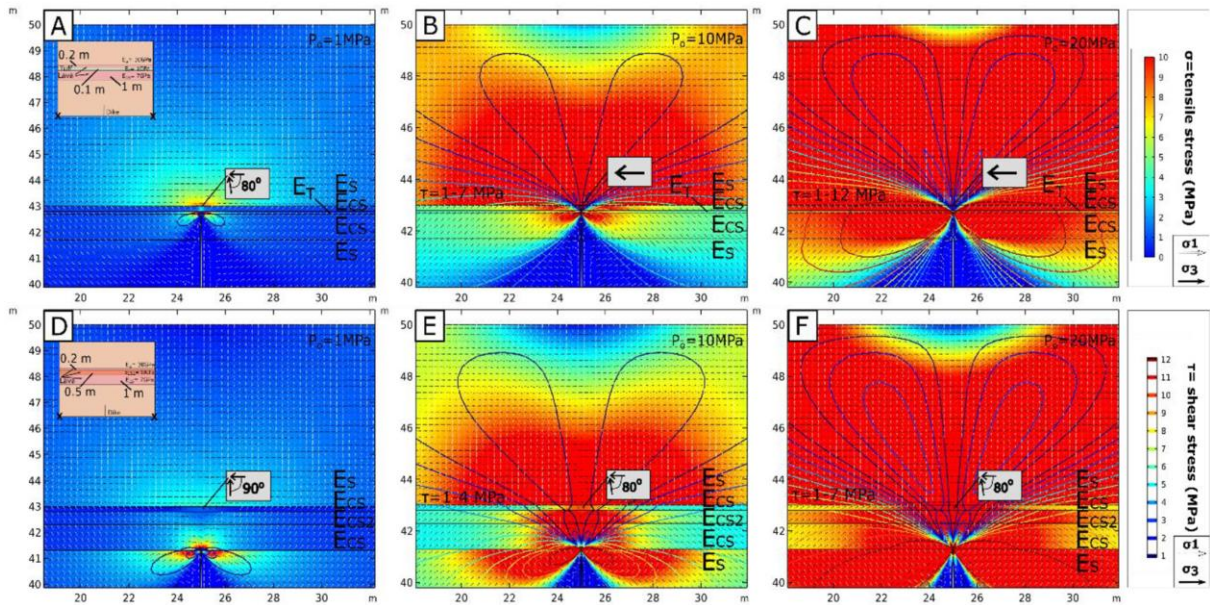
Fig. 23. Numerical models showing a vertical dike intruding in a layered host rock with a thinner tuff layer (A-B-C) and without tuff layers in the sequence (D-E-F). Layering properties are denoted in the insets. Tensile stress (σ_3) is represented as a color scale bar, and the absolute shear stress (τ, component of the von Mises shear stress on xy plane) as contours. The orientations of σ_1 and σ_3 are shown with white and black arrows, respectively. Dike overpressure is equal to 1 MPa (A-D), 10 MPa (B-E) and 20 MPa (C-F) (Tibaldi et al., 2022).

In Figure 24, the same models of Figure 23 were run, but with a dike inclined of 10°. The main difference consists in the asymmetrical distribution of tensile and absolute shear stresses, that reach the surface only in the right part of the model. When the overpressure is 1 MPa, tensile and shear stresses are not high enough to cause fracturing or faulting at the surface, both if a thin tuff layer is present in the sequence and if the tuff is missing. In both cases, the orientations of principal stresses show a rotation between 0° and 45° close to the tip of the dike, and an almost 90° rotation at the thin lava layer, suggesting the formation of a stress barrier in a stiff layer (Figs. 24A-D). Increasing the overpressure to 10 MPa, both tensile and shear stresses distribute closer to the surface reaching higher magnitudes in the top layer, up to 10 MPa and 8 MPa in the right side of the models, respectively (Figs. 24B-E). The orientations of σ_1 and σ_3 rotate less than 45° if the tuff layer is present in the stratigraphy (Fig. 24B), and up to 80° at the thin lava layer when the tuff is missing (Fig. 24E). Finally, with

higher overpressure (20 MPa), the magnitudes of stresses increase further, and shear stress reaches 8-12 MPa in the top lava layer (Figs. 24C-F). The rotations of principal stresses are similar to what observed in Figures 24B-E. This setting suggests the possibility of faulting at the right side of the model, whereas only fracturing is likely at the left side of the dike.
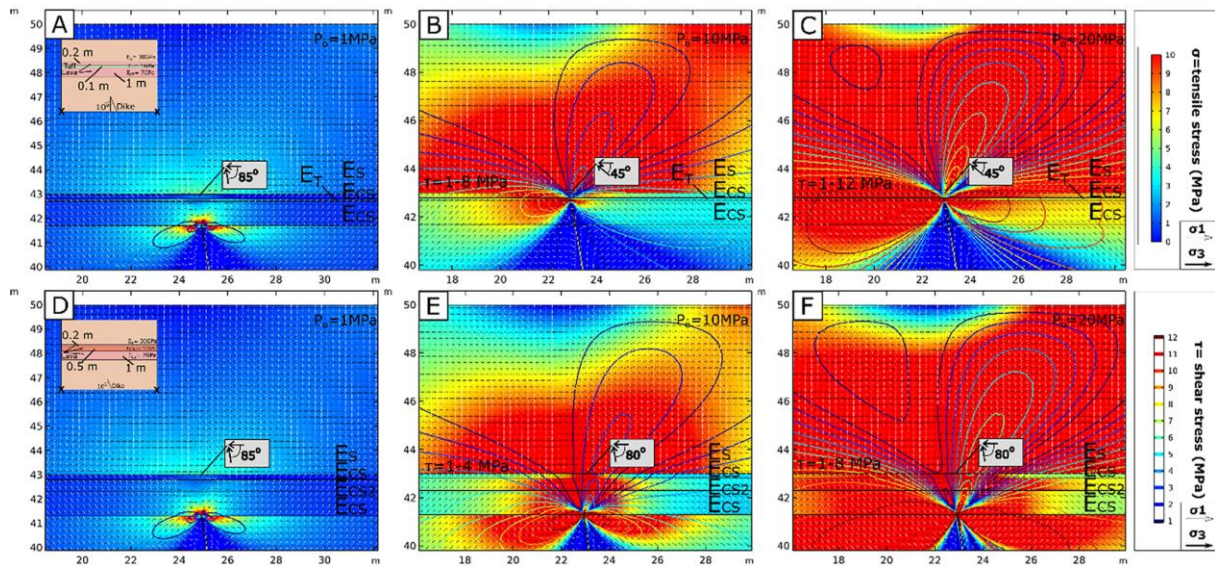
Fig. 24. Numerical models showing an inclined dike (10°) intruding in a layered host rock with a thinner tuff layer (A-B-C) and without tuff layers in the sequence (D-E-F). Layering properties are denoted in the insets. Tensile stress (σ_3) is represented as a color scale bar, and the absolute shear stress (τ, component of the von Mises shear stress on xy plane) as contours. The orientations of σ_1 and σ_3 are shown with white and black arrows, respectively. Dike overpressure is equal to 1 MPa (A-D), 10 MPa (B-E) and 20 MPa (C-F) (Tibaldi et al., 2022).

Now, other two sets of sensitivity analyses are presented. In Figure 25, the dike is modeled with an overpressure of 1 MPa, and an extensional stress field of 2 MPa, whereas in Figure 26 the overpressure is equal to 5 MPa, and extension is 0.5 MPa. In both sets, the host rock has a stiffness of 30 GPa, the lava layers of 10 GPa, the tuff layer of 5 GPa and the additional scoria layers of 0.5 GPa.

In Figure 25A, the stratigraphic sequence is the same of the previous models, with a greater thickness of the top lava layer (1 m). Rotations of 90° of stresses are observed at the tuff layer, with tensile and shear stresses that concentrate at the dike tip and at the stiffest layers. Moving the tuff layer at the bottom of the stratigraphy (Fig. 25B), principal stresses rotate of 45° both at the tuff and at the lava layers, with an increase of tensile stress in all the layers. In Figures 25C-D, a scoria layer was added at the top of the stratigraphy, with a thickness of 1 m and 0.1 m, respectively. In both cases, a 90° rotation of stresses is observed in the scoria layer, favoring the arrest of the dike. However, when the scoria layer at the top is thicker, tensile and shear stresses are suppressed and cannot distribute up to the surface (Fig. 25C), differently from the case with a thinner scoria layer at the top (Fig. 25D). If a thick (Fig. 25E) scoria layer is present at the bottom of the stratigraphy, stress rotations are promoted at the tuff/scoria contact, with low tensile stress concentration at the scoria layer, that occurs also in case of a thin scoria layer (Fig. 25F). Finally, in Figures 25G-H, the dike is inclined, keeping a thick and a thin scoria layer at the top of the stratigraphy, respectively. In both models, no 90° rotations are observed, but tensile and shear stress values are suppressed in case of a thick layer (Fig. 25G) and are higher when the scoria layer is thinner (Fig. 25H).
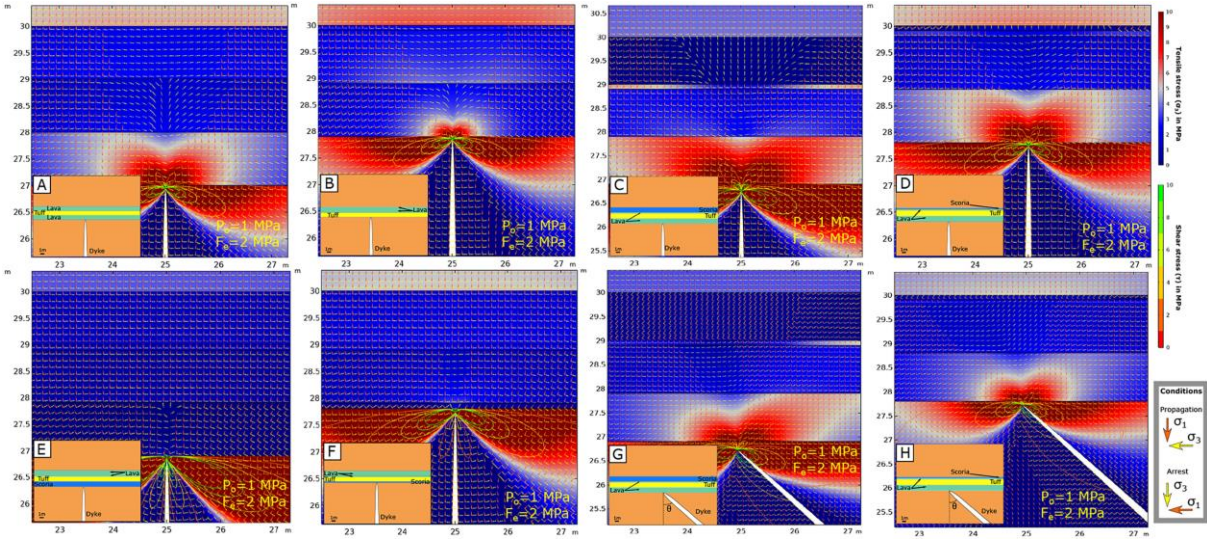
Fig. 25. Numerical models showing a dike with an overpressure of 1 MPa and subjected to an extension of 2 MPa. The different concepts from (A) to (H) are illustrated in the insets. Tensile stress (σ_3) is represented as a color scale bar, and the absolute shear stress (τ, component of

the von Mises shear stress on xy plane) as contours. The orientations of σ₁ and σ₃ are shown with orange and yellow arrows, respectively (Drymoni et al., 2023).

In Figure 26, the same concepts are investigated, but with a higher overpressure and a lower extension. In Figure 26A, 90° rotations of stresses are observed in the tuff layer, favoring the arrest of the dike. However, stresses at the surface are still high enough to allow fracturing and faulting, encouraging graben formation. A similar result is observed in Figure 26B, with the tuff at the bottom of the stratigraphy. When a thick scoria layer is at the top of the stratigraphy, a 90° rotation of stresses occurs in this layer (Fig. 26C), whereas rotations in the tuff and in the scoria are observed when the scoria is thinner, with a higher concentration of stresses at the surface (Fig. 26D). When a thick scoria layer is at the bottom of the stratigraphy (Fig. 26E), rotations occur in this layer favoring dike arrest, with low tensile stress that does not propagate to the upper part of the sequence. Instead, when the scoria layer at the bottom is thin (Fig. 26F), no rotations are observed, and tensile and shear stress are high in the succession. If the dike is inclined, stresses distribute asymmetrically, and stress rotations occur both in case of a thick (Fig. 26G) and of a thin (Fig. 26H) scoria layer at the top, with higher stress concentrations in Figure 26H.
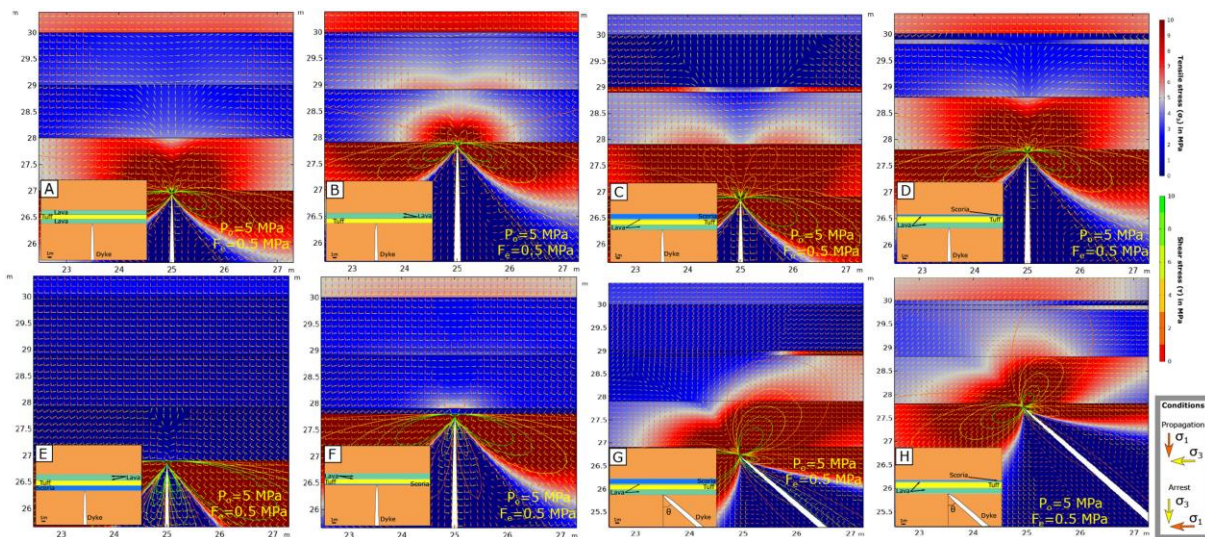
Fig. 26. Numerical models showing a dike with an overpressure of 5 MPa and subjected to an extension of 0.5 MPa. The different concepts from (A) to (H) are illustrated in the insets. Tensile stress (σ₃) is represented as a color scale bar, and the absolute shear stress (τ,

component of the von Mises shear stress on xy plane) as contours. The orientations of σ_1 and σ_3 are shown with orange and yellow arrows, respectively (Drymoni et al., 2023).

4.3.2.2 Western site with P_0 = 1-10 MPa and F_{ext} = 0.5 MPa

In this section, a dike intruding in a host rock characterized by the stratigraphy of the western site is modeled, as shown in Figure 16. In Figure 27, the dike is moved from C_{W1} to C_{W3}, varying the overpressure from 1 MPa, to 5 MPa and finally to 10 MPa, but always maintaining an extension of 0.5 MPa.

In Figure 27A, the dike is modeled at the contact C_{W1} with an overpressure of 1 MPa. Tensile stress concentrates at the tip of the dike and in the thin lava layer immediately above it, whereas it is suppressed in the softer layers. Regarding shear stress contours, they are concentrated below the contact, indicating a low concentration of shear stress in the host rock above the dike tip. In the breccia layer, it is possible to observe a stress rotation, which suggests dike arrest. If the overpressure increases to 5 MPa (Fig. 27B), tensile and shear stresses increase proportionally, with shear stress contours that become wider. Again, stress rotations are noticed in the breccia layer. When overpressure is equal to 10 MPa, tensile and shear stress concentrations further increase, with wider shear stress contours, and the breccia layer acts again as stress barrier (Fig. 27C).

If the dike is moved to the contact C_{W2} with a 1 MPa overpressure (Fig. 27D), tensile and shear stresses at the tip are suppressed by the presence of the breccia layer. Stress rotations occur at the stiff/soft contact between the lava and the breccia layer, and not inside the latter, suggesting an arrest of the dike. The same rotation is observed if the overpressure increases to 5 MPa (Fig. 27E), with an increase of tensile and shear stresses. When overpressure is 10 MPa, the results are similar, but shear stress contours also intersect the breccia and the lava layers (Fig. 27F).

Moving the dike to the contact C_{W3}, tensile stress is concentrated mostly at the lava layer above the tip and shear stress is suppressed, when overpressure is 1 MPa (Fig. 27G). No stress rotations are observed in this case. Increasing the overpressure (Figs. 27H-I), tensile and shear stress concentrations increase, with shear stress contours that distribute wider in the lava layer.
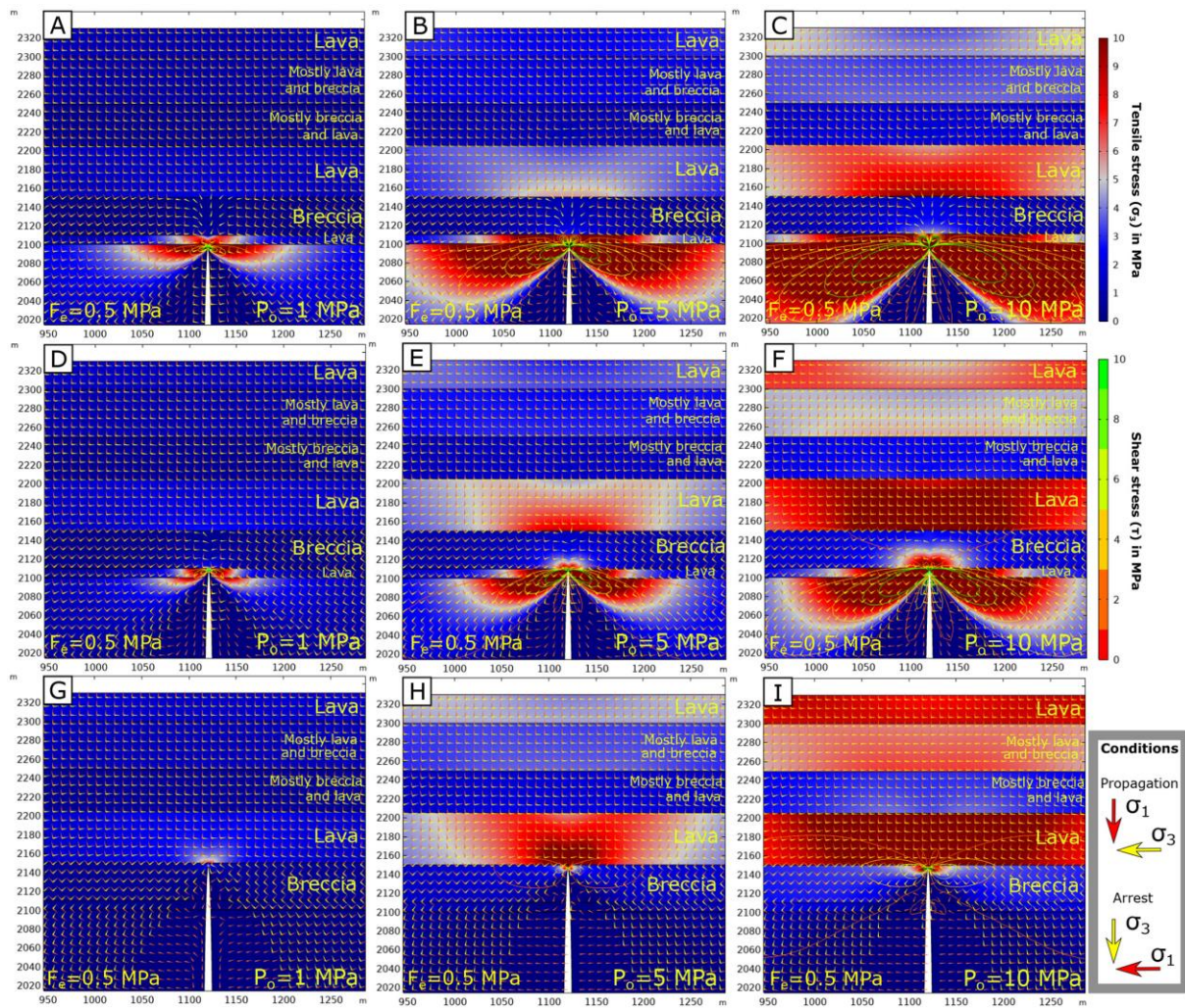
Fig. 27. Numerical models based on the stratigraphy of the western site, with the dike at the contacts C_{W1} (A-B-C), C_{W2} (D-E-F) and C_{W3} (G-H-I). Overpressure values are 1 MPa (A-D-G), 5 MPa (B-E-H) and 10 MPa (C-F-I), whereas the extensional field is 0.5 MPa in all the models. Tensile stress (σ_3) is represented as a color scale bar, and the absolute shear stress (τ, component of the von Mises shear stress on xy plane) as contours. The orientations of σ_1 and σ_3 are shown with orange and yellow arrows, respectively (Drymoni et al., 2023).

In Figure 28, the dike is modeled at the three upper contacts (C_{W4}, C_{W5}, C_{W6}). At contact C_{W4}, when overpressure is 1 MPa, tensile and shear stress concentrations are low. Stress rotations occur in the layer above the dike tip, but they are < 90°, thus not satisfying the conditions for dike arrest (Fig. 28A). Increasing the overpressure, tensile and shear stresses increase their

magnitudes, indicating likely fracturing at the surface (Figs. 28B-C). Also in these cases, no stress barriers form, indicating a likely propagation of the dike up to the surface.

If the dike is at contact C_{W5} with a 1 MPa overpressure, tensile and shear stresses are low and suppressed, respectively (Fig. 28D). Increasing the overpressure, tensile stress concentrates in the stiff layer, and no stress rotations occur (Figs. 28E-F). If overpressure is up to 10 MPa, shear stress contours reach the top of the succession (Fig. 28F).

Finally, moving the dike to contact C_{W6} (Figs. 28G-H-I), the models are similar to the ones observed at the previous contact. Still, shear stress contours arrive up to the surface when the overpressure is 10 MPa, suggesting the formation of a graben (Fig. 28I).
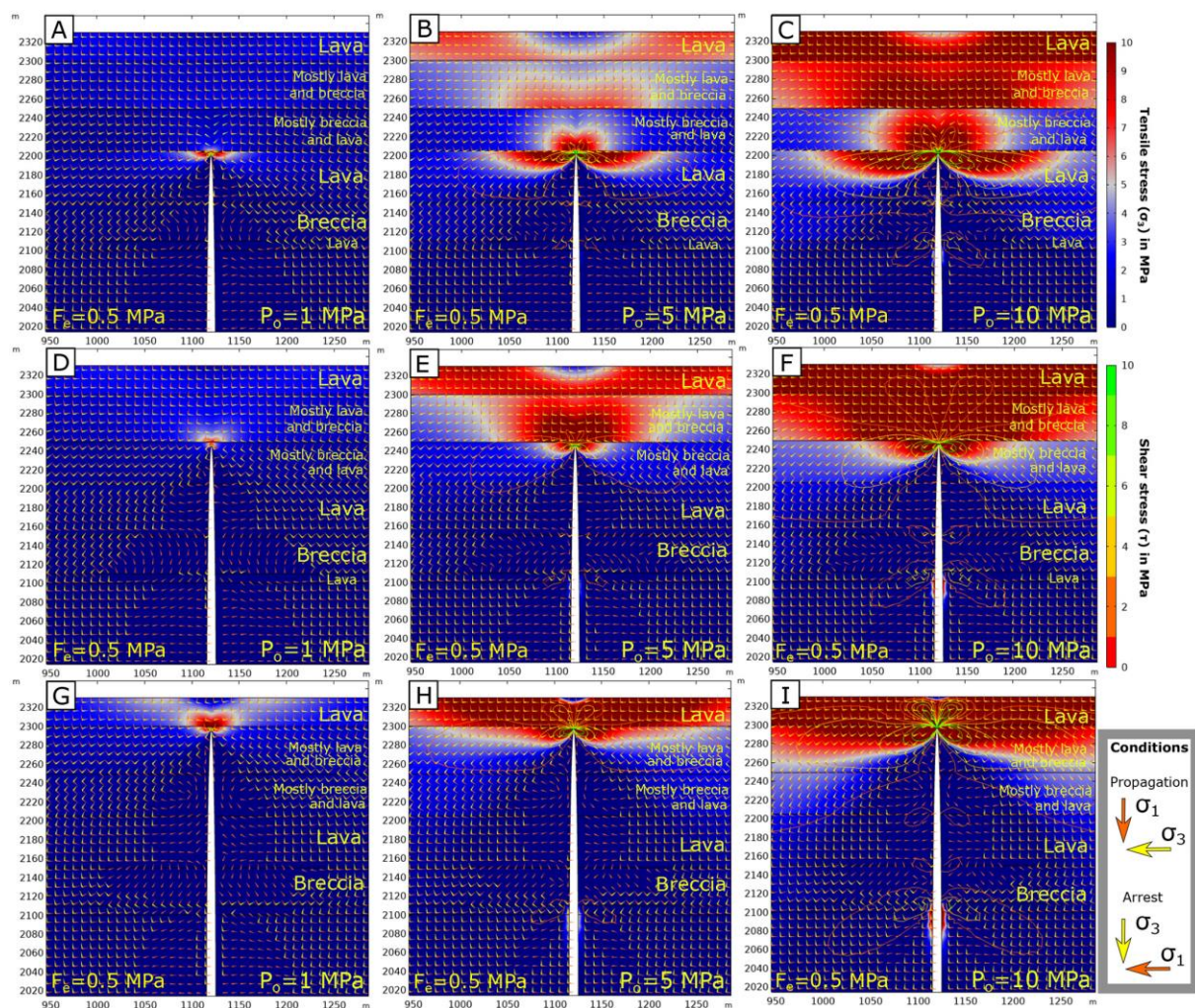
Fig. 28. Numerical models based on the stratigraphy of the western site, with the dike at the contacts C_{W4} (A-B-C), C_{W5} (D-E-F) and C_{W6} (G-H-I). Overpressure values are 1 MPa (A-D-G), 5 MPa (B-E-H) and 10 MPa (C-F-I), whereas the extensional field is 0.5 MPa in all the models. Tensile stress (σ_3) is represented as a color scale bar, and the absolute shear stress (τ,

component of the von Mises shear stress on xy plane) as contours. The orientations of σ₁ and

σ₃ are shown with orange and yellow arrows, respectively (Drymoni et al., 2023).

The von Mises shear stress (τ) concentration at the different contacts (and at the surface) is shown in Figure 29, for a dike that has a 5 MPa overpressure (Figs. 29A-B-C) and with an extra 0.5 MPa extension (Figs. 29D-E-F). Von Mises shear stress increases towards the surface in all cases, favoring the formation of a graben. The two peaks show maxima that become narrower with a decrease of the depth of the dike, as observed also by previous authors (Al Shehri and Gudmundsson, 2018). The distance between the two peaks is associated with the depth of the tip and with the mechanical properties of the layers (Bazargan and Gudmundsson, 2019). Considering that the 1928 dike propagated laterally, this means that the distance between the two peaks is also related to the depth of the top of the laterally propagating dike. Adding the extensional stress field, the magnitude of von Mises shear stress increases at the tip and at the surface, whereas the distance between the peaks is not affected.
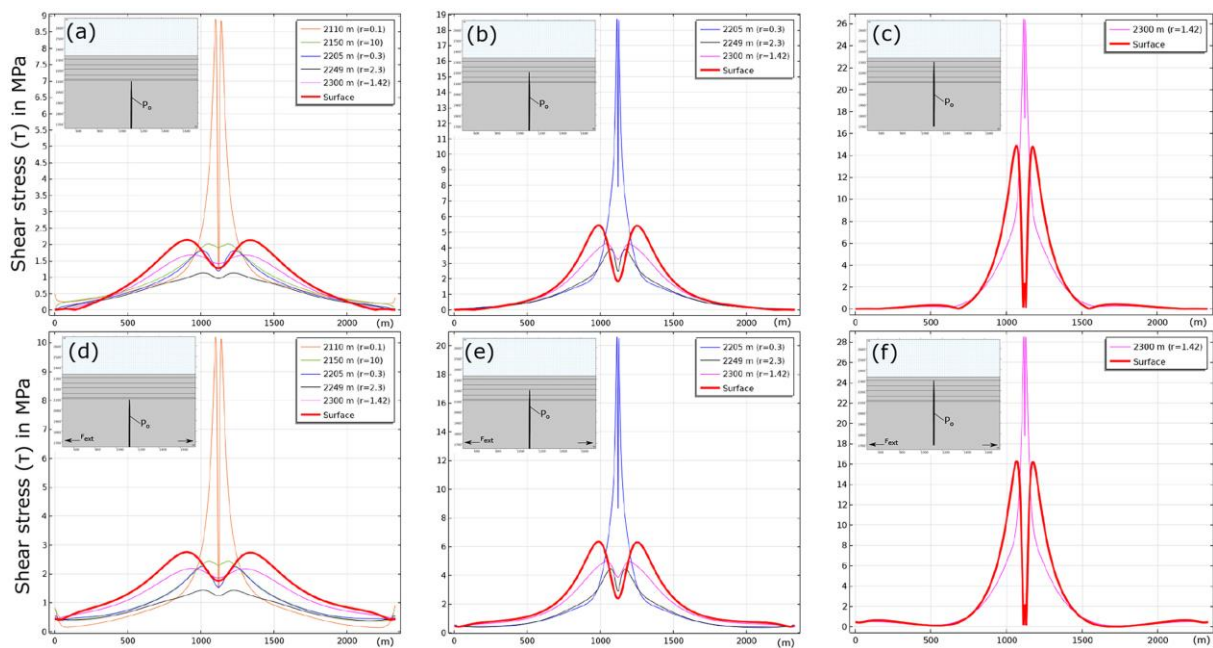
Fig. 29. 1D lines showing the von Mises shear stress (τ) concentration at the different contacts and at the surface, considering the stratigraphy of the western site. All the models, from (A) to (F), have a 5 MPa overpressure, from (D) to (F) a 0.5 MPa extensional stress load

is also applied. Surface represents the contact between the top layer and the atmosphere (Drymoni et al., 2023).

4.3.2.3. Eastern site with P_0 = 1-10 MPa and F_{ext} = 2 MPa

Finally, a dike intruding in a host rock characterized by the stratigraphy observed in the field at the eastern site is modeled (Fig. 16). In Figure 30, a dike with an overpressure ranging 1-10 MPa and with a constant extensional stress field of 2 MPa is modeled at the contacts. When the dike is modeled at contact C_{E1} with an overpressure of 1 MPa, tensile stress concentration is high at the tip and in the stiff lavas (Fig. 30A). Increasing the overpressure, tensile stress increases proportionally at the tip and at the top of the succession and shear stress contours distribute wider, reaching the surface (Figs. 30B-C). In all cases, no stress rotations are observed.

Moving the dike to C_{E2}, the results are similar to the previous models, but with higher concentrations of tensile stress inside the tuff layer and higher contours of shear stress. Still, no stress rotations are noticed (Figs. 30D-E-F).

Finally, if the dike is at contact C_{E3}, the results are similar to the previous cases, both regarding stress concentrations and rotations (Figs. 30G-H-I). In Figures 30J-K-L, the dike is modeled considering a host rock with a low Young's modulus (E = 1 GPa). In these cases, tensile concentration is lower in the host rock, but still no stress rotations are observed.

For the eastern site, the von Mises shear stress was also plotted at each contact and at the surface, as 1D graph (Fig. 31). In this case, values are very high, due to the vicinity of the tip to the surface. These values are not realistic, since rocks can break as soon as the tensile stress becomes equal to or greater than the *in-situ* tensile strength (Gudmundsson, 2011a), but the graphs can give information about the theoretical stress distribution. Again, the maximum peaks become narrower as the dike approaches the surface, with contacts characterized by higher stiffness ratios that concentrate higher stresses.
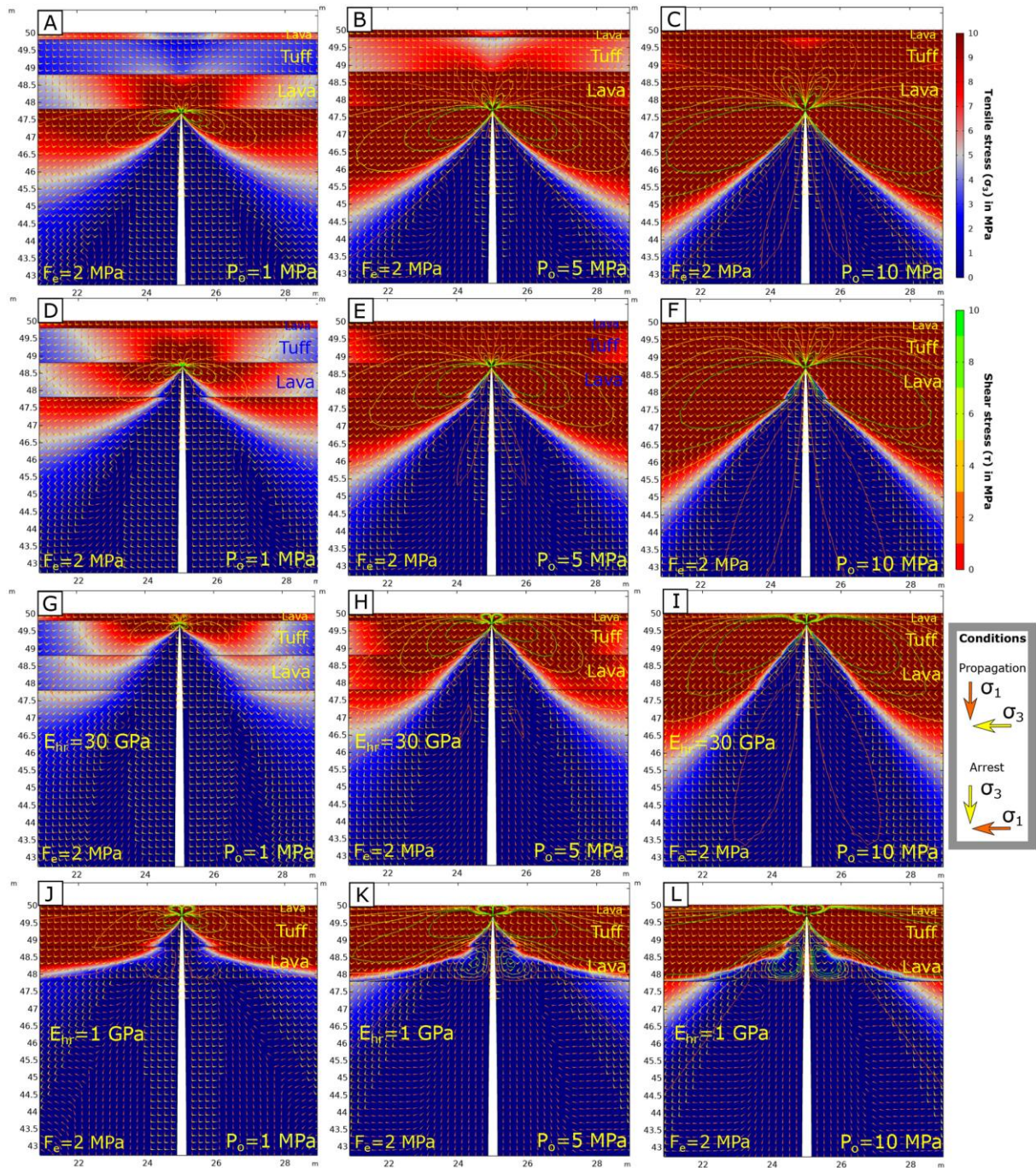
Fig. 30. Numerical models based on the stratigraphy of the eastern site, with the dike at the contacts C_{E1} (A-B-C), C_{E2} (D-E-F) and C_{E3} (G-H-I-J-K-L). Overpressure values are 1 MPa (A-D-G-J), 5 MPa (B-E-H-K) and 10 MPa (C-F-I-L), whereas the extensional field is 2 MPa in all the models. E values of the host rock are 30 GPa from (A) to (I), and 1 GPa from (J) to (L). Tensile stress (σ_3) is represented as a color scale bar, and the absolute shear stress (τ, component of the von Mises shear stress on xy plane) as contours. The orientations of σ_1 and σ_3 are shown with orange and yellow arrows, respectively (Drymoni et al., 2023).

66
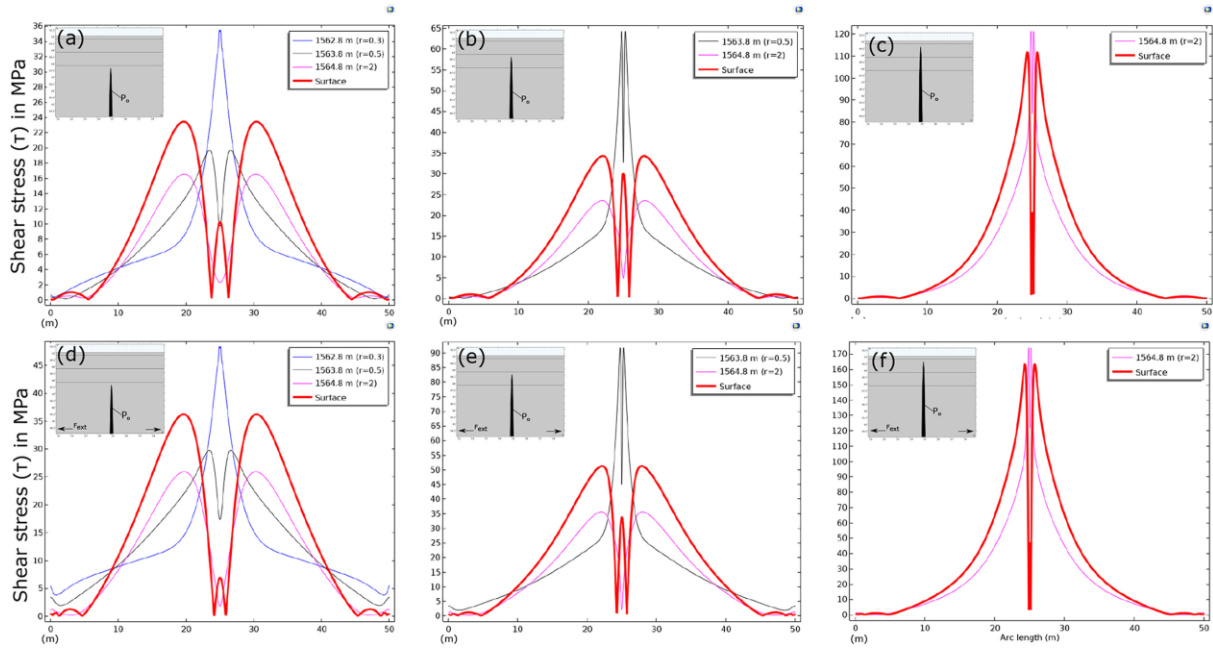
Fig. 31. 1D lines showing the von Mises shear stress (τ) concentration at the different contacts and at the surface, considering the stratigraphy of the eastern site. All the models, from (A) to (F), have a 5 MPa overpressure, from (D) to (F) a 2 MPa extensional stress load is also applied. Surface represents the contact between the top layer and the atmosphere (Drymoni et al., 2023).

4.4 Discussion

The relation between dike intrusion and surface deformation has been studied along both slow and fast divergent plate boundaries, using field observations, geophysical data, seismicity and analogue and numerical models (Stein et al., 1991; Rubin, 1992; Chadwick and Embley, 1998; Wright et al., 2006; Calais et al., 2008; Ebinger et al., 2008; Pallister et al., 2010; Nobile et al., 2012; Sigmundsson et al., 2015; Ágústsdóttir et al., 2016; Hjartardóttir et al., 2016; Ruch et al., 2016; Xu et al., 2016; Al Shehri and Gudmundsson, 2018; Trippanera et al., 2019; Acocella, 2021). On Mt. Etna, levelling data were used to model dike propagation in an elastic half-space during the 1983 eruption (Murray and Pullen, 1984), and the formation of several grabens during the 2001, 2002-2003, 2004-2005, 2008, 2013 and 2018 eruptions was reported (Acocella and Neri, 2003; Neri et al., 2004; Neri and Acocella, 2006; Bonaccorso et al., 2011; Falsaperla and Neri, 2015; Calvari et al., 2020).

4.4.1 Parameters that affect surface deformation and dike arrest

In this work, the structural analysis and the numerical study provide insights into the surface deformation related with the lateral propagation of a dike during the 1928 eruption. After having identified four sectors along the 1928 fissure, characterized by different types of surface deformation, numerical models were run to understand which parameters affected those deformation settings. More specifically, the effects of *i)* dike overpressure, *ii)* stratigraphic sequence, *iii)* layer thickness, and *iv)* dike dip were investigated.

Regarding the formation of stress barriers, sensitivity analyses showed that stress rotations are favored at the contacts with low stiffness contrast (E of the upper layer/E of the lower layer), and especially in soft layers. The variation of the thickness of the layers of one order of magnitude (0.1 to 1 m) can also promote stress barriers. Finally, models with an inclined dike showed that an increase of the dike dip can also favor stress rotations in soft layers (e.g., scoria, tuff).

To observe fracturing at the surface, the concentration of tensile stress should be at least equal to the tensile strength of the host rock (normally 2-4 MPa, Gudmundsson, 2011a). The shear strength is usually twice the tensile strength of the host rock (normally 4-8 MPa) and should be overcome to have fault slip (Haimson and Rummel, 1982; Schultz, 1995). In the numerical models of this work, it is evident that overpressure plays a role in the concentration of both tensile and shear stresses, which increase if the overpressure increases. Higher overpressure values can thus favor the formation of tension fractures or faults at the surface. The stiffness of the layers also affects stress distribution, with stiffer layers (e.g., lavas) that concentrate tensile and shear stresses, and softer layers (e.g., tuff, scoria) that suppress them. However, soft layers encourage the formation of narrower grabens, with shear stress contours that are steeper and with closer lobes. This is observed also in case of high overpressure. On the contrary, wider grabens formation is favored if the stratigraphy is mainly composed of stiff materials, such as lavas, and with smaller dike overpressures.

4.4.2 Different settings of surface deformation along the 1928 fissure

In this section, the four different settings of surface deformation observed along the 1928 fissure will be discussed, also considering the results of numerical models.

4.4.2.1 Volcanic vents and wider graben

In its westernmost sector (Sector 1), near the VdB rim, the 1928 fissure is characterized by a series of eight volcanic vents with explosive crater-like morphology, emplaced after an important Strombolian activity and surrounded by small spatter and scoria ramparts. The ENE alignment of the vents corresponds also to the direction of elongation of each one and of the ramparts, which are in turn parallel to the orientation of the whole 1928 fissure. According to Tibaldi (1995) and Tibaldi and Bonali (2017), these are all evidence of the direction of the propagating dike, which strikes ENE. In this segment, the dike produced a wide graben (385 m wide), with two sets of normal faults dipping inward with a strike subparallel to the alignment of the vents. The size of the vents decreases moving eastward, consistently with the documented eastward propagation of the dike (Branca et al., 2017).

In the numerical analysis, the formation of the graben can occur if shear stress expands towards the surface, reaching values that are at least equal to the shear strength of the host rock (4-8 MPa, as explained above). According to the presented models, this scenario is more possible in layered domains subjected to high overpressures (10-20 MPa), as observed in Figure 23. The width of the graben can also depend on the stratigraphic sequence, which affects the distribution of shear stress in the host rock and towards the surface. If a soft, thin layer is present in the sequence, the possible graben will be narrower, whereas if the sequence lacks soft layers, a wider graben will be formed (Figs. 23C-F). All these conditions should also be accompanied by the absence of stress barriers in the host rock, to allow the vertical propagation of the dike towards the surface. This condition is highly possible, especially if the overpressure of the dike is high, and could lead to the formation of an eruptive fissure after the dike-induced graben. This hypothesis also matches field data, since the graben faults do not affect the eruptive craters, that must postdate the faults.

4.4.2.2 Single fracture, half- and narrow graben

Moving eastward, the propagating dike generated a 2-km-long single eruptive fissure, characterized by a minor Strombolian activity, as testified to by the presence of ramparts with limited height (Sector 2). More to the east, no signs of eruption are evident, but a half-graben and a narrow graben (68 m wide) were generated by the propagation of the dike (Sector 3).

In Sector 3, both normal faults and tension fractures are observed, confirming that rocks in nature do not behave neither purely elastic nor purely Coulomb solids, but instead they behave like elasto-plastic materials (Jaeger et al., 2009; Gudmundsson, 2011a), allowing the occurrence of both deformation mechanisms during magma propagation. Shear failure has been demonstrated as a fundamental process at the tip of the magmatic body during magma propagation (Gudmundsson et al., 2008; White et al., 2011; Ágústsdóttir et al., 2016; Spacapan et al., 2017). The two sectors (2 and 3) are both located in a plane formed by a sequence of horizontal lava flows, with similar characteristics of the host rock around the dike in the two segments. Magma composition is also not expected to have changed during dike propagation, considering that the latter occurred in a few days. For these reasons, a change in the lithological characteristics of the host rock can be excluded as the reason of the variation from an eruptive fissure to a graben, differently from what observed by Vachon and Hieronymus (2017), as well as the intrusion of new magma with high viscosity (Spacapan et al., 2017).

According to numerical models, the intrusion of an inclined dike can produce an asymmetrical distribution of stresses (Figs. 24, 25G-H and 26G-H), that favor the formation of a half-graben. Furthermore, the variation in the style of deformation could be explained not only by a change of the dip of the dike or of the mechanical conditions of the host rock, but also by variations of the tip shape. Guldstrand et al. (2017), in fact, suggested that a change in the tip of the dike from a sharp to a narrow one favors the formation of a single tension fracture, whereas a blunt or rectangular shape leads to a half-graben. From a mechanical perspective, in our models the scenario of a single fracture can be likely in the cases with high tensile stress, that satisfy the conditions for Mode I fracturing. Instead, the half-graben can occur when both Mode I and Mode II conditions are satisfied, but with an asymmetrical

distribution of shear stress above the dike tip. Generally, a topographic gradient could also explain the asymmetry of the graben, as observed by Billi et al. (2003) during the 2001 Mt. Etna eruption. However, in this case, the area of Sector 3 is characterized by a very low topographic gradient, that probably did not affect graben geometry.

More to the east, the half-graben (74 m wide) becomes a narrow graben. The presence of a wider graben in Sector 1, and of a narrower graben in Sector 3, could be explained by the lateral propagation of the 1928 dike and the present topography. In fact, topographic data indicate a higher relief above the dike in the westernmost Sector 1 compared to Sector 3, and this could have affected the width of the resulting graben (Figs. 29-31). According to the "graben rule" by Pollard et al. (1983), the tip of the dike should be at a depth that is half of the graben width, namely 37 m below the half-graben and 34 m below the graben surface. However, most of the times, dikes that arrive at these shallow depths result in eruptions (Gudmundsson, 2003; Drymoni, 2020; Drymoni et al., 2020), and narrow grabens usually imply that the dike is very shallow and close to feed an eruption (Trippanera et al., 2014; Hjartardóttir et al., 2016). The setting observed in the field (with narrow graben but no signs of eruption) is therefore challenging these ideas, either that very shallow dike usually leads to an eruption, or that the "graben rule" cannot be always reliable. Magee and Jackson (2021) already discussed the graben rule, indicating that 3D fault geometry and kinematics should be considered to estimate the depth of the dike tip. Furthermore, the spreading rate can also play a role (Curewitz and Karson, 1998; Carbotte et al., 2006). According to numerical models, the narrow graben could have been generated by the intrusion of a vertical dike with a high overpressure, which became arrested despite its shallow depth. This last condition has been observed in several cases, especially in Figures 25-26, and could have been favored by the presence of soft layers in the sequence.

4.4.2.3 1928 fissure and Ripe della Naca faults

In the easternmost part of the 1928 fissure (Sector 4), the dike encountered the upper scarp of the Ripe della Naca faults, which helped the uprise of magma acting as a plane of weakness. However, limited field examples have been observed with dikes that deflect into a

pre-existing structure. Previous numerical studies at the Santorini caldera proposed that deflection occurs when the pre-existing structure is economical for the dike (Drymoni et al., 2021). This scenario is observed mostly in case of active heterogeneous or homogeneous fault cores, steeply dipping dike faults and low values of tensile strength, which can be close to zero (Gudmundsson, 2020). Also, Browning and Gudmundsson (2015) studied the Hafnarfjall extinct volcano (western Iceland), where they investigated different scenarios with varying dike properties and boundary conditions, showing that caldera ring faults can channel and deflect inclined sheets, forming ring dikes. Scenarios of high-angle faults capturing dikes at small depths have also been reported through analytical and numerical studies in Nevada, USA (Gaffney et al., 2007). Finally, Thiele et al. (2021) analyzed reactivated magma pathways at the Tamburiente caldera (Spain), suggesting that contrasting elastic properties of the magma-filled fractures and of the host rock can cause the deflection of the dikes, also forming multiple dikes.

In the numerical models of this work, the scenario of a channeled dike can be satisfied if Mode I conditions are met, but not Mode II. In Figure 22 shear stresses are distributing above the dike tip, but they are not high enough to reactivate pre-existing fractures near to the tip of the dike, due to the presence of the thick tuff layer that suppresses the distribution of stresses up to the surface.

4.4.2.4 Upwarping and regional considerations

According to field observations, topographic upwarping occurred at very local sites, indicating that the translation of the host rock upward, due to dike vertical propagation, was a minor process. This observation is consistent with Trippanera et al. (2015a), who suggested that the propagation of a dike occurs through the gradual lateral expansion of it.

More generally, along the 1928 fissure it is possible to observe a right-stepping arrangement of the structures, especially in two zones: i) where the 1928 fracture zone passes from the VdB floor to its rim, and ii) where it intersects the upper Ripe della Naca fault scarp. In both cases, the dike encountered a major topographic scarp, 130 m and 90-130 m high, respectively. The gravitational unbuttressing due to the presence of these two main

topographic scarps can therefore explain the southward deviation of the dike. Conversely, the dike propagated straight where the topography was characterized by a constant low-angle slope.

Regarding the general orientation of the 1928 fissure, this is sub-orthogonal to the main direction of sliding of the volcano flank, and parallel to the Ripe della Naca faults. These observations suggest that dike propagation was favored by the regional stress field, associated with the eastern sliding of the volcano flank under the effect of gravity and magmatic forces (Borgia et al., 1992; Groppelli and Tibaldi, 1999; Tibaldi and Groppelli, 2002; Neri et al., 2004, 2007, 2009; Walter et al., 2005a; Neri and Acocella, 2006; Solaro et al., 2010; Azzaro et al., 2012; Ruch et al., 2012; Siniscalchi et al., 2012; Bonforte et al., 2013; Le Corvec et al., 2014; Urlaub et al., 2018; De Novellis et al., 2019). Flank sliding causes decompression, which favors magma rising, that in turn can lead to an acceleration of the flank slip (Acocella et al., 2003a; Neri et al., 2004, 2009; Pezzo et al., 2020). This is consistent with the presence, in the study area, of other several eruptive fissures characterized by the same orientation, like the 1971 fissure (that will be the topic of Chapter 5) located 2 km to the south, the parallel pre-1928 fractures (green lines in Fig. 17F), and other ENE-aligned Holocene pyroclastic cones. Dike injection along this ENE direction could have been favored also by the development of a roll-over structure caused by flank sliding above a listric detachment, which leads to local extension, as suggested by Ruch et al. (2010).

5. Case study 2 – 1971 Fissure (Mt. Etna)

5.1 Introduction to the case study

As already introduced in the previous chapters, normal faults, grabens, and tension fractures are common features that can be generated in rift zones by crustal extension due to plate spreading (Thatcher and Hill, 1995; Rowland et al., 2007). Besides tectonic extension, the formation of these structures can be ascribed to dike injection and propagation, due to a concentration of tensile and shear stresses at the tip. When a vertical dike intrudes in the host rock, two maxima of tensile and shear stress form, one on each side of the dike plane, and a symmetric graben is expected to form at the surface. According to the "graben rule", the distance between the two maxima is roughly equal to twice the depth of the dike tip (Pollard et al., 1983; Mastin and Pollard, 1988). Instead, an inclined sheet intrusion would cause an asymmetrical distribution of stresses, with the resulting formation of a half-graben at the surface (Pollard et al., 1983; Mastin and Pollard, 1988; Bazargan and Gudmundsson, 2020), as observed also for the 1928 case study.

In this case study, a graben produced by an E-propagating dike during the 1971 eruption on Mt. Etna is investigated. This graben represents an exceptional case study, since it is a rare example of a dike-induced graben fully exposed in section view. Due to its location along the northern wall of the VdB, it is possible to reconstruct its geometry both in plan and section view, and to gain insights about the stratigraphic succession affected by the deformation. The work focuses on quantifying dike-induced deformation, with special attention to the asymmetrical geometry of the graben faults. Field observations were integrated with structural and geomorphological data collected thanks to historical aerial photographs from before and after the event, as well as drone surveys, carried out in the summer 2022. Finally, these data were used as inputs for FEM numerical models, to investigate the distribution and orientation of stresses at the dike tip and in the host rock, to understand which factors caused the asymmetry in the geometry of the dike-induced graben. In the models, the influence of different parameters was analyzed, varying: *i)* dip angles of the dike (75° and 90°), *ii)* the inclination of the topographic slope (0°-25°), and *iii)* layering of the host rock, considering first homogeneous and then heterogeneous models.

The here presented results have also been reported in Bonali et al. (submitted). I actively participated in the fieldwork, in the quantitative structural data collection on photogrammetry-derived models, and in the numerical modeling.

5.2 Specific materials and methodology

The study area, which includes the VdB floor and rim and part of the eastern flank of Mt. Etna (Figs. 8 and 9A), is in a logistically difficult location, characterized by rough and dangerous terrains. Furthermore, the last 50 years of eruptions have covered the area with meters of pyroclastic deposits, coming from the summit vents.

For these reasons, in this work the following methodologies were used: *i)* first, two sets of historical aerial photographs were analyzed, prior and after the 1971 event, to identify the dike-induced faults (Figs. 32A-B); *ii)* then, UAV-collected pictures were processed to reconstruct a high-resolution orthomosaic, DSM and 3D model for quantitative data collection; *iii)* classical field checks were carried out to locate the graben faults; *iv)* finally, numerical models were run to investigate dike-induced stresses distribution and orientation with different geometrical and mechanical conditions.

5.2.1. Mapping of dike-induced faults from historical aerial photos

To precisely identify the area affected by dike-induced deformation during the 1971 event, two sets of historical aerial photos, from prior and after the event, were compared. Specifically, 20 photos from 1954 and 1983, ten per each year, were bought in TIFF format from the Istituto Geografico Militare (IGM) (https://www.igmi.org/), with a resolution of 2400 dpi. Then, they were analyzed in stereoscopic view and processed to reconstruct two high-resolution orthomosaics and DSMs, using the photogrammetry techniques already explained in Section 2.2.2. In Agisoft Metashape, medium quality settings were used both for the alignment and the dense cloud building process. To georeference the two models, 15 GCPs were collected from the topographic map of 1955, covering an area of 9 x 5 km.

The two resulting DSMs were not reliable enough to collect quantitative data of the faults vertical offsets, due to a low accuracy. On the other hand, the resulting orthomosaics had a resolution of 29.0 and 19.5 cm/pixel, respectively (Figs. 32A-B), allowing to identify the 1971 dike-related faults, and produce a structural map of the area. Finally, this structural map was also used to plan field and drone surveys.
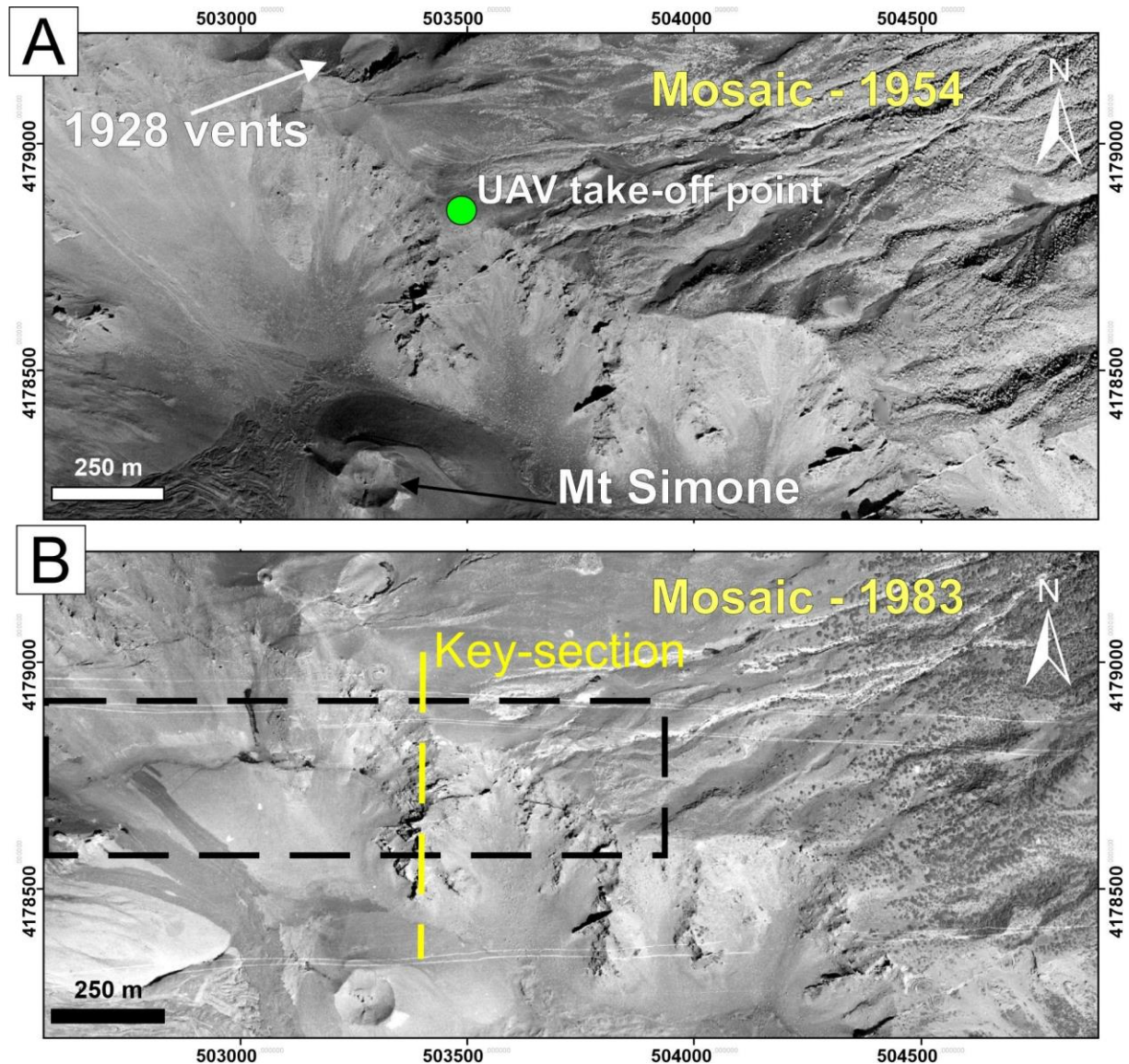
Fig. 32. Orthomosaics reconstructed from historical aerial photos from (A) 1954 and (B) 1983. The black box indicates the study area, affected by dike-induced graben formation during the 1971 event. In (A), the take-off point for UAV surveys is represented with the green dot. Coordinate Reference System: WGS 84 - UTM zone 33N (Bonali et al., submitted).

5.2.2. Quantitative data collection from UAV-SfM derived models and field surveys

To obtain high-resolution orthomosaics and DSMs, SfM photogrammetry processing was applied to UAV-collected pictures, with the workflow explained in detail in Section 2.2.1.

Regarding the collection of the pictures, a DJI Phantom 4 PRO was used, equipped with a high-resolution camera sensor (20 Megapixel) and a Real-Time Kinematic (RTK) technology. Due to the difficult logistic conditions and inaccessibility of part of the study area, the Unmanned Aerial System (UAS) integrated the RTK module, to improve the accuracy of the positioning data of the image up to a centimeter (Positioning accuracy: vertical 1.5 cm + 1 ppm; horizontal 1 cm + 1 ppm; 1 ppm = error increase of 1 mm per kilometer of aircraft displacement), without adding GCPs all over the area. The UAS was connected to the DJI D-RTK 2 High Precision Global Navigation Satellite System (GNSS) Mobile Station, a receiver that supports all the major satellite systems (GPS: L1, L2, L5; BEIDOU: B1, B2, B3; GLONASS: F1, F2; GALILEO: E1, E5A, E5B; for more technical information see: https://www.dji.com/it/phantom-4-rtk). The overall study area was divided in five subareas with five different flight surveys, planned considering weather conditions, that can vary fast, as well as the presence of natural obstacles such as topographic highs. The starting point was located along the rim of the VdB (Fig. 32A), and the flight height was set to 80-95 m. The flight path was determined based on wind speed and direction, with an overlap of 85% along the flight path and 80% in the lateral direction (Gerloni et al., 2018; Antoniou et al., 2019; Bonali et al., 2019, 2021a; Fallati et al., 2020). The flight was set with a constant speed velocity, and pictures were taken using equal time interval modality. The 656 collected pictures were then processed through Agisoft Metashape, to create a sparse and dense cloud (Fig. 33A), from which a DSM (resolution of 11 cm/pixel, Fig. 34A), an orthomosaic (resolution of 5.5 cm/pixel, Fig. 34B) and a 3D Tiled Model (resolution of 5.5 cm/pixel, Fig. 33B) were derived as final products. Details about the processing settings and results are reported in Tables 1 and 2.

Another drone survey was conducted in the VdB with a DJI Mavic 2 Enterprise, with the take-off point at about 2130 m a.s.l. (Fig. 33B), to collect 100 pictures with the camera facing the

vertical scarp. These further pictures enabled to confirm the observations made in the field and on the other resulting models.
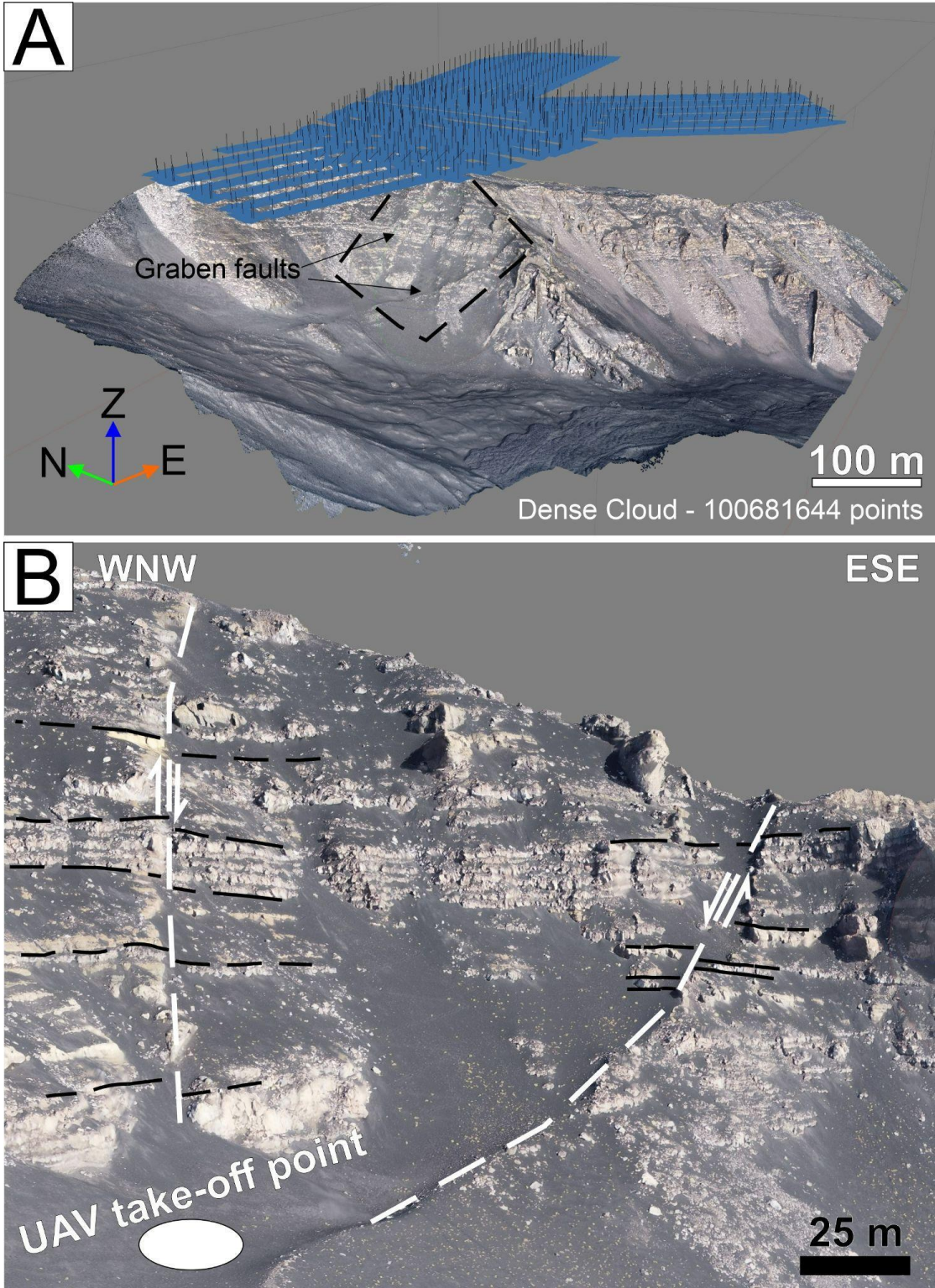
Fig. 33. (A) 3D view of the dense cloud and (B) 3D Tiled model derived from UAV-collected images through SfM photogrammetry processing. Black lines in (B) indicate the layers that

were used to measure the vertical offset along the graben faults, represented with white dashed lines. The white dot represents the UAV take-off point for the flight with the DJI Mavic 2 Enterprise (Bonali et al., submitted).

Table 1. Settings and results related to the SfM photogrammetry processing.

SfM Photogrammetry processing	Alignment processing settings	High accuracy / Generic and Reference Preselection
	Key Point / Tie Point limit	80000 / 20000
	Resulting Tie Points	948317
	Dense Cloud processing settings	High Accuracy / Aggressive Filtering
	Resulting Dense Cloud (Points)	100681644
	Resulting DSM Resolution	11 cm/pix
	Resulting Orthomosaic / 3D Texture	5.48 cm/pix

Table 2. Processing time for the DSM and orthomosaic, including the time for UAV survey and image acquisition.

UAV survey / Images Acquisition	SfM Photogrammetry Processing time								Overall total Total
	Tie Points		Depth maps	Dense Cloud	DSM	Orthomosaic	3D Tiled Model	Total for SfM	
	Matching	Alignment							
0:30:00	0:40:55	0:31:46	2:51:00	1:52:00	0:00:57	0:14:27	0:51:53	7:02:58	7:32:58

The resulting DSM and orthomosaic were analyzed in a GIS environment (ArcMap v. 10.8.1). Here, structures were identified and mapped, and through the "Linear Directional Mean" tool, it was possible to collect the strike, length, and the coordinate of the midpoint of each structure (Appendix 2, Table A2.1). Graben width was measured on the orthomosaic/DSM (Fig. 34) and related to the elevation a.s.l. (Appendix 2, Table A2.2). The 3D Tiled Model was explored with the immersive VR, as explained in Section 2.2.3, to collect quantitative structural data. Vertical offsets were measured as the difference in elevation of two segments of the same layer that was recognized as offset by the graben faults (Fig. 33B). These values were then related to the coordinates and the elevation a.s.l., to investigate variations of the vertical displacement and to estimate the dip angle of the two graben faults.

Finally, all the mapped structures were checked in the field during a campaign in the summer of 2022, both in the VdB and along the eastern flank of the volcano, from the VdB rim to the lower 1971 eruptive vents. The height of the morphological scarps was collected to have information about the vertical offset, even if this represents a minimum offset due to the presence of a thick pyroclastic cover. Fault scarps were observed in detail to recognize signs of reactivation, finding no evidence.
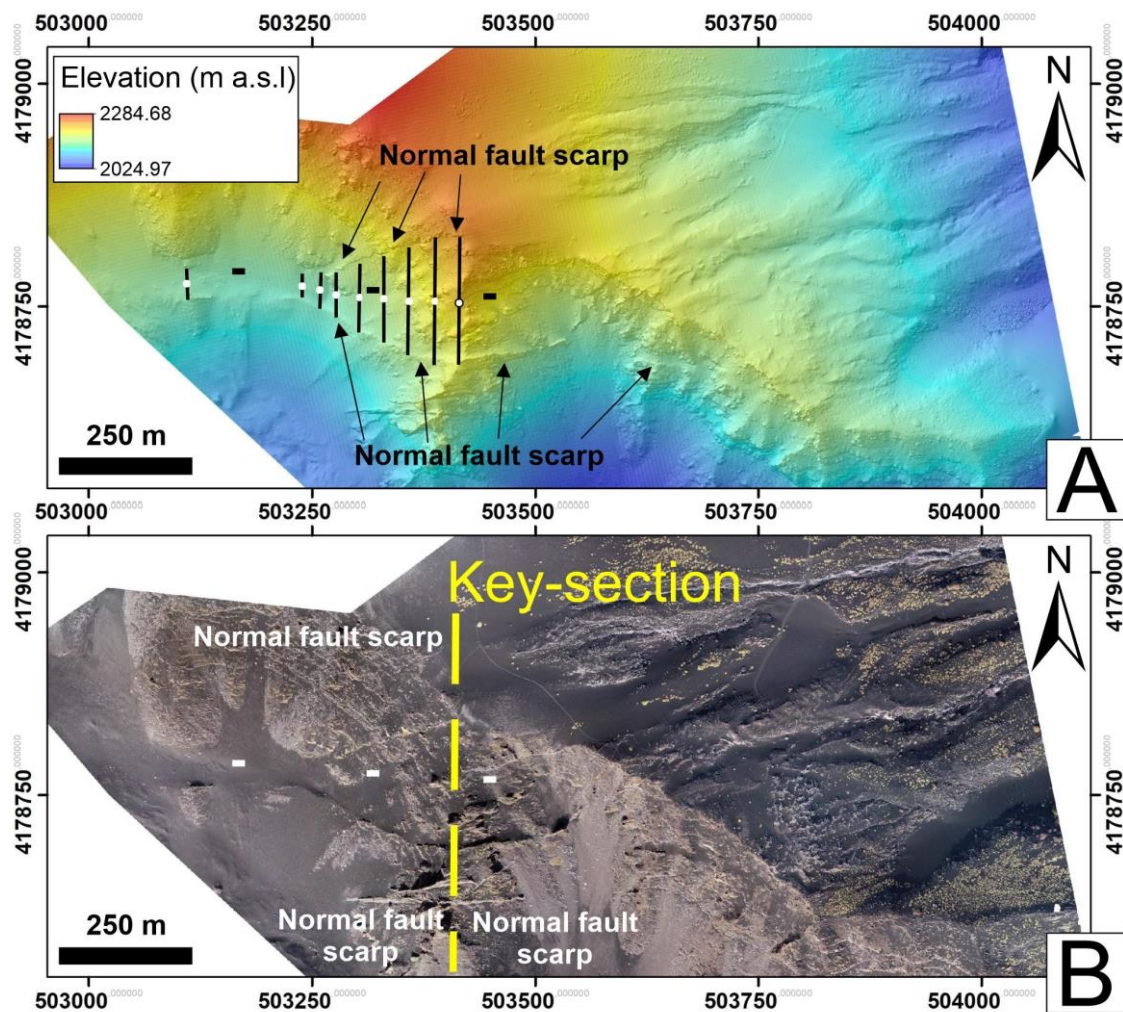
Fig. 34. SfM-derived (A) DSM and (B) orthomosaic, from UAV-collected pictures. Black lines in (A) indicate the graben width, white dots represent the sites where elevation values were collected. Coordinate Reference System: WGS 84 - UTM zone 33N (Bonali et al., submitted).

5.2.3. Setup of models

For this case study, the main goal was to analyze the distribution and orientation of stresses around the dike tip and in the host rock, based on the following parameters: *i)* dike dip; *ii)* host rock layering; *iii)* topographic slope. As explained in Section 2.3, the models were run through the FEM software COMSOL Multiphysics (v. 6.1). In detail, numerical models focus on a key cross-section (Fig. 34B), almost orthogonal to the graben faults and to the direction of dike propagation. In this section, the stratigraphy is known, as presented by Branca et al. (2011a) (Fig. 9B).

The dike was modeled as a cavity with a constant overpressure of 6 MPa, consistently with other papers on this topic (e.g., Gudmundsson, 1986a, 2011b; Drymoni et al., 2020). Indeed, the thickness of the 1971 dike is unknown, but this overpressure value is coherent with the thickness of dikes along the northern part of the VdB, which ranges 0.2-5 m (Ferrari et al., 1991). Furthermore, all the models were subjected to an extensional stress field (F_{ext}) of 1 and 3 MPa, to reproduce the extensional regime that is dominant on the eastern flank of Mt. Etna, due to the gradual slip of this volcano flank towards east, as testified to by *i)* the presence of normal faults and tension fractures (Neri et al., 1991; Tibaldi and Groppelli, 2002) and *ii)* stress inversion with extensional component (Cocina et al., 1997). All the models were fastened at the bottom edge to avoid rigid-body rotation and translation, with a fixed constraint in the midpoint of the bottom edge and a roller boundary condition (Figs. 35A-C). The dike was designed at two different depths: Y_1, with the top at the contact between layers A and B, and Y_2, with the top located 30 m deeper (Figs. 35B-D). Depth Y_1 corresponds to the depth of convergence of the graben faults at depth (around 2100 m a.s.l.), accordingly with what observed by Magee and Jackson (2021). The dike was designed also 30 m deeper (Y_2), to investigate if this can have effects on the distribution and orientation of stresses above the dike tip. Furthermore, dike dip was varied, considering both a vertical dike, and a dike dipping 75° to the north and to the south (Figs. 35B-D). This is consistent with dike dip angles measured in the field by previous authors, who reported that 70% of the dikes in the northern part of the VdB are vertical or subvertical, whereas the remaining 30% were intruded along inclined planes, even greater than 60° (Ferrari et al., 1991).

The topographic surface was also modeled in two different ways, as a horizontal surface and as a 25°-dipping free surface, the latter mimicking the real topographic slope of the study area. To do that, two different settings were created:

- A 3000 x 3000 m square box to reproduce a flat topography. The box was discretized by a very fine triangular meshing, with a minimum element quality of 0.5572 m and 42754 boundary triangular elements (Figs. 35A-B);

- A 3000 x 3000 m square box, cut in the upper right corner to obtain an upper boundary with a 25° inclination, to better reproduce the topography of the study area (Figs. 9A). The box was discretized by a very fine triangular meshing, with a minimum element quality of 0.4167 m and 40049 boundary triangular elements (Figs. 35C-D).
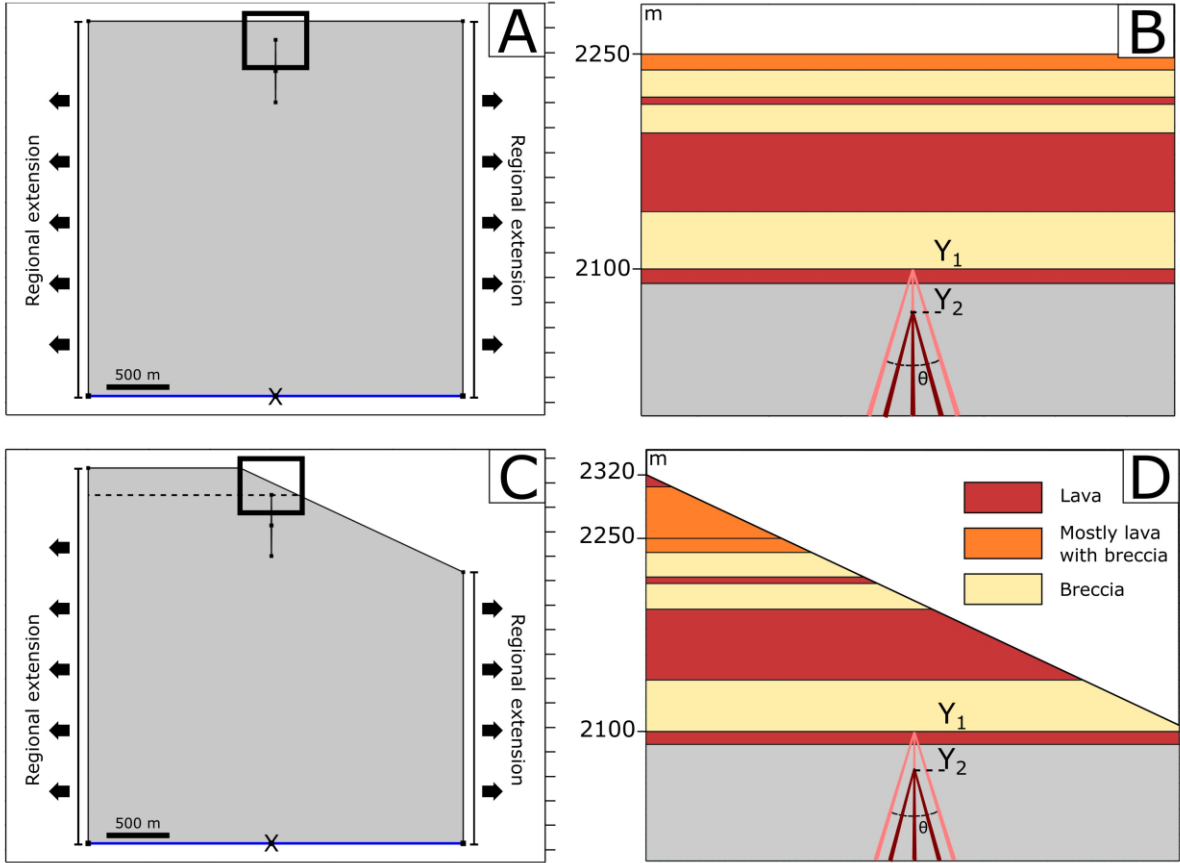
Fig. 35. (A) Numerical model setup to reproduce a flat topography. (B) Zoom on the dike tip in case of a flat topography. (C) Numerical model setup to reproduce a 25°-inclined topography. The dashed line indicates the location of the contact for the case study with a single

mechanical contrast. (D) Zoom on the dike tip in case of a 25°-inclined topography. In (A) and (C) the arrows represent regional extension. The X symbol at the bottom indicates a fixed constraint, the blue line specifies the roller boundary condition. In (B) and (D), different colors of the dike represent different depths, and the different dip angles of the dike are shown; stratigraphy is from literature data (see Fig. 9B) and observations on the 3D UAV-derived model (Bonali et al., submitted).

Regarding host rock layering, first a homogeneous host rock was considered for both settings (flat and inclined topography), with E = 10 GPa, ν = 0.25 and ρ = 2600 kg/m^3. Then, the role of a single mechanical contrast was investigated, adding a contact above the tip of the dike at depth Y_1 in the models with an inclined topography (Fig. 35C). Four different values of mechanical contrasts were tested, given by the ratio between the E of the upper layer and the E of the lower layer (Kavanagh et al., 2006; Drymoni et al., 2020), namely 1/10, 1/4, 4/10 and 10/4. Finally, for both settings the dike was modeled within a layered host rock, considering the stratigraphy observed on the 3D UAV-derived model and literature data (Branca et al., 2011a) (Figs. 35B-D). The stratigraphic column is the one showed in Figure 9B. To assign E values to the lava layers, the Hoek-Diederichs equation was used (Hoek and Diederichs, 2006), as suggested by Heap et al. (2020). This equation calculates the E value of a rock mass starting from the E value of the intact rock (E_i), and using the GSI, a unitless value that describes the rock mass structure (Marinos et al., 2005). To estimate the GSI, I employed the high-resolution 3D model, obtaining values of 40-55. Considering the E_i values by Heap et al. (2020) for basalts from Mt. Etna and this GSI range, E of the lava layers resulted between 4 and 9 MPa. The upper value is similar to the one of 10 MPa suggested by Gudmundsson (2011a), who considered the most common values in the literature. The lower value is consistent with the one by Apuani et al. (2005), who used laboratory tests and GSI index of lithotechnical units of Stromboli. Therefore, these two sets of values were applied for the models of this case study, as shown in Table 3.

Table 3. Mechanical properties of the layers of the numerical models. ρ = density of the material; v = Poisson's ratio; E = Young's modulus (Set 1 from Gudmundsson, 2011a and Set 2 from Apuani et al., 2005).

Layer	ρ (kg/m^3)	v	Set 1 - E (GPa)	Set 2 - E (GPa)
Lava	2600	0.25	10	4
Breccia	2300	0.25	1	1
Mostly lava with breccia	2500	0.25	7	3
Basement	2600	0.25	10	10

Tensile and von Mises shear stresses in the host rock were plotted, to investigate the distribution of stress around the dike tip and to understand the likelihood of fracturing and/or faulting, based on the variations of the above-listed parameters. Considering that the values of *in-situ* tensile strength in crustal rocks (presented in Section 2.3) can be lower than the most used values (2-4 MPa), for this case study the attention is focused on the areas of main concentration of stresses as favorable for fracturing/faulting, without considering a specific threshold. Furthermore, the orientation of the maximum (σ_1) and minimum (σ_3) compressive stresses was plotted as arrows within the host rock.

5.3 Results

5.3.1. Structural data

The comparison between the orthomosaics of 1954 and 1983 allowed to obtain a structural map of the study area, and to recognize a graben structure with a length of about 2 km and an overall E-W trend (Fig. 36). This graben affects both the floor of the VdB and its rim, as well as the eastern flank of Mt. Etna (Figs. 33-34-36).

In the area, 13 fault scarps with dip-slip movement, related to the graben, are present, as well as two eruptive fissures and 13 lineaments (Fig. 36). Regarding the strike, the linear structures that were identified mostly present an E-W direction, with an average of N83.3°E

and a standard deviation (SD) of 16.2°. The 13 structures classified as lineaments show an E-W trend, with an average of N85.3°E and a SD of 17.3° (Fig. 36B), and probably represent the expression of graben faults as well. However, along these structures the vertical offset is not measurable on historical photos and in the field, due to the thick coverage of pyroclastic material (e.g., Fig. 9A). Normal faults also present an E-W trend, with an average of N85.6°E and a SD of 12.3° (Fig. 36B). Differently, eruptive fissures are present on the eastern flank of Mt. Etna and present a NE-SW orientation, with an average of N54.9°E and a SD of 1.1° (Fig. 36B). All the collected measurements are listed in Appendix 2, Tables A2.1.
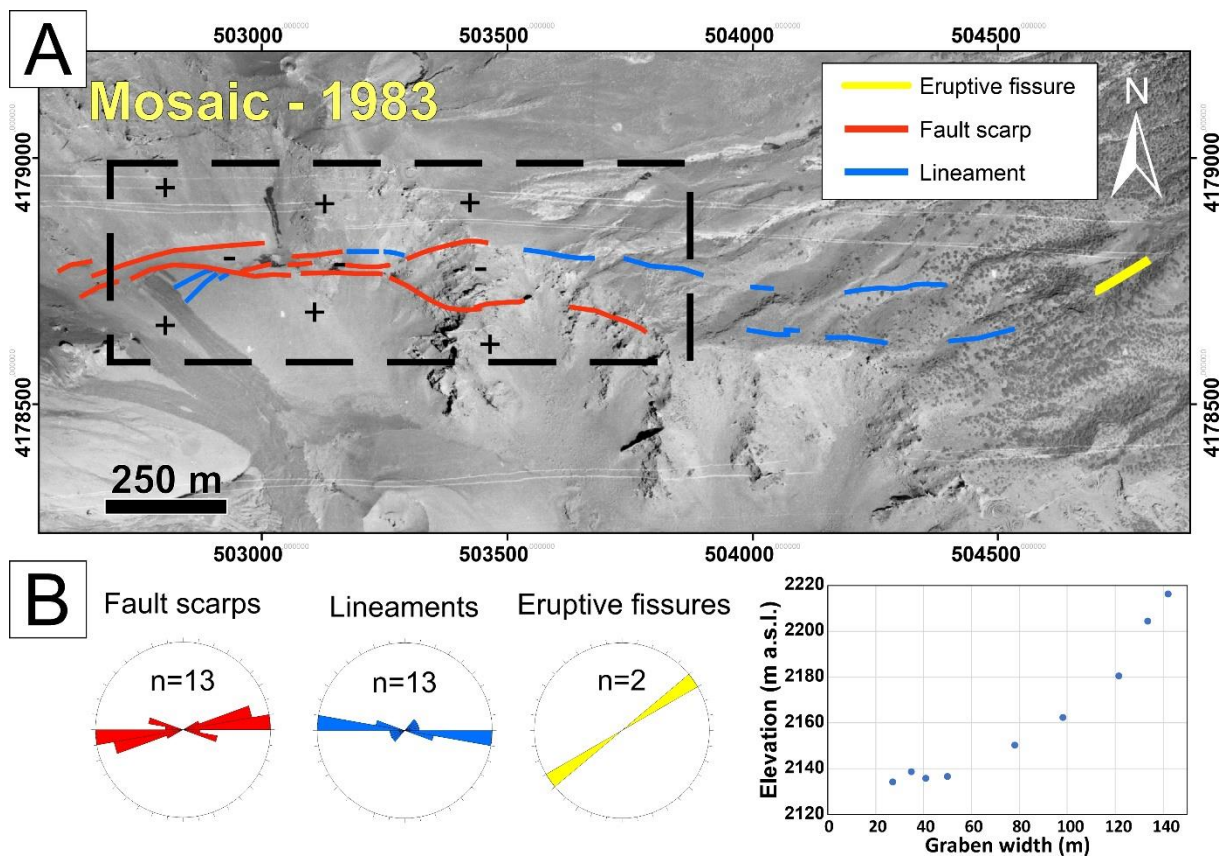
Fig. 36. (A) Orthomosaic derived from the historical aerial photos of 1983, with all the mapped structures. The downthrown block is indicated with the symbol "−". The black rectangle represents the area covered by drone survey. Coordinate Reference System: WGS 84 - UTM zone 33N. (B) Rose diagrams showing the strike of fault scarps, lineaments and eruptive fissures in the study area, and graph showing the relation between graben width and elevation (modified after Bonali et al., submitted).

The graben width was measured and related with the elevation a.s.l. (Fig. 36B). Width values are between 27 and 143 m, and they increase with the elevation, which is between 2134 and 2219 m a.s.l. (Fig. 34A). All the collected measurements about the graben width are listed in Appendix 2, Tables A2.2.

In section view, it was possible to observe the geometry of the fault, and to measure their dip angle, obtaining a value of 70° for the south-dipping fault, and of 50° for the north-dipping one (Fig. 33B). Finally, the vertical offset along the graben faults was measured, mostly thanks to the SfM-derived 3D model and DSM, due to the dangerousness of the area and to the presence of pyroclastic coverage. On the VdB floor, the height of the morphological scarps is only in the order of decimeters, differently from the values of vertical offset collected along the VdB wall in section view, which are in the order of meters. In more detail, the south-dipping fault shows values between 2.4 and 3.0 m, and the north-dipping one shows values between 1.9 and 2.8 m (Table 4). In both cases, the highest values are measured at the highest elevation. Considering the average dip angles of the two faults (70° and 50°), the resulting net slip is between 2.6 and 3.2 m (average of 2.9 m), and between 2.5 and 3.6 m (average of 3.0 m), respectively.

Table 4. Displacement along the two graben faults. The vertical offset was measured on the SfM-derived 3D model (Fig. 33B). The net slip was calculated using the average dip angle measured for the two faults.

Elevation (m a.s.l.)	Vertical offset (m)	Net slip (m)	Dip dir. (°)	Av. Dip angle (°)
2151	2.5	2.7	South	70
2170	2.8	3.0	South	70
2182	2.4	2.6	South	70
2192	3.0	3.2	South	70
2210	2.7	2.9	South	70
2153	1.9	2.5	North	50
2155	1.9	2.5	North	50
2160	2.8	3.6	North	50
2178	2.6	3.4	North	50

5.3.2. Numerical modeling

5.3.2.1. Models with a homogeneous host rock

First, the dike was modeled in a homogeneous host rock, to investigate the role of only dike inclination and topography on the distribution and orientation of stresses. In all cases, the models are subjected to an extensional stress field of 1 MPa.

If the topography is flat (Fig. 37), both tensile and von Mises shear stress reach high concentration above the dike tip, suggesting favorable conditions for fracturing and faulting in the host rock and at the surface, regardless of dike inclination. Inclining the dike to 75°, stresses distribute asymmetrically, but fracturing and faulting are still expected (Figs. 37B-D).
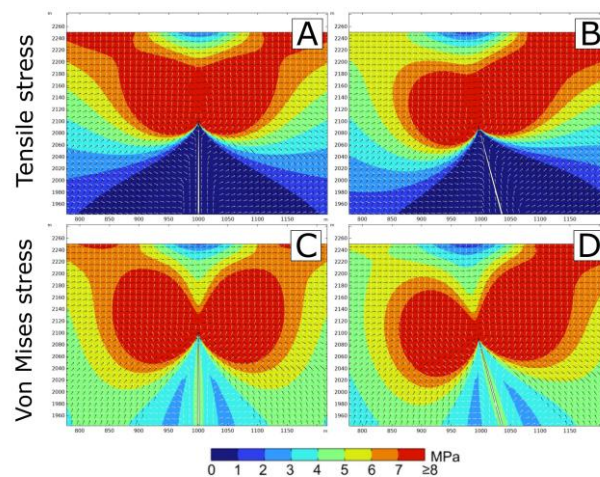
Fig. 37. Numerical models with a homogeneous host rock, an extensional stress field of 1 MPa, a flat topography and different dike inclinations. The distributions of tensile (A-B) and von Mises shear (C-D) stresses are shown with the same color scale. Orientations of σ_1 and σ_3 are shown by white and black arrows, respectively (Bonali et al., submitted).

If topography presents a 25°-south-dipping slope (Fig. 38), the asymmetrical distribution of stresses is even more evident. In this case, a north-dipping dike is the most favorable to the formation of fractures and faults at both sides of the dike, as observed in the field (Figs. 38C-

F). The intrusion of a vertical dike also promotes fracturing and faulting at both sides of the dike, but with a lower concentration of stresses compared to the north-dipping one (Figs. 38A-D). A south-dipping dike, on the other hand, would lead to the formation of faults only to the south, not consistently with what is observed in the field (Fig. 38E). Furthermore, in all cases, a strong clockwise rotation of σ_1 and σ_3 is observed, regardless of dike inclination.
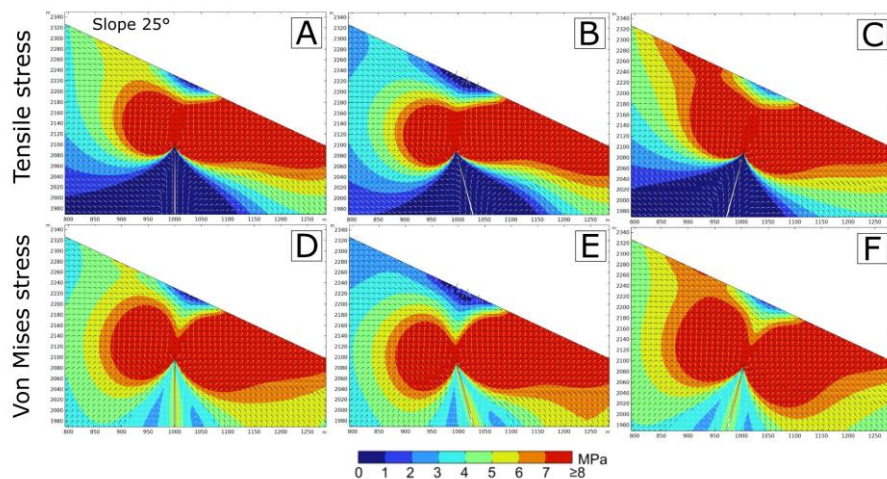
Fig. 38. Numerical models with a homogeneous host rock, an extensional stress field of 1 MPa, and a 25°-inclined south-dipping topography. The dike is modeled with different attitudes. The distributions of tensile (A-B-C) and von Mises shear (D-E-F) stresses are shown with the same color scale. Orientations of σ_1 and σ_3 are shown by white and black arrows, respectively (Bonali et al., submitted).

5.3.2.2. Models with reliable layering and flat topography

In these sets of models, the stratigraphy observed in the field was introduced (Fig. 9B), with a flat topography, to investigate the effect of layering in the host rock. As explained in Section 5.2.3, two different sets of stiffness values were used: Set 1, with values consistent with Gudmundsson (2011a) and Set 2, with values consistent with Apuani et al. (2005). An extensional stress field of 1 and 3 MPa is applied to the models, with the dike at two different depths (Y_1 and Y_2).

In Figure 39, the dike is modeled at depth Y_1. In Set 1, considering an extension of 1 MPa, tensile stress results mostly concentrated in the lava layers and suppressed in the breccia layers (Figs. 39A-B). When the dike is vertical, the distribution of tensile stress is symmetrical above the dike tip (Fig. 39A), whereas it becomes asymmetrical if the dike is inclined (Fig. 39B). This asymmetrical distribution makes fracturing at one side of the dike more likely, compared to the other side. If the extensional stress field is increased up to 3 MPa, tensile stress distribution does not change, but its magnitude increases in all the layers (Figs. 39I-J).

Fig. 39. Numerical models with layering based on field observations, a flat topography, and the dike at depth Y_1. E values are consistent with Gudmundsson (2011a) for Set 1, and with Apuani et al. (2005) for Set 2; B: breccia, ML: mostly lava with breccia, L: lava. The dike is modeled with different inclinations and is subjected to an extensional stress field of 1 and 3 MPa. The distributions of tensile (A-B-C-D-I-J-K-L) and von Mises shear (E-F-G-H-M-N-O-P)

stresses are shown with the same color scale. Orientations of σ₁ and σ₃ are shown by white and black arrows, respectively (Bonali et al., submitted).

Regarding von Mises shear stress, it shows a high concentration in the first level of breccia and in all the lava layers, decreasing in the uppermost breccia layers (Figs. 39E-F). Also in this case, the distribution is symmetrical when the dike is vertical (Fig. 39E), whereas it becomes asymmetrical if the dike is inclined, with a more favorable setting for faulting at one side of the dike (Fig. 39F). If the extensional stress field is 3 MPa, the magnitude of von Mises shear stress increases in all the layers (Figs. 39M-N). Finally, in Set 1, regardless of the extensional stress field, the orientations of σ_1 and σ_3 become asymmetrical when the dike is inclined. In Set 2, magnitudes of both tensile and von Mises shear stresses are more homogeneous among the layers, compared to Set 1, with lower values in the lava layers and higher values in the breccia layers (Figs. 39C-D-G-H-K-L-O-P). The distribution of the stresses and the orientations of σ_1 and σ_3 are similar to the models of Set 1.

If the dike is at depth Y_2, with an extension of 1 MPa for Set 1, tensile stress is again more concentrated in the lavas and suppressed in the more compliant layers, but with lower magnitudes in all the layers compared to the models with the dike at depth Y_1. Also in this case, when the dike is vertical, tensile stress distributes symmetrically (Fig. 40A), whereas it distributes asymmetrically if the dike is inclined, favoring fracturing at one side compared to the other (Fig. 40B). If the extensional stress field increases to 3 MPa, the magnitude of tensile stress increases in all the layers, but its distribution does not show significative variations (Figs. 40I-J).

Also, the von Mises shear stress, with an extension of 1 MPa, is more concentrated in the lava layers and less in the two uppermost breccia layers, but with lower magnitudes than the case with the dike at depth Y_1. Von Mises shear stress distribution is symmetrical if the dike is vertical (Fig. 40E), whereas it becomes asymmetrical if the dike is inclined (Fig. 40F). Increasing the extension to 3 MPa, von Mises shear stress distribution remains similar, but the magnitude increases (Figs. 40M-N). In all the models of Set 1, the orientation of σ_1 and σ_3 is affected by the inclination of the dike, which causes their rotation, regardless of the magnitude of the extensional stress field. In Set 2 (Figs. 40C-D-G-H-K-L-O-P), the distribution

and orientation of stresses show the same pattern of Set 1, again with lower magnitudes compared to the models with the dike at depth Y_1. The main difference from Set 1 is represented by the magnitude of the stresses, that in Set 2 are more homogeneous, with lower values in the lavas and higher magnitudes in the more compliant layers.

Fig. 40. Numerical models with layering based on field observations, a flat topography, and the dike at depth Y_2. E values are consistent with Gudmundsson (2011a) for Set 1, and with Apuani et al. (2005) for Set 2; B: breccia, ML: mostly lava with breccia, L: lava. The dike is modeled with different inclinations and is subjected to an extensional stress field of 1 and 3 MPa. The distributions of tensile (A-B-C-D-I-J-K-L) and von Mises shear (E-F-G-H-M-N-O-P) stresses are shown with the same color scale. Orientations of σ_1 and σ_3 are shown by white and black arrows, respectively (Bonali et al., submitted).

5.3.2.3. Models with one mechanical contrast and reliable topography

In these models, a mechanical contrast was introduced at depth Y_1 (Fig. 35C), maintaining a 25°-inclined topography and an extensional stress field of 1 MPa.

In Figures 41A-B-C-D-E-F, the mechanical contrast, given by the ratio between the E of the upper layer and the E of the lower layer, is 1/10. In this case, both tensile and von Mises shear stresses concentrate in the lower layer, characterized by a greater stiffness, whereas they are suppressed in the upper layer. This inhibits fracturing and faulting at the surface, regardless of the dike attitude. In all the models, σ_1 and σ_3 rotate clockwise.

If the mechanical contrast is equal to 1/4 (Figs. 41G-H-I-J-K-L), both stresses reach higher values of magnitude in the upper layer, allowing fracturing and faulting at the surface. Fracturing is expected at both sides of the dike if the dike is vertical or north-dipping, whereas faulting occurs at both sides only if the dike is north-dipping. In the case of a south-dipping dike, both fracturing and faulting occur only at the southern side. Also in this case, a clockwise rotation of σ_1 and σ_3 is observed.

Varying the mechanical contrast to 4/10 (Figs. 42A-B-C-D-E-F), tensile and von Mises shear stresses show higher concentrations in the upper layer, but fracturing and faulting are expected at both sides only if the dike is vertical or north-dipping. Also in this case, when the dike is south-dipping, faulting is expected only at the southern side. A clockwise rotation of σ_1 and σ_3 is observed, similarly to the previous cases.

Finally, in Figures 42G-H-I-J-K-L, the mechanical contrast is 10/4, with the upper layer that has a greater stiffness than the lower one. Tensile and von Mises shear stresses are more concentrated in the upper layer than in the lower one, but also in this case faulting is expected only at the southern side if the dike is south-dipping. The orientation of σ_1 and σ_3 is rotated clockwise also in this case.
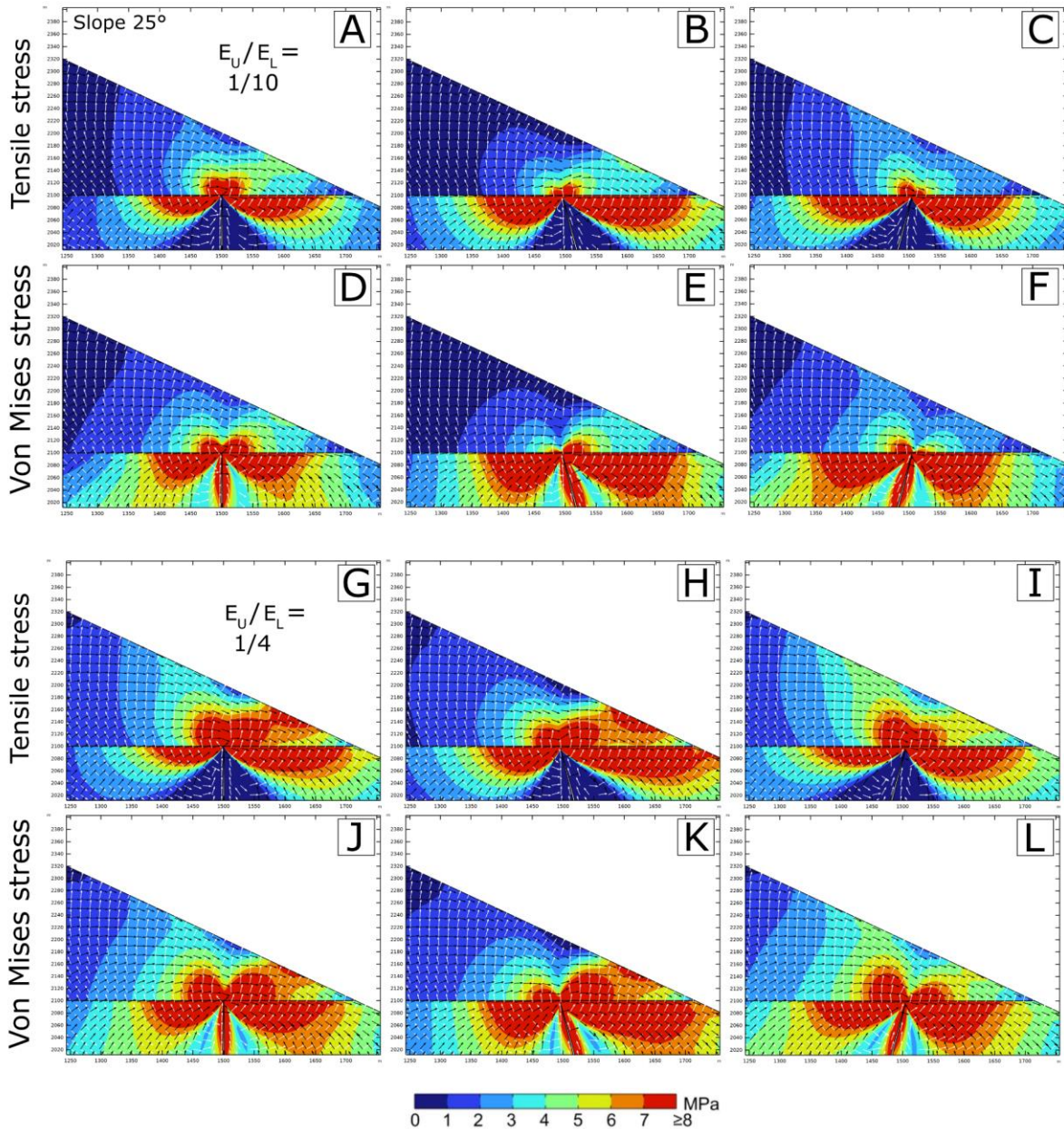
Fig. 41. Numerical models with one mechanical contrast, equal to 1/10 from (A) to (F) and 1/4 from (G) to (L), an inclined topography, and subjected to an extensional stress field of 1 MPa. E_U: Young's modulus of the upper layer, E_L: Young's modulus of the lower layer. The dike is modeled with different attitudes. The distributions of tensile (A-B-C-G-H-I) and von Mises shear (D-E-F-J-K-L) stresses are shown with the same color scale. Orientations of σ_1 and σ_3 are shown by white and black arrows, respectively (Bonali et al., submitted).
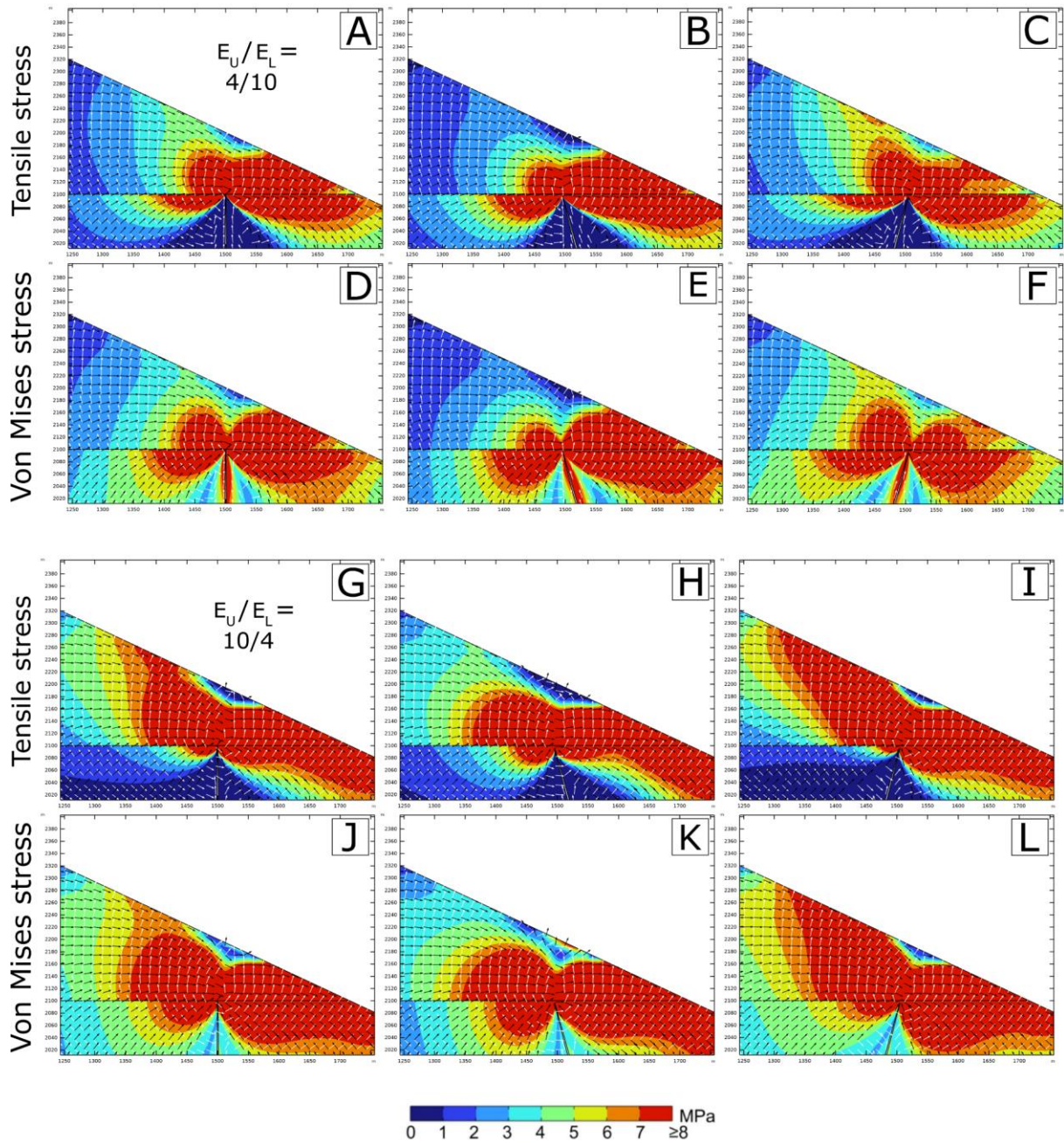
Fig. 42. Numerical models with one mechanical contrast, equal to 4/10 from (A) to (F) and 10/4 from (G) to (L), an inclined topography, and subjected to an extensional stress field of 1 MPa. E_U: Young's modulus of the upper layer, E_L: Young's modulus of the lower layer. The dike is modeled with different attitudes. The distributions of tensile (A-B-C-G-H-I) and von Mises shear (D-E-F-J-K-L) stresses are shown with the same color scale. Orientations of σ_1 and σ_3 are shown by white and black arrows, respectively (Bonali et al., submitted).

5.3.2.4. Models with reliable layering and topography

Finally, the stratigraphy observed in the field was introduced, with a 25°-inclined south-dipping topographic surface (Fig. 35D). Also in this case, two different sets of E values were used (Table 3). The dike is subjected to an extensional stress field of 1 and 3 MPa and is modeled at two different depths (Y_1 and Y_2).

If the dike is at depth Y_1 with an extension of 1 MPa, for Set 1 tensile stress is mostly concentrated in the lava layers and suppressed in the breccia layers (Figs. 43A-B-C). Fracturing is expected at both sides if the dike is north-dipping, or if it is vertical. When the dike is south-dipping, fracturing is possible only at the southern side, not consistently with what is observed in the field. Increasing the extensional stress field to 3 MPa, stress distribution does not change, but the magnitude increases (Figs. 43G-H-I). With an extension of 1 MPa, von Mises shear stress shows a higher concentration in the first level of breccia and in the upper lavas, compared to the uppermost breccia layers (Figs. 43D-E-F). Faulting is promoted at both sides of the dike only if the dike is north-dipping or vertical, whereas it is expected only at the southern side if the dike is south-dipping. If the extensional stress field increases to 3 MPa (Figs. 43J-K-L), the magnitude of von Mises shear stress increases. Finally, the orientation of σ_1 and σ_3 is rotated clockwise in all the models, regardless of the magnitude of the extensional stress field.

For Set 2 (Fig. 44), the results are similar to Set 1, but with more homogeneous magnitudes of stresses, as already observed for the case with a flat topography. Stress distribution and rotation do not show great differences from Set 1.
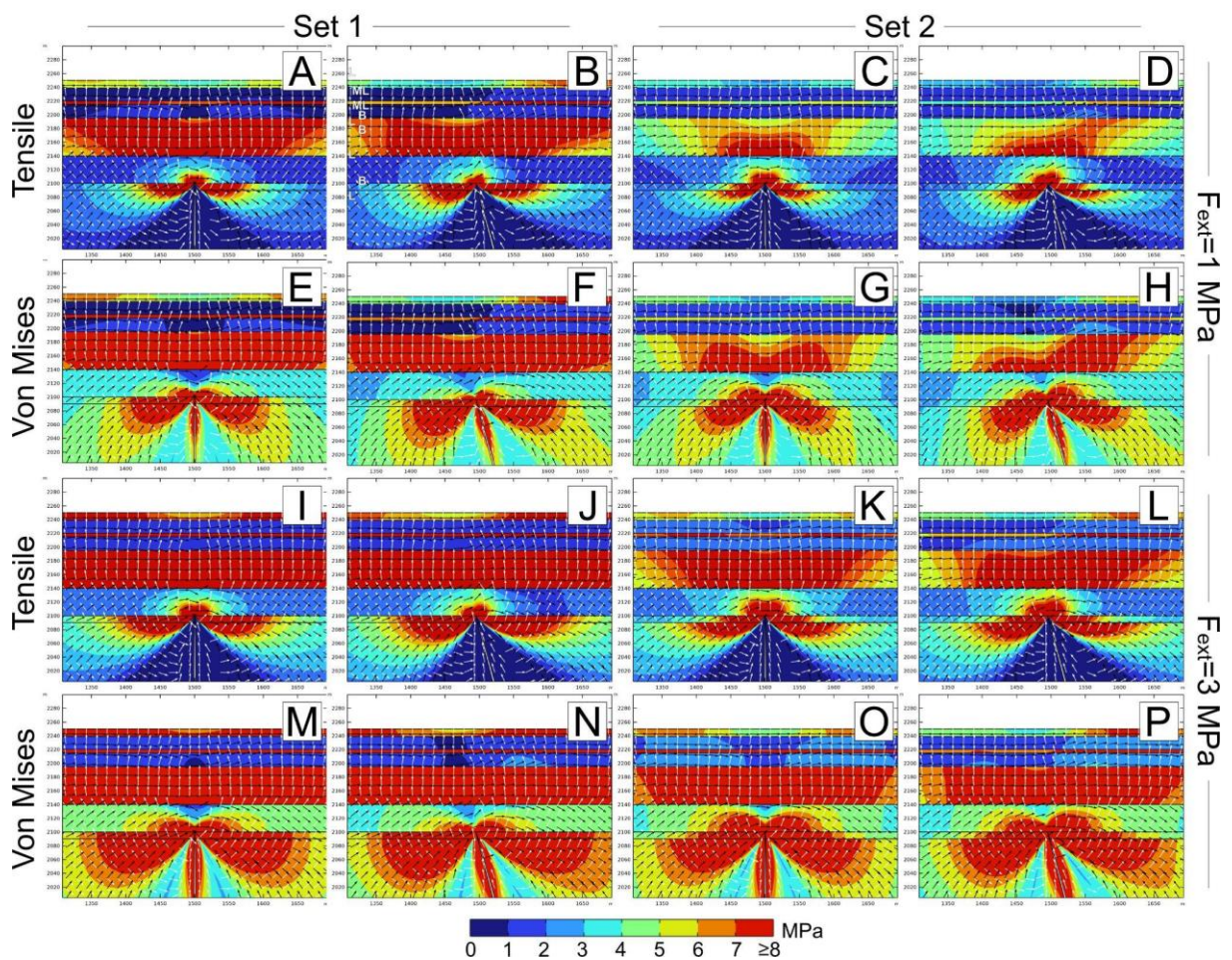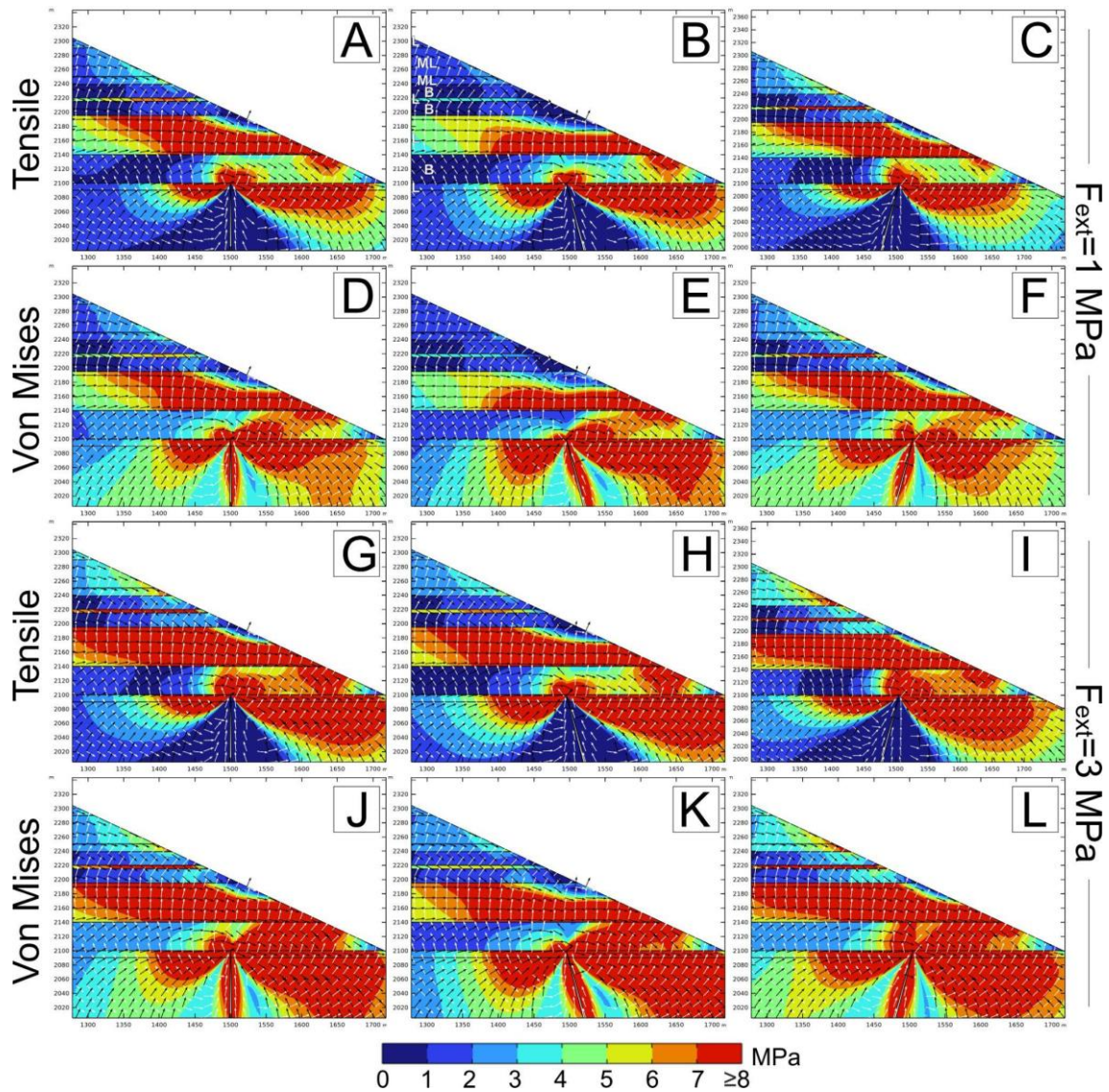
Fig. 43. Numerical models with layering based on field observations, an inclined topography, and the dike at depth Y_1. E values are consistent with Gudmundsson (2011a) (Set 1). B: breccia, ML: mostly lava with breccia, L: lava. The dike is modeled with different attitudes and is subjected to an extensional stress field of 1 and 3 MPa. The distributions of tensile (A-B-C-G-H-I) and von Mises shear (D-E-F-J-K-L) stresses are shown with the same color scale. Orientations of σ_1 and σ_3 are shown by white and black arrows, respectively (Bonali et al., submitted).
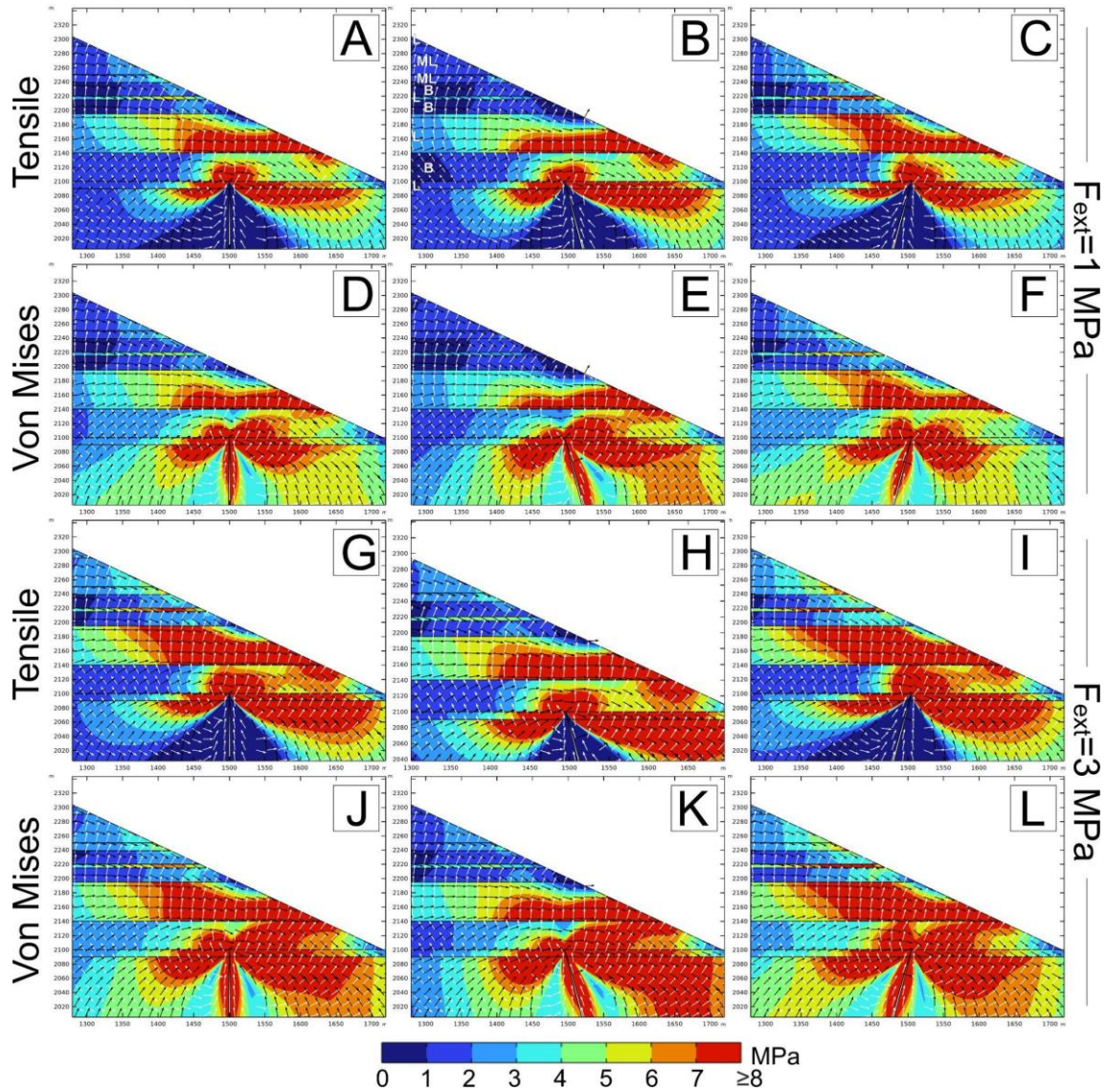
Fig. 44. Numerical models with layering based on field observations, an inclined topography, and the dike at depth Y$_1$. E values are consistent with Apuani et al. (2005) (Set 2). B: breccia, ML: mostly lava with breccia, L: lava. The dike is modeled with different attitudes and is subjected to an extensional stress field of 1 and 3 MPa. The distributions of tensile (A-B-C-G-H-I) and von Mises shear (D-E-F-J-K-L) stresses are shown with the same color scale. Orientations of σ$_1$ and σ$_3$ are shown by white and black arrows, respectively (Bonali et al., submitted).

Deepening the dike at depth Y$_2$ (Figs. 45-46), the results are similar, but with a general decrease of both tensile and von Mises shear stresses compared to the models with the dike

97

at depth Y_1. This behavior is observed both for Set 1 (Fig. 45) and Set 2 (Fig. 46). In both cases, tensile stress concentrates mostly in the lava layers, and is suppressed in the more compliant breccias. Its distribution favors fracturing at both sides when the dike is north-dipping or vertical, and only at the southern side if the dike is south-dipping. The same distribution is observed for the von Mises shear stress. Increasing the extensional stress field, the magnitude of tensile and von Mises shear stresses increase. For Set 2, both stresses become more homogeneous between the different layers. Regarding the orientation of σ_1 and σ_3, in all the models they show a clockwise rotation, regardless of the magnitude of the extensional stress field and of the used set of E values.
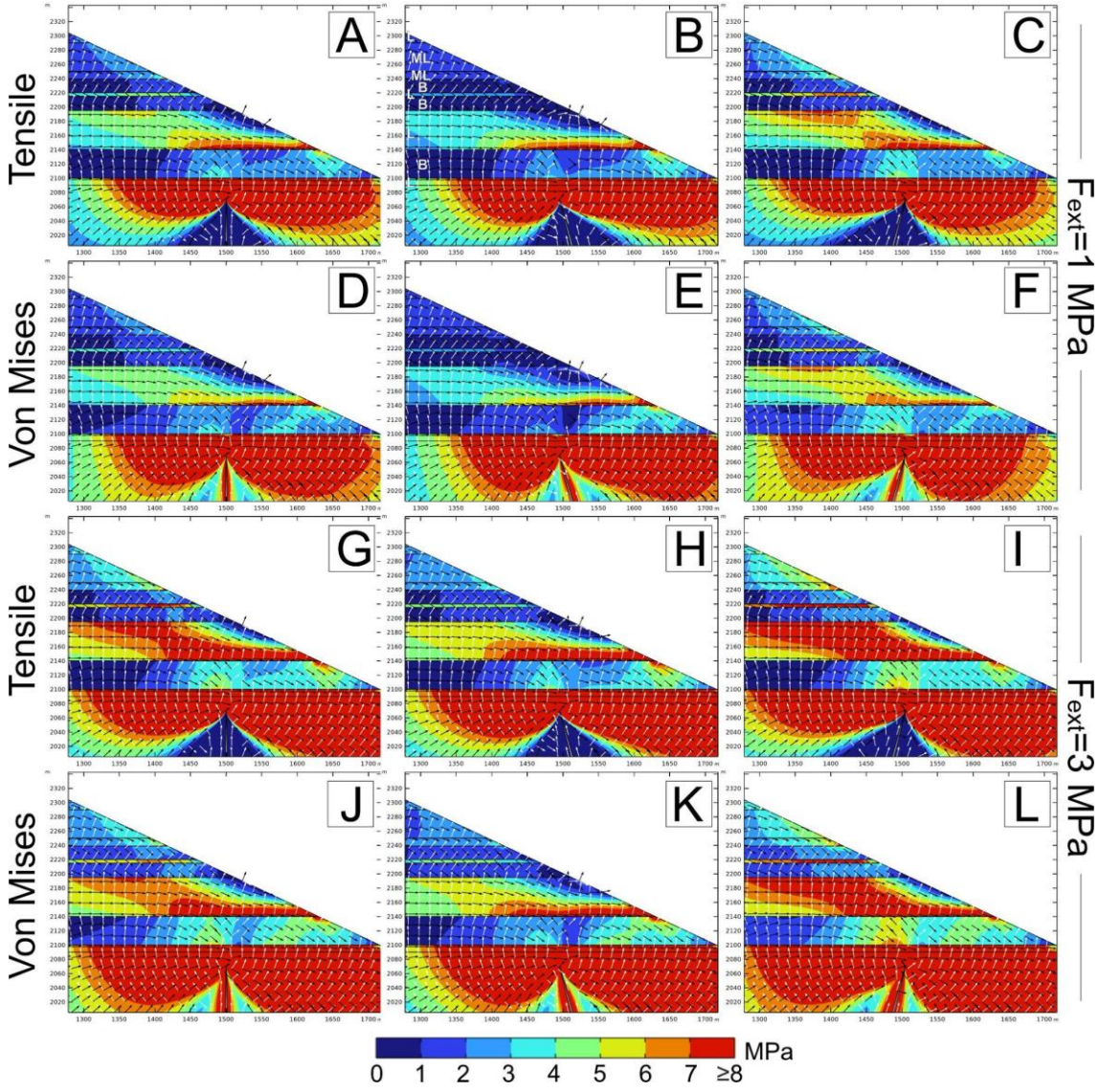
Fig. 45. Numerical models with layering based on field observations, an inclined topography, and the dike at depth Y_2. E values are consistent with Gudmundsson (2011a) (Set 1). B:

breccia, ML: mostly lava with breccia, L: lava. The dike is modeled with different attitudes and is subjected to an extensional stress field of 1 and 3 MPa. The distributions of tensile (A-B-C-G-H-I) and von Mises shear (D-E-F-J-K-L) stresses are shown with the same color scale. Orientations of σ_1 and σ_3 are shown by white and black arrows, respectively (*Bonali et al., submitted*).
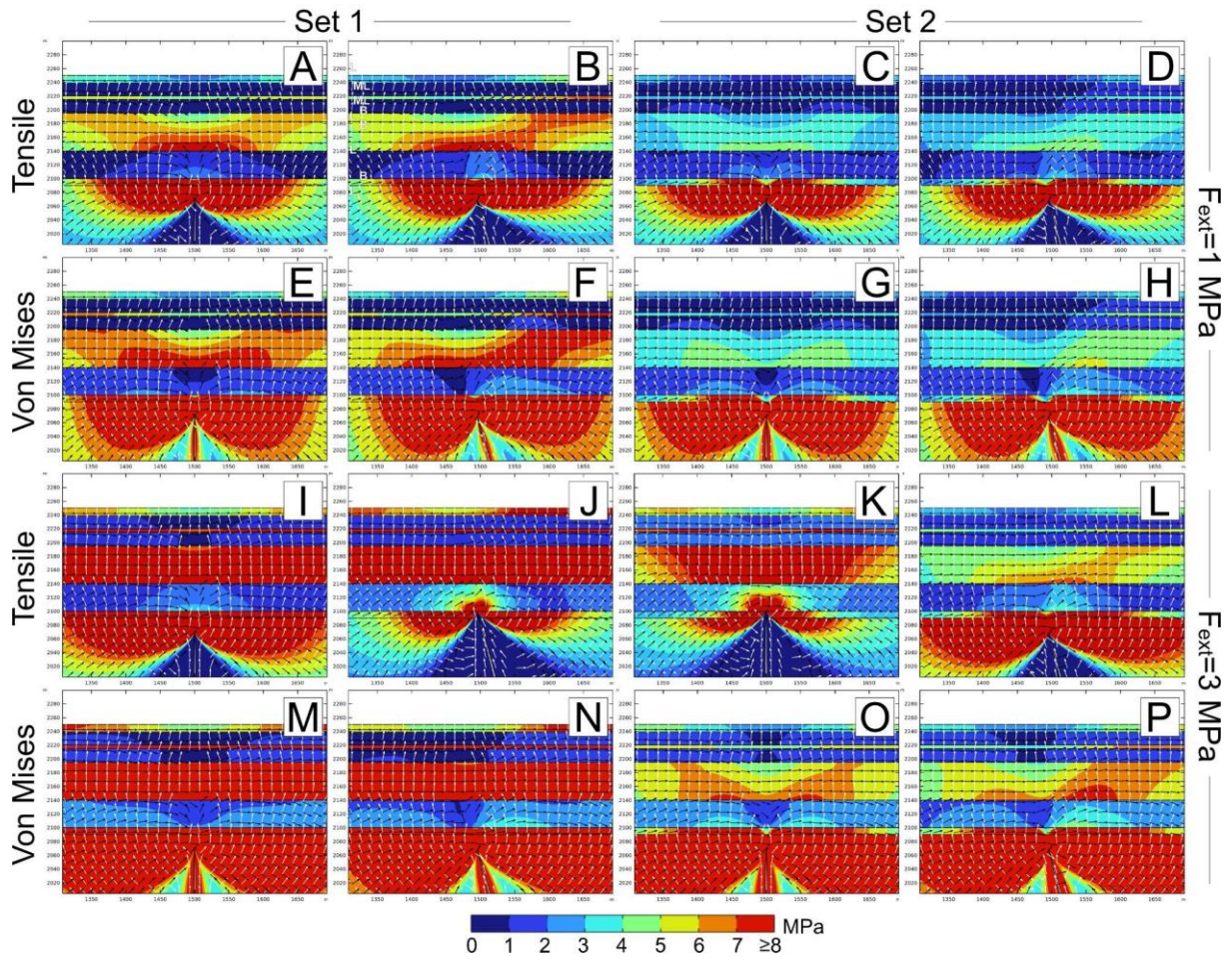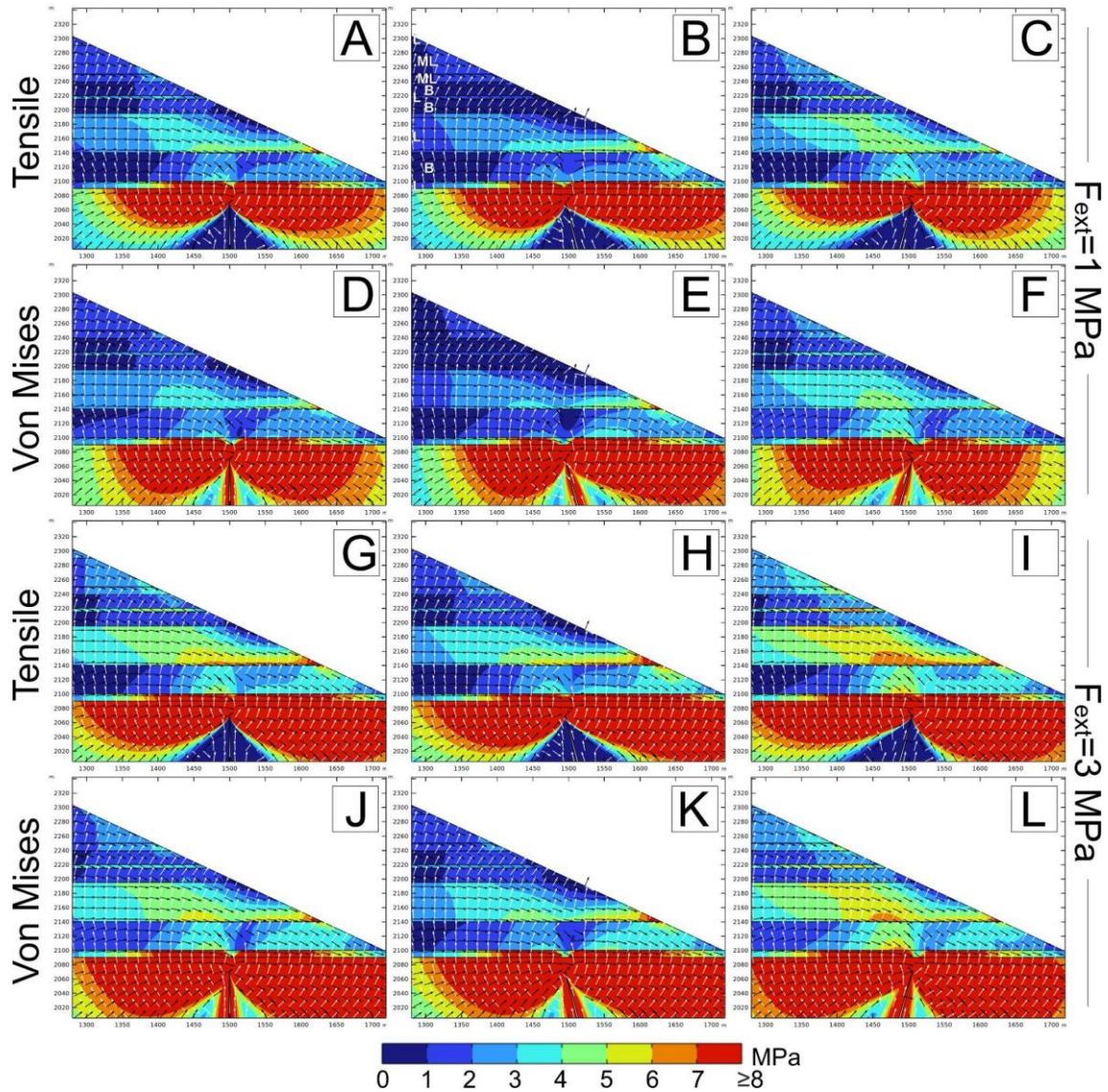

Fig. 46. Numerical models with layering based on field observations, an inclined topography, and the dike at depth Y_2. E values are consistent with Apuani et al. (2005) (Set 2). B: breccia, ML: mostly lava with breccia, L: lava. The dike is modeled with different attitudes and is subjected to an extensional stress field of 1 and 3 MPa. The distributions of tensile (A-B-C-G-

99

H-I) and von Mises shear (D-E-F-J-K-L) stresses are shown with the same color scale. Orientations of σ_1 and σ_3 are shown by white and black arrows, respectively (Bonali et al., submitted).

5.4 Discussion

Understanding the relation between surface deformation and dike intrusions is crucial for volcanotectonics, also due to the major implications for both volcanic and seismic hazard at different scales. As an example, the 2021, 2022 and 2023 Fagradalsfjall eruptions in Iceland were all preceded by intense seismic swarms, reaching M_L 5.3 on February 24th, 2021 (Fischer et al., 2022), M_W 5.4 on July 31st, 2022 and M_W 4.8 on July 5th, 2023 (https://en.vedur.is/). A seismic swarm was also detected before the eruption in the Bardarbunga volcanic system (Iceland) in 2014 (Sigmundsson et al., 2015). During this event, the formation of a graben associated with the dike intrusion was also recognized at the surface, a few days before the beginning of the eruption (Ruch et al., 2016). In Japan, the Izu volcanic islands were also affected by a seismic swarm related to the lateral propagation of a dike in 2000, as is common in the Izu peninsula (Ukawa and Tsukahara, 1996; Aoki et al., 1999), with five events with M > 6 (Toda et al., 2002). At Mt. Etna, the opening of a ~4 km-long system of eruptive fissures during the 2002-2003 eruption was accompanied by the reactivation of flank slippage along the Pernicana Fault System (Monaco et al., 2005), with seismic activity and surface fracturing (Neri et al., 2004). Furthermore, the propagation of the dike was related with the formation of grabens at the surface (Neri et al., 2004). Seismic swarms also accompanied the lateral propagation of the dike during the 1971 event.

5.4.1. Magnitude of deformation and graben geometry

The normal faults recognized on the orthomosaics (Fig. 36) show an overall E-W trend, with a rotation to an ENE-WSW trend in the easternmost part, where the eruption occurred. Faulting affects an area that is between 1 and 2 km long, with the lower value that includes only the structures classified as normal faults, and the higher value that includes also the

structures classified as lineaments. These values of length are not within the range given by the classical empirical relationship between magnitude and fracture length for normal faults (Wells and Coppersmith, 1994; Blaser et al., 2010), but the formation of these faults surely caused earthquakes with M < 4.5, as observed in other diking events (e.g., Ruch et al., 2016; Fischer et al., 2022), based on the minimum value provided by Blaser et al. (2010).

Due to the thick coverage of pyroclastic deposits in the study area (Fig. 9A), most structural data were collected along the graben faults in section view, thanks to field observations and on the UAV-SfM-derived 3D Tiled Model (Figs. 33A-B), DSM and orthomosaic (Figs. 34A-B). The width of the graben goes from 27 to 143 m moving eastward, with a difference in elevation of 84 m from the bottom to the upper part of the section view. According to the "graben rule" (Pollard et al., 1983; Mastin and Pollard, 1988), these width values suggest a depth of the dike top equal to 13.5 and 71.5 m, respectively. This means that the dike top should be at an elevation of about 2125 m a.s.l. below the narrower part of the graben, and at 2150 m a.s.l. below the wider part, indicating an upward propagation of the dike top of about 25-30 m during its eastward propagation. However, the lower location of the eruptive vents on the eastern flank of the volcano indicates a downward propagation of the dike top, as shown in the inset of Figure 8. These observations suggest a more complex relation between graben width and dike depth than the one proposed by the "graben rule". Furthermore, some authors suggested that the depth of the dike top could be located at the convergence of the normal faults (e.g., Magee and Jackson, 2021). In this case study, the exposure in section view of the normal faults is consistent with this hypothesis, with the dike top located around their convergence.

Regarding vertical offset values, the highest were measured at the highest elevation, indicating a surface subsidence of 2.5-3 m. These values are consistent with the subsidence observed during the Afar event in 2005, that caused a subsidence of 2-3 m in the northern part of the rift, due to the intrusion of a dike that was inferred at a depth of 2 km (Wright et al., 2006). Higher values of vertical offsets were measured during the Bardarbunga event (Iceland) in 2014, with maximum displacements of 6 m (Ruch et al., 2016), and a dike depth hypothesized at 300 m (Hjartardóttir et al., 2016). The values measured in this case study are also consistent with the values observed for the 1928 fissure, with average values of 2.4 m in the western graben and 1.1 m in the eastern one (Chapter 4).

Finally, field data and the SfM-derived models showed that the 1971 graben is asymmetric with regards to the dip angle of the faults. The south-dipping fault has an inclination of 70°, whereas the north-dipping one has a dip angle of 50°. This feature would have not been detected with classical plan-view studies (e.g., Sigurdsson, 1980; Gudmundsson and Bäckström, 1991; Rubin, 1992; Acocella and Neri, 2003; Billi et al., 2003; Ebinger et al., 2010; Pallister et al., 2010; Bonaccorso et al., 2011; Trippanera et al., 2015b, 2019; Acocella and Trippanera, 2016; Hjartardóttir et al., 2016; Ruch et al., 2016; Al Shehri and Gudmundsson, 2018; Tibaldi et al., 2020b), considering that the offset between the two faults is similar.

5.4.2. Geometry of the faults, dike-induced stresses and topography

The main goal of numerical models was to understand how dike-induced stresses affected the geometry of the faults, causing the asymmetry (with regards to inclination) observed in section view (Figs. 9 and 33). Structural data showed a dip angle of 70° for the south-dipping fault, which lays in the typical range of 60-80° usually observed in nature, and a lower one for the north-dipping fault (50°). The conditions that could have favored fracturing and/or faulting were also analyzed, considering the variations of tensile and von Mises shear stress induced by dike overpressure (e.g., Al Shehri and Gudmundsson, 2018; Bazargan and Gudmundsson, 2019). The role of the following parameters was investigated: *i)* homogeneous and layered host rock; *ii)* dike dip and depth; *iii)* horizontal and inclined (25°) topographic surface; *iv)* presence of an extensional stress field. With a homogeneous host rock, both tensile and von Mises shear stresses increase due to dike overpressure, regardless of all the other parameters. When layering is added in the host rock, soft layers suppress both tensile and von Mises shear stresses, which concentrate in the stiffer lava layers, as expected from previous studies (Al Shehri and Gudmundsson, 2018; Bazargan and Gudmundsson, 2019). Increasing the dike depth causes a decrease in the magnitude of stresses, but not on the distribution, whereas the inclination of the dike plays a significant role, causing an asymmetrical distribution of stresses and a rotation of σ_1 and σ_3. With an inclined topography, an asymmetrical distribution of stresses and a clockwise rotation of σ_1 and σ_3 are observed, even with a vertical dike. In this case, the most favorable conditions for fracturing and faulting as observed in the field are found with a vertical dike, or with a dike

that dips opposite to the topographic surface. Finally, the application of an extensional stress field to the models does not cause variations in the distribution or orientation of stresses, but only in their magnitude.

Considering the classical likelihood-arrangement of a fault plane with respect to the σ_1 and σ_3 orientation (Anderson, 1905; Hafner, 1951; Ramsay and Lisle, 2000; Fossen, 2016), an asymmetrical orientation of σ_1 and σ_3 can suggest an asymmetrical geometry of the fault planes. According to numerical models, the following observations can be made: *i)* varying stiffness values of the lava layers does not affect σ_1 and σ_3 orientation; *ii)* different dip angles of the dike promote an asymmetrical orientation of σ_1 and σ_3; *iii)* an inclined topography always causes a rotation of σ_1 and σ_3, regardless of dike attitude, depth and layering of the host rock; *iv)* varying the depth of the dike does not affect σ_1 and σ_3 orientation. All these considerations suggest a key role of topography on σ_1 and σ_3 orientation and, in turn, on the geometry of the faults that are observed in section view.

The effect of topography had already been observed by previous authors through analytical models, that showed how the presence of a relief can affect the width of the graben (Trippanera et al., 2015a). The presence of a topographic gradient can also affect the amount of deformation along the graben faults, with greater offsets along the fault that dips in the same direction of the slope, as observed by Billi et al. (2003) on Mt. Etna and by Tibaldi et al. (2020b) in the Krafla Fissure Swarm (Iceland). Numerical models here show that deformation depends also on the inclination of the dike, although the amount of deformation in the models was not determined. According to the structural data, however, the offsets of the two graben faults are similar in this case study, and the asymmetry regards only the inclination of the structures, as explained above. In the 1971 case study, topography affects dike propagation and surface deformation also at a larger scale. In Figure 36, it is evident that the 1971 swarm of fissures and faults has an E-W trend when it cuts the VdB bottom and after it intersects its lateral escarpment. More to the east, above the shoulder of the VdB, the swarm runs exactly parallel to the VdB rim, again with a general E-W trend. This behavior was observed also at Stromboli, where dikes strike parallel to the Sciara del Fuoco lateral collapse scarps (e.g., Tibaldi, 1996; Neri et al., 2008). Furthermore, this tendency of dikes to intrude parallel to topographic scarps was also demonstrated by analogue modeling (Acocella and Tibaldi, 2005), and similar results were obtained for an unstable flank that has not collapsed

yet (Walter and Troll, 2003). For the 1971 Mt. Etna event, structural data suggest that the propagation of the dike was mostly affected by the topography of the volcanic edifice, related to the unbuttressing caused by the presence of the VdB depression. In the easternmost sector of the 1971 swarm, the eruptive fissures are reoriented ENE-WSW. This can be explained by the intersection of the dike with an already existing structure with this orientation, related to the eastward sliding of the eastern flank of Mt. Etna.

5.4.3. Fault nucleation

Another discussed topic about dike-induced faults regards the nucleation of graben faults. In the last decades, this subject has been investigated mostly by analogue modeling. Mastin and Pollard (1988) observed the formation of fractures at the top of the dike, and then at the surface, which subsequently connect within each other developing the graben faults. More recently, Trippanera et al. (2015a) noticed in their analogue models that the throw of normal faults was higher at the surface, decreasing towards the dike tip. Furthermore, they calculated the 2D Coulomb stress change due to a vertical opening fracture, showing that normal faulting is favored at the surface at the two sides of the dike. Considering these observations, they suggested a downward propagation of the graben faults, which develop near the surface and then propagate towards the tip of the dike. This hypothesis is consistent with field observations from previous authors (Gudmundsson and Bäckström, 1991; Forslund and Gudmundsson, 1992; Acocella et al., 2003b), and with numerical models by Gudmundsson (1998), who proposed a downward propagation of caldera faults. In the 1971 Mt. Etna case study, vertical offset values are also higher at higher elevation along both graben faults (Table 4), suggesting their downward propagation.

Other authors suggested an upward propagation of the graben faults, from the dike top to the surface, based on field data and numerical models, but without providing quantitative data in section view that can be compared with this case study (Grant and Kattenhorn, 2004; Tentler, 2005). More recently, a hybrid model of dike-induced fault nucleation has been proposed based on analytical modeling applied on three grabens on Mars (Rivas-Dorado et al., 2023), which suggests that in shallow narrow dikes mode I cracks form near the surface and mode II discontinuities are generated near to the tip of the dike. Folch and Marti (2004)

also suggested the synchronous nucleation of downward moving tensile fractures at the surface and of upward moving shear fractures at depth, that both contribute to the development of large plate-subsidence calderas. Considering the numerical models of this case study, dike overpressure causes an increase of tensile stress at the surface (especially if the dike is vertical or dips opposite to the topography), as well as an increase of von Mises shear stress near the dike tip. Such results support both the hypothesis for fault nucleation given by Trippanera et al. (2015a) and Rivas-Dorado et al. (2023) for a shallow dyke, whereas our structural data, with greater offsets at higher elevations, support a downward propagation of the graben faults.

6. Case study 3 – Younger Stampar eruption (SW Iceland)

6.1 Introduction to the case study

Most of the dikes that intrude in the upper crust do not result in an eruption, but they become arrested, or deflected into sills, mainly at contacts between mechanically dissimilar layers (e.g., Gudmundsson, 1986a, 2011a, b; Maccaferri et al., 2011; Drymoni et al., 2020). When they emplace in the host rock, they also generate stresses (Rubin and Gillard, 1998; Gudmundsson, 2003, 2011a; Roman and Cashman, 2006; Ágústsdóttir et al., 2016; Bazargan and Gudmundsson, 2019, 2020; Heimisson and Segall, 2020), which can cause brittle deformation at the surface, such as grabens (e.g., Acocella and Trippanera, 2016, and references within). However, field observations of dikes in different volcanic areas showed no evidence of fracturing/faulting around the tip or at the surface (e.g., Gudmundsson, 2003), and recent numerical models suggested that no dike-induced surface deformation should be expected, unless the dike tip is at < 1 km of depth (Al Shehri and Gudmundsson, 2018).

In this case study, two dikes are analyzed, both associated with the Younger Stampar eruption (1210-1240 AD, Sæmundsson et al., 2016) on the Reykjanes Peninsula (RP), SW Iceland (Fig. 11). One dike became arrested only 5 m below the topographic surface of an active rift zone, without inducing deformation at the surface. The other dike is a feeder and is located at a distance of just 30 m to the NW (Sigurgeirsson, 1995; Gudmundsson, 2017). New structural data were collected through SfM-derived high-resolution models and field surveys, both along the outcrop where the two dikes are exposed and along the crater row associated with the Younger Stampar eruption. Structural data were then used as inputs for 2D FEM numerical models, to address the two following issues: *i)* which parameters contribute to the arrest of the second dike? and *ii)* why is there no brittle deformation at the surface induced by the arrested dike? This case study is focused on a fissure swarm of the RP, where the eruptive activity is cyclic (Sæmundsson et al., 2020). For this reason, the results of this case study should enhance the understanding of present-day (2021-2023 eruptions at Fagradalsfjall) and future eruptions on the RP, with implications also for other volcanic areas around the world.

The results of this case study have been published in one paper (Corti et al., 2023). I actively participated in the fieldwork, in the quantitative structural data collection on the SfM-derived models, and in the numerical modeling.

6.2 Specific materials and methodology

For this case study, structural data were collected using mainly SfM-derived 3D models and field surveys. Subsequently, these data were used as inputs for FEM numerical models, to investigate the parameters that could have controlled magma path and dike-induced deformation. As shown in Figure 47, the role of dike overpressure and depth, the stiffness of the layers, and the effect of regional extension and local compression were analyzed, to have a final interpretation of the Stampar case study. The thickness of the dikes and of the volcanic layers of the outcrop had been already measured by Gudmundsson (2017) through field surveys. This work, however, provides new measurements collected through SfM-derived 3D models, which allowed to collect data also on the highest part of the cliff with greater accuracy. Moreover, marine erosion strongly affects the outcrop, changing the exposed parts of the dike in time, and explaining differences between the old measurements and the ones presented here. In the following subsections, the specific methodologies are illustrated in detail.
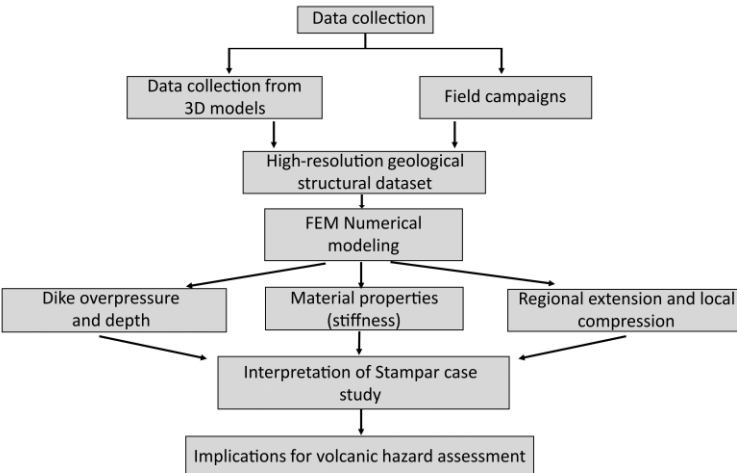
Fig. 47. Workflow showing the steps followed in this case study (modified after Corti et al., 2023).

6.2.1. Structural data collection through field surveys and 3D models

Aerial photographs of 1981, 1984 and 1988, available from the National Land Survey of Iceland website (https://www.lmi.is/), were processed with SfM techniques, as explained in detail in Section 2.2.2. Orthomosaics and DSMs were generated with a resolution up to 20 and 40 cm/pixel, respectively, covering the whole area affected by the Younger Stampar eruption. With the help of the geological map of SW Iceland at the scale of 1:100,000 (Sæmundsson et al., 2016), I mapped on these SfM-derived models all the geological units of the area, the lava flows and the main structures, highlighting the volcanic fissures of the Stampar craters (Fig. 12A). Normal faults were distinguished from tension fractures thanks to the shaded DSM, where shaded or brighter-lit slopes indicate the presence of a fault scarp (e.g., Corti et al., 2021). The base of each vent along the crater rows was mapped in a GIS environment, and the eruptive fissures were traced based on the elongation of each cone, considering the latter parallel to the orientation of the underlying dike (Tibaldi, 1995; Tibaldi and Bonali, 2017). All the mapped structures were then validated through field survey during the summers of 2021 and 2022. After the mapping, the strike of all the eruptive fissures was calculated in ArcMap (v. 10.8.1), using the tool "Line Directional Mean". All the structural data collected along the crater rows are presented in Appendix 3, Table A3.1.

To collect data from the dikes and along the outcrop, a drone survey was conducted using a DJI Spark, a small quadcopter with a camera of 12 Megapixel, already used successfully in other volcanic areas (e.g., Bonali et al., 2020). The camera had a classical nadiral orientation for most of the pictures, but for 360 pictures (out of a total of 1073), it was set with an oblique orientation, orthogonal to the cliff. The UAV was manually flown with a speed of 2 m/s, at a distance of about 20-25 m from the target and capturing images every 2 seconds. The processing of the photos was conducted as explained in detail in Section 2.2.1, and finally a high-resolution 3D model was reconstructed, with a texture resolution of 0.8 cm/pixel, as well as an orthomosaic (0.8 cm/pixel) (Fig. 12C), and a DSM (1 cm/pixel). The models were georeferenced thanks to 6 GCPs, collected using Real-Time Kinematics (RTK) positioning configuration, with an accuracy of 2 cm. These models were used to collect quantitative structural data in Agisoft Metashape and in ArcMap (v. 10.8.1), such as the

thickness of the volcanic layers, and the attitude and the thickness of the dikes. These data are presented in Appendix 3, Table A3.2 and A3.3.

6.2.2. Setup of models

With COMSOL Multiphysics (v. 5.6), a 500 x 500 m square domain was designed, and discretized by a very fine triangular meshing, with a minimum element quality of 0.4534 m and 1100 boundary triangular elements. The models were all fastened with fixed constraints in the two bottom corners, to avoid rigid-body rotation and translation (as explained in detail in Section 2.3).

The host rock was modeled as a layered elastic medium, considering previous field observations (Sigurgeirsson, 1995; Gudmundsson, 2017) and the new collected 3D structural data to replicate the stratigraphy seen in the field. To distinguish the layers, different mechanical properties (Young's modulus (E), density (ρ) and Poisson's ratio (ν)) were assigned to each of them, with typical values from the literature (Gudmundsson, 2011a; 2020). The layers, from top to bottom, are the following:

- Upper lava unit, 2 m thick, E_{UL} = 10 GPa, ρ = 2600 kg/m^3, ν = 0.25;
- Lower lava unit, 2.6 m thick, E_{LL} = 11 GPa, ρ = 2600 kg/m^3, ν = 0.25;
- Consolidated ash, 0.4 m thick, E_A = 5 GPa, ρ = 2300 kg/m^3, ν = 0.25;
- Tuff, 10 m thick, E_T = 1 GPa, ρ = 2000 kg/m^3, ν = 0.25;
- Pillow lavas, E_{PL} = 10 GPa, ρ = 2700 kg/m^3, ν = 0.25. This layer is not present in the outcrop but was included based on the offshore available data.

The dike was subjected to different boundary conditions, namely: *i)* overpressure (P_0) between 2-4 MPa, according to previous authors (Gudmundsson, 2011a, 2020; Drymoni et al., 2020), *ii)* an extensional stress field of 1 MPa (Figs. 48A-B), to reproduce plate motion (Fig. 11), and *iii)* a horizontal compressional stress (1-4 MPa), applied to all the layers cut by the feeder dike (Fig. 48C), to investigate the effect of its previous intrusion, as suggested by Gudmundsson (2017). Overpressure is related to the thickness of the dike (Sneddon, 1946;

Gudmundsson, 2011a; Becerril, 2013), therefore varying the overpressure also allows to investigate the role of dike thickness.

The maximum principal tensile stress (σ_3) and the absolute shear stress (τ, component of the von Mises shear stress on the xy plane) were plotted at the tip of the dike and in the host rock, and 1D graphs of tensile stress and von Mises shear stress (τ) were produced at the surface, to investigate the possibility of fracturing/faulting (details in Section 2.3). Finally, the orientations of the maximum (σ_1) and minimum (σ_3) principal compressive stresses were plotted as arrows, to analyze the likelihood of dike propagation or arrest.
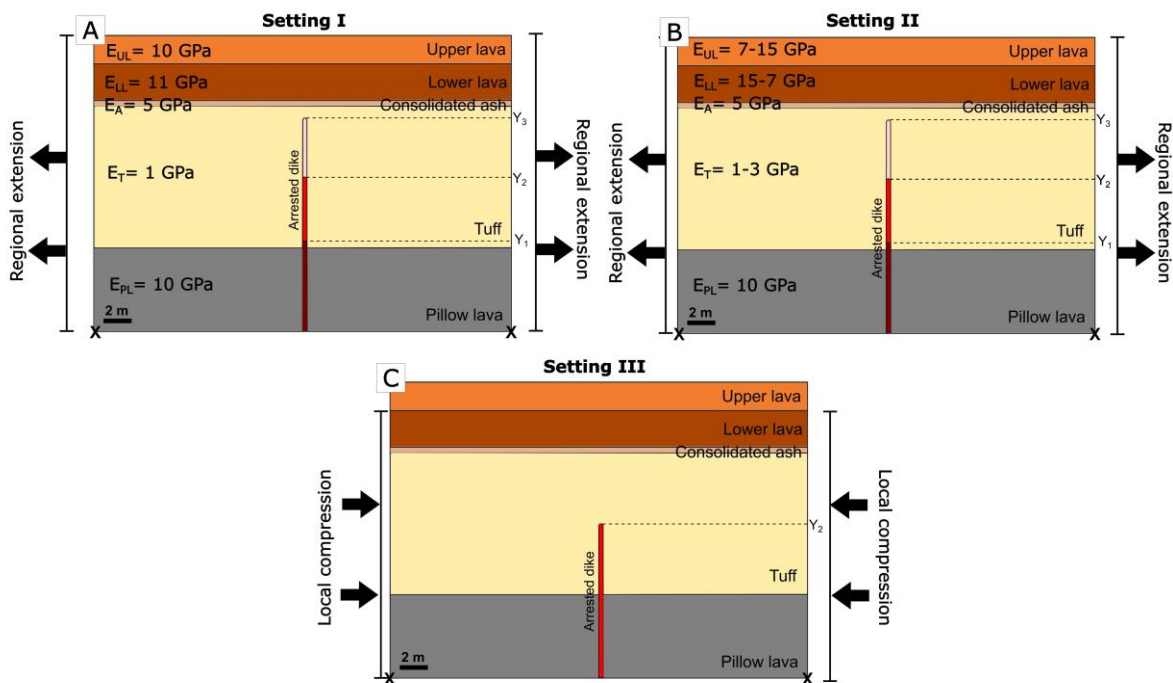
Fig. 48. Setups of numerical models. Stratigraphy is based upon field observations, X symbols at the bottom corners indicate fixed constraints. (A) Setting I: the dike propagates in the tuff layer with an overpressure and subjected to a regional extension, indicated by the black arrows. Different Y positions (Y_1, Y_2, Y_3) of the tip of the dike are shown with different colors, dark red, light red and pink, respectively. (B) Setting II: E values of the tuff and lava layers are varied to analyze their effect on dike propagation and dike-induced stresses. (C) Setting III: a compressional stress field due to the previous intrusion of the nearby feeder dike is applied to

the arrested dike. The compressional stress field is indicated by the black arrows. The dike is at the constant depth Y_2 (Corti et al., 2023).

Sensitivity analyses were run, creating three different settings:

- Setting I: the vertical dike propagation within the tuff layer was investigated. The depth of the dike was varied within the tuff (Y_1, Y_2, Y_3), different overpressure values were applied (2-4 MPa), without extension and with an extensional stress field of 1 MPa (Fig. 48A);

- Setting II: the role of mechanical properties of the tuff and lava layers was analyzed. Stiffness values were varied between 1-3 GPa for the tuff layer, and 7-15 GPa for the lava layers. Dike overpressure was constant at 3 MPa, with an extensional stress field of 1 MPa (Fig. 48B);

- Setting III: the effect of compression caused by a previous intrusion of the feeder dike (Gudmundsson, 2017) was studied. The two dikes have a similar strike, so the horizontal compressive stress induced by the feeder was considered perpendicular to the non-feeder dike. Dike overpressure was between 2 and 4 MPa, with a compressional stress field of 1 to 4 MPa (Fig. 48C).

6.3 Results

6.3.1. Geological and structural data

All the spatter and scoria cones belonging to the Older and Younger Stampar crater rows were recognized through historical aerial photos and field campaigns, mapping their bases (Fig. 49A). The two crater rows were distinguished thanks to the help pf maps available in the literature (Sigurgeirsson, 1995), and during field survey, since the cones belonging to the Older Stampar were characterized by a higher vegetation coverage than the ones belonging to the Younger Stampar fissure. Based on the alignment of the vents, both crater rows present a NE-trending orientation (Figs. 49A-B).

Considering the elongation of each cone, 23 eruptive fissures were mapped for the Older Stampar. These fissures show a strike between N21°E and N51°E, with an average value of N33.2°E and a SD of 6.5°, consistent with the crater row alignment (Fig. 49C). Regarding the Younger Stampar crater row, 49 fissures were identified, that present a strike between N23°E and N50°E, with an average of N38.8°E and a SD of 5.7° (Fig. 49D). All the data regarding strike and length of eruptive fissures are shown in Appendix 3, Table A3.1. In the area affected by the Younger Stampar eruption, no fractures were found apart from the eruptive fissure itself, as visible in the 3D model in Figure 49B.

The stratigraphy of the cliff where the two dikes are exposed was analyzed thanks to the high-resolution 3D model derived from UAV survey, identifying the volcanic layers, and measuring their thickness (Fig. 49G). From the bottom to the top, the following units were recognized: *i)* a tuff layer, covered in its lowest part by fallen blocks, with a maximum exposed thickness of 10 m (due to the fallen blocks, the actual thickness could be greater than this value); *ii)* a thin layer of consolidated (baked) ash, with a thickness of 0.4 m; *iii)* a lower lava layer, with a thickness of 2.6 m; *iv)* an upper lava layer, with a thickness that decreases towards the southeast, reaching a value of 2 m above the arrested dike. Above the tip of the feeder dike, the lava flow fed by the dike itself is visible, with a thickness that decreases moving away from the dike (Figs. 49G and 50A).

The feeder dike cuts the tuff, the consolidated ash layer, and the lower lava flow, before feeding the lava flow above. The other dike arrested at the contact between the tuff and the consolidated ash layer (Fig. 49G). The strike of the dikes was measured, obtaining values between N27°E and N46°E for the feeder dike, with an average of N36.2°E and a SD of 7.5° (Fig. 49F). Strike values of the arrested dike are between N18°E and N47°E, with an average of N32.2°E and a SD of 12.6° (Fig. 49E). Both dikes present values that are consistent with the orientations of the crater rows. All the values are presented in Appendix 3, Table A3.2.
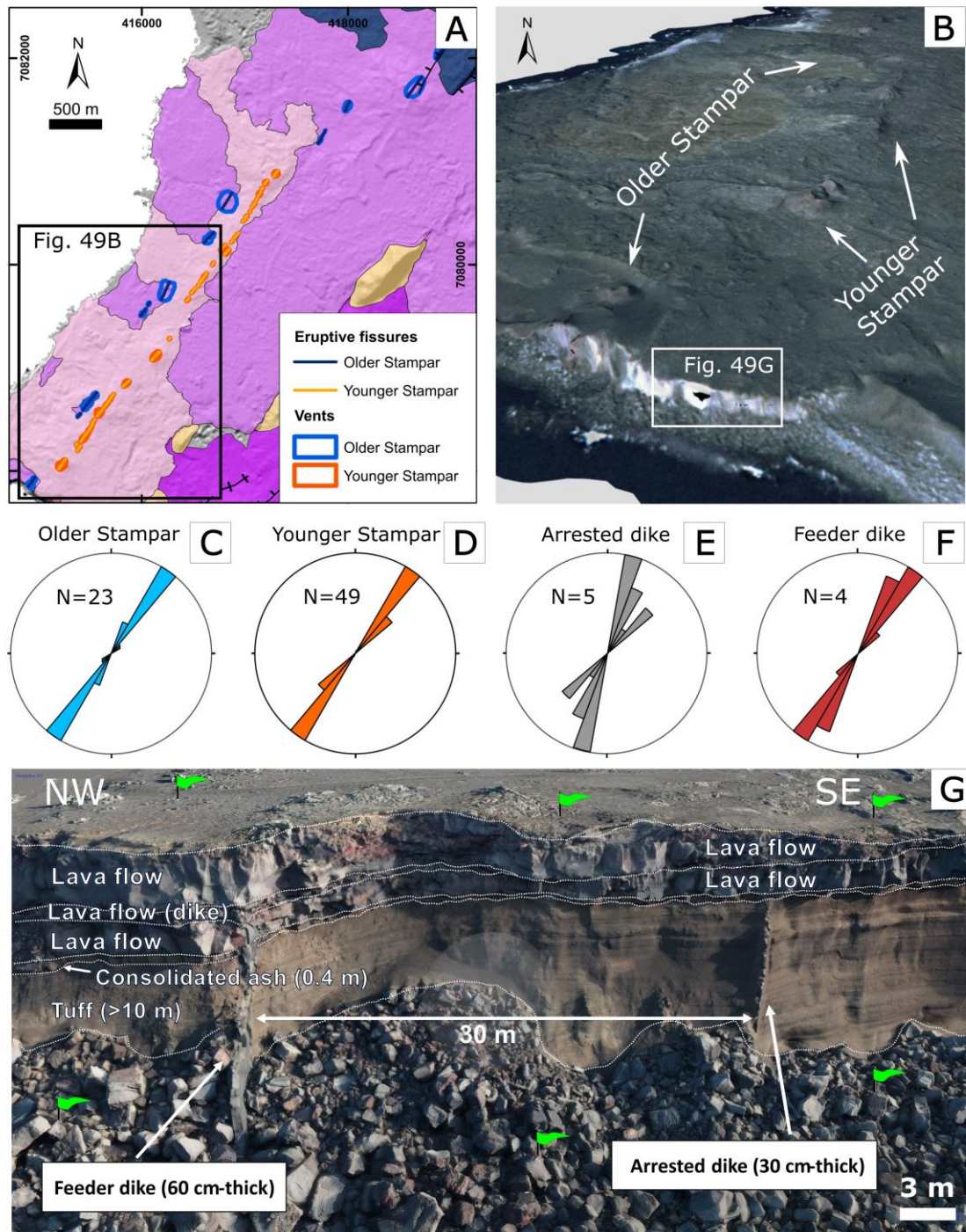
Fig. 49. (A) Map of the Younger and Older Stampar crater rows, with all the vents and the eruptive fissures derived from their elongation. For lava units, see legend in Figure 12A. Coordinate Reference System: WGS 84 - UTM 27N. (B) View of the 3D model obtained from historical aerial photos, showing the absence of tension fractures and faults in the area affected by the Younger Stampar eruption (location in Fig. 49A). Rose diagrams showing the strike of the (C) Older and (D) Younger Stampar eruptive fissures, and of the exposed

segments of the (E) arrested and (F) feeder dike. (G) UAV-derived 3D model of the outcrop, with the volcanic layers and the two dikes (location in Fig. 49B). Green flags represent the GCPs used to georeference the model (modified after Corti et al., 2023).

The feeder dike has an average thickness of 30 cm, with a maximum value of 57 cm at the base of the outcrop that decreases going upward, especially when the dike enters the lava flow (Fig. 50A). Regarding its dip angle, the dike is mostly vertical or subvertical, deflecting up to 83° to the NW when it cuts the lava (Fig. 50C). The arrested dike is composed of two exposed segments (Fig. 50B). The upper segment has a maximum thickness of 16 cm and an average of 10 cm, whereas the lower segment has a maximum thickness of 32 cm at the base of the outcrop, and an average of 23 cm. The upper segment is mostly vertical, but it deflects up to 70° to the NW just before it becomes arrested at the contact between the tuff and the consolidated ash layer (Fig. 50D). The lower segment is vertical in the lowest part, but it deflects up to 80° to the NW at its top (Fig. 50E). All the values of thickness and dip angle, related to the elevation a.s.l., are shown in Appendix 3, Table A3.3.
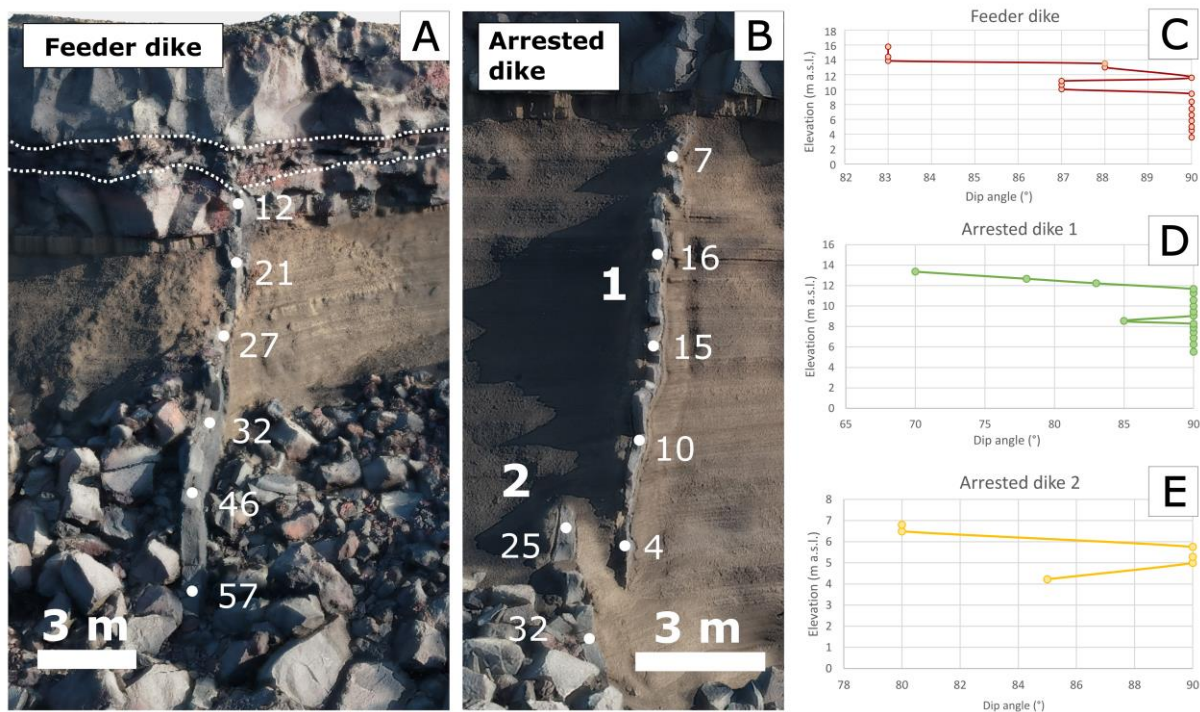
Fig. 50. View of the (A) feeder and (B) arrested dikes on the UAV-derived 3D model, with the measured thickness values expressed in centimeters. The lava flow fed by the feeder dike is

highlighted in (A). Values of dip angles related to the elevation a.s.l. are shown in the graphs for (C) the feeder dike, (D) the upper segment of the arrested dike, and (E) the lower segment of the arrested dike.

6.3.2. Numerical modeling

6.3.2.1. Setting I

In Setting I, the dike was modeled with an overpressure ranging 2 to 4 MPa, at three different depths, at first without being subjected to any extensional stress field (Fig. 51).

When the dike is at depth Y_1, no rotations of principal stresses are observed at its tip regardless of its overpressure, suggesting a propagation towards the surface (Figs. 51D-E-F). Increasing the overpressure, the concentration of tensile stress increases at the tip (Figs. 51D-E-F) and at the surface, from 2.8 MPa to 5 MPa (Figs. 51A-B-C), indicating likely fracturing. Von Mises shear stress increases as well at the surface, from 2.45 MPa to 4.9 MPa (Figs. 51A-B-C), reaching values that are high enough for fault formation only when overpressure is 4 MPa (Fig. 51C).

If the dike tip is at depth Y_2, principal stresses do not rotate regardless of the overpressure, indicating again a likely propagation of the dike (Figs. 51J-K-L). If the overpressure increases, tensile stress increases at the tip (Figs. 51J-K-L) and at the surface, from 3.4 MPa to 6.6 MPa (Figs. 51G-H-I), suggesting fracturing. Increasing the overpressure, also von Mises shear stress increases at the surface from 3 to 6 MPa (Figs. 51G-H-I), promoting fault formation when the overpressure is 3 and 4 MPa (Figs. 51H-I).

Finally, when the dike moves to Y_3, no rotations are observed regardless of its overpressure, favoring again the propagation of the dike (Figs. 51P-Q-R). Increasing the overpressure, tensile stress increases at the tip (Figs. 51P-Q-R) and at the surface, from 4.5 MPa to 9.1 MPa, suggesting fracturing (Figs. 51M-N-O). Von Mises shear stress also increases at the surface from 4.1 MPa to 8.1 MPa, indicating likely faulting in all cases (Figs. 51M-N-O).

In all the models, when the dike approaches the tuff-lava contact, tensile stress at the dike tip decreases, whereas it increases inside the upper lavas. This is due to the greater stiffness of the lava layers, that concentrate stresses more than softer layers (Inskip et al., 2020).
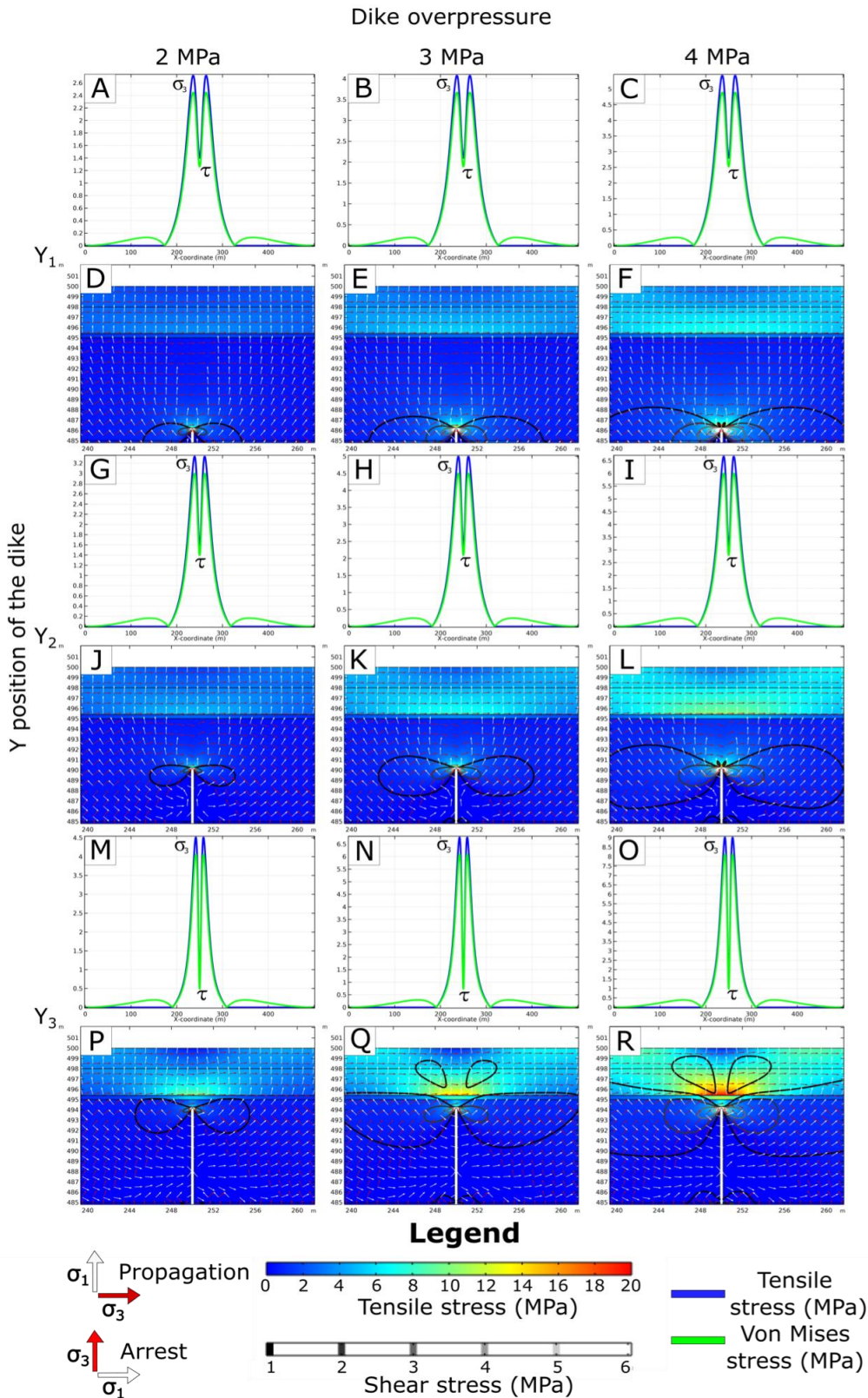
Fig. 51. Numerical models with the dike located at different depths (Y$_1$, Y$_2$, Y$_3$), with overpressure ranging 2 to 4 MPa. Tensile stress (σ$_3$) distribution is represented with the color scale bar, whereas the absolute shear stress (τ) (von Mises shear stress component in xy

plane) is shown with contour lines. Orientations of σ_1 and σ_3 are represented by white and red arrows, respectively. The 1D graphs show tensile (σ_3, blue line) and von Mises shear (τ, green line) stresses at the surface (Corti et al., 2023).

In Figure 52, an extensional stress field of 1 MPa was applied to the same models of Figure 51. If the dike is at depth Y_1, principal stresses do not rotate regardless of its overpressure, suggesting the propagation of the dike up to the surface (Figs. 52D-E-F). Increasing the overpressure, tensile and von Mises shear stress values increase at the surface, from 5.5 MPa to 8.1 MPa and from 4.8 MPa to 7.4 MPa, respectively, favoring fracturing and faulting in all the models (Figs. 52A-B-C).

Moving the dike to Y_2, the orientation of the principal stresses promotes again dike propagation in all the models (Figs. 52J-K-L). Increasing the overpressure, tensile stress increases from 6.1 MPa to 9.5 MPa, and von Mises shear stress increases from 5.5 MPa to 8.5 MPa at the surface, indicating likely fracturing and faulting (Figs. 52G-H-I).

When the dike is at depth Y_3, no principal stress rotation occurs at the tip regardless of dike overpressure (Figs. 52P-Q-R). If the overpressure increases, tensile stress increases from 7.4 MPa to 11.5 MPa, and von Mises shear stress increases from 6.5 MPa to 10.6 MPa at the surface, suggesting fracturing and faulting (Figs. 52M-N-O).

In all the models, when the dike approaches the tuff-lava contact, tensile stress decreases at the tip and increases in the upper lava layers, as explained above. Stress values are higher than the models without an extensional stress field (Fig. 51), both at the dike tip and at the surface, whereas no differences are observed in terms of principal stresses orientation.
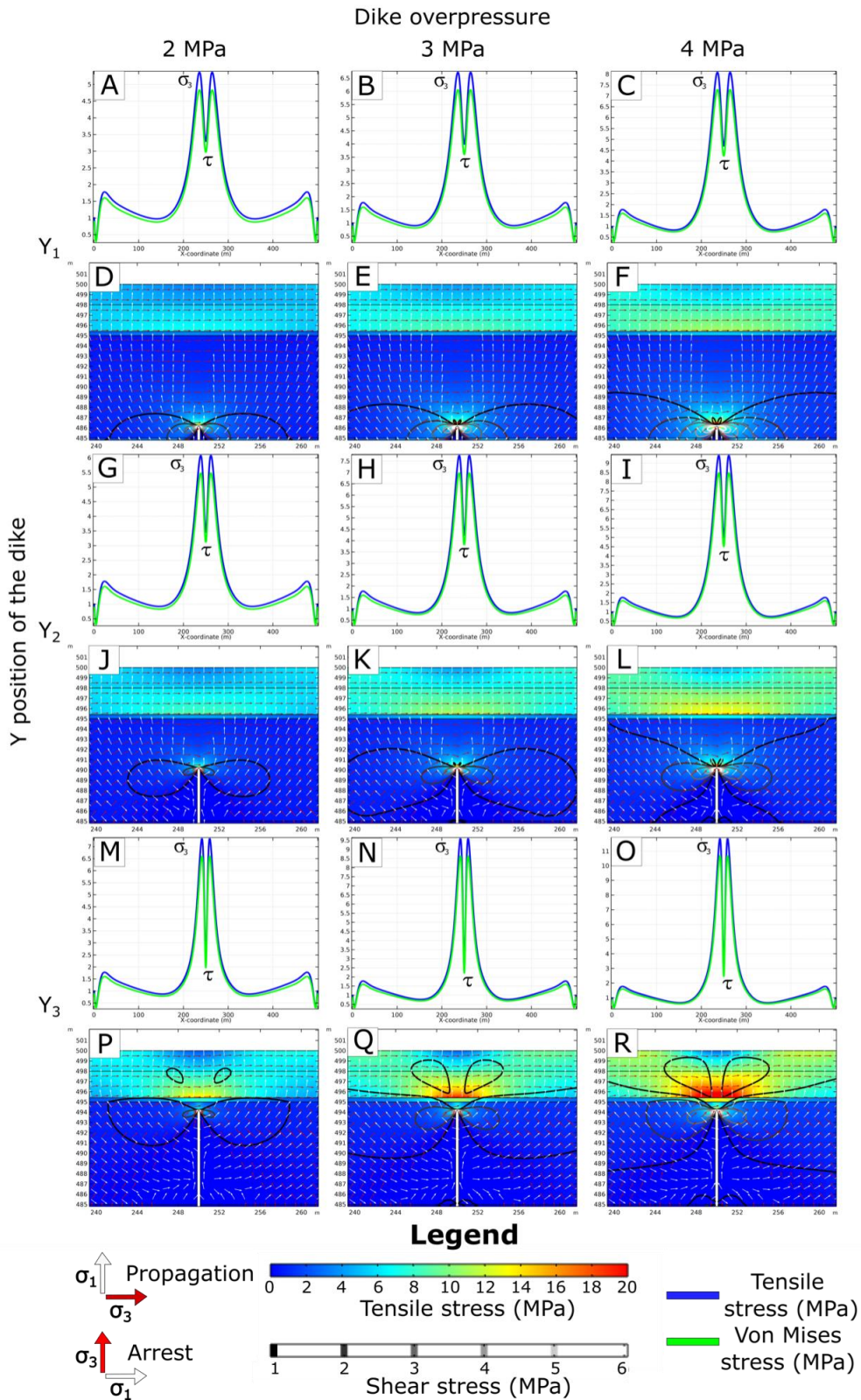
Fig. 52. Numerical models with the dike located at different depths (Y_1, Y_2, Y_3), with overpressure ranging 2 to 4 MPa, and subjected to an extensional stress field of 1 MPa.

Tensile stress (σ_3) distribution is represented with the color scale bar, whereas the absolute shear stress (τ) (von Mises shear stress component in xy plane) is shown with contour lines. Orientations of σ_1 and σ_3 are represented by white and red arrows, respectively. The 1D graphs show tensile (σ_3, blue line) and von Mises shear (τ, green line) stresses at the surface (Corti et al., 2023).

6.3.2.2. Setting II

In Setting II, the effect of stiffness of the volcanic layers on dike propagation and dike-induced deformation was investigated. In all the models, the dike was subjected to an overpressure of 3 MPa and an extensional stress field of 1 MPa.

In Figure 53, the role of tuff stiffness is analyzed. If the dike is at depth Y_1, no rotations of principal stresses are observed, regardless of E values of the tuff (Figs. 53D-E-F). Increasing the stiffness of the tuff, tensile stress increases at the tip of the dike from a maximum of 6-8 MPa (Fig. 53D), to 10-12 MPa (Fig. 53E), and finally to 14-16 MPa (Fig. 12F), and absolute shear stress forms greater lobes in the tuff (Figs. 53D-E-F). Tensile and von Mises shear stresses at the surface are greater than 2 and 4 MPa in all the models, indicating likely fracturing and faulting (Figs. 53A-B-C).

Moving the dike to Y_2, no rotations of the principal stresses are observed regardless of E values (Figs. 53J-K-L). Increasing the stiffness, tensile stress magnitudes increase at the tip of the dike, and absolute shear stress forms greater lobes in the tuff (Figs. 53J-K-L). In all the models, tensile and von Mises shear stresses at the surface are high enough to favor fracturing and faulting (Figs. 53G-H-I).

Finally, if the dike is at Y_3, no stress rotations are observed (Figs. 53P-Q-R). Increasing E values of the tuff, tensile stress increases in the consolidated ash layer and in the lower lava layers, reaching 16-18 MPa (Fig. 12R), and absolute shear stress contours get closer to the surface (Figs. 53P-Q-R). At the surface, tensile stress increases from 9.5 MPa (Fig. 12M), to 10.2 MPa (Fig. 12N), and finally to 10.4 MPa (Fig. 12O), indicating that fracturing is likely. Von Mises shear stress also increases from 8.6 MPa (Fig. 12M), to 9.3 MPa (Fig. 12N), and finally to 9.4 MPa (Fig. 12O), suggesting faulting.
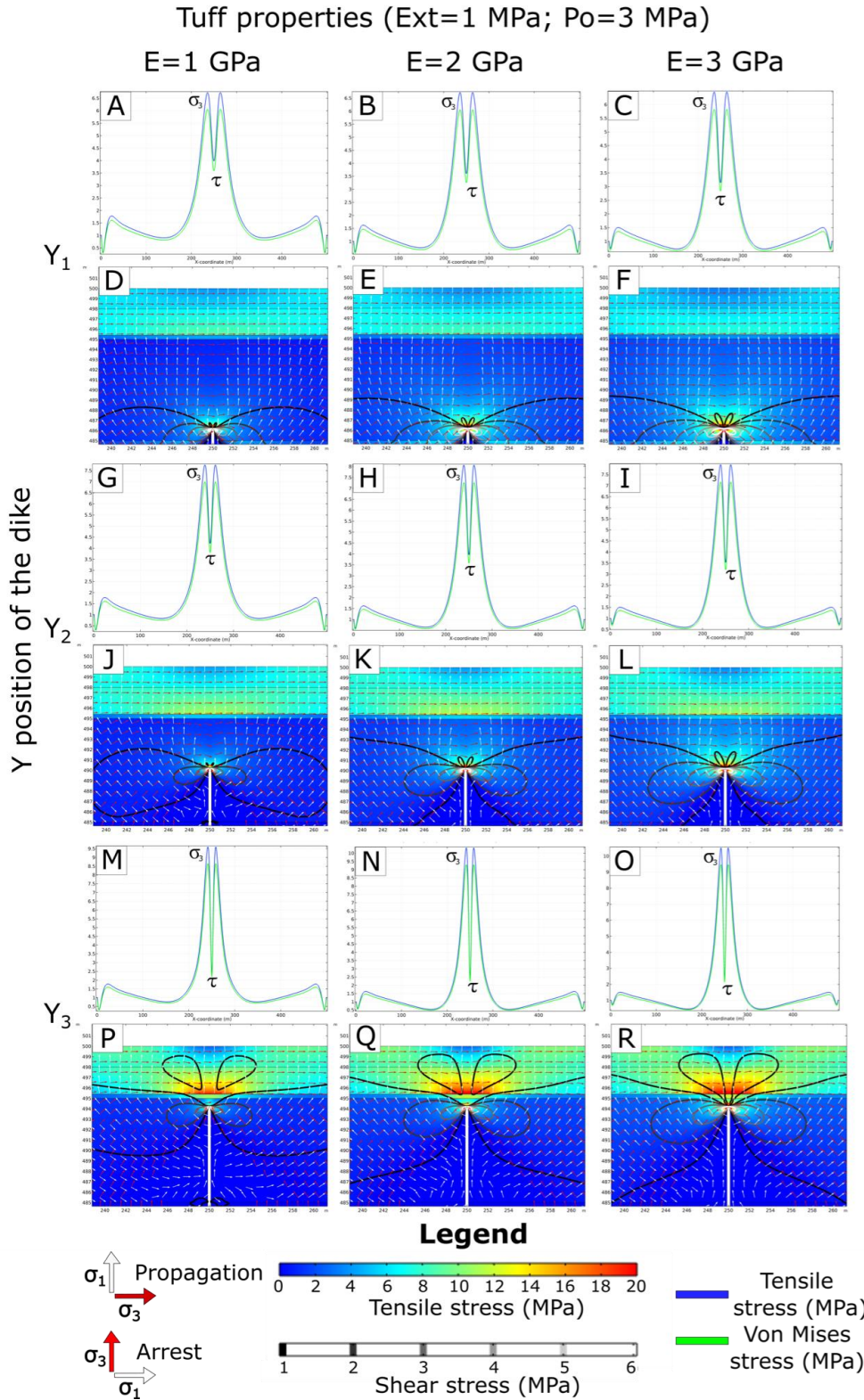
Fig. 53. Numerical models with the dike located at different depths (Y_1, Y_2, Y_3), and with varying values of Young's modulus of the tuff (1-3 GPa). The dike is subjected to an overpressure of 3 MPa, and to an extensional stress field of 1 MPa. Tensile stress (σ_3)

distribution is represented with the color scale bar, whereas the absolute shear stress (τ) (von Mises shear stress component in xy plane) is shown with contour lines. Orientations of σ₁ and σ₃ are represented by white and red arrows, respectively. The 1D graphs show tensile (σ₃, blue line) and von Mises shear (τ, green line) stresses at the surface (Corti et al., 2023).

In Figure 54, the role of lava stiffness is investigated. If the dike is at depth Y_1, no rotations of the principal stresses are observed, suggesting dike propagation (Figs. 54C-D). Tensile stress concentrates in the lava layer with greater stiffness, namely the upper one (UL) in Figure 54C and the lower one (LL) in Figure 54D. If E_{UL} is greater than E_{LL}, tensile and von Mises shear stresses at the surface are higher, reaching 9.8 MPa and 8.8 MPa, respectively (Fig. 54A). On the other hand, when E_{UL} is smaller than E_{LL} they reach smaller magnitudes, up to 4.7 MPa and 4.2 MPa (Fig. 54B).

Moving the dike at depth Y_2, no stress rotations are observed, and tensile stress always concentrates in the lava layer with greater stiffness (Figs. 54G-H). If E_{UL} is greater than E_{LL}, tensile and von Mises shear stresses at the surface are higher, up to 11.3 MPa and 10.2 MPa, respectively (Fig. 54E). When E_{UL} is smaller than E_{LL}, they are lower at the surface, reaching 5.4 MPa and 4.8 MPa (Fig. 54F).

Finally, when the dike moves at Y_3, stress orientations do not rotate, and tensile stress is always more concentrated in the lava with greater E value (Figs. 54K-L). When E_{UL} is greater than E_{LL}, tensile and von Mises shear stresses at the surface are up to 13.9 MPa and 12.6 MPa, respectively (Fig. 54I). If E_{UL} is smaller than E_{LL}, they reach 6.6 MPa and 6 MPa, respectively (Fig. 54J).

In all the models of Setting II, the magnitudes of tensile and von Mises shear stresses at the surface suggest that fracturing and faulting are likely. Furthermore, moving the dike closer to the tuff-lava contact, tensile stress at the tip always decreases, and it increases within the lava layers (Figs. 53-54).
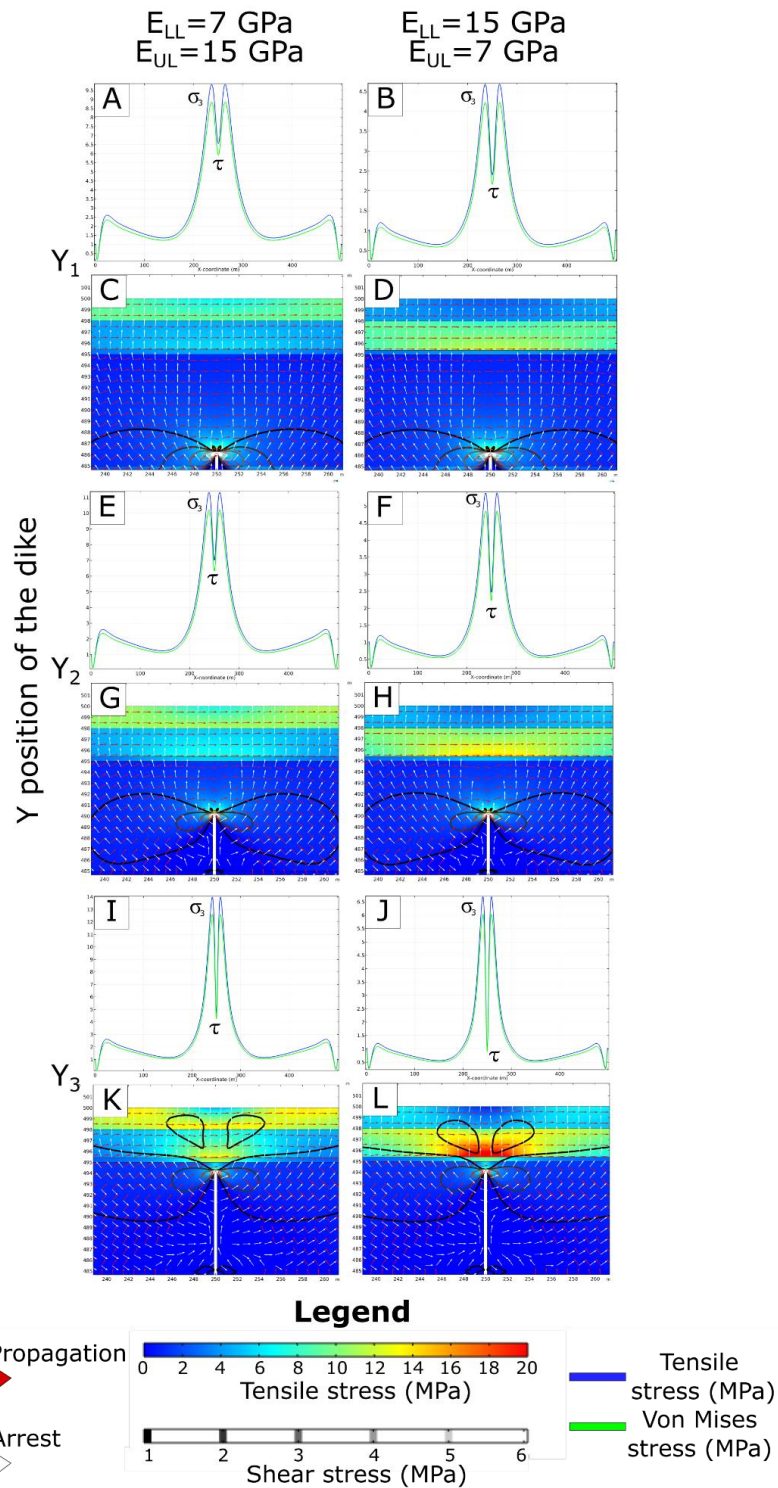
Fig. 54. Numerical models with the dike located at different depths (Y_1, Y_2, Y_3), and with varying values of Young's modulus of the lava layers (7-15 GPa). The dike is subjected to an overpressure of 3 MPa, and to an extensional stress field of 1 MPa. Tensile stress (σ_3) distribution is represented with the color scale bar, whereas the absolute shear stress (τ) (von

Mises shear stress component in xy plane) is shown with contour lines. Orientations of σ₁ and

σ₃ are represented by white and red arrows, respectively. The 1D graphs show tensile (σ₃,

blue line) and von Mises shear (τ, green line) stresses at the surface (Corti et al., 2023).

6.3.2.3. Setting III

In Setting III, the effect of horizontal compression, caused by the previous intrusion of the nearby feeder dike (as suggested by Gudmundsson, 2017), was investigated. The feeder dike cut the tuff layer, the thin consolidated ash layer, and the lower part of the lava flow, before reaching the former topographic surface and generating a new lava flow (Figs. 49G and 50A). Its overpressure caused a horizontal compression in the host rock that could have affected the propagation of the nearby arrested dike (Gudmundsson, 2003; Menand et al., 2010), which was intruded later, as explained by the conceptual model in Figure 55.
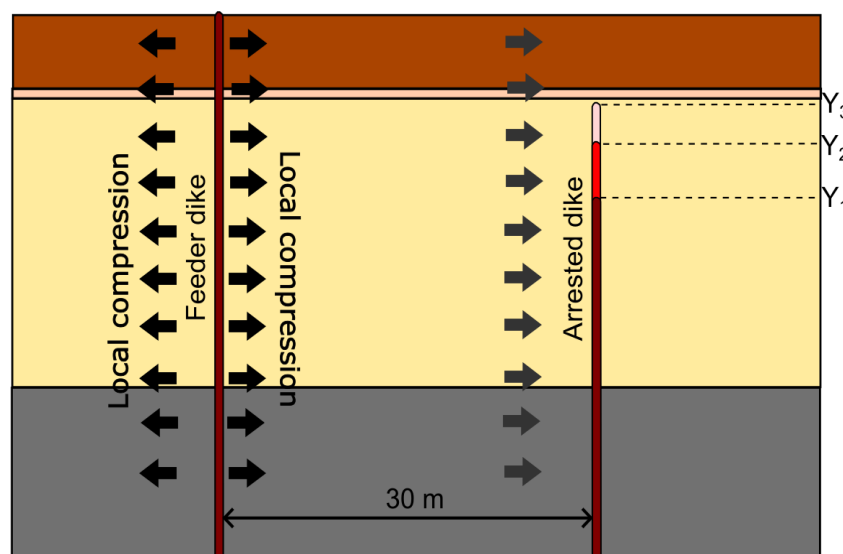
Fig. 55. Conceptual model of the feeder dike intruding in the observed stratigraphy, and inducing local horizontal compression, which affects the propagation of the later arrested dike (Corti et al., 2023).

Considering this scenario, in Figure 56 the arrested dike is modeled with an overpressure of 2-4 MPa and is subjected to a horizontal compressional stress ranging 1 to 4 MPa (as shown in Fig. 48C).
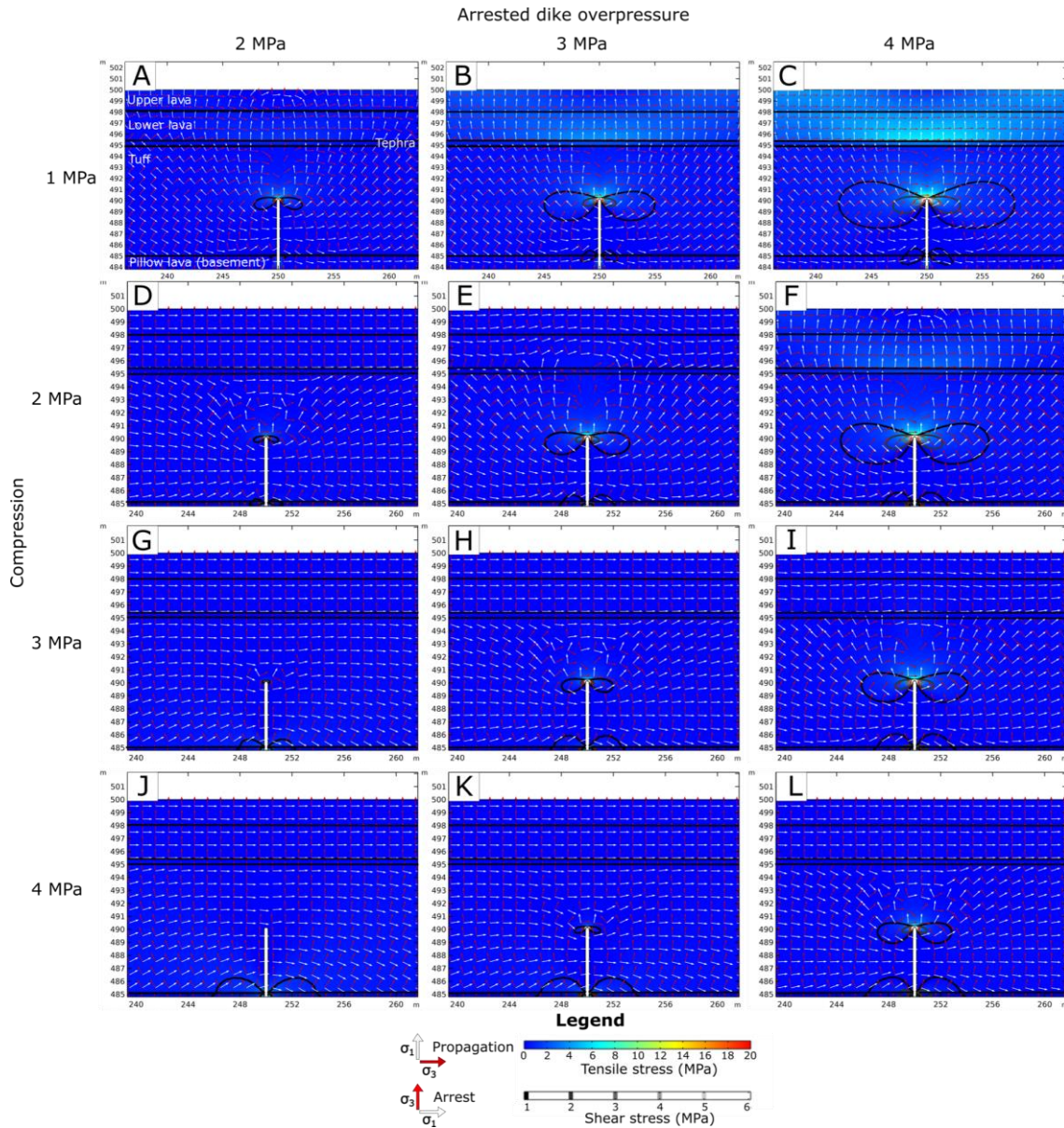
Fig. 56. Numerical models with the dike located at depth Y_2, with overpressure ranging 2 to 4 MPa, and subjected to a compressional stress field between 1 and 4 MPa. Tensile stress (σ_3) distribution is represented with the color scale bar, whereas the absolute shear stress (τ) (von Mises shear stress component in xy plane) is shown with contour lines. Orientations of σ_1 and σ_3 are represented by white and red arrows, respectively (Corti et al., 2023).

124

When compression is equal to 1 MPa, regardless of dike overpressure, stress rotations are up to 45°, but always less than 90° (Figs. 56A-B-C). Tensile stress concentration in the upper lavas reaches 5-6 MPa only when the overpressure is 4 MPa, suggesting fracturing (Fig. 56C), whereas it is too low in the other models.

If compression increases to 2 MPa (Figs. 56D-E-F), principal stresses rotate of 90° when the overpressure is 2 MPa (Fig. 56D), suggesting dike arrest. When the overpressure is 3 MPa (Fig. 56E) and 4 MPa (Fig. 56F), stress rotations are less than 90°, up to 80° and 60°, respectively. Tensile stress magnitude at the tip and in the upper lavas is always less than 2-3 MPa, indicating that fracturing is unlikely.

Increasing compression to 3 MPa (Figs. 56G-H-I), a 90° rotation of stresses is observed when the dike overpressure is 2 (Fig. 56G) and 3 MPa (Fig. 56H). On the other hand, when overpressure is 4 MPa, the rotation is up to 80° (Fig. 56I). Stresses magnitudes at the tip and in the host rock decrease as well.

Finally, if compression is 4 MPa (Figs. 56J-K-L), a 90° rotation of the principal stresses is observed in all cases, suggesting the arrest of the dike. Furthermore, the concentrations of tensile and absolute shear stresses at the tip and in the lava layers decrease.

6.3.2.4. Synthesis of the numerical models

In Table 5, the main results of numerical models of the Stampar case study are summarized, in terms of formation of stress barriers and stress decrease at the dike tip, two mechanisms that can explain dike arrest and the absence of brittle deformation at the surface. Decreasing dike overpressure, stress concentrations at the tip of the dike also decreases, but the orientation of principal stresses is not affected (Figs. 51-52). In these models, changes in the mechanical properties (stiffness) of the layers do not cause the formation of stress barriers (Figs. 53-54). However, tensile stress decreases at the tip of the dike and increases in the lava layers, as the dike is moved closer to the contact between the softer tuff and the stiffer lava layer (Figs. 51-52-53-54). Finally, when local horizontal compression is applied, a decrease of the stresses magnitude is observed at the tip and in the host rock, with the formation of a stress barrier that occurs when compression is equal to or greater than dike overpressure (Fig. 56).

Table 5. Synthesis of the results of numerical models, showing the effect of the following parameters on stress barrier formation and on the decrease of the magnitude of stress at the tip of the dike.

Modelled parameter	Stress barrier	Stress decrease at the tip
Dike overpressure	No	Yes
Layers' mechanical parameters (Young's modulus)	No	Yes
Compression < dike overpressure	No	Yes
Compression ≥ dike overpressure	Yes	Yes

6.4 Discussion

Since mid-December 2019 up to this date (October 2023), the RP has been affected by a rifting episode at Fagradalsfjall, with unrest characterized by periods of high seismicity and repeated dike-segment intrusions (Sigmundsson et al., 2022). However, up to this date only three dikes managed to reach the surface generating an eruption. Before this rifting activity, the last episode in the RP dates back to the 13th century, between 1210 and 1240 AD, and included the Younger Stampar eruption (Sæmundsson et al., 2016, 2020) (Fig. 11).

In this case study, the orientation of the Younger Stampar eruptive fissures was measured, obtaining an average of N38.8°E, consistent with the average strike of the Older Stampar fissure (N33.2°E), and of the eruptive fissures associated with historical and prehistoric eruption in the RP (about N40°E) shown in Figure 11 (Clifton and Schlische, 2003; Clifton and Kattenhorn, 2006; Sæmundsson et al., 2016). This value is also similar to the orientation of the eruptive fissures at Fagradalsfjall, that have a strike of N25°E, N45°E and N22°E (Flóvenz et al., 2022; Sigmundsson et al., 2022; Barsotti et al., 2023). All these fissures are parallel to the main structures of the volcanic systems of the RP, which are oriented between N21°E and N60°E (Clifton and Schlische, 2003; Clifton and Kattenhorn, 2006). The volcanic systems are arranged *en-échelon* compared to the plate boundary, that trends about N70°E in the western part and about N80°E in the eastern part (Gudmundsson, 1986b, 1987). This trend is

oblique to the spreading direction (N101°E) in this region (DeMets et al., 2010), forming a transtensional zone. The Younger Stampar fissure orientation is also consistent with the strike of the two exposed dikes.

Through numerical models, I tried to investigate the reasons of the arrest of one of these two dikes, and the lack of brittle deformation at the surface, despite the shallow depth of dike arrest (5 m below the surface). In the last decades, dike propagation has been investigated with numerical models by many authors (e.g., Gudmundsson, 2003; Maccaferri et al., 2010, 2011, 2016; Geshi et al., 2012; Philipp et al., 2013; Barnett and Gudmundsson, 2014; Rivalta et al., 2015; Urbani et al., 2017; Drymoni et al., 2020). These works showed that dike can arrest or deflect into sills due to the presence of a stress barrier, which can consist of layers or units with a local stress field that is unfavorable to dike propagation (Gretener, 1969; Gudmundsson, 1986a). Furthermore, elastic mismatch between two layers, intended as a strong contrast in Young's modulus across a contact between the layer below (and hosting the dike) and above the contact, can cause dike arrest (Gudmundsson et al., 2011b). In this case study, the effect of the following parameters was analyzed: *i)* dike overpressure (and thickness); *ii)* layers mechanical properties (stiffness); *iii)* extensional or compressional tectonic stress field.

The effects of magmatic overpressure on dike propagation were already discussed by Geshi et al. (2012) and Drymoni et al. (2020). In the models of this case study, its decrease causes a decrease of tensile stress concentration at the tip of the dike, inhibiting dike propagation and brittle deformation above the tip.

Regarding the influence of layering, previous numerical studies showed that dike arrest mostly occurs due to the heterogeneity of the shallow crust, that strongly affects also dike-induced stress fields (Gudmundsson, 2003; Bazargan and Gudmundsson, 2019). Stress rotations and stress barriers were observed at contacts with stiffness contrasts, especially between stiff lavas and soft breccia or scoria layers (Gudmundsson and Brenner, 2001). The key role of soft layers in arresting hydrofractures had already been observed before during laboratory experiments (Charlez, 1997; Yew and Weng, 1997). In the models of this case study, the variation of the stiffness of the layers is never enough to create a stress barrier that could have affected dike propagation (Figs. 53-54), but the specific layering observed in the outcrop strongly affects stress concentrations at the dike tip and at the surface.

Specifically, moving the dike closer to the soft-stiff (tuff-lava) contact, tensile stress at the tip decreases, whereas it increases in the upper lava layer, due to its greater stiffness (Figs. 51-52-53-54). This behavior is coherent with what observed by Inskip et al. (2020), and it suggests that the specific layering observed in this outcrop could have favored dike arrest.

Adding an extensional stress field of 1 MPa, stresses concentrations increase in the stiffer layers, but no 90° rotations of principal stresses are observed (Figs. 52-53-54). When compression is applied as boundary load, tensile stress at the tip decreases favoring dike arrest. Furthermore, principal stresses rotate, reaching a 90° rotation when the compressional stress is equal to or greater than dike overpressure (Fig. 56). If the principal stresses rotate, the dike can deflect if tensile stress at the tip is high enough to favor dike propagation. Otherwise, if tensile stress at the tip is too low, the dike will arrest. Therefore, the presence of a local compressional stress field could explain dike arrest, as already demonstrated through analogue (Menand et al., 2010) and numerical models (Gudmundsson, 2003; Drymoni et al., 2020). Generally, the presence of normal faults or the intrusion of earlier dikes could explain local compression in an area characterized by regional extensional tectonics, since they can modify the regional horizontal σ_3 to either σ_2 or σ_1 (Gudmundsson, 2003, 2020). In the Stampar area, normal faults are not present, therefore compression could have been caused by the previous intrusion of the nearby feeder dike (Gudmundsson, 2017), that led to the arrest of the later dike (Fig. 55). Previous analytical models showed that Mode I cracks with an internal overpressure (such as dikes), generate an area subjected to compressive stress, up to a distance that is about half its length (Gudmundsson, 2011a). This zone of compression around a dike was observed also in numerical models (Andrew and Gudmundsson, 2008). The effect of previous dike intrusions on the local state of stress, and subsequently on later dikes propagation paths has been observed also by Ruz et al. (2020). If we consider the thickness of the Stampar feeder dike, and the typical length/thickness ratios for dikes in Iceland (300 to 1500; Gudmundsson, 2020), we can assume with certainty that the host rock was subjected to compressive stresses induced by the feeder dike at a distance of 30 m. Additionally, in the Stampar case, when the feeder dike propagated up to the surface, the dike-induced compressive stress concentrated in the stiffer lava layer. The increase of compressive stress leads to a decrease of the overpressure of the dike as it approaches the contact between the tuff and the lava,

since the overpressure is defined as the difference between the total magmatic pressure in the dike and the minimum principal compressive stress σ_3 acting on the dike walls (Kusumoto et al., 2013). Therefore, in this case, layering again plays a role in the arrest of the non-feeder dike.

During recent rifting episodes in Iceland, normal faults and grabens formation was observed, like during the 1975-1984 Krafla Fires (Sigurdsson, 1980; Rubin, 1992) and the 2014 Bardarbunga episode (Sigmundsson et al., 2015; Hjartardóttir et al., 2016; Ruch et al., 2016). In the Stampar area, however, no brittle deformation occurred at the surface, even if the dike arrested only 5 m below the surface (Fig. 49B). Previous research demonstrated through numerical models the role of layering in inhibiting dike-induced deformation, showing how the presence of soft layers in the stratigraphy can make fracturing at the surface difficult, unless the dike is very shallow, has a great overpressure, or both (Al Shehri and Gudmundsson, 2018; Bazargan and Gudmundsson, 2019). In this case study, numerical models showed that stresses at the surface increase if the stiffness of the upper layer increases (Fig. 54). However, when an extensional stress field is applied, stresses at the surface are always high enough to generate brittle deformation, regardless of the mechanical properties of the layers (Figs. 52-53-54). These results are different from what observed by Bazargan and Gudmundsson (2019), probably because of the very shallow depth of the dike (5 m), compared to the depth of 500 m tested in their models. In the models of this work, however, the presence of a compressional stress field and layering causes a decrease of tensile stress at the tip of the dike. Considering that stresses at the surface are much lower than the ones at the tip of the dike (Gudmundsson, 2003), if stresses are low at the tip, they will be too low also to generate fracturing and faulting at the surface. Therefore, for the Stampar case study, besides a low dike overpressure and thickness, the presence of compression (caused by the previous intrusion of the feeder dike) together with layering, can explain not only the arrest of the later dike, but also the lack of fracturing and faulting at the surface.

7. Discussion

The three case studies analyzed in this thesis represent good examples of dike intrusions and dike-induced brittle surface deformation. As observed in the previous chapters, the two Mt. Etna case studies offer the possibility to investigate several settings of surface deformation, whereas the Stampar case study in Iceland gives the opportunity to survey two exposed dikes, one feeder and one arrested, that did not cause brittle deformation at the surface.

The high-resolution structural data collected through field campaigns, UAV surveys and historical aerial photographs, integrated with FEM numerical modeling, will be discussed in the following sections to contribute to the following volcanotectonics topics: *i)* what can favor or inhibit dike-induced brittle deformation at the surface? *ii)* which parameters affect the geometry of dike-induced graben faults? *iii)* what can promote dike arrest? Regarding point *ii)*, available data from the literature will also be summarized, highlighting the diversities in the geometry between dike-induced grabens formed in different geodynamic contexts.

7.1. Dike-induced brittle deformation at the surface

The intrusion of dikes and inclined sheets at shallow depths generates stresses and deformation in the host rock and at the surface, that can be measured. Analytical (Isida, 1955) and half-space numerical models (Pollard et al., 1983; Rubin and Pollard, 1988) demonstrated that a dike intrusion leads to a double peak of stresses and displacement at the surface, one to each side of the dike tip. On the other hand, no displacements were observed above the dike tip. More recent models, however, showed subsidence above the dike tip (Dzurisin, 2006; Segall, 2010), explaining the graben subsidence above the magmatic intrusion that is commonly observed during rifting episodes (e.g., Acocella and Trippanera, 2016, and references therein). All these cited works, however, considered only a dike intruding in a homogeneous, isotropic, elastic half-space. More recently, numerical models were run to investigate stress distributions in a layered elastic host rock, showing the influence of layering on stress distribution (Gudmundsson, 2003; Philipp et al., 2013; Al Shehri and Gudmundsson, 2018; Bazargan and Gudmundsson, 2019; Clunes et al., 2023).

Analogue models have also been used to investigate dike-induced deformation (Mastin and Pollard, 1988; Trippanera et al., 2015a; Xu et al., 2016), confirming that dike emplacement can generate tension fractures that propagate ahead of the dike tip. In the last decades, graben formation has also been observed during dike intrusions, also on Mt. Etna (Murray and Pullen, 1984; Acocella and Neri, 2003; Neri et al., 2004; Neri and Acocella, 2006; Bonaccorso et al., 2011; Falsaperla and Neri, 2015; Calvari et al., 2020) and in Iceland (Sigurdsson, 1980; Rubin, 1992; Hjartardóttir et al., 2016; Ruch et al., 2016). However, cases of dikes arrested at very shallow depths and not associated with surface deformation have been reported (Bazargan and Gudmundsson, 2019), and no connection between dike tips and normal faults was found in Iceland (Forslund and Gudmundsson, 1991, 1992). The Stampar case study also shows a very shallow arrested dike that did not cause brittle deformation at the surface, as shown in Figure 49B.

In the numerical models presented in this thesis, I investigated the parameters that can favor, or inhibit, dike-induced brittle surface deformation. As explained in Section 2.3, tension fractures and faults can form at the surface only if the local stresses overcome the tensile and shear strength of the host rock (Gudmundsson, 2011a). The most typical values of tensile strength of rocks are 2-4 MPa, whereas shear strength is commonly about double the tensile strength, so mostly 4-8 MPa (Haimson and Rummel, 1982; Schultz, 1995; Amadei and Stephansson, 1997). In the models, I observed a role of the following parameters (Fig. 57), that will be presented in more detail hereunder: *i)* dike overpressure; *ii)* layering of the host rock; *iii)* extensional or compressional boundary loads.

Regarding dike overpressure, numerical models showed that its decrease leads to a decrease of tensile stress concentration, both at the tip and at the surface (Fig. 57). This was observed in the 1928 case study, with variations in the overpressure of at least one order of magnitude (from 1 to 10 MPa in Figs. 27-28-30, and from 1 to 20 MPa in Figs. 22-23-24), and in the Stampar case study, with smaller ranges (from 2 to 4 MPa, Figs. 51-52). This result is consistent with numerical models by Geshi et al. (2012) and Drymoni et al. (2020), who defined magmatic overpressure as an important parameter that controls dike propagation. Furthermore, in the models tensile and shear stress concentrations at the dike tip are directly proportional to the overpressure, since linear elastic materials were used for the crustal layers, as done in previous research (e.g., Bazargan and Gudmundsson, 2019).

Layering of the host rock plays a significant role in the distribution of both tensile and shear stress, as observed in all the case studies. This agrees with Gudmundsson (2003) and Philipp et al. (2013), who demonstrated that abrupt changes in Young's moduli (E) may have great effects on dike-induced stress fields. Specifically, stiffer layers (e.g., lavas) concentrate stresses, favoring fracturing and faulting at the surface when they are at the top of the stratigraphic succession. On the other hand, softer layers (e.g., breccia, tuff) suppress stresses, making fracturing and faulting at the surface more difficult (Fig. 57). This distribution of stresses is clear in the layered models of the 1928 (Figs. from 22 to 31, E ranging 1-30 GPa), 1971 (Figs. from 39 to 46, E ranging 1-10 GPa), and Stampar (Figs. from 51 to 54, E ranging 1-15 GPa) case studies. This result is coherent with Al Shehri and Gudmundsson (2018), who illustrated that even a single moderately soft layer reduces the induced surface stresses, and with Bazargan and Gudmundsson (2019), who showed that when the stiffness of the more compliant layer becomes as low as 0.01 GPa, this layer transports hardly any stresses to the shallower levels.

The role of regional extensional stress field as boundary load was evaluated for the 1928 fissure (Figs. 25-30 with an extension of 2 MPa, Figs. 26-27-28 with an extension of 0.5 MPa), for the 1971 fissure (Figs. 39-40 and from 43 to 46), and in the Stampar case study, where models not subjected to an extensional stress field were compared to models where a 1 MPa extensional stress field was applied (Figs. 51-52). In all the models, it is evident that an increase of extension leads to a higher concentration of stresses in the stiff layers, favoring fracturing and faulting (Fig. 57). Finally, in the Stampar case study the role of a dike-induced horizontal compression was also evaluated (Fig. 56), observing how this leads to a decrease of stresses at the tip and in the host rock, making fracturing more difficult (Fig. 57).
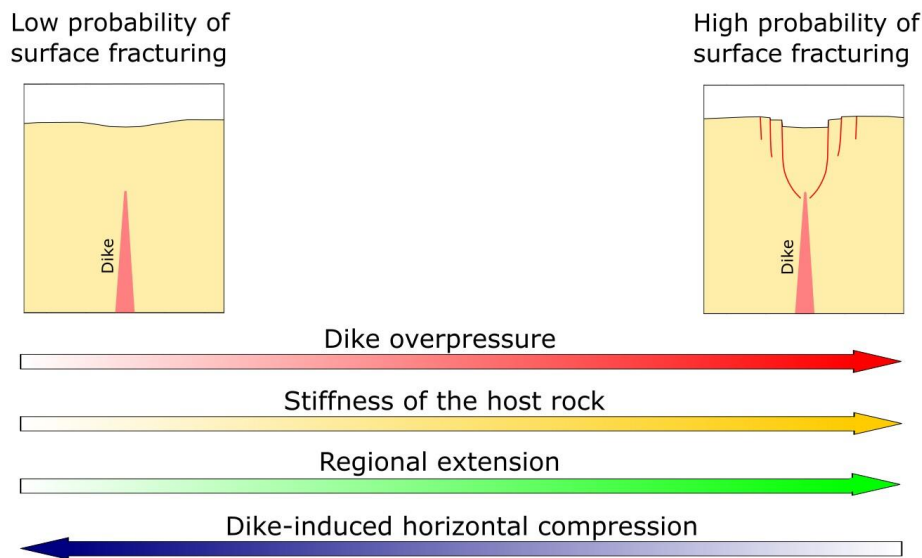
Fig. 57. Summary of the parameters that can favor or inhibit brittle surface deformation induced by dike emplacement.

7.2. Geometry of dike-induced grabens

In this section, I will first summarize the geometrical features of the best-known dike-induced grabens reported in the literature, presenting them in chronological order. These grabens are all related to diking episodes occurred in the last centuries, both along slow, intermediate, and fast spreading plate boundaries, and on volcanic edifices.

Along slow spreading plate boundaries, the oldest known example is dated back to 1783 AD, when the Grimsvotn Fissure Swarm (Eastern Volcanic Zone, Iceland) was affected by a major diking episode, leading to the Lakagigar (Laki) eruption (Thordarson and Self, 1993). Dike propagation generated a 5-6 km-long graben, with a width of 150-450 m that increases up to 700-800 m at the Laki Hill (Andrew et al., 2008; Trippanera et al., 2015a). Average vertical offset is 3 m, with maximum values of 7 m (Andrew et al., 2008).

Moving to the Northern Volcanic Zone (NVZ) of Iceland, the Askja Fissure Swarm was affected by a diking episode in 1875 AD, that led to the formation of the 34-km-long Sveinagja graben. Its northern part is completely associated with this event and is characterized by a maximum width of 2.5 km and a vertical offset of 4-7 m (Gudmundsson and Bäckström, 1991). In the NVZ, the Krafla Fissure Swarm was also affected by a rifting

episode between 1975 and 1984 AD, that included about 20 dike intrusions. Rubin (1992) reported two grabens with a width of 5-6 km, and vertical offsets < 2 m. A narrower graben was observed by Tibaldi et al. (2020b), with a width up to 36 m, and vertical offsets of 2-3.5 m.

In eastern Afar (Ethiopia), the Asal-Ghoubbet Rifts were affected by two dikes that emplaced at the same time, forming a 2-km-wide graben with a vertical displacement along faults of 0.7 m at maximum (Abdallah et al., 1979; Tarantola et al., 1979, 1980). At Dabbahu (Afar), a major intrusive event occurred in 2005, leading to the reactivation of older faults, with average vertical displacements of 2.5 m (Rowland et al., 2007) along a 2 to 4 km-wide graben (Grandin et al., 2009; Ebinger et al., 2010).

In 2007, the East African Rift was affected by a diking episode in the Natron basin (Tanzania), with the formation of a graben characterized by a width of 2-3 km, and an average vertical offset of 0.35 m (Calais et al., 2008; Biggs et al., 2009).

A dike intrusion occurred in Harrat Lunayyir, along the Red Sea side of Saudi Arabia, in 2009, leading to a half-graben formation. Along the boundary faults, the vertical displacement is 0.8 m, whereas the half-graben width decreases from the NW (6-7 km) to the SE (< 2 km), indicating a shallower dike depth (Pallister et al., 2010).

Finally, the NVZ in Iceland was affected by another diking episode in 2014, in the Bardarbunga Fissure Swarm (Sigmundsson et al., 2015). Here, dike propagation generated a graben structure at the surface, characterized by a width of 0.7-1 km and a maximum vertical displacement of 6 m (Hjartardóttir et al., 2016; Ruch et al., 2016).

Generally, we can notice that all these grabens have widths that range from hundreds of meters to kilometers, except for the narrower graben reported by Tibaldi et al. (2020b) (Figs. 58A-C). Vertical displacements along faults, newly formed or reactivated, are between centimeters and meters, with a maximum value of 6 m at Bardarbunga (Figs. 58A-B).

These geometries change if we consider dike-induced grabens observed along intermediate and fast boundaries, as observed by Chadwick and Embley (1998). These authors reported the width, length, and vertical displacement for several grabens, related to diking events along the submarine Cleft segment (1983-1987) and Co-Axial segment (1993) of the Juan de Fuca Ridge, an intermediate spreading ridge. These grabens are characterized by vertical displacements between 2 and 30 m and are 10-100 m wide. The same authors also proposed

that the axial summit troughs of the fast spreading East Pacific Rise (at 9-10° N of latitude) are dike-induced grabens. Soule et al. (2009) described them in detail, reporting widths between 50 and 300 m, and depths between 1 and 20 m. In view of these data, dike-induced grabens along intermediate to fast spreading ridges seem narrower and deeper than the ones measured along slow spreading ridges (Fig. 58A). This means that the stress state is less favorable to the formation of dike induced faults, and dikes have to arrive closer to the surface to create faults. This occurs because diking events along intermediate and fast spreading ridges are more frequent than along slow spreading ridges. Therefore, gradual plate spreading has not enough time to contrast the horizontal compression due to dike intrusions (Chadwick and Embley, 1998). This concept can also explain why the graben reported by Tibaldi et al. (2020b) is narrower than expected along slow spreading plate boundaries, considering that the area was affected by several intrusions during the latest 1975-1984 Krafla rifting episode. In the case of a laterally propagating dike, the graben width is affected also by the relief above the dike top, as explained for the 1928 case study. However, differently from the flank of Mt. Etna, in the Krafla case study topography does not present variations that can explain the smaller width of the graben.

In the last decades, dike-induced grabens were observed also on volcanic edifices. Mastin and Pollard (1988) described a graben related to an older intrusive event at Inyo Craters (California, USA), dated back to 650-550 ka BP. In this case, the graben has a width of 500-700 m, whereas no data are available about the offset. On Kilauea (Hawaii, USA), a graben formed due to a dike intrusion in 1981, with a width of 2 km and a vertical displacement of 0.9 m (Duffield et al., 1982; Pollard et al., 1983).

On Mt. Etna, two grabens formed in 1983, characterized by width values of 200 and 1000 m, and by maximum vertical displacements of 1.40 and 0.85 m (Murray and Pullen, 1984). Also, in 2001 two grabens were reported, with a width of 500 m and 30-50 m, and vertical offsets up to 1 m (Acocella and Neri, 2003). Other dike-induced grabens were generated on Mt. Etna in 2008 and 2013, with a width of 200-800 m and 120 m, and vertical offsets of 0.2 m and up to 1 m, respectively (Bonaccorso et al., 2011; Falsaperla and Neri, 2015).

In 2021, a 50-m-wide and 170-m-long graben was detected also at Cumbre Vieja (La Palma, Spain), with a maximum vertical offset of 4 m, and an average of 2.45 m (Walter et al., 2023).

Finally, in the present thesis new data have been collected on Mt. Etna, along two grabens formed during the 1928 eruption and one graben created in 1971. Average vertical offsets of 2.4 and 1.1 m were measured for the 1928 grabens, with widths of 385 and 68 m, respectively (Chapter 4). For the 1971 graben, the average width is 85 m, and the average vertical offset is 2.5 m (Chapter 5).

Comparing these data with the geometries observed along divergent plate boundaries, we notice that dike-induced grabens on volcanic edifices are characterized by smaller vertical offsets (Figs. 58A-B), and by relatively small width (Figs. 58A-C). Instead, grabens along slow spreading ridges are the longest and the widest (Fig. 58C), whereas grabens located along intermediate to fast spreading ridges are the narrowest and the deepest (Fig. 58A). All the data shown in Figure 58 are presented in Appendix 4, Table A4.1.
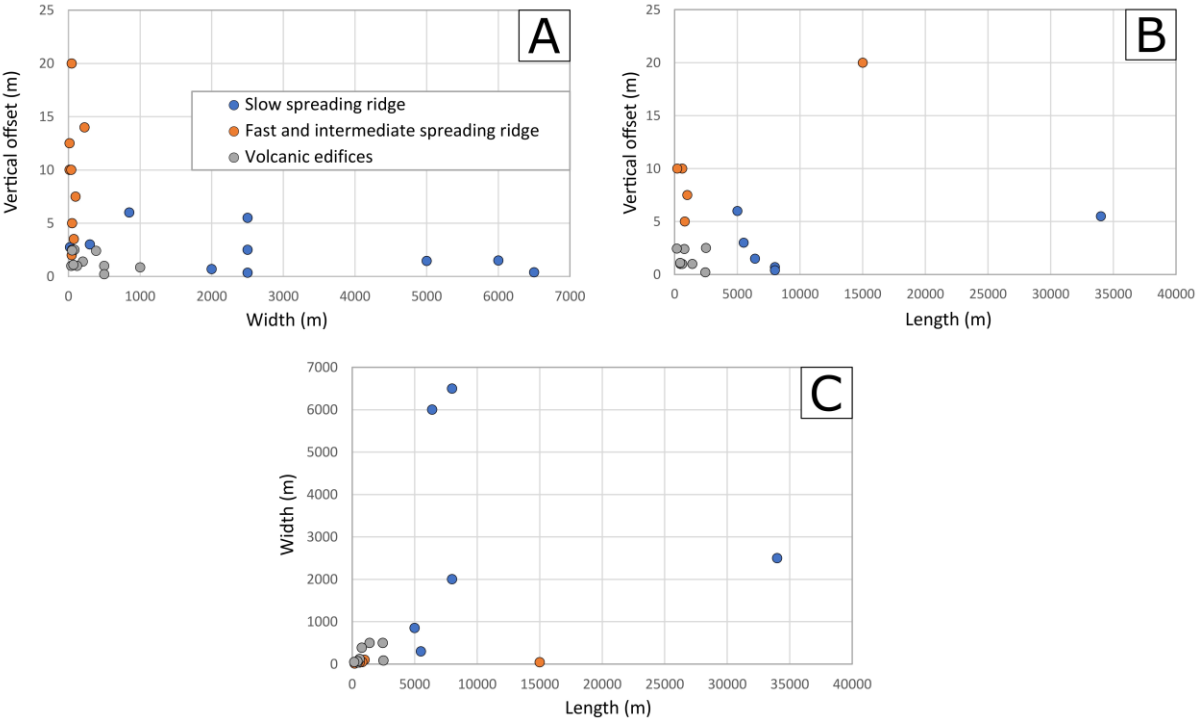
Fig. 58. Graphs showing (A) width vs vertical offset, (B) length vs vertical offset, (C) length vs width of dike-induced grabens reported in the literature. Different colors indicate different geodynamic settings.

7.2.1. Graben width and faults geometry

In the last decades, many authors analyzed the geometry of dike-induced grabens, mostly to infer the properties of the underlying dike (e.g., depth, thickness) through inversion techniques. The most popular half-space models used to estimate dike geometries are the elastic-dislocations models, reviewed in detail by Okada (1985, 1992), Dzurisin (2006) and Segall (2010). These models use deformation data, commonly from geodesy, GPS or InSAR measurements, and invert them to find the best dike that fits the data (e.g., Stein et al., 1991; Wright et al., 2006; Calais et al., 2008; Nobile et al., 2012; Sigmundsson et al., 2015). Still, they do not consider layering, while results by Al Shehri and Gudmundsson (2018) demonstrated that the presence of soft layers disadvantages surface deformation, as confirmed also by my work, leading to errors in the estimation of dike depth provided by dislocation models.

Other works focused on the width of the graben, to infer the depth of the dike tip. Regarding this relation, numerical models were run by Pollard et al. (1983) considering an elastic half-space with homogeneous conditions, suggesting that the distance between the two tensile stress maxima (where fracturing is more expected) is about twice the depth of the top of the crack. This result was obtained also by Mastin and Pollard (1988) through numerical models, again with an elastic half-space and a homogeneous host rock. However, the same authors observed a different relation through analogue models since numerical models do not consider the effects of inelastic deformation with formation of fissures above the crack. More recently, Trippanera et al. (2015a) designed analogue models with a setup similar to Mastin and Pollard (1988), observing a direct relation between dike depth and graben width, but highlighting how relations regarding dike geometry are more complicated in nature compared to the ones obtained in the experiments (Fig. 16 in Trippanera et al., 2015a). The "graben rule", based on the results by Pollard et al. (1983), has been widely used since then in the literature to estimate the depth of the dike tip (e.g., Hjartardóttir et al., 2016). However, dike depth values collected from the literature along the above-presented grabens (listed in Appendix 4, Table A4.2) show that this relation is more complex (Fig. 59). Also, we observed that structural data from the 1971 case study are not supporting the "graben rule" (Chapter 5). This complexity was claimed also by Magee and Jackson (2021), who concluded

that more information about fault geometries is needed to infer the depth of the underlying dike.
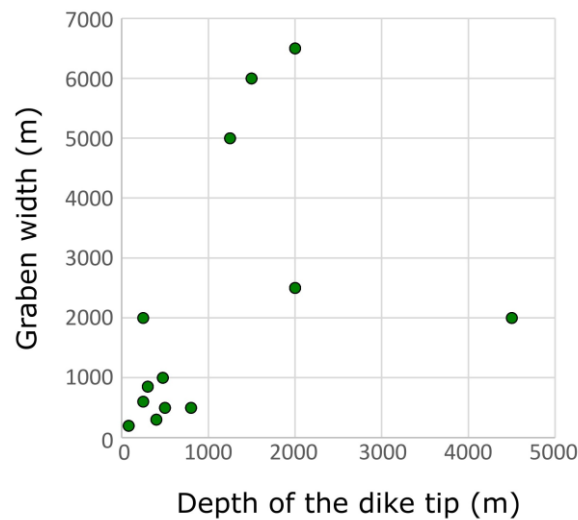
Fig. 59. Graph showing the depth of the dike tip vs the graben width, for dike-induced grabens reported in the literature (full list and references in Appendix 4, Table A4.2).

For this reason, in this work I investigated the role of several parameters, other than the depth of the top of the dike (which is affected also by dike lateral propagation), on graben width and faults geometry, observing an influence of: *i)* dike inclination; *ii)* layering of the host rock; *iii)* topography.

Inclining the dike, both tensile and shear stress distributions become asymmetrical, as observed in the models of the 1928 fissure (Figs. 24, 25G-H and 26G-H), where the dike was inclined of 10°, and of the 1971 fissure (Figs. 37-39-40), with a dike inclined of 15°. In the latter case, the asymmetry is evident both with a homogeneous (Fig. 37) and a layered (Figs. 39-40) host rock. This result is coherent with Pollard et al. (1983) and Mastin and Pollard (1988), who observed an asymmetrical deformation in a homogeneous domain if the dike was not vertical, and with Bazargan and Gudmundsson (2020), who modeled stresses induced by inclined sheets in a layered host rock. This asymmetry in tensile and shear stress distributions could favor the formation of an asymmetric graben or half-graben, as observed in the 1928 case (Sector 3, Section 4.3.1).

Regarding the effect of layering on the geometry of brittle surface deformation, the main effect is observed in the 1928 fissure case study (Figs. from 22 to 30). Here, shear stress contours clearly show how soft layers distribute shear stress concentration closer to the surface, favoring the formation of narrow grabens, whereas stiff layers tend to disperse shear stress, generating wider grabens. Therefore, although soft layers, like tuffs and breccia, concentrate low shear stress values, at the same time they also distribute it closer to the surface. This result thus highlights how layering affects the graben width, supporting Al Shehri and Gudmundsson (2018) in claiming the importance of host rock heterogeneities in numerical models.

In the 1928 and 1971 case studies, the role of topography was also analyzed. Numerical models of the 1971 fissure show how the asymmetry of the graben faults can be ascribed to the present topography, which is inclined of ~25° toward the south (Fig. 38, and from 41 to 46). Specifically, the 25°-inclined topography causes a rotation of the principal stresses, as summarized in Fig. 60, and, in turn, the orientation of σ_1 and σ_3 affects the attitude of the faults.
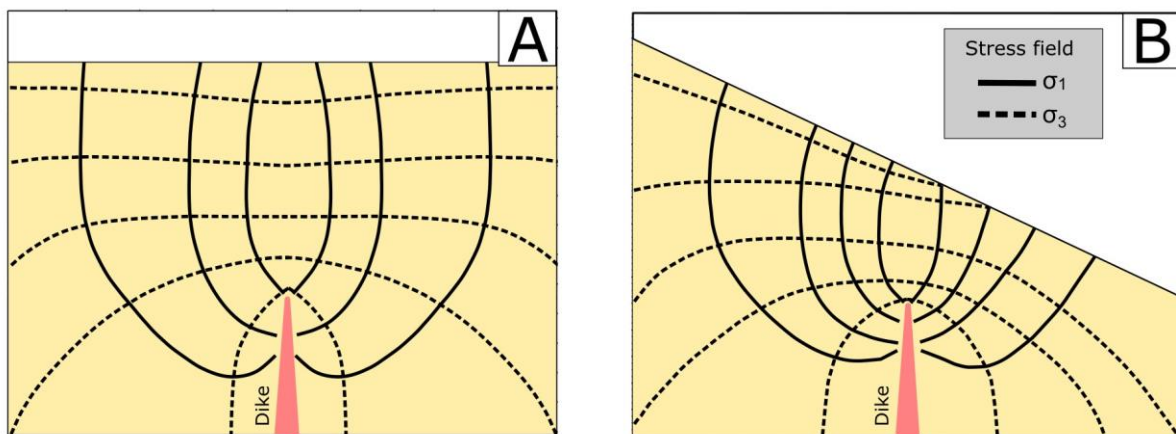
Fig. 60. Schematic illustration of the principal stresses orientations above the dike tip, in case of (A) a flat topography, and (B) an inclined topography. In both cases the dike is vertical, and the host rock is homogeneous. When the topography is inclined, a rotation of the principal stresses and an asymmetry of the stress field is observable.

The effect of topography was observed also by Trippanera et al. (2015a) and by Walter et al. (2023) through analogue models, which showed that the presence of a relief affects the graben width and the displacement along the graben faults. Divergence of graben faults at topographic highs was observed also in Iceland, during the 2014 Bardarbunga event (Müller et al., 2017). The 1971 fissure trend is also affected by topography, as observed in Fig. 36A. Specifically, the structures are mostly parallel to the VdB escarpment, indicating that the dike propagated with the same trend following the collapse scarp, as observed by previous authors in Stromboli (Tibaldi, 1996, 2001, 2003, 2004; Neri et al., 2008), in Chile (Vezzoli et al., 2008), in Tenerife (Walter and Schmincke, 2002; Walter et al., 2005b), and through analogue models (Acocella and Tibaldi, 2005). More to the east, the 1971 dike propagated with an ENE-WSW trend, as suggested by the orientation of the easternmost eruptive fissures (Fig. 36A), coherently with the stress state of the area, which is affected by the sliding of the volcano flank (Borgia et al., 1992; Tibaldi and Groppelli, 2002; Walter et al., 2005a; Neri and Acocella, 2006; Solaro et al., 2010). The structures along the 1928 fissure are also affected by topography, showing a right-stepping arrangement in the two zones characterized by the presence of high topographic scarps (Fig. 17F). This observation suggests that a dike is expected to propagate straightforward mostly in case of a flat topography (or a constant slope angle), whereas topographic variation can deviate the dike-propagation path (Acocella and Neri, 2009).

7.3. Dike arrest/propagation up to the surface

During its vertical propagation up to the surface, a dike takes its path considering the general principles of least action and minimum potential energy (Gudmundsson, 1984, 2011a). Most of the dikes, however, do not reach the surface generating an eruption, but they arrest in the crust, mostly because of differences in the mechanical properties of the layers (especially stiffness), that promote variations in the local stress field (Gudmundsson, 2003, 2011b; Philipp et al., 2013). According to analogue (Hutchinson, 1996), numerical models (Gudmundsson, 2006), and field observations (Gudmundsson, 2020), four scenarios are possible when a dike meets a contact between two dissimilar layers: *i)* it penetrates the contact and continues its vertical propagation; *ii)* it becomes arrested; *iii)* it becomes

deflected along the contact and then arrested; *iv)* it becomes deflected along the contact and continues its propagation laterally, possibly reaching shallower levels at some distance in case of favorable conditions.

For a dike to propagate, tensile stress at the tip should be at least equal to the tensile strength of the crustal rocks, to create an extension fracture above the tip (Gudmundsson, 2011a). Considering this, in Section 7.1 we have already observed how some parameters cause a decrease of tensile stress at the dike tip, favoring dike arrest. Specifically, overpressure plays a key role, as observed in the 1928 fissure and in the Stampar case studies, as well as the presence of compression due to the previous intrusions (Fig. 57). In the Stampar case study, the role of mechanical contrasts was also observed, with stiffer layers (such as lavas) that concentrate stresses, favoring dike arrest at the contact between a soft layer (below) and a stiff layer (above). In this case, the mechanism responsible for dike arrest is the elastic mismatch, due to a difference in E values between the layer hosting the dike and the one above the contact (Gudmundsson, 2011b). The likelihood that a dike arrests or deflects into a sill along a contact is determined by the Dundurs elastic mismatch parameter (Dundurs, 1969; He et al., 1994; Hutchinson, 1996). According to this parameter, a large elastic mismatch encourages dike arrest or deflection at the contact, when the layer above the contact is stiffer than the layer below. This conclusion agrees with analogue experiments on sill emplacement (Kavanagh et al., 2006; Menand, 2008), numerical models (Geshi et al., 2012; Inskip et al., 2020), and field observations (Gudmundsson, 2020).

Another known cause of dike arrest is represented by stress barriers (Anderson, 1951; Gretener, 1969; Gudmundsson, 1986a, 2011b). These are layers characterized by a local stress field that is unfavorable to the propagation of a fracture. Specifically, a layer with horizontal σ_1 and vertical σ_3 is a barrier to the vertical propagation of dikes and can lead to dike arrest (Fig. 61). In this work, I observed the effect of the following parameters on stress barrier formation, that will be now discussed: *i)* layering of the host rock; *ii)* dike dip angle; *iii)* presence of horizontal compression.

In the 1928 fissure case study, numerical models show that 90° rotations of σ_1 and σ_3 can form both in soft and stiff materials, due to mechanical contrasts between two adjacent layers in the stratigraphy (Figs. 22-25-26). Low stiffness contrasts seem to be the most favorable for stress barrier formation (Figs. 25-26), in agreement with numerical models by

Drymoni et al. (2020), but stress rotation occurs also at high stiffness contrasts, coherently with Geshi et al. (2012). Gudmundsson and Brenner (2001) and Gudmundsson and Philipp (2006) also observed that the presence of soft layers in an extensional regime can favor the formation of stress barriers, leading to dike arrest. Furthermore, this work shows that variations in layer thickness can favor σ_1 and σ_3 rotations, especially if thickness changes of one order of magnitude (Figs. 23-25-26).

Regarding dike dip angle, models of the 1928 and 1971 case studies suggest that, increasing the inclination, σ_1 and σ_3 rotations are favored (Figs. 24-25-26, and from 37 to 46). This can promote the formation of stress barriers, and dike arrest concepts.

Finally, in the Stampar case study the role of horizontal compression was investigated (Fig. 56). Results demonstrate that stress barriers are expected if compression is equal to or greater than dike overpressure, in agreement with Gudmundsson and Marinoni (1999) and Maccaferri et al. (2011), who observed that the greater the overpressure is, the lower the effect of the external stress field becomes. The influence of horizontal compression on dike arrest was suggested also by Menand et al. (2010) through analogue models, and by Drymoni et al. (2020) through numerical models. As explained in Chapter 6, the presence of horizontal compression in an area characterized by regional extensional tectonics can be explained by the presence of normal faults (or grabens), or by the overpressure of earlier dikes (Fig. 55; Gudmundsson, 2003, 2020).
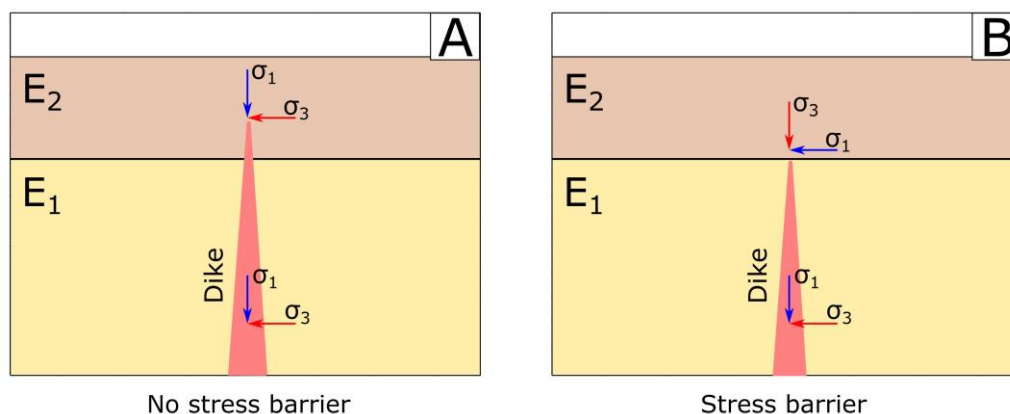
Fig. 61. Schematic illustration of the stress barrier mechanism. (A) σ_1 and σ_3 orientations are favorable to vertical dike propagation both in the layer below (E_1) and above (E_2) the contact. (B) σ_1 and σ_3 in the upper layer (E_2) are rotated of 90°, with a vertical σ_3 and a horizontal σ_1, leading to dike arrest at the contact.

8. Conclusions

- This PhD project analyzes the relation between dike emplacement at shallow depth and brittle deformation at the surface, as well as the factors that encourage dike arrest during its vertical propagation. The case studies are located at Mt. Etna (Italy) and in SW Iceland.

- Specifically, my work contributes to a better understanding of *i)* which parameters favor or inhibit dike-induced brittle deformation at the surface, *ii)* what affects the geometry of dike-induced grabens, and *iii)* what can promote dike arrest. Furthermore, I integrated my new data about dike-induced graben geometries with the ones found in the literature, highlighting the differences between grabens formed in different geodynamic contexts.

- New structural data were collected through fieldwork and high-resolution SfM-derived models. These data were successively used as inputs for FEM numerical modeling, anchoring the models to field cases and making them more realistic, if compared to the ones already present in the literature.

- Numerical models point out the role of layering on dike-induced stresses, with stiffer materials that concentrate stresses and softer materials that suppress them, in continuity with previous works on this topic that used numerical modeling. However, in the models presented here, layering is always based on field data, and dikes are plotted at shallower depths. In addition, the role of stiffness on the distribution of shear stress within the host rock is here investigated, suggesting that the presence of softer layers in the stratigraphy favors the formation of narrow grabens, whereas stiffer layers promote wider grabens.

- My thesis also confirms the influence of dike overpressure and inclination on its propagation and on the concentration and distribution of dike-induced stresses, as already observed by previous authors.

- Structural data confirm that topographic variations affect the dike propagation path. Besides, numerical models show that topography favors the asymmetry of the graben

faults. In one case study field data were collected in section view, and the geometry of the faults above the dike tip could be observed directly in the field.

- Finally, this work highlights the role of lateral compression on encouraging dike arrest and the lack of brittle deformation at the surface. Differently from previous studies, this concept is demonstrated through numerical models not only in terms of stress rotations, but also considering the decrease of stress concentrations above the dike tip.

- Considering this latter point, my project validates through numerical models what was suggested by previous authors, only through conceptual models, regarding the geometry of dike-induced grabens along fast spreading plate boundaries. These are narrower than the ones observed in other geodynamic contexts due to the greater number of intrusions, which generate compression in the host rock making dike-induced surface deformation more difficult. This conclusion can also explain why some grabens reported by previous authors along slow spreading plate boundaries are narrower than expected, especially in areas affected by several intrusions, like the Krafla Fissure Swarm (Iceland).

Appendix 1

Structural measurements along the 1928 fissure (Mt. Etna)

Table A1.1 Quantitative structural data collected through GIS analysis along the 1928 fissure, with the classification of the structures.

X midpoint (m)	Y midpoint (m)	Length (m)	Strike (°N)	Type
506095.152421	4180360.350520	96.82	61.54	Dry tension fracture
507248.221510	4180755.415960	54.12	65.70	Dry tension fracture
507316.233504	4180773.740830	55.12	73.14	Dry tension fracture
506686.811957	4180411.527830	144.97	70.73	Pre-1928 fracture
505410.052542	4179846.709760	248.84	72.84	Pre-1928 fracture
504921.184248	4179650.106820	494.43	67.68	Pre-1928 fracture
504294.238763	4179805.891340	309.69	67.92	Pre-1928 fracture
504774.330160	4179961.546140	153.74	68.40	Pre-1928 fracture
505517.627487	4180204.850670	474.51	69.67	Pre-1928 fracture
509806.480344	4181349.057320	1099.26	62.51	Pre-1928 fracture
507361.719060	4180490.308980	543.91	60.59	Pre-1928 fracture
507837.165786	4180419.187950	555.32	64.42	Pre-1928 fracture
507021.158775	4180483.655170	94.33	59.53	Pre-1928 fracture
508242.942049	4180611.915160	87.15	74.05	Pre-1928 fracture
502622.242770	4179371.292710	93.55	71.15	Normal Fault
502728.468587	4179398.795850	139.01	90.66	Normal Fault
502864.917294	4179409.720930	109.91	83.05	Normal Fault
503057.838514	4179424.190980	253.47	84.02	Normal Fault
503317.595359	4179447.048820	264.85	88.91	Normal Fault
503162.902430	4179061.260260	131.89	85.06	Normal Fault
503238.660344	4179069.245640	127.83	68.20	Normal Fault
503230.512969	4179089.604880	94.55	86.83	Normal Fault
503232.543865	4179109.012030	34.72	75.03	Normal Fault
503299.662079	4179118.940080	56.41	70.28	Normal Fault
503292.081329	4179081.760310	12.40	90.00	Normal Fault
503399.509585	4179104.635380	208.27	78.71	Normal Fault
503400.099690	4179116.608220	81.09	67.63	Normal Fault
503435.240778	4179093.653450	309.22	79.95	Normal Fault
503456.890832	4179148.603800	91.32	71.14	Normal Fault
503670.903062	4179272.438490	211.46	63.18	Normal Fault
504344.744382	4179641.833000	982.55	66.16	Eruptive fissure
504342.243665	4179653.258290	967.63	66.16	Eruptive fissure
504917.372111	4179887.831760	262.12	68.61	Eruptive fissure
504920.802062	4179881.590730	262.74	68.61	Eruptive fissure
505128.899925	4179962.920110	106.83	72.99	Eruptive fissure
505130.218752	4179957.769360	108.11	72.99	Eruptive fissure

505217.398650	4179996.913760	46.52	73.01	Eruptive fissure
505217.235110	4179990.078070	51.36	73.01	Eruptive fissure
505283.919715	4180014.687960	67.99	70.92	Eruptive fissure
505282.386357	4180018.376830	64.30	70.92	Eruptive fissure
505339.963283	4180035.456390	21.88	70.27	Eruptive fissure
505339.264691	4180038.787430	22.22	70.27	Eruptive fissure
505481.539467	4180112.186840	232.28	65.13	Eruptive fissure
505483.988148	4180103.147950	236.60	65.13	Eruptive fissure
505721.285445	4180201.632910	235.38	69.98	Dry tension fracture
505867.970872	4180242.928710	50.72	68.92	Eruptive fissure
505866.749455	4180247.924680	52.96	69.60	Eruptive fissure
506019.703768	4180298.451070	96.46	69.35	Eruptive fissure
506018.517329	4180302.040280	95.74	69.35	Eruptive fissure
506095.879382	4180325.077820	32.04	74.12	Eruptive fissure
506095.537520	4180328.029450	31.67	74.12	Eruptive fissure
506133.537429	4180343.956890	38.48	54.46	Eruptive fissure
506129.729507	4180346.309700	33.94	54.46	Eruptive fissure
506171.985363	4180367.343470	63.22	59.63	Eruptive fissure
506166.751907	4180375.323380	63.95	59.63	Eruptive fissure
505750.210763	4179983.436690	131.94	71.24	Pre-1928 fracture
506890.412954	4180616.975680	66.44	74.20	Normal Fault
506225.481135	4180426.069430	134.59	66.11	Dry tension fracture
506224.437109	4180413.835380	127.62	70.01	Dry tension fracture
506292.954084	4180428.847430	169.69	64.33	Normal Fault
506288.253685	4180415.122520	196.22	63.51	Normal Fault
506318.967905	4180412.742280	111.32	66.40	Normal Fault
506400.628883	4180462.453440	149.20	62.80	Normal Fault
506406.856691	4180486.726520	56.00	60.98	Normal Fault
506489.901327	4180492.492680	139.52	63.01	Normal Fault
506617.669434	4180533.488350	202.76	72.08	Normal Fault
506705.851269	4180552.696910	34.77	77.59	Normal Fault
506750.119221	4180570.691100	48.62	56.31	Normal Fault
506813.289072	4180592.694040	60.72	71.37	Normal Fault
506625.495167	4180530.027870	38.64	56.31	Normal Fault
506340.226186	4180399.545120	81.55	78.96	Dry tension fracture
506327.212874	4180372.938360	59.56	64.31	Dry tension fracture
506346.326960	4180374.428140	93.51	58.41	Dry tension fracture
506503.340934	4180450.417550	175.67	71.39	Dry tension fracture
506519.362529	4180457.917280	21.94	65.22	Dry tension fracture
506710.240115	4180545.595150	121.39	71.01	Normal Fault
506751.076896	4180527.167440	118.18	68.09	Normal Fault
506599.437769	4180470.801920	165.00	72.27	Normal Fault
506860.265845	4180575.713850	98.80	72.74	Dry tension fracture
506875.210666	4180593.409290	26.85	66.47	Dry tension fracture
506888.592861	4180593.953750	22.90	67.46	Dry tension fracture
506912.798466	4180559.897450	120.86	74.95	Dry tension fracture

506888.868124	4180529.967540	118.79	68.32	Dry tension fracture
506966.734621	4180612.962850	129.03	71.77	Dry tension fracture
507027.276055	4180657.744830	162.97	75.85	Dry tension fracture
507131.327670	4180723.777050	242.48	66.38	Dry tension fracture
507091.442584	4180645.708240	49.84	72.29	Dry tension fracture
507219.247238	4180688.285550	178.98	70.95	Dry tension fracture
507334.195732	4180724.111700	40.16	88.87	Dry tension fracture
507234.175321	4180651.438350	214.24	65.59	Dry tension fracture
506460.384040	4180318.714740	247.98	68.51	Pre-1928 fracture
506670.342152	4180195.112750	153.10	71.44	Pre-1928 fracture
506764.262155	4180351.750750	206.51	67.38	Pre-1928 fracture
506886.171754	4180458.953130	171.27	59.28	Pre-1928 fracture
506888.706520	4180412.366930	71.67	53.47	Pre-1928 fracture
507310.739517	4180629.185350	244.24	55.29	Pre-1928 fracture
507164.420419	4180588.032220	191.92	60.14	Pre-1928 fracture
507326.604518	4180507.602910	109.64	62.19	Pre-1928 fracture
507461.259094	4180471.753390	231.60	57.04	Pre-1928 fracture
507702.379698	4180831.920930	124.22	72.54	Dry tension fracture
507887.119759	4180734.236810	461.42	67.76	Pre-1928 fracture
507766.524809	4180529.620710	104.66	60.04	Pre-1928 fracture
507663.445818	4180531.546260	112.48	71.74	Pre-1928 fracture
508219.405122	4180887.749640	230.08	77.36	Pre-1928 fracture
508294.266600	4180872.628410	116.99	78.69	Dry tension fracture
508393.239688	4180971.671600	269.32	86.52	Pre-1928 fracture
508530.149809	4181027.129050	152.78	81.53	Pre-1928 fracture
508722.689941	4181086.277760	173.84	74.34	Pre-1928 fracture
508604.006606	4181079.413660	275.43	70.44	Pre-1928 fracture
508404.547802	4180921.253570	63.04	81.53	Pre-1928 fracture
508421.249153	4180916.795670	31.86	85.24	Pre-1928 fracture
508580.584615	4180958.576660	248.85	73.57	Pre-1928 fracture
508440.882457	4180885.473910	201.80	76.65	Dry tension fracture
508396.224172	4180809.930510	93.97	55.18	Pre-1928 fracture
508580.608839	4180859.697510	260.04	66.89	Pre-1928 fracture
508462.052601	4180832.467880	154.36	57.39	Pre-1928 fracture
508803.603484	4180871.350500	82.34	83.29	Dry tension fracture
508915.796571	4180916.514930	148.22	69.78	Eruptive fissure
508921.435474	4180904.066150	147.11	69.78	Eruptive fissure
509191.162030	4181044.851950	360.29	61.86	Pre-1928 fracture
506453.884819	4180459.736480	45.53	65.49	Dry tension fracture
506488.161050	4180469.059940	21.07	73.23	Dry tension fracture
506549.242464	4180492.151070	37.53	62.29	Dry tension fracture
506829.094862	4180583.127800	57.29	63.99	Dry tension fracture
506845.050906	4180555.203620	54.27	76.79	Dry tension fracture
506752.400745	4180508.404010	146.54	63.79	Normal Fault
506636.566490	4180508.605340	98.56	77.54	Dry tension fracture
506726.780374	4180528.798810	68.36	70.42	Dry tension fracture

506890.300917	4180562.737460	112.65	67.34	Normal Fault
501722.041650	4178868.711000	62.94	56.77	Eruptive fissure
501744.144199	4178881.596490	27.35	49.50	Eruptive fissure
501785.535038	4178908.588680	115.33	58.02	Eruptive fissure
501838.169524	4178939.059870	22.20	72.80	Eruptive fissure
501882.037228	4178961.436680	46.38	56.16	Eruptive fissure
501611.795937	4178794.129370	128.06	56.09	Eruptive fissure
501611.220057	4178799.417120	125.04	56.09	Eruptive fissure

Table A1.2 Quantitative structural data collected in the field at the structural stations along the 1928 fissure.

X (m)	Y (m)	Altitude (m a.s.l.)	Description	Strike (°N)	Opening direction (°N)	Opening (m)	Vertical offset (m)	Lifted wall
502664.432917	4179398.962370	2536.65	Normal fault	88.00			1.00	N
502807.209857	4179403.225780	2469.65	Normal fault	80.00			1.00	N
502871.594396	4179156.833390	2350.56	Eruptive vent	64.00				
502911.582368	4179411.028320	2430.57	Normal fault	76.00			1.00	N
502994.557842	4179400.518030	2413.16	Normal fault	78.00			1.70	N
503059.025540	4179419.846590	2363.88	Normal fault	80.00			3.00	N
503115.344736	4179057.650110	2370.70	Normal fault	84.00			0.50	S
503180.051899	4179409.130490	2300.67	Normal fault	74.00			0.50	N
503190.354261	4179069.159500	2355.70	Normal fault	84.00			0.50	S
503212.727666	4179414.357700	2280.69	Normal fault	74.00			1.00	N
503230.947189	4179091.120240	2371.30	Normal fault	85.00			1.00	S
503234.072126	4179115.917060	2335.70	Normal fault	75.00			10.00	S
503235.164846	4179110.566880	2380.00	Normal fault	75.00			2.00	S
503245.839205	4179431.234710	2257.24	Normal fault	74.00			1.50	N
503263.764819	4179094.293990	2337.23	Normal fault	81.00			3.00	S
503276.476309	4179081.065780	2370.00	Normal fault	82.00			1.00	S

503303.295190	4179120.158040	2351.50	Normal fault	75.00			0.50	S
503307.831648	4179251.524260	2267.55	Eruptive vent	69.00				S
503310.461318	4179283.367270	2272.08	Eruptive vent	69.00				
503360.377220	4179077.512460	2332.50	Normal fault	75.00			1.00	S
503366.993755	4179096.147060	2327.80	Normal fault	78.00			10.00	S
503387.377385	4179447.157180	2220.20	Normal fault	82.00			2.00	N
503394.036758	4179103.666210	2295.83	Normal fault	74.00			5.50	S
503399.405278	4179115.660120	2306.90	Normal fault	74.00			4.00	S
503422.424084	4179257.007480	2225.71	Eruptive vent	63.00				
503437.905033	4179308.493610	2226.71	Eruptive vent	63.00				
503457.282998	4179152.847380	2282.40	Normal fault	74.00			0.50	S
503477.788248	4179123.266900	2277.20	Normal fault	75.00			2.00	S
503502.885118	4179103.886620	2272.40	Normal fault	74.00			4.00	S
503614.816230	4179241.615270	2220.30	Normal fault	65.00			0.50	S
503687.584232	4179379.164220	2144.22	Eruptive vent	67.00				S
503722.902116	4179384.616530	2119.79	Eruptive vent	64.00			2.00	S
503723.546641	4179300.597830	2175.40	Normal fault	65.00			0.50	S
503746.419986	4179383.850550	2105.72	Eruptive fissure	70.00		0.80		
503786.320854	4179383.092160	2101.03	Eruptive fissure	68.00		0.70		
503789.137648	4179386.976620	2101.99	Flow direction	72.00				
503794.158394	4179386.646080	2101.72	Eruptive fissure	65.00		0.40		
503801.288774	4179395.636130	2094.72	Eruptive fissure	64.00		0.50		
503811.052982	4179423.155640	2093.72	Eruptive vent	62.00				
503853.518679	4179399.543550	2096.73	Eruptive fissure	61.00		0.40		
503859.507992	4179399.879200	2078.39	Eruptive fissure	62.00		0.40		
503888.000000	4179412.995000	2075.92	Eruptive fissure	62.00				
503937.772315	4179481.906510	2019.73	Eruptive fissure	64.00				

504352.1 02935	4179640.5 48150	1881.38	Dry fracture	69.00				
504391.4 52984	4179679.5 11660	1875.74	Dry fracture	68.00				
504534.9 83192	4179745.0 48530	1821.80	Dry fracture	64.00				
504720.0 75387	4179823.9 25340	1786.72	Dry fracture	62.00				
504849.0 78575	4179871.5 96810	1757.43	Dry fracture	64.00				
504882.4 50143	4179886.8 16360	1748.76	Dry fracture	64.00				
504933.8 77111	4179901.8 24930	1735.78	Normal fault	63.00		7.00	1.70	S
504952.7 20708	4179909.2 69730	1732.77	Dry fracture	67.00		6.00		
505006.4 54948	4179895.3 22800	1719.00	Dry fracture	58.00		3.05		
505006.9 64993	4179925.6 11830	1724.00	Dry fracture	60.00		3.12		
505011.5 58448	4179903.3 14130	1717.00	Dry fracture	52.00		1.01		
505011.7 39322	4179895.5 47900	1721.00	Dry fracture	59.00		3.54		
505032.6 79859	4179930.5 09200	1718.00	Dry fracture	60.00		3.19		
505038.2 23956	4179938.0 57030	1713.00	Dry fracture	69.00				
505063.1 44457	4179945.6 16750	1711.00	Dry fracture	56.00		5.47		
505089.7 42576	4179946.2 98830	1705.00	Dry fracture	62.00		1.50		
505112.3 69901	4179958.9 60880	1718.03	Eruptive vent	62.00		7.00		
505112.3 69901	4179958.9 60880	1718.03	Eruptive fissure	62.00		0.64		
505113.6 89090	4179962.0 68230	1717.78	Eruptive fissure	64.00				
505120.5 58964	4179961.9 61550	1716.83	Eruptive fissure	69.00				
505143.1 93608	4179962.7 52280	1704.80	Eruptive vent	69.00		4.00		
505208.2 58423	4179995.2 15430	1747.90	Eruptive vent	63.00		1.15		
505212.0 93581	4179996.3 08830	1743.20	Eruptive vent	63.00				
505240.7 46268	4180015.9 57720	1693.81	Eruptive vent	63.00				
505249.7 31215	4180013.7 44490	1692.74	Eruptive vent	68.00		0.40		
505269.6 34989	4180015.1 99510	1682.78	Eruptive fissure	66.00		0.80		
505278.9 72596	4180012.4 31800	1683.12	Dike	68.00				

505280.296193	4180008.549470	1683.78	Eruptive vent	62.00				
505282.312078	4180023.861550	1689.79	Eruptive vent	62.00				
505291.499610	4179980.486880	1680.00	Dry fracture	90.00				
505301.331729	4180030.530640	1677.00	Dry fracture	60.00		5.13		
505344.659672	4180037.215490	1681.00	Dry fracture	60.00		4.54		
505365.968071	4180045.550420	1679.00	Dry fracture	69.00				
505390.798640	4180054.997190	1681.79	Sinkhole	65.00				
505401.616980	4180077.415720	1677.80	Sinkhole	65.00			1.60	N
505417.906656	4180083.306650	1680.78	Sinkhole	65.00				
505420.108484	4180083.308100	1680.54	Sinkhole	65.00			1.70	N
505420.548704	4180083.530280	1678.88	Sinkhole	65.00				
505428.121239	4180086.198010	1674.82	Sinkhole	61.00				
505497.061608	4180117.530990	1664.79	Sinkhole	62.00				
505500.850886	4180114.316040	1658.76	Sinkhole	62.00				
505503.847288	4180111.433400	1649.79	Sinkhole	62.00			4.00	N
505511.858799	4180116.098560	1658.00	Dry fracture	68.00				
505515.907770	4180119.651600	1646.49	Sinkhole	65.00				
505521.021120	4180111.999620	1654.00	Dry fracture	64.00		4.36		
505523.773023	4180079.715670	1653.00	Eruptive vent	71.00				
505542.675319	4180129.432960	1656.79	Sinkhole-eruptive fissure	64.00			4.00	N
505546.631119	4180140.530400	1647.36	Sinkhole	65.00			2.50	N
505549.706333	4180151.405350	1641.00	Sinkhole	62.00				
505550.591830	4180139.848480	353.80	Sinkhole-eruptive fissure	62.00			1.50	N
505562.743972	4180147.087180	1651.79	Sinkhole	65.00			6.00	N
505581.331620	4180140.664780	1635.86	Sinkhole	65.00			1.50	N
505583.617896	4180145.991830	1635.19	Sinkhole-eruptive fissure	69.00			1.50	N
505585.713714	4180156.392100	1676.60	Dike	70.00				

505592.158968	4180148.882260	1644.80	Sinkhole-eruptive fissure	66.00		0.40		
505618.308614	4180160.438620	1637.14	Sinkhole	65.00			3.00	N
505643.055795	4180162.119750	1638.80	Sinkhole	66.00			5.50	N
505670.281101	4180183.643730	721.70	Sinkhole	68.00			1.00	N
505672.636858	4180178.449390	1630.30	Sinkhole	68.00			1.00	N
505673.337921	4180183.553470	1623.78	Sinkhole	68.00			1.00	N
505680.469540	4180186.775870	1619.79	Sinkhole	68.00			1.00	N
505685.135128	4180189.996570	1629.80	Sinkhole	70.00				
505694.327043	4180197.972090	1670.15	Sinkhole	70.00				
505703.485701	4180201.357500	1670.00	Sinkhole	70.00			3.00	S
505744.304593	4180211.450540	1614.00	Dry fracture	62.00		0.53		
505751.877991	4180212.565300	1618.00	Dry fracture	68.00		5.80		
505783.310575	4180225.457250	1604.43	Dry fracture	66.00		0.80		
505804.543285	4180234.358430	1651.00	Sinkhole	67.00			1.70	S
505808.221000	4180245.667000	1607.00	Sinkhole	67.00				
505813.684481	4180240.789420	1606.00	Sinkhole	67.00				
505823.579285	4180237.579580	1662.80	Sinkhole	67.00			1.70	S
505827.421903	4180243.239980	1627.80	Sinkhole	65.00				
505829.097222	4180240.467470	1599.00	Sinkhole	65.00				
505841.462526	4180239.433250	1653.70	Dry fracture	66.00		0.40		
505846.789744	4180254.348480	1598.00	Dry fracture	64.00		0.30		
505858.934222	4180246.331010	1652.70	Sinkhole	68.00			1.00	N
505859.863867	4180243.416750	1658.40	Sinkhole	68.00				
505878.034798	4180250.274460	1617.00	Sinkhole	68.00				
505879.145264	4180251.838780	1632.50	Sinkhole	68.00				
505880.347925	4180250.156340	1596.00	Dry fracture	68.00		0.90		
505883.135580	4180258.152440	1637.50	Dry fracture	63.00		0.90		

505885.761686	4180258.477360	1645.60	Sinkhole	68.00				
505889.855031	4180256.598110	1596.00	Sinkhole	68.00				
505889.862784	4180237.050970	1660.00	Sinkhole	66.00				
505941.098282	4180276.383610	1589.00	Dry fracture	40.00	112.00	0.37		
505969.663115	4180287.538980	1631.68	Sinkhole	62.00				
505978.053473	4180291.409380	1630.19	Sinkhole	62.00		0.35		
505980.149289	4180291.785900	1631.05	Sinkhole	62.00				
505985.839374	4180290.821460	1626.89	Sinkhole	62.00		0.45		
505995.661195	4180299.091990	1616.80	Sinkhole	62.00				
505999.127228	4180305.739180	1617.39	Sinkhole	68.00		3.50	1.20	N
506000.289838	4180313.383550	1630.00	Sinkhole	65.00		0.40		
506001.726881	4180323.766390	1632.00	Sinkhole	65.00				
506008.330660	4180309.318410	1619.60	Sinkhole	65.00			0.80	N
506017.167143	4180310.056000	1574.00	Sinkhole	65.00				
506019.369722	4180308.948130	1573.00	Sinkhole	68.00				
506019.881104	4180315.397900	1620.97	Sinkhole	68.00				
506023.501515	4180334.595370	1626.90	Dry fracture	80.00		0.50		
506029.531687	4180313.271440	1619.90	Sinkhole	67.00		1.10		
506030.125911	4180305.195980	1613.99	Normal fault	64.00			1.58	N
506036.185542	4180316.726780	1577.00	Sinkhole	67.00				
506038.751804	4180316.887320	1621.49	Normal fault	64.00		2.80	0.60	N
506039.441716	4180320.057610	1576.00	Sinkhole	67.00				
506046.973160	4180319.346410	1620.16	Dry fracture	60.00		0.30		
506050.896114	4180318.956530	1616.80	Dry fracture	68.00		0.26		
506052.299944	4180320.177990	1577.00	Dry fracture	72.00		0.90		
506059.513866	4180315.314900	1619.45	Normal fault	72.00			0.25	S
506061.196137	4180318.742210	1574.00	Dry fracture	56.00		6.00		

506063.5 73666	4180326.4 38190	1618.31	Sinkhole	65.00				
506070.9 66663	4180325.9 61010	1573.00	Dry fracture	68.00		0.25		
506072.4 35849	4180325.7 32430	1619.66	Sinkhole	69.00				
506076.1 34655	4180324.7 54380	1620.05	Sinkhole	69.00		2.80		
506085.6 70712	4180328.6 41260	1608.25	Eruptive fissure	69.00		3.00	0.30	N
506088.1 36731	4180330.9 66330	1565.00	Sinkhole	69.00				
506091.7 67521	4180325.4 97070	1606.40	Dry fracture	69.00		2.40	0.15	S
506103.0 37058	4180324.2 78330	1610.99	Dry fracture	65.00				
506126.4 57952	4180340.4 89650	1610.08	Sinkhole	61.00			0.90	N
506126.8 13306	4180345.8 33170	1604.73	Sinkhole	65.00		0.55	0.20	N
506127.7 54592	4180349.6 34940	1564.00	Sinkhole-dike	61.00				
506129.1 85121	4180345.7 26200	1603.34	Eruptive fissure	62.00		1.40	0.50	N
506136.8 66595	4180333.9 37060	1598.71	Flow direction	170.0 0				
506141.9 21504	4180366.2 87660	1563.00	Sinkhole	65.00				
506143.2 62494	4180339.5 50240	1566.00	Sinkhole	65.00				
506143.8 24529	4180357.0 69320	1602.89	Eruptive fissure	65.00		5.30	2.30	N
506157.0 75120	4180358.8 65470	1561.00	Sinkhole-dike	65.00				
506157.5 09086	4180367.4 08780	1562.00	Sinkhole-dike	65.00				
506157.9 38016	4180367.3 71370	1608.31	Sinkhole	65.00				
506168.6 14144	4180356.4 33250	1556.00	Dry fracture	66.00		1.80		
506177.4 71544	4180376.1 70850	1606.42	Dry fracture	65.00		2.40		
506191.7 42948	4180418.7 37180	1608.20	Sinkhole	65.00				
506192.2 16067	4180388.1 11030	1597.59	Dry fracture	84.00		2.30		
506196.6 88602	4180382.9 70850	1560.00	Dry fracture	64.00		0.85		
506202.4 50501	4180384.8 32450	1596.20	Dry fracture	74.00		2.13		
506206.3 86117	4180386.3 07690	1591.55	Dry fracture	68.00		2.80		
506212.3 48387	4180392.2 35690	1594.90	Dry fracture	66.00		0.91		

506262.641635	4180428.649140	1595.60	Normal fault	68.00			1.00	N
506266.151232	4180415.309210	1554.00	Normal fault	62.00			0.40	N
506275.300380	4180428.570120	1595.39	Sinkhole	68.00				
506278.528628	4180468.351700	1549.00	Sinkhole	65.00				
506283.223534	4180432.630070	1550.00	Normal fault	62.00			0.20	N
506286.025133	4180408.248100	1597.26	Depression	55.00				
506287.936422	4180432.183590	574.40	Sinkhole	62.00				
506288.778989	4180434.095080	600.00	Dry fracture	62.00		0.85		
506292.002342	4180469.471460	1548.00	Sinkhole	65.00				
506293.755162	4180480.678530	1546.00	Sinkhole	65.00				
506295.623431	4180435.968320	1599.00	Normal fault	65.00		2.90	0.60	N
506298.897090	4180436.303320	1548.00	Dry fracture	62.00				
506308.140824	4180440.948020	1589.36	Dry fracture	73.00		0.40		
506317.726227	4180372.131090	1586.67	Dry fracture	68.00				
506320.718923	4180370.886330	1583.79	Dry fracture	66.00		3.00		
506324.347235	4180445.581050	1582.50	Dry fracture	68.00		4.00		
506334.047690	4180422.128950	1541.00	Older lineament	64.00			1.00	N
506337.217222	4180378.743020	1582.01	Sinkhole	68.00				
506340.947019	4180375.269890	1592.97	Dry fracture	68.00				
506346.674539	4180379.423750	1545.00	Dry fracture	60.00				
506349.387529	4180377.719460	1589.25	Dry fracture	60.00		0.30		
506350.032994	4180507.458550	1550.43	Sinkhole	65.00				
506350.461720	4180379.204770	1546.00	Dry fracture	60.00				
506356.084351	4180377.752360	1586.62	Dry fracture	63.00	158.00	0.90		
506360.266030	4180386.732380	1584.43	Dry fracture	84.00		0.40		
506361.196039	4180465.443940	1580.04	Dry fracture	67.00				
506361.551085	4180388.865790	1547.00	Dry fracture	60.00				

506361.5 86506	4180466.1 69840	1586.08	Normal fault	67.00	174.00	0.70	0.30	N
506361.9 31716	4180466.1 96730	1547.00	Normal fault	63.00			0.22	N
506362.4 65614	4180459.0 96480	1544.00	Dry fracture	49.00		0.35		
506363.2 96775	4180385.2 58010	1583.10	Dry fracture	62.00	165.00	0.70		
506363.9 28886	4180388.9 78570	1543.00	Dry fracture	60.00			0.10	S
506367.3 84274	4180462.5 20800	1584.64	Dry fracture	67.00	164.00	0.60		
506368.4 14304	4180387.8 18200	1582.30	Dry fracture	64.00		2.50		
506368.5 81814	4180462.7 79130	1583.54	Dry fracture	76.00		0.30		
506370.5 34912	4180456.4 00330	1578.18	Dry fracture	75.00				
506370.9 61311	4180452.7 00250	1578.56	Dry fracture	65.00		0.40		
506371.3 00785	4180447.6 17990	1582.61	Dry fracture	66.00	152.00	0.50		
506371.9 16168	4180462.7 06260	1582.78	Dry fracture	72.00				
506375.8 54613	4180455.8 89340	1545.00	Dry fracture	72.00				
506379.1 03969	4180456.4 03330	1580.55	Dry fracture	63.00	130.00	0.50		
506387.0 71495	4180457.6 62100	1583.38	Normal fault	53.00		0.60	1.20	N
506392.1 24297	4180460.7 17090	1579.78	Sinkhole	65.00				
506392.2 04227	4180456.4 51210	1579.74	Sinkhole	66.00				
506397.4 62383	4180457.0 39980	1581.62	Dry fracture	66.00				
506404.8 03923	4180488.6 41420	1541.00	Dry fracture	59.00		1.00		
506408.2 33991	4180417.5 89750	1571.91	Dry fracture	80.00		0.40		
506408.9 06852	4180474.1 60500	1578.28	Dry fracture	76.00				
506418.2 45184	4180418.3 10940	1536.00	Normal fault	74.00			0.30	S
506418.8 02883	4180416.9 01230	1577.07	Dry fracture	76.00	177.00	0.60		
506419.4 44281	4180417.7 09430	1576.49	Dry fracture	76.00				
506423.8 43803	4180478.1 29510	1578.77	Normal fault	78.00		4.30	1.20	N
506426.8 26246	4180422.2 65160	1569.76	Dry fracture	80.00	170.00	0.90		
506426.8 27779	4180446.2 65390	1570.10	Sinkhole	72.00				

506427.0 77381	4180479.9 62250	1636.50	Normal fault	78.00			1.00	N
506429.6 35586	4180425.7 52220	1566.16	Dry fracture	76.00				
506429.7 26093	4180427.1 43580	1564.36	Dry fracture	78.00				
506433.6 92457	4180425.2 56120	1573.68	Dry fracture	76.00		0.15		
506435.4 24835	4180424.0 64790	1573.88	Dry fracture	76.00				
506436.0 06635	4180422.2 44590	1573.69	Dry fracture	60.00		0.50		
506439.8 22564	4180478.7 37770	1576.44	Dry fracture	76.00		0.80		
506439.9 07931	4180421.3 56720	1580.43	Dry fracture	80.00				
506440.2 41796	4180307.7 88660	1576.80	Dry fracture	64.00		2.90		
506443.5 41420	4180483.1 80490	1583.90	Dry fracture	76.00				
506445.0 99684	4180423.5 43130	1581.09	Dry fracture	84.00				
506445.5 11321	4180425.3 45240	1579.60	Dry fracture	83.00		0.30		
506445.8 97727	4180419.9 96750	1537.00	Normal fault	82.00			0.30	S
506448.1 22425	4180423.2 95860	1578.96	Dry fracture	84.00				
506449.2 37174	4180421.3 16310	1576.75	Dry fracture	82.00				
506449.7 27735	4180485.4 19040	1572.19	Dry fracture	66.00		2.50		
506452.0 74890	4180429.0 42720	1584.56	Dry fracture	75.00	164.00	1.20		
506452.6 77356	4180487.4 20630	1572.01	Dry fracture	66.00				
506452.9 06238	4180423.4 57150	1576.62	Dry fracture	76.00				
506455.9 53449	4180427.9 47380	1572.20	Dry fracture	70.00	170.00	0.80		
506456.5 01189	4180487.5 72290	1538.00	Normal fault	66.00			1.00	N
506456.7 33379	4180484.9 85870	1581.80	Dry fracture	65.00				
506456.9 02202	4180429.8 83050	1575.76	Dry fracture	68.00				
506457.5 41775	4180425.1 48300	1574.12	Dry fracture	66.00				
506458.0 43052	4180429.4 36830	1573.39	Dry fracture	64.00				
506460.3 69205	4180466.1 95670	1578.92	Sinkhole	72.00				
506461.8 20999	4180442.0 87840	1534.00	Dry fracture	70.00				

506462.8 76566	4180438.0 86780	1575.00	Dry fracture	68.00		0.45		
506463.6 01505	4180488.4 36600	1579.73	Dry fracture	72.00		2.00		
506464.1 37881	4180434.5 15250	1570.36	Dry fracture	67.00	171.00	0.90		
506464.5 74687	4180439.0 27840	1578.12	Dry fracture	70.00				
506464.8 60968	4180470.3 80820	1563.86	Sinkhole	72.00				
506466.2 47630	4180438.3 84550	1576.39	Dry fracture	70.00				
506466.7 18783	4180438.4 08220	1575.36	Dry fracture	62.00	152.00	0.50		
506472.8 86379	4180444.7 77440	1563.76	Sinkhole	70.00				
506472.8 86379	4180444.7 77440	1563.16	Sinkhole	65.00				
506473.7 03828	4180562.4 75600	1536.00	Older lineament	96.00		4.46		
506476.4 02827	4180444.0 96360	1563.16	Dry fracture	64.00		1.04		
506478.8 79405	4180446.2 49580	1568.94	Dry fracture	66.00		1.10		
506484.9 21723	4180441.9 25150	1573.99	Dry fracture	72.00				
506488.2 50631	4180445.4 24850	1560.19	Dry fracture	76.00		1.60		
506489.9 75388	4180438.2 61200	1570.80	Dry fracture	74.00				
506490.6 75054	4180438.8 77510	1574.26	Dry fracture	70.00				
506493.7 21764	4180445.0 87440	1561.15	Dry fracture	64.00		2.00		
506495.9 96215	4180493.5 94530	1575.24	Sinkhole	65.00				
506497.7 64639	4180499.2 81960	1567.82	Normal fault	63.00			1.00	N
506498.2 44151	4180489.7 13120	1525.00	Normal fault	64.00			1.35	N
506498.5 66988	4180451.1 14620	1557.67	Dry fracture	72.00		0.40		
506500.9 15545	4180452.5 47700	1525.00	Dry fracture	70.00				
506501.3 38310	4180498.2 60770	1567.63	Dry fracture	63.00		2.00		
506503.7 31852	4180456.9 82020	1576.10	Sinkhole	72.00				
506509.4 03302	4180451.8 86500	1560.18	Dry fracture	70.00				
506510.2 96514	4180506.2 53870	1526.00	Normal fault	65.00			1.50	N
506510.7 25156	4180464.5 24450	1550.30	Dry fracture	78.00		0.55		

506516.616884	4180506.722140	1615.20	Dry fracture	65.00				
506522.147305	4180554.858410	1528.00	Older lineament	110.00		2.14		
506524.875757	4180504.696600	1560.82	Normal fault	72.00		1.90	0.40	N
506527.001967	4180506.919680	593.30	Dry fracture	66.00				
506529.543180	4180557.194170	1527.00	Older lineament	96.00		4.50		
506536.234635	4180516.502590	1580.80	Dry fracture	62.00		1.20		
506536.460711	4180508.636670	1560.18	Dry fracture	76.00	162.00	1.10		
506540.975939	4180509.810750	1561.37	Dry fracture	65.00				
506545.051708	4180454.927220	1598.40	Dry fracture	72.00		0.50		
506550.779379	4180502.587530	1563.50	Dry fracture	62.00				
506551.060782	4180463.695160	37.20	Sinkhole	75.00				
506556.130496	4180487.848100	1592.90	Sinkhole	64.00				
506557.136232	4180463.560110	1559.40	Sinkhole	75.00				
506567.240036	4180552.564330	1523.00	Older lineament	164.00		3.10		
506579.019284	4180467.116160	1559.20	Normal fault	75.00		0.50	0.50	N
506582.425682	4180528.576230	1561.23	Scarp	67.00			1.00	
506601.140990	4180487.478210	1567.90	Depression	72.00				
506605.601307	4180525.547020	1561.36	Dry fracture	74.00				
506607.213105	4180474.228950	1559.45	Sinkhole	68.00				
506613.290116	4180537.335800	1523.80	Normal fault	70.00		0.70	0.40	N
506616.533923	4180520.320160	1567.73	Dry fracture	72.00		2.10		
506617.730027	4180537.034970	1546.20	Normal fault	72.00			1.00	N
506618.163132	4180539.348040	1545.40	Dry fracture	71.00				
506625.647058	4180531.515470	1564.90	Normal fault	72.00		1.50	1.20	N
506625.947131	4180524.149880	1569.60	Normal fault	76.00		0.80	0.30	N
506631.219081	4180532.691080	1588.90	Normal fault	74.00			1.00	N
506631.472437	4180623.844320	1526.00	Older lineament	164.00		5.50		

506637.058045	4180533.749160	1558.12	Dry fracture	66.00	159.00	2.00		N
506637.338276	4180530.255640	1566.34	Normal fault	57.00	140.00	0.70	0.30	N
506640.301530	4180529.471400	1558.19	Dry fracture	70.00				
506659.244291	4180527.144590	1555.48	Normal fault	74.00		1.70	3.50	N
506691.671944	4180556.463320	1548.71	Dry fracture	70.00				
506697.081045	4180553.269090	1551.44	Older lineament	72.00		4.50	1.60	N
506697.517295	4180500.672690	1544.10	Dry fracture	70.00		0.70		
506700.217341	4180519.471370	1559.77	Sinkhole	76.00				
506702.408722	4180531.088280	1550.14	Older lineament	71.00		4.70	1.30	N
506705.046981	4180492.468370	1561.15	Normal fault	71.00		4.20	1.50	S
506705.870943	4180504.814210	1552.10	Normal fault	73.00	156.00		0.70	S
506710.727108	4180559.882700	1553.93	Older lineament	72.00		4.90	1.60	N
506713.900783	4180544.041930	1546.93	Older lineament	71.00		0.90	0.70	N
506715.051820	4180504.084990	1549.16	Dry fracture	72.00				
506720.143020	4180525.741730	1543.78	Sinkhole	75.00				
506727.889125	4180553.188790	1549.42	Normal fault	68.00		1.70	1.70	N
506729.886226	4180498.998610	1579.60	Dry fracture	70.00		0.70		
506734.877415	4180511.079800	1551.82	Older lineament	71.00		5.30	0.70	S
506740.392036	4180532.896660	1549.05	Older lineament	75.00		3.50		
506744.843935	4180518.863180	1552.75	Older lineament	72.00		2.90	0.60	S
506750.861241	4180524.747240	1552.32	Older lineament	74.00		2.70		
506770.382631	4180527.807670	1542.37	Sinkhole	70.00			1.80	N
506781.943184	4180533.392310	1539.08	Scarp	72.00				
506812.479063	4180589.931020	1504.00	Dry fracture	66.00				
506852.534657	4180608.270640	1498.00	Sinkhole	63.00				
506859.213471	4180625.473130	1494.00	Dry fracture	68.00		3.40		
506875.319512	4180532.290330	1495.00	Older lineament	92.00		3.50		

506875.398321	4180543.385180	1492.00	Older lineament	56.00		3.80		
506875.654331	4180514.162840	1532.49	Dry fracture	67.00		0.10		
506888.240420	4180562.368000	1495.00	Dry fracture	60.00		2.36		
506895.353501	4180586.782480	1494.00	Older lineament	65.00				
506896.250732	4180532.292290	1527.81	Dry fracture	66.00				
506898.012100	4180522.827700	1526.53	Scarp	67.00				
506905.979533	4180535.584500	1530.60	Sinkhole	52.00			0.70	S
506906.449568	4180566.346300	1520.91	Older lineament	42.00		3.30	0.20	S
506917.128521	4180594.878860	1518.96	Sinkhole	80.00			1.60	N
506942.497540	4180607.154390	1550.94	Sinkhole	94.00			0.20	S
506985.152904	4180616.724200	1511.24	Older lineament	60.00				
507030.125426	4180657.015470	1484.00	Dry fracture	68.00				
507173.336086	4180742.568820	1466.00	Dry fracture	64.00				
507183.386434	4180629.188810	1469.00	Dry fracture	88.00		3.02		
507183.741800	4180625.638790	1462.00	Sinkhole	70.00		2.56		
507200.572267	4180614.669640	1463.00	Dry fracture	88.00		3.23		
507208.812630	4180456.798010	1460.00	Normal fault	90.00		5.90	0.50	N
507214.430110	4180478.437760	1464.00	Normal fault	88.00		3.10	0.50	N
507268.169097	4180459.291020	1450.00	Older lineament	75.00				
507291.843809	4180775.735350	1451.00	Dry fracture	75.00		0.50		
507341.453543	4180644.749930	1460.00	Dry fracture	69.00		5.45		
507399.705071	4180699.277470	1443.00	Older lineament	69.00				
507407.893068	4180701.725690	1446.00	Older lineament	68.00		2.03		
507489.175674	4180704.905730	1429.00	Older lineament	100.00		2.30		
507496.830797	4180712.235250	1433.00	Dry fracture	74.00		0.51		
507502.468869	4180710.243320	1432.00	Dry fracture	68.00		1.20		
507677.813427	4180758.851780	1474.80	Older lineament	63.00				

507716.959606	4180760.718630	1444.04	Older lineament	63.00				
507795.974944	4180824.126560	1400.00	Dry fracture	78.00		5.00		
507822.044050	4180822.265160	1400.00	Dry fracture	65.00		3.50		
507824.598470	4180821.712850	1400.00	Dry fracture	71.00		4.80		
507831.187333	4180838.583200	1395.00	Dry fracture	68.00		4.70		
507877.262988	4180728.122970	1391.00	Normal fault	72.00		3.10	0.50	S
507919.424657	4180751.129620	1388.00	Dry fracture	80.00		0.85		
507923.392964	4180745.586040	1390.00	Dry fracture	71.00		0.60		
508076.851024	4180825.419010	1395.62	Sinkhole	65.00		0.50	0.30	?
508092.614094	4180847.388460	1422.50	Dry fracture	74.00				
508155.796547	4180662.443360	1407.70	Dry fracture	75.00				
508158.999007	4180662.589180	1400.10	Dry fracture	74.00				
508170.904189	4180877.523070	1359.00	Dry fracture	74.00		2.90		
508171.872791	4180877.634980	1361.00	Dry fracture	74.00		1.70		
508191.355464	4180653.472890	1381.03	Dry fracture	75.00				
508191.423056	4180652.808380	1380.94	Dry fracture	90.00				
508197.780870	4180633.745430	1409.80	Normal fault	70.00			0.60	S
508204.641297	4180632.760370	1413.80	Sinkhole	64.00				
508209.370588	4180645.416030	1392.91	Older lineament	136.00				
508304.858076	4180870.223530	1340.00	Dry fracture	79.00				
508308.378428	4180872.446030	1341.00	Sinkhole	78.00			0.90	N
508330.915373	4180880.013260	1338.00	Normal fault	79.00		0.90	0.40	N
508335.308053	4180890.446810	1335.00	Dry fracture	73.00		0.90		
508360.936189	4180889.141410	1339.00	Dry fracture	87.00	163.00	0.80	0.10	N
508362.194673	4180777.196180	1330.00	Dry fracture	82.00		0.70		
508366.159886	4180774.981250	1327.00	Dry fracture	83.00		1.60		
508380.049361	4180886.054290	1334.00	Normal fault	79.00		0.50	0.30	N

508383.9 22735	4180887.5 00560	1339.00	Normal fault	75.00		1.10	1.00	N
508393.5 32176	4180877.3 03130	1338.00	Normal fault	73.00	165.00	1.24	0.40	N
508405.0 55179	4180890.5 17690	1339.00	Dry fracture	70.00	160.00	0.67	0.15	N
508408.6 80549	4180876.0 98150	1336.00	Normal fault	45.00	164.00	0.75	0.20	N
508432.6 33014	4180877.2 32120	1332.00	Normal fault	77.00	194.00	1.54	1.20	N
508463.2 72233	4180884.3 64210	1328.00	Normal fault	86.00	186.00	1.23	1.20	N
508467.7 58168	4180889.5 83380	1327.00	Normal fault	83.00		0.72	1.00	N
508474.1 95442	4180881.2 68900	1321.00	Normal fault	73.00	169.00	0.71	0.40	N
508480.5 26502	4180890.5 95050	1320.00	Dry fracture	108.00		0.66		
508482.5 27079	4180914.7 83770	1322.00	Older lineament					
508493.6 86127	4180768.3 43930	1298.00	Bulge					
508509.7 38062	4181000.9 07480	1310.00	Dry fracture	86.00		9.80		
508523.1 89490	4181107.5 42440	1311.00	Normal fault	145.00		5.50	0.50	N
508541.6 60540	4181043.8 77410	1308.00	Dry fracture	75.00		6.70		
508585.5 67683	4180994.2 18350	1303.00	Dry fracture	78.00		3.90		
508626.3 28871	4180921.8 11890	1296.00	Older lineament					
508635.3 55039	4180880.2 15850	1285.00	Dry fracture	112.00		3.60		
508675.3 97236	4180906.1 08810	1283.00	Dry fracture	62.00		0.30		
508682.5 47176	4180890.2 50780	1279.00	Dry fracture	62.00		0.60		
508683.9 54220	4180892.1 38380	1279.00	Dry fracture	82.00	190.00	0.83		
508688.6 71145	4180845.2 12350	1261.00	Older lineament	117.00		3.60	1.70	S
508757.7 51548	4180812.4 58300	1368.59	Older lineament	65.00				
508765.0 25157	4181092.0 41620	1282.00	Older lineament	90.00		2.00		
508791.0 44025	4181136.6 70470	1286.00	Normal fault	107.00		8.60	1.00	N
508823.6 21862	4180833.4 39350	1363.90	Older lineament	65.00				
508847.8 07469	4180886.4 36530	1242.50	Sinkhole	60.00				
508889.5 94524	4180883.8 14420	1234.20	Eruptive vent	68.00				

508890.5 50241	4180885.9 02340	1260.80	Eruptive vent	68.00				
508890.8 77713	4180888.2 80680	1220.33	Eruptive vent	74.00		1.60		
508891.5 76997	4180884.6 43250	1254.30	Eruptive vent	70.00				
508892.7 00736	4180884.1 02850	1260.50	Eruptive vent	68.00				
508895.5 95735	4180901.7 75940	1234.71	Eruptive vent	65.00				
508896.8 58901	4180887.8 38670	1261.70	Eruptive vent	62.00				
508905.5 59610	4180892.9 40260	1248.50	Eruptive vent	65.00				
508929.6 80813	4180920.7 40550	1225.64	Eruptive vent	64.00				
508941.0 37052	4180896.4 52040	1272.70	Eruptive vent	65.00				
508941.1 07356	4180920.4 27520	1241.70	Eruptive vent	65.00				
508946.4 85450	4180918.1 24880	1231.39	Eruptive vent	64.00				
508952.5 44754	4180908.7 75220	1231.25	Eruptive vent	65.00			0.30	S
508961.0 33628	4180917.4 36600	1235.10	Dike	65.00				
508968.3 91992	4180924.7 82960	1230.10	Eruptive vent	63.00				
508970.9 22595	4180913.9 33210	1230.51	Eruptive vent	65.00				
508988.1 45607	4180894.3 31940	1261.04	Eruptive vent	65.00				
509016.1 53427	4180921.1 14340	1225.24	Eruptive vent	66.00				
509022.7 73085	4180908.1 68520	1237.10	Eruptive vent	63.00				

Appendix 2

Structural measurements along the 1971 fissure (Mt. Etna)

Table A2.1. Quantitative structural data collected through GIS analysis along the 1971 fissure, with the classification of the structures.

X midpoint (m)	Y midpoint (m)	Length (m)	Strike (°N)	Type
504725.676903	4178747.307870	33.02	55.71	Eruptive fissure
504772.797198	4178773.348030	27.53	54.16	Eruptive fissure
503483.704950	4178704.568280	104.79	82.23	Normal fault
503706.556576	4178676.645920	167.59	107.84	Normal fault
502893.979149	4178770.210730	334.95	88.65	Normal fault
502667.665945	4178735.431320	87.65	67.14	Normal fault
502617.613691	4178782.732440	74.19	72.28	Normal fault
503377.099951	4178818.417290	173.64	78.90	Normal fault
503112.174494	4178803.892830	105.52	85.47	Normal fault
502826.341841	4178803.961600	360.53	79.16	Normal fault
502988.371116	4178776.761750	63.81	75.79	Normal fault
503077.252783	4178784.148330	51.83	86.53	Normal fault
503162.618518	4178765.737140	167.82	90.80	Normal fault
503351.100814	4178714.584000	203.19	109.08	Normal fault
503215.876678	4178780.433750	93.60	89.04	Normal fault
503606.240399	4178803.149220	147.24	97.17	Lineament
502875.944598	4178737.178150	86.30	48.63	Lineament
504466.382317	4178636.767980	138.08	79.09	Lineament
504290.862748	4178736.868660	209.50	85.84	Lineament
504019.714211	4178736.065990	48.31	96.34	Lineament
502922.525040	4178758.993680	22.51	59.04	Lineament
502860.037511	4178756.543300	85.58	65.18	Lineament
503269.240642	4178806.870380	43.57	101.56	Lineament
503205.809844	4178809.666430	66.61	90.83	Lineament
504031.176925	4178643.984510	89.94	96.34	Lineament
504079.012847	4178649.347250	33.50	92.12	Lineament
504211.800953	4178630.921740	125.88	95.09	Lineament
503818.009580	4178778.882430	167.80	101.98	Lineament

Table A2.2. Graben width values measured at the points shown in Figure 34A, with the respective elevation a.s.l.

X (m)	Y (m)	Width (m)	Elevation (m a.s.l.)
503110.9737	4178778.522	27.14	2134
503239.6374	4178776.146	41.16	2136
503259.7255	4178771.166	50.04	2137
503277.6931	4178765.842	35.44	2139
503303.4708	4178762.769	78.10	2150
503331.2402	4178760.948	98.21	2162
503358.3836	4178758.957	121.59	2181
503387.8601	4178758.843	137.40	2206
503417.8599	4178758.724	143.10	2219

Appendix 3

Structural measurements along the Stampar fissures and dikes (Iceland)

Table A3.1. Length and strike values of the eruptive fissures of the Older and Younger Stampar crater rows, collected through GIS analysis.

X midpoint (m)	Y midpoint (m)	Length (m)	Strike (°N)	Crater row
417714.153638	7081184.221190	18.02	33.50	Older Stampar
417728.160284	7081202.624020	26.80	28.63	Older Stampar
417743.977120	7081232.542390	18.43	30.01	Older Stampar
417757.454165	7081254.825770	14.43	28.12	Older Stampar
417774.267092	7081284.233890	14.11	25.80	Older Stampar
417778.593038	7081297.238190	9.80	21.37	Older Stampar
417991.348620	7081532.250540	103.10	26.56	Older Stampar
414919.451512	7077873.829060	62.01	36.47	Older Stampar
414950.850803	7077921.585770	42.40	38.16	Older Stampar
415379.697750	7078531.339770	17.71	28.71	Older Stampar
415395.922752	7078546.914290	26.26	37.63	Older Stampar
415468.778645	7078643.817350	128.65	38.60	Older Stampar
415539.025359	7078729.009730	73.14	37.95	Older Stampar
416005.279845	7079524.530800	54.25	38.17	Older Stampar
416032.887442	7079560.659210	21.86	31.68	Older Stampar
416066.902268	7079620.507380	30.17	31.44	Older Stampar
416228.484308	7079744.560090	188.86	24.64	Older Stampar
416649.890187	7080260.910160	133.89	42.60	Older Stampar
416826.899869	7080617.072280	179.72	32.01	Older Stampar
418893.671808	7082063.322310	152.09	32.47	Older Stampar
418936.150474	7082170.544100	117.88	51.47	Older Stampar
419089.536855	7082347.720770	79.55	33.06	Older Stampar
418644.771382	7081724.255360	230.87	35.77	Older Stampar
415225.738291	7078065.694760	114.08	35.66	Younger Stampar
415463.785315	7078363.820610	195.25	35.44	Younger Stampar
415529.960937	7078475.420430	58.54	30.56	Younger Stampar
415592.045093	7078561.800050	78.24	39.34	Younger Stampar
415650.708192	7078639.503210	70.67	39.87	Younger Stampar
415688.576757	7078689.278050	39.56	35.82	Younger Stampar
415704.948358	7078719.820520	16.42	35.73	Younger Stampar
415725.287327	7078742.335930	13.85	38.80	Younger Stampar
415847.423627	7078846.395290	82.31	46.48	Younger Stampar
416133.613858	7079114.415580	109.11	44.02	Younger Stampar
416266.683898	7079282.210480	18.36	36.21	Younger Stampar

416436.984337	7079651.684640	19.35	50.36	Younger Stampar
416450.100839	7079667.686610	23.98	41.56	Younger Stampar
416490.463858	7079737.453480	40.23	35.36	Younger Stampar
416515.429950	7079766.144990	12.57	45.14	Younger Stampar
416546.980909	7079795.336290	18.16	37.50	Younger Stampar
416556.578907	7079807.430160	9.29	23.87	Younger Stampar
416571.153778	7079838.407660	11.96	35.10	Younger Stampar
416580.171016	7079840.209030	6.91	36.43	Younger Stampar
416585.727277	7079852.313740	17.78	46.21	Younger Stampar
416582.646209	7079863.060740	20.07	46.60	Younger Stampar
416605.982495	7079883.616220	47.05	35.48	Younger Stampar
416625.636687	7079912.754590	16.06	36.41	Younger Stampar
416688.813560	7080008.356490	35.72	36.87	Younger Stampar
416760.459854	7080142.320550	14.35	47.38	Younger Stampar
416773.963261	7080156.164060	14.46	34.56	Younger Stampar
416806.302024	7080185.755560	24.64	49.88	Younger Stampar
416825.046688	7080122.983030	68.51	43.12	Younger Stampar
416872.408302	7080228.380020	25.29	42.03	Younger Stampar
416902.703154	7080264.628010	24.32	45.00	Younger Stampar
416915.138555	7080283.148920	7.49	42.14	Younger Stampar
416923.791325	7080291.534930	9.96	47.14	Younger Stampar
416929.774131	7080297.384750	5.25	36.79	Younger Stampar
416936.625010	7080305.671580	8.43	37.56	Younger Stampar
416981.819042	7080424.907090	16.22	39.88	Younger Stampar
416996.255360	7080436.088570	19.05	34.32	Younger Stampar
417004.744331	7080451.678870	12.91	45.50	Younger Stampar
417015.762703	7080469.285020	24.88	47.35	Younger Stampar
417049.498647	7080515.448120	12.21	35.33	Younger Stampar
417070.590875	7080561.656460	20.44	31.88	Younger Stampar
417091.840239	7080592.807440	25.34	36.68	Younger Stampar
417113.305294	7080632.459110	9.91	31.91	Younger Stampar
417138.941733	7080681.972720	49.13	33.63	Younger Stampar
417165.906271	7080734.602440	21.19	39.10	Younger Stampar
417201.889074	7080796.723790	46.04	43.60	Younger Stampar
417297.580237	7080881.831600	66.04	37.51	Younger Stampar
415379.202476	7078202.224070	19.83	31.36	Younger Stampar
415397.326471	7078230.005380	27.45	34.00	Younger Stampar
415368.077645	7078254.708000	26.03	29.93	Younger Stampar

Table A3.2. Strike values measured on the UAV-derived orthomosaic along the two exposed dikes.

X midpoint (m)	Y midpoint (m)	Strike (°N)	Dike
415016.418662	7077752.469430	27.53	Feeder
415018.221140	7077754.586100	37.07	Feeder
415019.432846	7077756.379320	34.44	Feeder
415020.520285	7077757.585820	45.71	Feeder
415050.400799	7077741.755770	46.97	Arrested 1
415051.735890	7077742.925230	38.75	Arrested 1
415046.120362	7077735.015500	18.18	Arrested 2
415046.955388	7077736.810700	28.69	Arrested 2
415047.624256	7077739.951310	18.60	Arrested 2

Table A3.3. Thickness and dip angles measured on the UAV-derived 3D model along the two exposed dikes, with the respective elevation a.s.l.

X midpoint (m)	Y midpoint (m)	Thickness (m)	Dip angle (°)	Elevation (m a.s.l.)	Dike
415015.317263	7077750.182748	0.57	90	3.58	Feeder
415015.640867	7077750.440930	0.45	90	4.50	Feeder
415015.945921	7077751.036400	0.45	90	5.00	Feeder
415016.093169	7077751.503810	0.46	90	5.80	Feeder
415016.168995	7077751.578980	0.42	90	6.56	Feeder
415016.434170	7077752.033320	0.43	90	7.39	Feeder
415017.636962	7077754.052370	0.32	90	8.38	Feeder
415018.184420	7077754.709980	0.42	90	9.44	Feeder
415019.174327	7077756.296910	0.26	87	10.05	Feeder
415019.772636	7077757.089550	0.25	87	10.63	Feeder
415020.155780	7077757.447070	0.30	87	11.15	Feeder
415020.167377	7077757.449990	0.27	90	11.60	Feeder
415020.478230	7077758.082920	0.22	88	12.98	Feeder
415020.692656	7077758.120760	0.11	88	13.50	Feeder
415020.740567	7077758.168690	0.11	83	13.86	Feeder
415020.672273	7077758.253630	0.12	83	14.41	Feeder
415020.639270	7077758.297467	0.00	83	15.77	Feeder
415048.449763	7077740.219170	0.00	90	5.52	Arrested 1
415048.673821	7077740.367328	0.04	90	6.25	Arrested 1
415048.833188	7077740.553040	0.11	90	6.86	Arrested 1
415049.008525	7077740.660680	0.12	90	7.43	Arrested 1
415049.343361	7077740.989390	0.12	90	7.89	Arrested 1
415049.322604	7077741.003980	0.13	90	8.27	Arrested 1
415049.714212	7077741.156840	0.15	85	8.55	Arrested 1
415049.937050	7077741.355980	0.14	90	9.06	Arrested 1

415050.047654	7077741.499370	0.16	90	9.45	Arrested 1
415050.094253	7077741.591270	0.13	90	9.99	Arrested 1
415050.353001	7077741.890280	0.11	90	10.59	Arrested 1
415050.498133	7077742.051790	0.16	90	11.27	Arrested 1
415050.766213	7077742.365210	0.08	90	11.67	Arrested 1
415051.516914	7077742.872540	0.07	83	12.23	Arrested 1
415051.737969	7077743.110550	0.07	78	12.67	Arrested 1
415051.916388	7077743.317829	0.00	70	13.36	Arrested 1
415046.949517	7077737.195680	0.32	85	4.22	Arrested 2
415047.190224	7077739.124890	0.26	90	4.99	Arrested 2
415047.275141	7077739.443590	0.23	90	5.29	Arrested 2
415047.504526	7077740.028290	0.30	90	5.75	Arrested 2
415047.863627	7077740.840600	0.25	80	6.49	Arrested 2
415047.996433	7077749.972627	0.00	80	6.80	Arrested 2

Appendix 4

Data from the literature regarding graben geometry

Table A4.1. Length, width, and vertical offset values of dike-induced grabens reported in the literature (references are presented in the main text, Section 7.2). SSR = slow spreading ridges; ISR = intermediate spreading ridges; FSR = fast spreading ridges; VE = volcanic edifices.

Event	Geodynamic setting	Length (m)	Width (m)	V. Offset (m)
Laki (1783)	SSR	5500	300.00	3.00
Sveinagja (1875)	SSR	34000	2500.00	5.50
Kelduhverfi (1978)	SSR	6400	6000.00	1.50
Namafjall (1977-1980)	SSR		5000.00	1.45
Hituholar (1975-1984)	SSR		21.25	2.75
Asal - Ghoubbet (1978-1979)	SSR	8000	2000.00	0.70
Dabbahu (2005)	SSR		2500.00	2.50
Natron (2007)	SSR		2500.00	0.35
Harrat Lunayyir (2009)	SSR	8000	6500.00	0.80
Bardarbunga (2014)	SSR	5000	850.00	6.00
Cleft System - Juan de Fuca Ridge (1983-1987)	ISR	1000	100.00	7.50
Cleft System - Juan de Fuca Ridge (1983-1987)	ISR		50.00	2.50
Cleft System - Juan de Fuca Ridge (1983-1987)	ISR	800	50.00	5.00
Cleft System - Juan de Fuca Ridge (1983-1987)	ISR	15000	45.00	20.00
Co-Axial segment - Juan de Fuca Ridge (1993)	ISR	200	15.00	10.00
Co-Axial segment - Juan de Fuca Ridge (1993)	ISR		45.00	2.00
Co-Axial segment - Juan de Fuca Ridge (1993)	ISR	600	40.00	10.00
Co-Axial segment - Juan de Fuca Ridge (1993)	ISR		15.00	12.50
East Pacific Rise (2005-2006)	FSR		75.00	3.50
East Pacific Rise (2005-2006)	FSR		225.00	14.00
Inyo Craters (650-550 yr BP)	VE	2500	600.00	
Kilauea (1981)	VE		2000.00	0.90
Mt. Etna (1983)	VE		200.00	1.40
Mt. Etna (1983)	VE		1000.00	0.85
Mt. Etna (2001)	VE	1400	500.00	1.00
Mt. Etna (2001)	VE	450	40.00	1.00
Mt. Etna (2008)	VE	2450	500.00	0.20
Mt Etna (2013)	VE	600	120.00	1.00
Mt. Etna (1928)	VE	780	385.00	2.40
Mt. Etna (1928)	VE	430	68.00	1.10
Mt. Etna (1971)	VE	2500	85.00	2.50
Cumbre Vieja (2021)	VE	170	50.00	2.45

Table A4.2. Depth of the dike tip and width of dike-induced grabens reported in the literature (references are indicated in the specific column). Information about how the depth of the dike was derived has been added.

Event	Tip Depth (m)	Graben Width (m)	How was tip depth derived?	Reference
Laki (1783)	400	300	Estimated using trigonometry	Trippanera et al., 2015a
Kelduhverfi (1978)	1500	6000	Inversion of geodetic data	Rubin, 1992
Namafjall (1977-1980)	1250	5000	Inversion of geodetic data	Rubin, 1992
Asal - Ghoubbet (1978-1979)	4500	2000	Inversion of geodetic and seismic data	Stein et al., 1991
Dabbahu (2005)	2000	2500	Inversion of InSAR and seismic data	Wright et al., 2006
Natron (2007)	2000	2500	Inversion of InSAR and seismic data	Calais et al., 2008
Harrat Lunayyir (2009)	2000	6500	Inversion of InSAR and seismic data	Pallister et al., 2010
Bardarbunga (2014)	300	850	Assumed from graben geometry	Hjartardóttir et al., 2016
Inyo Craters (650-550 yr BP)	250	600	Numerical models	Mastin and Pollard, 1988
Kilauea (1981)	250	2000	Numerical models	Pollard et al., 1983
Mt Etna (1983)	80	200	Inversion of geodetic data	Murray and Pullen, 1984
Mt Etna (1983)	475	1000	Inversion of geodetic data	Murray and Pullen, 1984
Mt Etna (2001)	500	500	Assumed from graben geometry	Acocella and Neri, 2003
Mt Etna (2008)	800	500	Assumed from graben geometry	Bonaccorso et al., 2011

Bibliography

Abdallah, A., Courtillot, V., Kasser, M., Le Dain, A. Y., Lépine, J. C., Robineau, B., Ruegg, J. C., Tapponnier, P., & Tarantola, A. (1979). Relevance of Afar seismicity and volcanism to the mechanics of accreting plate boundaries. Nature, 282(5734), 17-23.

Abdelmalak, M. M., Mourgues, R., Galland, O., & Bureau, D. (2012). Fracture mode analysis and related surface deformation during dyke intrusion: Results from 2D experimental modelling. Earth and Planetary Science Letters, 359, 93-105.

Acocella, V. (2021). Volcano-tectonic processes (Vol. 567). Switzerland: Springer.

Acocella, V., & Neri, M. (2003). What makes flank eruptions? The 2001 Etna eruption and its possible triggering mechanisms. Bulletin of Volcanology, 65, 517-529.

Acocella, V., & Tibaldi, A. (2005). Dike propagation driven by volcano collapse: a general model tested at Stromboli, Italy. Geophysical Research Letters, 32(8).

Acocella, V., & Neri, M. (2009). Dike propagation in volcanic edifices: overview and possible developments. Tectonophysics, 471(1-2), 67-77.

Acocella, V., & Trippanera, D. (2016). How diking affects the tectonomagmatic evolution of slow spreading plate boundaries: Overview and model. Geosphere, 12(3), 867-883.

Acocella, V., Behncke, B., Neri, M., & D'Amico, S. (2003a). Link between major flank slip and 2002–2003 eruption at Mt. Etna (Italy). Geophysical Research Letters, 30(24).

Acocella, V., Korme, T., & Salvini, F. (2003b). Formation of normal faults along the axial zone of the Ethiopian Rift. Journal of structural Geology, 25(4), 503-513.

Acocella, V., Porreca, M., Neri, M., Mattei, M., & Funiciello, R. (2006). Fissure eruptions at Mount Vesuvius (Italy): insights on the shallow propagation of dikes at volcanoes. Geology, 34(8), 673-676.

Acocella, V., Neri, M., & Sulpizio, R. (2009). Dike propagation within active central volcanic edifices: constraints from Somma-Vesuvius, Etna and analogue models. Bulletin of volcanology, 71, 219-223.

Agisoft LLC. (2018). PhotoScan user manual, professional edition. http://www.agisoft.com/pdf/photoscan-pro_1_4_en.pdf, version 1.4.

Aguilar, M. A., Aguilar, F. J., Fernández, I., & Mills, J. P. (2013). Accuracy assessment of commercial self-calibrating bundle adjustment routines applied to archival aerial photography. The Photogrammetric Record, 28(141), 96-114.

Ágústsdóttir, T., Woods, J., Greenfield, T., Green, R. G., White, R. S., Winder, T., Brandsdóttir, B., Steinthórsson, S., & Soosalu, H. (2016). Strike-slip faulting during the 2014 Bárðarbunga-Holuhraun dike intrusion, central Iceland. Geophysical Research Letters, 43(4), 1495-1503.

Al Shehri, A., & Gudmundsson, A. (2018). Modelling of surface stresses and fracturing during dyke emplacement: Application to the 2009 episode at Harrat Lunayyir, Saudi Arabia. Journal of Volcanology and Geothermal Research, 356, 278-303.

Amadei, B., & Stephansson, O. (1997). Rock stress and its measurement. Springer Science & Business Media.

Anderson, E. M. (1905). The dynamics of faulting. Transactions of the Edinburgh Geological Society, 8(3), 387-402.

Anderson, E. M. (1951). Dynamics of faulting and dyke formation with applications to Britain, 2nd edn. Olivier and Boyd, Edinburgh.

Andrew, R. E., & Gudmundsson, A. (2008). Volcanoes as elastic inclusions: their effects on the propagation of dykes, volcanic fissures, and volcanic zones in Iceland. Journal of Volcanology and Geothermal Research, 177(4), 1045-1054.

Andrew, R. E. B., Gudmundsson, A., & Letourneur, L. (2008). Mechanical interaction between the fissure and graben of the 1783 Skaftareldar Eruption and the hyaloclastite Laki Mountain.

Antoniou, V., Nomikou, P., Pavlina, B., Pantelia, S., Bonali, F. L., Lemonia, R., & Andreas, M. (2019, May). The story map for Metaxa mine (Santorini, Greece): A unique site where history and volcanology meet each other. In Proceedings of the 5th International Conference on

Geographical Information Systems Theory, Applications and Management (GISTAM 2019), Heraklion, Crete, Greece (pp. 3-5).

Aoki, Y., Segall, P., Kato, T., Cervelli, P., & Shimada, S. (1999). Imaging magma transport during the 1997 seismic swarm off the Izu Peninsula, Japan. Science, 286(5441), 927-930.

Apuani, T., Corazzato, C., Cancelli, A., & Tibaldi, A. (2005). Physical and mechanical properties of rock masses at Stromboli: a dataset for volcano instability evaluation. Bulletin of Engineering Geology and the Environment, 64, 419-431.

Azzaro, R., Branca, S., Gwinner, K., & Coltelli, M. (2012). The volcano-tectonic map of Etna volcano, 1: 100.000 scale: an integrated approach based on a morphotectonic analysis from high-resolution DEM constrained by geologic, active faulting and seismotectonic data. Italian journal of geosciences, 131(1), 153-170.

Babiker, M., & Gudmundsson, A. (2004). The effects of dykes and faults on groundwater flow in an arid land: the Red Sea Hills, Sudan. Journal of Hydrology, 297(1-4), 256-273.

Bakker, M., & Lane, S. N. (2017). Archival photogrammetric analysis of river–floodplain systems using Structure from Motion (SfM) methods. Earth Surface Processes and Landforms, 42(8), 1274-1286.

Barnett, Z. A., & Gudmundsson, A. (2014). Numerical modelling of dykes deflected into sills to form a magma chamber. Journal of Volcanology and Geothermal Research, 281, 1-11.

Barreca, G., Branca, S., & Monaco, C. (2018). Three-dimensional modeling of mount Etna Volcano: Volume Assessment, trend of eruption rates, and geodynamic significance. Tectonics, 37(3), 842-857.

Barsotti, S., Parks, M. M., Pfeffer, M. A., Óladóttir, B. A., Barnie, T., Titos, M. M., Jónsdóttir, K., Pedersen, G. B. M., Hjartardóttir, Á. R., Stefansdóttir, G., Johannsson, T., Arason, Þ., Gudmundsson, M. T., Oddsson, B., Þrastarson, R. H., Ófeigsson, B. G., Vogfjörd, K., Geirsson, H., Hjörvar, T., von Löwis, S., Petersen, N., & Sigurðsson, E. M. (2023). The eruption in Fagradalsfjall (2021, Iceland): how the operational monitoring and the volcanic hazard assessment contributed to its safe access. Natural Hazards, 1-30.

Battaglia, M., Di Bari, M., Acocella, V., & Neri, M. (2011). Dike emplacement and flank instability at Mount Etna: constraints from a poro-elastic-model of flank collapse. Journal of volcanology and geothermal research, 199(1-2), 153-164.

Bazargan, M., & Gudmundsson, A. (2019). Dike-induced stresses and displacements in layered volcanic zones. Journal of Volcanology and Geothermal Research, 384, 189-205.

Bazargan, M., & Gudmundsson, A. (2020). Stresses and displacements in layered rocks induced by inclined (cone) sheets. Journal of Volcanology and Geothermal Research, 401, 106965.

Becerril, L., Galindo, I., Gudmundsson, A., & Morales, J. M. (2013). Depth of origin of magma in eruptions. Scientific reports, 3(1), 1-6.

Benassi, F., Dall'Asta, E., Diotri, F., Forlani, G., Morra di Cella, U., Roncella, R., & Santise, M. (2017). Testing accuracy and repeatability of UAV blocks oriented with GNSS-supported aerial triangulation. Remote Sensing, 9(2), 172.

Biggs, J., Amelung, F., Gourmelen, N., Dixon, T. H., & Kim, S. W. (2009). InSAR observations of 2007 Tanzania rifting episode reveal mixed fault and dyke extension in an immature continental rift. Geophysical Journal International, 179(1), 549-558.

Billi, A., Acocella, V., Funiciello, R., Giordano, G., Lanzafame, G., & Neri, M. (2003). Mechanisms for ground-surface fracturing and incipient slope failure associated with the 2001 eruption of Mt. Etna, Italy: analysis of ephemeral field data. Journal of Volcanology and Geothermal Research, 122(3-4), 281-294.

Blaser, L., Krüger, F., Ohrnberger, M., & Scherbaum, F. (2010). Scaling relations of earthquake source parameter estimates with special focus on subduction environment. Bulletin of the Seismological Society of America, 100(6), 2914-2926.

Bonaccorso, A., Bonforte, A., Calvari, S., Del Negro, C., Di Grazia, G., Ganci, G., Neri, M., Vicari, A. & Boschi, E. (2011). The initial phases of the 2008–2009 Mount Etna eruption: A multidisciplinary approach for hazard assessment. Journal of Geophysical Research: Solid Earth, 116(B3).

Bonali, F. L., Tibaldi, A., Marchese, F., Fallati, L., Russo, E., Corselli, C., & Savini, A. (2019). UAV-based surveying in volcano-tectonics: An example from the Iceland rift. Journal of Structural Geology, 121, 46-64.

Bonali, F. L., Tibaldi, A., Corti, N., Fallati, L., & Russo, E. (2020). Reconstruction of Late Pleistocene-Holocene Deformation through Massive Data Collection at Krafla Rift (NE Iceland) Owing to Drone-Based Structure-from-Motion Photogrammetry. Applied Sciences, 10(19), 6759.

Bonali, F. L., Corti, N., Russo, E., Marchese, F., Fallati, L., Pasquaré Mariotto, F., & Tibaldi, A. (2021a). Commercial-UAV-based Structure from Motion for geological and geohazard studies. In Building knowledge for geohazard assessment and management in the Caucasus and other orogenic regions (pp. 389-427). Springer Netherlands.

Bonali, F. L., Russo, E., Vitello, F., Antoniou, V., Marchese, F., Fallati, L., Bracchi, V., Corti, N., Savini, A., Whitworth, M., Drymoni, K., Pasquaré Mariotto, F., Nomikou, P., Sciacca, E., Bressan, S., Falsaperla, S., Reitano, D., van Wyk de Vries, B., Krokos, M., Panieri, G., Stiller-Reeve, M. A., Vizzari, G., Becciani, U., & Tibaldi, A. (2021b). How academics and the public experienced immersive virtual reality for geo-education. Geosciences, 12(1), 9.

Bonali, F. L., Corti, N., Pasquaré Mariotto, F., De Beni, E., Bressan, S., Cantarero, M., Russo, E., Neri, M., & Tibaldi, A. (submitted). 3D study of dyke-induced asymmetric graben: the 1971 Mt. Etna (Italy) case by structural data and numerical modelling. Journal of Structural Geology.

Bonforte, A., Gambino, S., Guglielmino, F., Obrizzo, F., Palano, M., & Puglisi, G. (2007). Ground deformation modeling of flank dynamics prior to the 2002 eruption of Mt. Etna. Bulletin of Volcanology, 69, 757-768.

Bonforte, A., Guglielmino, F., & Puglisi, G. (2013). Interaction between magma intrusion and flank dynamics at Mt. Etna in 2008, imaged by integrated dense GPS and DInSAR data. Geochemistry, Geophysics, Geosystems, 14(8), 2818-2835.

Borgia, A., Ferrari, L., & Pasquaré, G. (1992). Importance of gravitational spreading in the tectonic and volcanic evolution of Mount Etna. Nature, 357(6375), 231-235.

Branca, S., Coltelli, M., Groppelli, G., Lentini, F. (2011a). Geological Map Of Etna Volcano, 1:50,000 Scale. Italian Journal of Geosciences, 130 (3), 265–291. https://doi.org/10.3301/IJG.2011.15.

Branca, S., Coltelli, M., & Groppelli, G. (2011b). Geological evolution of a complex basaltic stratovolcano: Mount Etna, Italy. Italian Journal of Geosciences, 130(3), 306-317.

Branca, S., De Beni, E., Chester, D., Duncan, A., & Lotteri, A. (2017). The 1928 eruption of Mount Etna (Italy): Reconstructing lava flow evolution and the destruction and recovery of the town of Mascali. Journal of Volcanology and Geothermal Research, 335, 54-70.

Branca, S., Musumeci, D., & Ingaliso, L. (2021). The significance of the 1971 flank eruption of Etna from volcanological and historic viewpoints. Annals of Geophysics.

Brandsdóttir, B., Menke, W., Einarsson, P., White, R. S., & Staples, R. K. (1997). Färoe-Iceland ridge experiment 2. Crustal structure of the Krafla central volcano. Journal of Geophysical Research: Solid Earth, 102(B4), 7867-7886.

Browning, J., & Gudmundsson, A. (2015). Caldera faults capture and deflect inclined sheets: an alternative mechanism of ring dike formation. Bulletin of Volcanology, 77, 1-13.

Browning, J., Karaoğlu, Ö. Z. G. Ü. R., Bayer, Ö., Turgay, M. B., & Acocella, V. (2021). Stress fields around magma chambers influenced by elastic thermo-mechanical deformation: implications for forecasting chamber failure. Bulletin of Volcanology, 83, 1-13.

Burns, J. H. R., & Delparte, D. (2017). Comparison of commercial structure-from-motion photogrammety software used for underwater three-dimensional modeling of coral reef environments. The International Archives of Photogrammetry, Remote Sensing and Spatial Information Sciences, 42, 127.

Calais, E., d'Oreye, N., Albaric, J., Deschamps, A., Delvaux, D., Déverchere, J., Ebinger, C., Ferdinand, R. W., Kervyn, F., Macheyeki, A. S., Oyen, A., Perrot, J., Saria, E., Smets, B., Stamps, D. S., & Wauthier, C. (2008). Strain accommodation by slow slip and dyking in a youthful continental rift, East Africa. Nature, 456(7223), 783-787.

Calvari, S., Tanner, L.H., Groppelli, G., & Norini, G. (2004). Valle del Bove, eastern flank of Etna volcano: a comprehensive model for the opening of the depression and implications for future hazards Etna Volcano Laboratory, American Geophysical Union (2004).

Calvari S., Billotta, G., Bonaccorso, A., Caltabiano, T., Cappello, A., Corradino, C., Del Negro, C., Ganci, G., Neri, M., Pecora, E., Salerno, G., & Spampinato, L. (2020). The VEI 2 Christmas 2018 Etna Eruption: A Small But Intense Eruptive Event or the Starting Phase of a Larger One? Remote Sensing, 12(6), 905.

Cappello, A., Neri, M., Acocella, V., Gallo, G., Vicari, A., & Del Negro, C. (2012). Spatial vent opening probability map of Etna volcano (Sicily, Italy). Bulletin of Volcanology, 74, 2083-2094.

Carbotte, S. M., Detrick, R. S., Harding, A., Canales, J. P., Babcock, J., Kent, G., Van Ark, E., Nedimovic, M., & Diebold, J. (2006). Rift topography linked to magmatism at the intermediate spreading Juan de Fuca Ridge. Geology, 34(3), 209-212.

Carnemolla, F., De Guidi, G., Bonforte, A., Brighenti, F., & Briole, P. (2023). The ground deformation of the south-eastern flank of Mount Etna monitored by GNSS and SAR interferometry from 2016 to 2019. Geophysical Journal International, 234(1), 664-682.

Carvalho, R. C., Kennedy, D. M., Niyazi, Y., Leach, C., Konlechner, T. M., & Ierodiaconou, D. (2020). Structure-from-motion photogrammetry analysis of historical aerial photography: Determining beach volumetric change over decadal scales. Earth Surface Processes and Landforms, 45(11), 2540-2555.

Chadwick Jr, W. W., & Embley, R. W. (1998). Graben formation associated with recent dike intrusions and volcanic eruptions on the mid-ocean ridge. Journal of Geophysical Research: Solid Earth, 103(B5), 9807-9825.

Chandler, J. H., & Buckley, S. (2016). Structure from motion (SFM) photogrammetry vs terrestrial laser scanning.

Charlez, P. A. (1997). Rock Mechanics. Volume 2. Petroleum Applications.

Choi, D. H., Dailey-Hebert, A., & Estes, J. S. (Eds.) (2016). Emerging tools and applications of virtual reality in education. Hershey, PA, USA: Information Science Reference.

Clifton, A. E., & Schlische, R. W. (2003). Fracture populations on the Reykjanes Peninsula, Iceland: Comparison with experimental clay models of oblique rifting. Journal of Geophysical Research: Solid Earth, 108(B2).

Clifton, A. E., & Kattenhorn, S. A. (2006). Structural architecture of a highly oblique divergent plate boundary segment. Tectonophysics, 419(1-4), 27-40.

Clunes, M., Browning, J., Marquardt, C., Cortez, J., Drymoni, K., & Kavanagh, J. (2023). Inclination and heterogeneity of layered geological sequences influence dike-induced ground deformation. Geology, 51(3), 278-283.

Cocina, O., Neri, G., Privitera, E., & Spampinato, S. (1997). Stress tensor computations in the Mount Etna area (Southern Italy) and tectonic implications. Journal of Geodynamics, 23(2), 109-127.

Cocina, O., Neri, G., Privitera, E., & Spampinato, S. (1998). Seismogenic stress field beneath Mt. Etna (South Italy) and possible relationships with volcano-tectonic features. Journal of volcanology and geothermal research, 83(3-4), 335-348.

Cook, K. L. (2017). An evaluation of the effectiveness of low-cost UAVs and structure from motion for geomorphic change detection. Geomorphology, 278, 195-208.

Corti, N., Bonali, F. L., Pasquaré Mariotto, F., Tibaldi, A., Russo, E., Hjartardóttir, Á. R., Einarsson, P., Rigoni, V., & Bressan, S. (2021). Fracture Kinematics and Holocene Stress Field at the Krafla Rift, Northern Iceland. Geosciences, 11(2), 101.

Corti, N., Bonali, F. L., Russo, E., Drymoni, K., Pasquaré Mariotto, F., Gudmundsson, A., Esposito, R., Cavallo, A., & Tibaldi, A. (2023). Feeders vs arrested dikes: A case study from the Younger Stampar eruption in Iceland. Journal of Volcanology and Geothermal Research, 107914.

Curewitz, D., & Karson, J. A. (1998). Geological consequences of dike intrusion at mid-ocean ridge spreading centers. GEOPHYSICAL MONOGRAPH-AMERICAN GEOPHYSICAL UNION, 106, 117-136.

Darmawan, H., Walter, T. R., Brotopuspito, K. S., & Nandaka, I. G. M. A. (2018). Morphological and structural changes at the Merapi lava dome monitored in 2012–15 using unmanned aerial vehicles (UAVs). Journal of Volcanology and Geothermal Research, 349, 256-267.

De Beni, E., Cantarero, M., & Messina, A. (2019). UAVs for volcano monitoring: A new approach applied on an active lava flow on Mt. Etna (Italy), during the 27 February–02 March 2017 eruption. Journal of Volcanology and Geothermal Research, 369, 250-262.

De Guidi, G., Brighenti, F., Carnemolla, F., Imposa, S., Marchese, S. A., Palano, M., Scudero, S., & Vecchio, A. (2018). The unstable eastern flank of Mt. Etna volcano (Italy): First results of a GNSS-based network at its southeastern edge. Journal of Volcanology and Geothermal Research, 357, 418-424.

Delaney, P. T., Pollard, D. D., Ziony, J. I., & McKee, E. H. (1986). Field relations between dikes and joints: Emplacement processes and paleostress analysis. Journal of Geophysical Research: Solid Earth, 91(B5), 4920-4938.

DeMets, C., Gordon, R. G., Argus, D. F., & Stein, S. (1994). Effect of recent revisions to the geomagnetic reversal time scale on estimates of current plate motions. Geophysical research letters, 21(20), 2191-2194.

DeMets, C., Gordon, R. G., & Argus, D. F. (2010). Geologically current plate motions. Geophysical journal international, 181(1), 1-80.

De Novellis, V., Atzori, S., De Luca, C., Manzo, M., Valerio, E., Bonano, M., Cardaci, C., Castaldo, R., Di Bucci, D., Manunta, M., Onorato, G., Pepe, S., Solaro, G., Tizzani, P., Zinno, I., Neri, M., Lanari, R., & Casu, F. (2019). DInSAR analysis and analytical modeling of Mount Etna displacements: The December 2018 volcano-tectonic crisis. Geophysical Research Letters, 46(11), 5817-5827.

Drymoni, K. (2020). Dyke propagation paths: the movement of magma from the source to the surface (Doctoral dissertation, Royal Holloway, University of London).

Drymoni, K., Browning, J., & Gudmundsson, A. (2020). Dyke-arrest scenarios in extensional regimes: Insights from field observations and numerical models, Santorini, Greece. Journal of Volcanology and Geothermal Research, 396, 106854.

Drymoni, K., Browning, J., & Gudmundsson, A. (2021). Volcanotectonic interactions between inclined sheets, dykes, and faults at the Santorini Volcano, Greece. Journal of Volcanology and Geothermal Research, 416, 107294.

Drymoni, K., Russo, E., Tibaldi, A., Corti, N., Bonali, F. L., & Mariotto, F. P. (2023). Dyke-induced graben formation in a heterogeneous succession on Mt. Etna: Insights from field observations and FEM numerical models. Journal of Volcanology and Geothermal Research, 433, 107712.

Ducrocq, C., Geirsson, H., Árnadóttir, T., Juncu, D., Drouin, V., Gunnarsson, G., Kristjánsson, B. R., Sigmundsson, F., Hreinsdóttir, S., Tómasdóttir, S., & Blanck, H. (2021). Inflation-deflation episodes in the Hengill and Hrómundartindur volcanic complexes, SW Iceland. Frontiers in Earth Science, 9, 725109.

Duffield, W. A., Christiansen, R. L., Koyanagi, R. Y., & Peterson, D. W. (1982). Storage, migration, and eruption of magma at Kilauea volcano, Hawaii, 1971–1972. Journal of Volcanology and Geothermal Research, 13(3-4), 273-307.

Duncan, A. M., Dibben, C., Chester, D. K., & Guest, J. E. (1996). The 1928 eruption of Mount Etna Volcano, Sicily, and the destruction of the town of Mascali. Disasters, 20(1), 1-20.

Dundurs, J. (1969). Edge-bonded dissimilar orthogonal elastic wedges under normal and shear loading. J. Appl. Mech., 35, 460–466.

Dzurisin, D. (2006). Volcano deformation: new geodetic monitoring techniques. Springer Science & Business Media.

Ebinger, C. J., Keir, D., Ayele, A., Calais, E., Wright, T. J., Belachew, M., Hammond, J. O. S., Campbell, E., & Buck, W. R. (2008). Capturing magma intrusion and faulting processes during continental rupture: seismicity of the Dabbahu (Afar) rift. Geophysical Journal International, 174(3), 1138-1152.

Ebinger, C., Ayele, A., Keir, D., Rowland, J., Yirgu, G., Wright, T., Belachew, M., & Hamling, I. (2010). Length and timescales of rift faulting and magma intrusion: The Afar rifting cycle from 2005 to present. Annual Review of Earth and Planetary Sciences, 38, 439-466.

Einarsson, P. (1991). Earthquakes and present-day tectonism in Iceland. Tectonophysics, 189(1-4), 261-279.

Einarsson, P. (2008). Plate boundaries, rifts and transforms in Iceland. Jökull, 58(12), 35-58.

Einarsson, P., & Sæmundsson, K. (1987). Earthquake epicenters 1982–1985 and volcanic systems in Iceland. In: Sigfússon, Þ.I. (Ed.), Í hlutarins eðli, Festschrift for Þorbjörn Sigurgeirsson. Menningarsjóður, Reykjavík (map).

Fallati, L., Saponari, L., Savini, A., Marchese, F., Corselli, C., and Galli, P. (2020). Multi-Temporal UAV Data and Object-Based Image Analysis (OBIA) for Estimation of Substrate Changes in a Post-Bleaching Scenario on a Maldivian Reef, Remote Sens., 12, 2093.

Falsaperla, S., & Neri, M. (2015). Seismic footprints of shallow dyke propagation at Etna, Italy. Scientific Reports, 5(1), 1-9.

Favalli, M., Fornaciai, A., Nannipieri, L., Harris, A., Calvari, S., & Lormand, C. (2018). UAV-based remote sensing surveys of lava flow fields: a case study from Etna's 1974 channel-fed lava flows. Bulletin of Volcanology, 80, 1-18.

Ferrari, L., Garduno, V. H., & Neri, M. (1991). I dicchi della Valle del Bove, Etna: un metodo per stimare le dilatazioni di un apparato vulcanico. Memorie della Società Geologica Italiana, 47, 495-508.

Fischer, T., Hrubcová, P., Salama, A., Doubravová, J., Ágústsdóttir, T., Gudnason, E. Á., Horálek, J., & Hersir, G. P. (2022). Swarm seismicity illuminates stress transfer prior to the 2021 Fagradalsfjall eruption in Iceland. Earth and Planetary Science Letters, 594, 117685.

Flóvenz, Ó. G., Wang, R., Hersir, G. P., Dahm, T., Hainzl, S., Vassileva, M., Drouin, V., Heimann, S., Isken, M. P., Gudnason, E. Á., Ágústsson, K., Ágústsdóttir, T., Horálek, J., Motagh, M., Walter, T. R., Rivalta, E., Jousset, P., Krawczyk, C. M., & Milkereit, C. (2022). Cyclical

geothermal unrest as a precursor to Iceland's 2021 Fagradalsfjall eruption. Nature Geoscience, 15(5), 397-404.

Folch, A., & Martı, J. (2004). Geometrical and mechanical constraints on the formation of ring-fault calderas. Earth and Planetary Science Letters, 221(1-4), 215-225.

Forslund, T., & Gudmundsson, A. (1991). Crustal spreading due to dikes and faults in southwest Iceland. Journal of Structural Geology, 13(4), 443-457.

Forslund, T., & Gudmundsson, A. (1992). Structure of Tertiary and Pleistocene normal faults in Iceland. Tectonics, 11(1), 57-68.

Fossen, H. (2016). Structural geology. Cambridge university press.

Friedlander, I. (1929). Vulkanische ereignisse. Der Atna-Ausbruch 1928. Zeitschrift fur Vulkanologie, Band XII.

Gaffney, E. S., Damjanac, B., & Valentine, G. A. (2007). Localization of volcanic activity: 2. Effects of pre-existing structure. Earth and Planetary Science Letters, 263(3-4), 323-338.

Gambino, S., Barreca, G., Bruno, V., De Guidi, G., Ferlito, C., Gross, F., Mattia, M., Scarfi. L., & Monaco, C. (2022). Transtension at the Northern Termination of the Alfeo-Etna Fault System (Western Ionian Sea, Italy): Seismotectonic Implications and Relation with Mt. Etna Volcanism. Geosciences, 12(3), 128.

Gerloni, I. G., Carchiolo, V., Vitello, F. R., Sciacca, E., Becciani, U., Costa, A., Riggi, S., Bonali, F. L., Russo, E., Fallati, L., Marchese, F., & Tibaldi, A. (2018, September). Immersive virtual reality for earth sciences. In 2018 Federated Conference on Computer Science and Information Systems (FedCSIS) (pp. 527-534). IEEE.

Geshi, N., Kusumoto, S., & Gudmundsson, A. (2012). Effects of mechanical layering of host rocks on dike growth and arrest. Journal of Volcanology and Geothermal Research, 223, 74-82.

Geyer, A., & Gottsmann, J. (2010). The influence of mechanical stiffness on caldera deformation and implications for the 1971–1984 Rabaul uplift (Papua New Guinea). Tectonophysics, 483(3-4), 399-412.

Gomez, C., Hayakawa, Y., & Obanawa, H. (2015). A study of Japanese landscapes using structure from motion derived DSMs and DEMs based on historical aerial photographs: New opportunities for vegetation monitoring and diachronic geomorphology. Geomorphology, 242, 11-20.

Grandin, R., Socquet, A., Binet, R., Klinger, Y., Jacques, E., De Chabalier, J. B., King, G. C. P., Lasserre, C., Tait, S., Tapponnier, P., Delorme, A., & Pinzuti, P. (2009). September 2005 Manda Hararo-Dabbahu rifting event, Afar (Ethiopia): constraints provided by geodetic data. Journal of Geophysical Research: Solid Earth, 114(B8).

Granshaw, F. D., & Duggan-Haas, D. (2012). Virtual fieldwork in geoscience teacher education: Issues, techniques, and models. Geological society of America special papers, 492, 285-303.

Grant, J. V., & Kattenhorn, S. A. (2004). Evolution of vertical faults at an extensional plate boundary, southwest Iceland. Journal of Structural Geology, 26(3), 537-557.

Graue, B., Siegesmund, S., & Middendorf, B. (2011). Quality assessment of replacement stones for the Cologne Cathedral: mineralogical and petrophysical requirements. Environmental Earth Sciences, 63, 1799-1822.

Gretener, P. E. (1969). On the mechanics of the intrusion of sills. Canadian Journal of Earth Sciences, 6(6), 1415-1419.

Groppelli, G., & Tibaldi, A. (1999). Control of rock rheology on deformation style and slip-rate along the active Pernicana Fault, Mt. Etna, Italy. Tectonophysics, 305(4), 521-537.

Grottoli, E., Biausque, M., Rogers, D., Jackson, D. W., & Cooper, J. A. G. (2020). Structure-from-motion-derived digital surface models from historical aerial photographs: A new 3D application for coastal dune monitoring. Remote Sensing, 13(1), 95.

Gudmundsson, A. (1984). Formation of dykes, feeder-dykes, and the intrusion of dykes from magma chambers. Bulletin Volcanologique, 47(3), 537-550.

Gudmundsson, A. (1986a). Formation of crystal magma chambers in Iceland. Geology, 14(2), 164-166.

Gudmundsson, A. (1986b). Mechanical aspects of postglacial volcanism and tectonics of the Reykjanes Peninsula, southwest Iceland. Journal of Geophysical Research: Solid Earth, 91(B12), 12711-12721.

Gudmundsson, A. (1987). Geometry, formation and development of tectonic fractures on the Reykjanes Peninsula, southwest Iceland. Tectonophysics, 139(3-4), 295-308.

Gudmundsson, A. (1998). Formation and development of normal-fault calderas and the initiation of large explosive eruptions. Bulletin of Volcanology, 60, 160-170.

Gudmundsson, A. (2000). Dynamics of volcanic systems in Iceland: example of tectonism and volcanism at juxtaposed hot spot and mid-ocean ridge systems. Annual Review of Earth and Planetary Sciences, 28(1), 107-140.

Gudmundsson, A. (2003). Surface stresses associated with arrested dykes in rift zones. Bulletin of Volcanology, 65(8), 606-619.

Gudmundsson, A. (2006). How local stresses control magma-chamber ruptures, dyke injections, and eruptions in composite volcanoes. Earth-science reviews, 79(1-2), 1-31.

Gudmundsson, A. (2011a). Rock fractures in geological processes. Cambridge University Press.

Gudmundsson, A. (2011b). Deflection of dykes into sills at discontinuities and magma-chamber formation. Tectonophysics, 500(1-4), 50-64.

Gudmundsson, A. (2012). Magma chambers: Formation, local stresses, excess pressures, and compartments. Journal of Volcanology and Geothermal Research, 237, 19-41.

Gudmundsson, A. (2017). The Glorious Geology of Iceland's Golden Circle.

Gudmundsson, A. (2020). Volcanotectonics: Understanding the structure, deformation and dynamics of volcanoes. Cambridge University Press.

Gudmundsson, A., & Bäckström, K. (1991). Structure and development of the Sveinagja graben, Northeast Iceland. Tectonophysics, 200(1-3), 111-125.

Gudmundsson, A., & Marinoni, L. B. (1999). Geometry, emplacement, and arrest of dykes. In Annales Tectonicae (Vol. 13, No. 1/2, pp. 71-92). EDITRICE SEDICESIMO.

Gudmundsson, A., & Brenner, S. L. (2001). How hydrofractures become arrested. Terra Nova, 13(6), 456-462.

Gudmundsson, A., & Brenner, S. L. (2004). Local stresses, dyke arrest and surface deformation in volcanic edifices and rift zones. Annals of Geophysics, 47(4), 1433-1454.

Gudmundsson, A., & Philipp, S. L. (2006). How local stress fields prevent volcanic eruptions. Journal of Volcanology and Geothermal research, 158(3-4), 257-268.

Gudmundsson, A., Marinoni, L. B., & Marti, J. (1999). Injection and arrest of dykes: implications for volcanic hazards. Journal of Volcanology and Geothermal Research, 88(1-2), 1-13.

Gudmundsson, A., Friese, N., Galindo, I., & Philipp, S. L. (2008). Dike-induced reverse faulting in a graben. Geology, 36(2), 123-126.

Guldstrand, F., Burchardt, S., Hallot, E., & Galland, O. (2017). Dynamics of surface deformation induced by dikes and cone sheets in a cohesive Coulomb brittle crust. Journal of Geophysical Research: Solid Earth, 122(10), 8511-8524.

Gwinner, K., Coltelli, M., Flohrer, J., Jaumann, R., Matz, K. D., Marsella, M., Roatsch, T., Scholten, F., & Trauthan, F. (2006). The HRSC-AX Mt. Etna project: High-resolution orthoimages and 1 m DEM at regional scale. International Archives of Photogrammetry and Remote Sensing, XXXVI (Part 1), http://isprs. free. fr/documents/Papers/T05-23. pdf.

Hafner, W. (1951). Stress distributions and faulting. Geological Society of America Bulletin, 62(4), 373-398.

Haimson, B. C., & Rummel, F. (1982). Hydrofracturing stress measurements in the Iceland research drilling project drill hole at Reydarfjordur, Iceland. Journal of Geophysical Research: Solid Earth, 87(B8), 6631-6649.

He, M. Y., Evans, A. G., & Hutchinson, J. W. (1994). Crack deflection at an interface between dissimilar elastic materials: role of residual stresses. International Journal of Solids and Structures, 31(24), 3443-3455.

Heap, M. J., Villeneuve, M., Albino, F., Farquharson, J. I., Brothelande, E., Amelung, F., Got, J. L., & Baud, P. (2020). Towards more realistic values of elastic moduli for volcano modelling. Journal of Volcanology and Geothermal Research, 390, 106684.

Heimisson, E. R., & Segall, P. (2020). Physically consistent modeling of dike-Induced deformation and seismicity: Application to the 2014 Bárðarbunga dike, Iceland. Journal of Geophysical Research: Solid Earth, 125(2), e2019JB018141.

Hjartardóttir, Á. R., & Einarsson, P. (2015). The interaction of fissure swarms and monogenetic lava shields in the rift zones of Iceland. Journal of Volcanology and Geothermal Research, 299, 91-102.

Hjartardóttir, Á. R., Einarsson, P., Gudmundsson, M. T., & Högnadóttir, T. (2016). Fracture movements and graben subsidence during the 2014 Bárðarbunga dike intrusion in Iceland. Journal of Volcanology and Geothermal Research, 310, 242-252.

Hoek, E., & Diederichs, M. S. (2006). Empirical estimation of rock mass modulus. International journal of rock mechanics and mining sciences, 43(2), 203-215.

Hutchinson, J. W. (1996). Stresses and failure modes in thin films and multilayers. Notes for a Dcamm Course. Technical University of Denmark, Lyngby, 1, 14.

Imbò, G. (1928). Osservazioni e ricerche in relazione all'eruzione etnea 2–20 Novembre 1928. Bulletin volcanologique, 5, 120-176.

Inskip, N. D. F., Browning, J., Meredith, P. G., & Gudmundsson, A. (2020). Conditions for fracture arrest in layered rock sequences. Results in Geophysical Sciences, 1, 100001.

Isida, M. (1955). On the tension of a strip with a central elliptic hole (Part 1). Trans. Jpn. Soc. Mech. Eng., 21(107), 507.

Jacoby, W., & Gudmundsson, M. T. (2007). Hotspot Iceland: an introduction. Journal of Geodynamics, 43(1), 1-5.

Jaeger, J. C., Cook, N. G., & Zimmerman, R. (2009). Fundamentals of rock mechanics. John Wiley & Sons.

James, M. R., & Robson, S. (2012). Straightforward reconstruction of 3D surfaces and topography with a camera: Accuracy and geoscience application. Journal of Geophysical Research: Earth Surface, 117(F3).

James, M. R., Robson, S., d'Oleire-Oltmanns, S., & Niethammer, U. (2017). Optimising UAV topographic surveys processed with structure-from-motion: Ground control quality, quantity and bundle adjustment. Geomorphology, 280, 51-66.

Kavanagh, J. L., Menand, T., & Sparks, R. S. J. (2006). An experimental investigation of sill formation and propagation in layered elastic media. Earth and Planetary Science Letters, 245(3-4), 799-813.

Kieffer, G. (1975). Pillows and hyaloclastites associated to subaerial lavas at the South-West of the base of Mount Etna (Sicily, Italy). Geologie mediterraneenne, 2(4), 179-183.

Kieffer, G. (1985). Évolution structurale et dynamique d'un grand Vulcan polygénique: stade d'édification et activité actuelle de l'Etna. These d'état, Université de Clermont-Ferrand, II.

Krokos, M., Bonali, F.L., Vitello, F.R., Antoniou, V., Becciani, U., Russo, E., Marchese, F., Fallati, L., Nomikou, P., Kearl, M., Sciacca, E., & Whitworth, M. (2019). Workflows for virtual reality visualisation and navigation scenarios in earth sciences.

Kusumoto, S., Geshi, N., & Gudmundsson, A. (2013). Aspect ratios and magma overpressures of non-feeder dikes observed in the Miyake-jima volcano (Japan), and fracture toughness of its upper part. Geophysical Research Letters, 40(6), 1065-1068.

Lanzafame, G., Neri, M., Coltelli, M., Lodato, L., & Rust, D. (1997). North-South compression in the Nit. Etna region (Sicily): spatial and temporal distribution. Acta Vulcanologica, 9, 121-134.

Le Corvec, N., Walter, T. R., Ruch, J., Bonforte, A., & Puglisi, G. (2014). Experimental study of the interplay between magmatic rift intrusion and flank instability with application to the 2001 Mount Etna eruption. Journal of Geophysical Research: Solid Earth, 119(7), 5356-5368.

Lo Giudice, E., Patanè, G., Rasà, R., & Romano, R. (1982). The structural framework of Mount Etna. Memorie della Società Geologica Italiana, 23, 125-158.

Maccaferri, F., Bonafede, M., & Rivalta, E. (2010). A numerical model of dyke propagation in layered elastic media. Geophysical Journal International, 180(3), 1107-1123.

Maccaferri, F., Bonafede, M., & Rivalta, E. (2011). A quantitative study of the mechanisms governing dike propagation, dike arrest and sill formation. Journal of Volcanology and Geothermal Research, 208(1-2), 39-50.

Maccaferri, F., Rivalta, E., Passarelli, L., & Aoki, Y. (2016). On the mechanisms governing dike arrest: Insight from the 2000 Miyakejima dike injection. Earth and Planetary Science Letters, 434, 64-74.

Magee, C., & Jackson, C. A. L. (2021). Can we relate the surface expression of dike-induced normal faults to subsurface dike geometry?. Geology, 49(4), 366-371.

Magnúsdóttir, S., & Brandsdóttir, B. (2011). Tectonics of the Þeistareykir fissure swarm. Jökull, 61, 65-79.

Marinos, V. I. I. I., Marinos, P., & Hoek, E. (2005). The geological strength index: applications and limitations. Bulletin of Engineering Geology and the Environment, 64, 55-65.

Mastin, L. G., & Pollard, D. D. (1988). Surface deformation and shallow dike intrusion processes at Inyo Craters, Long Valley, California. Journal of Geophysical Research: Solid Earth, 93(B11), 13221-13235.

McGuire, W. J., & Pullen, A. D. (1989). Location and orientation of eruptive fissures and feederdykes at Mount Etna; influence of gravitational and regional tectonic stress regimes. Journal of Volcanology and Geothermal Research, 38(3-4), 325-344.

McGuire, W. J., & Saunders, S. J. (1993). Recent earth movements at active volcanoes: a review. In Quaternary Proceedings (Vol. 3, No. 3). Cambridge: Quaternary Research Association.

Menand, T. (2008). The mechanics and dynamics of sills in layered elastic rocks and their implications for the growth of laccoliths and other igneous complexes. Earth and Planetary Science Letters, 267(1-2), 93-99.

Menand, T., Daniels, K. A., & Benghiat, P. (2010). Dyke propagation and sill formation in a compressive tectonic environment. Journal of Geophysical Research: Solid Earth, 115(B8).

Mertes, J. R., Gulley, J. D., Benn, D. I., Thompson, S. S., & Nicholson, L. I. (2017). Using structure-from-motion to create glacier DEMs and orthoimagery from historical terrestrial and oblique aerial imagery. Earth Surface Processes and Landforms, 42(14), 2350-2364.

Micheletti, N., Lane, S. N., & Chandler, J. H. (2015). Application of archival aerial photogrammetry to quantify climate forcing of alpine landscapes. The photogrammetric record, 30(150), 143-165.

Modica, G., Praticò, S., & Di Fazio, S. (2017). Abandonment of traditional terraced landscape: A change detection approach (a case study in Costa Viola, Calabria, Italy). Land Degradation & Development, 28(8), 2608-2622.

Mölg, N., & Bolch, T. (2017). Structure-from-motion using historical aerial images to analyse changes in glacier surface elevation. Remote Sensing, 9(10), 1021.

Monaco, C., Catalano, S., Cocina, O., De Guidi, G., Ferlito, C., Gresta, S., Musumeci, C., & Tortorici, L. (2005). Tectonic control on the eruptive dynamics at Mt. Etna Volcano (Sicily) during the 2001 and 2002–2003 eruptions. Journal of Volcanology and Geothermal Research, 144(1-4), 211-233.

Müller, D., Walter, T. R., Schöpa, A., Witt, T., Steinke, B., Gudmundsson, M. T., & Dürig, T. (2017). High-resolution digital elevation modeling from TLS and UAV campaign reveals structural complexity at the 2014/2015 Holuhraun eruption site, Iceland. Frontiers in Earth Science, 5, 59.

Murray, J. B., & Pullen, A. D. (1984). Three-dimensional model of the feeder conduit of the 1983 eruption of Mt. Etna volcano, from ground deformation measurements. Bulletin Volcanologique, 47, 1145-1163.

Neri, M., & Acocella, V. (2006). The 2004–2005 Etna eruption: Implications for flank deformation and structural behaviour of the volcano. Journal of Volcanology and Geothermal Research, 158(1-2), 195-206.

Neri, M., Garduno, V. H., Pasquaré, G., & Rasà, R. (1991). Studio strutturale e modello cinematico della Valle del Bove. Acta Vulcanologica, 1, 17-24.

Neri, M., Acocella, V., & Behncke, B. (2004). The role of the Pernicana Fault System in the spreading of Mt. Etna (Italy) during the 2002–2003 eruption. Bulletin of Volcanology, 66, 417-430.

Neri, M., Guglielmino, F., & Rust, D. (2007). Flank instability on Mount Etna: Radon, radar interferometry, and geodetic data from the southwestern boundary of the unstable sector. Journal of Geophysical Research: Solid Earth, 112(B4).

Neri, M., Lanzafame, G., & Acocella, V. (2008). Dyke emplacement and related hazard in volcanoes with sector collapse: the 2007 Stromboli (Italy) eruption. Journal of the Geological Society, 165(5), 883-886.

Neri, M., Casu, F., Acocella, V., Solaro, G., Pepe, S., Berardino, P., Sansosti, E., Caltabiano, T., Lundgren, P., & Lanari, R. (2009). Deformation and eruptions at Mt. Etna (Italy): A lesson from 15 years of observations. Geophysical Research Letters, 36(2).

Neri, M., Acocella, V., Behncke, B., Giammanco, S., Mazzarini, F., & Rust, D. (2011). Structural analysis of the eruptive fissures at Mount Etna (Italy). Annals of Geophysics.

Nobile, A., Pagli, C., Keir, D., Wright, T. J., Ayele, A., Ruch, J., & Acocella, V. (2012). Dike-fault interaction during the 2004 Dallol intrusion at the northern edge of the Erta Ale Ridge (Afar, Ethiopia). Geophysical Research Letters, 39(19).

Okada, Y. (1985). Surface deformation due to shear and tensile faults in a half-space. Bulletin of the seismological society of America, 75(4), 1135-1154.

Okada, Y. (1992). Internal deformation due to shear and tensile faults in a half-space. Bulletin of the seismological society of America, 82(2), 1018-1040.

Opheim, J. A., & Gudmundsson, A. (1989). Formation and geometry of fractures, and related volcanism, of the Krafla fissure swarm, northeast Iceland. Geological Society of America Bulletin, 101(12), 1608-1622.

Ouédraogo, M. M., Degré, A., Debouche, C., & Lisein, J. (2014). The evaluation of unmanned aerial system-based photogrammetry and terrestrial laser scanning to generate DEMs of agricultural watersheds. Geomorphology, 214, 339-355.

Palano, M. (2016). Episodic slow slip events and seaward flank motion at Mt. Etna volcano (Italy). Journal of Volcanology and Geothermal Research, 324, 8-14.

Palano, M., Gresta, S., & Puglisi, G. (2009). Time-dependent deformation of the eastern flank of Mt. Etna: after-slip or viscoelastic relaxation?. Tectonophysics, 473(3-4), 300-311.

Pallister, J. S., McCausland, W. A., Jónsson, S., Lu, Z., Zahran, H. M., Hadidy, S. E., Aburukbah, A., Stewart, I. C. F., Lundgren, P. R., White, R. A., & Moufti, M. R. H. (2010). Broad accommodation of rift-related extension recorded by dyke intrusion in Saudi Arabia. Nature Geoscience, 3(10), 705-712.

Parsons, T., Sleep, N. H., & Thompson, G. A. (1992). Host rock rheology controls on the emplacement of tabular intrusions: Implications for underplating of extending crust. Tectonics, 11(6), 1348-1356.

Pasquaré Mariotto, F., & Bonali, F. L. (2021). Virtual geosites as innovative tools for geoheritage popularization: A case study from Eastern Iceland. Geosciences, 11(4), 149.

Patanè, D., Aliotta, M., Cannata, A., Cassisi, C., Coltelli, M., Di Grazia, G., Montalto, P., & Zuccarello, L. (2011). Interplay between Tectonics and Mount Etna's volcanism: insights into the geometry of the plumbing system. In New frontiers in tectonic research-at the midst of plate convergence. InTech.

Pedersen, R., & Sigmundsson, F. (2006). Temporal development of the 1999 intrusive episode in the Eyjafjallajökull volcano, Iceland, derived from InSAR images. Bulletin of Volcanology, 68, 377-393.

Perras, M. A., & Diederichs, M. S. (2014). A review of the tensile strength of rock: concepts and testing. Geotechnical and geological engineering, 32, 525-546.

Pezzo, G., Palano, M., Tolomei, C., De Gori, P., Calcaterra, S., Gambino, P., & Chiarabba, C. (2020). Flank sliding: a valve and a sentinel for paroxysmal eruptions and magma ascent at Mount Etna, Italy. Geology, 48(11), 1077-1082.

Philipp, S. L., Afşar, F., & Gudmundsson, A. (2013). Effects of mechanical layering on hydrofracture emplacement and fluid transport in reservoirs. Frontiers in Earth Science, 1, 4.

Pollard, D. D., Delaney, P. T., Duffield, W. A., Endo, E. T., & Okamura, A. T. (1983). Surface deformation in volcanic rift zones. In Developments in Geotectonics (Vol. 19, pp. 541-584). Elsevier.

Ponte, G. (1928). L'eruzione etnea del novembre 1928. Rivista di Fisica, Matematica e Scienze Naturali, 3, 113-122.

Ponte, G. (1929). Bollettino dell'Istituto Vulcanologico Etneo. Rivista dell'-Industria, Anno II (12), December 1928, Tip. C., Galàtola, Catania.

Ramsay, J. G., & Lisle, R. J. (2000). Applications of continuum mechanics in structural geology (Techniques of modern structural geology. Vol. 3) (Vol. 3). Academic Press.

Ray, R., Sheth, H. C., & Mallik, J. (2007). Structure and emplacement of the Nandurbar–Dhule mafic dyke swarm, Deccan Traps, and the tectonomagmatic evolution of flood basalts. Bulletin of Volcanology, 69, 537-551.

Redweik, P., Garzón, V., & Pereira, T. S. (2016). Recovery of stereo aerial coverage from 1934 and 1938 into the digital era. The Photogrammetric Record, 31(153), 9-28.

Rivalta, E., Böttinger, M., & Dahm, T. (2005). Buoyancy-driven fracture ascent: Experiments in layered gelatine. Journal of Volcanology and Geothermal Research, 144(1-4), 273-285.

Rivalta, E., Taisne, B., Bunger, A. P., & Katz, R. F. (2015). A review of mechanical models of dike propagation: Schools of thought, results and future directions. Tectonophysics, 638, 1-42.

Rivas-Dorado, S., Ruíz, J., & Romeo, I. (2023). Modeling of dike-induced graben nucleation in the Elysium region, Mars: The role of planetary gravity. Journal of Structural Geology, 167, 104778.

Roman, D. C., & Cashman, K. V. (2006). The origin of volcano-tectonic earthquake swarms. Geology, 34(6), 457-460.

Romano, R., Sturiale, C., & Patanè, G. (1981). Annual report of the world volcanic eruption in 1974. Bull Volc Erupt, 19, 10-12.

Rowland, J. V., Baker, E., Ebinger, C. J., Keir, D., Kidane, T., Biggs, J., Hayward, N. & Wright, T. J. (2007). Fault growth at a nascent slow-spreading ridge: 2005 Dabbahu rifting episode, Afar. Geophysical Journal International, 171(3), 1226-1246.

Rubin, A. M. (1992). Dike-induced faulting and graben subsidence in volcanic rift zones. Journal of Geophysical Research: Solid Earth, 97(B2), 1839-1858.

Rubin, A.M., Pollard, D.D. (1987). Origins of blade-like dikes in volcanic rift zones. In: Decker, R.W., Wight, T.L., Stuffer, P.H. (Eds.), Volcanism in Hawaii. US Geological Survey Professional Papers 1350, pp. 1449–1470.

Rubin, A. M., & Pollard, D. D. (1988). Dike-induced faulting in rift zones of Iceland and Afar. Geology, 16(5), 413-417.

Rubin, A. M., & Gillard, D. (1998). Dike-induced earthquakes: Theoretical considerations. Journal of Geophysical Research: Solid Earth, 103(B5), 10017-10030.

Ruch, J., Acocella, V., Storti, F., Neri, M., Pepe, S., Solaro, G., & Sansosti, E. (2010). Detachment depth revealed by rollover deformation: An integrated approach at Mount Etna. Geophysical Research Letters, 37(16).

Ruch, J., Pepe, S., Casu, F., Acocella, V., Neri, M., Solaro, G., & Sansosti, E. (2012). How do volcanic rift zones relate to flank instability? Evidence from collapsing rifts at Etna. Geophysical research letters, 39(20).

Ruch, J., Wang, T., Xu, W., Hensch, M., & Jónsson, S. (2016). Oblique rift opening revealed by reoccurring magma injection in central Iceland. Nature communications, 7(1), 1-7.

Ruz, J., Browning, J., Cembrano, J., Iturrieta, P., Gerbault, M., & Sielfeld, G. (2020). Field observations and numerical models of a Pleistocene-Holocene feeder dyke swarm associated with a fissure complex to the east of the Tatara-San Pedro-Pellado complex, Southern Volcanic Zone, Chile. Journal of Volcanology and Geothermal Research, 404, 107033.

Ruzgienė, B., Berteška, T., Gečyte, S., Jakubauskienė, E., & Aksamitauskas, V. Č. (2015). The surface modelling based on UAV Photogrammetry and qualitative estimation. Measurement, 73, 619-627.

Sæmundsson, K. (1978). Fissure swarms and central volcanoes of the neovolcanic zones of Iceland in Crustal evolution in northern Britain and adjacent regions. Geological journal Liverpool, (10), 415-432.

Sæmundsson, K., Sigurgeirsson, M. Á., Hjartarson, A., Kaldal, I., Kristinsson, S. G. (2016). Geological Map of of Southwest Iceland, 1:100 000 (2nd ed.). Reykjavík: Iceland GeoSurvey.

Sæmundsson, K., Sigurgeirsson, M. Á., & Friðleifsson, G. Ó. (2020). Geology and structure of the Reykjanes volcanic system, Iceland. Journal of Volcanology and Geothermal Research, 391, 106501.

Schonberger, J. L., & Frahm, J. M. (2016). Structure-from-motion revisited. In Proceedings of the IEEE conference on computer vision and pattern recognition (pp. 4104-4113).

Schultz, R. (1995). Limits on strength and deformation properties of jointed basaltic rock masses. Rock Mechanics and Rock Engineering, 28(1), 1-15.

Segall, P. (2010). Earthquake and volcano deformation. Princeton University Press.

Sevara, C., Verhoeven, G., Doneus, M., & Draganits, E. (2018). Surfaces from the visual past: Recovering high-resolution terrain data from historic aerial imagery for multitemporal landscape analysis. Journal of archaeological method and theory, 25, 611-642.

Sigmundsson, F. (2006). Iceland geodynamics: crustal deformation and divergent plate tectonics. Springer Science & Business Media.

Sigmundsson, F., & Sæmundsson, K. (2008). Iceland: a window on North-Atlantic divergent plate tectonics and geologic processes. Episodes Journal of International Geoscience, 31(1), 92-97.

Sigmundsson, F., Hooper, A., Hreinsdóttir, S., Vogfjörd, K. S., Ófeigsson, B. G., Heimisson, E. R., Dumont, S., Parks, M., Spaans, K., Gudmundsson, G. B., Drouin, V., Árnadóttir, T., Jónsdóttir, K., Gudmundsson, M. T., Högnadóttir, T., Fridriksdóttir, H. M., Hensch, M., Einarsson, P., Magnússon, E., Samsonov, S., Brandsdóttir, B., White, R. S., Ágústsdóttir, T., Greenfield, T., Green, R. G., Hjartardóttir, Á. R., Pedersen, R., Bennett, R. A., Geirsson, H., La Femina, P. C., Björnsson, H., Pálsson, F., Sturkell, E., Bean, C. J., Möllhoff, M., Braiden, A. K., & Eibl, E. P. S. (2015). Segmented lateral dyke growth in a rifting event at Bárðarbunga volcanic system, Iceland. Nature, 517(7533), 191-195.

Sigmundsson, F., Parks, M., Hooper, A., Geirsson, H., Vogfjörd, K. S., Drouin, V., Ófeigsson, B. G., Hreinsdóttir, S., Hjaltadóttir, S., Jónsdóttir, K., Einarsson, P., Barsotti, S., Horálek, J., & Ágústsdóttir, T. (2022). Deformation and seismicity decline before the 2021 Fagradalsfjall eruption. Nature, 609(7927), 523-528.

Sigurdsson, O. (1980). Surface deformation of the Krafla fissure swarm in two rifting events. Journal of geophysics, 47(1), 154-159.

Sigurgeirsson, M. Á. (1992). Tephra formation at Reykjanes (Gjóskumyndanir á Reykjanesi, in Icelandic) (Doctoral dissertation, MS-thesis, University of Iceland).

Sigurgeirsson, M. Á. (1995), Yngra-Stampagosid In Reykjanes (in Icelandic), Náttúrufræðingurinn 64 (3), bls. 211-230.

Siniscalchi, A., Tripaldi, S., Neri, M., Balasco, M., Romano, G., Ruch, J., & Schiavone, D. (2012). Flank instability structure of Mt. Etna inferred by a magnetotelluric survey. Journal of Geophysical Research: Solid Earth, 117(B3).

Solaro, G., Acocella, V., Pepe, S., Ruch, J., Neri, M., & Sansosti, E. (2010). Anatomy of an unstable volcano from InSAR: Multiple processes affecting flank instability at Mt. Etna, 1994–2008. Journal of Geophysical Research: Solid Earth, 115(B10).

Soule, S. A., Escartín, J., & Fornari, D. J. (2009). A record of eruption and intrusion at a fast spreading ridge axis: Axial summit trough of the East Pacific Rise at 9–10 N. Geochemistry, Geophysics, Geosystems, 10(10).

Sneddon, I. N. (1946). The distribution of stress in the neighbourhood of a crack in an elastic solid. Proceedings of the Royal Society of London. Series A. Mathematical and Physical Sciences, 187(1009), 229-260.

Spacapan, J. B., Galland, O., Leanza, H. A., & Planke, S. (2017). Igneous sill and finger emplacement mechanism in shale-dominated formations: a field study at Cuesta del Chihuido, Neuquén Basin, Argentina. Journal of the Geological Society, 174(3), 422-433.

Stal, C., Bourgeois, J., De Maeyer, P., De Mulder, G., De Wulf, A., Goossens, R., Hendrickx, M., Nuttens, T., & Stichelbaut, B. (2012). Test case on the quality analysis of structure from motion in airborne applications. In 32nd EARSeL Symposium: Advances in geosciences. European Association of Remote Sensing Laboratories (EARSeL).

Stein, R. S., Briole, P., Ruegg, J. C., Tapponnier, P., & Gasse, F. (1991). Contemporary, Holocene, and Quaternary deformation of the Asal Rift, Djibouti: Implications for the mechanics of slow spreading ridges. Journal of Geophysical Research: Solid Earth, 96(B13), 21789-21806.

Sturkell, E., Einarsson, P., Sigmundsson, F., Geirsson, H., Olafsson, H., Pedersen, R., de Zeeuw-van Dalfsen, E., Linde, A. T., Sacks, S. I., & Stefánsson, R. (2006). Volcano geodesy and magma dynamics in Iceland. Journal of Volcanology and Geothermal Research, 150(1-3), 14-34.

Tarantola, A., Ruegg, J. C., & Lépine, J. C. (1979). Geodetic evidence for rifting in Afar a brittle-elastic model of the behaviour of the lithosphere. Earth and Planetary Science Letters, 45(2), 435-444.

Tarantola, A., Ruegg, J. C., & Lepine, J. P. (1980). Geodetic evidence for rifting in Afar, 2. Vertical displacements. Earth and Planetary Science Letters, 48(2), 363-370.

Tavani, S., Granado, P., Corradetti, A., Girundo, M., Iannace, A., Arbués, P., Muñoz, J. A., & Mazzoli, S. (2014). Building a virtual outcrop, extracting geological information from it, and sharing the results in Google Earth via OpenPlot and Photoscan: An example from the Khaviz Anticline (Iran). Computers & Geosciences, 63, 44-53.

Tentler, T. (2005). Propagation of brittle failure triggered by magma in Iceland. Tectonophysics, 406(1-2), 17-38.

Thatcher, W., & Hill, D. P. (1995). A simple model for the fault-generated morphology of slow-spreading mid-oceanic ridges. Journal of Geophysical Research: Solid Earth, 100(B1), 561-570.

Thiele, S. T., Cruden, A. R., Zhang, X., Micklethwaite, S., & Matchan, E. L. (2021). Reactivation of magma pathways: Insights from field observations, geochronology, geomechanical tests, and numerical models. Journal of Geophysical Research: Solid Earth, 126(5), e2020JB021477.

Thomson, K. (2007). Determining magma flow in sills, dykes and laccoliths and their implications for sill emplacement mechanisms. Bulletin of Volcanology, 70(2), 183-201.

Thordarson, T., & Self, S. (1993). The Laki (Skaftár fires) and Grímsvötn eruptions in 1783–1785. Bulletin of Volcanology, 55, 233-263.

Thordarson, T., & Larsen, G. (2007). Volcanism in Iceland in historical time: Volcano types, eruption styles and eruptive history. Journal of Geodynamics, 43(1), 118-152.

Thordarson, T., & Höskuldsson, Á. (2014). Iceland. Dunedin Academic Press Ltd.

Tibaldi, A. (1995). Morphology of pyroclastic cones and tectonics. Journal of Geophysical Research: Solid Earth, 100(B12), 24521-24535.

Tibaldi, A. (1996). Mutual influence of dyking and collapses at Stromboli volcano, Italy. Geological Society, London, Special Publications, 110(1), 55-63.

Tibaldi, A. (2001). Multiple sector collapses at Stromboli volcano, Italy: how they work. Bulletin of Volcanology, 63, 112-125.

Tibaldi, A. (2003). Influence of cone morphology on dykes, Stromboli, Italy. Journal of Volcanology and Geothermal Research, 126(1-2), 79-95.

Tibaldi, A. (2004). Major changes in volcano behaviour after a sector collapse: insights from Stromboli, Italy. Terra Nova, 16(1), 2-8.

Tibaldi, A., & Groppelli, G. (2002). Volcano-tectonic activity along structures of the unstable NE flank of Mt. Etna (Italy) and their possible origin. Journal of Volcanology and Geothermal Research, 115(3-4), 277-302.

Tibaldi, A., & Bonali, F. L. (2017). Intra-arc and back-arc volcano-tectonics: Magma pathways at Holocene Alaska-Aleutian volcanoes. Earth-Science Reviews, 167, 1-26.

Tibaldi, A., Bonali, F. L., Vitello, F., Delage, E., Nomikou, P., Antoniou, V., Becciani, U., van Wyk de Vries, B., Krokos, M., & Whitworth, M. (2020a). Real world–based immersive Virtual Reality for research, teaching and communication in volcanology. Bulletin of Volcanology, 82, 1-12.

Tibaldi, A., Bonali, F. L., Russo, E., & Fallati, L. (2020b). Surface deformation and strike-slip faulting controlled by dyking and host rock lithology: A compendium from the Krafla Rift, Iceland. Journal of Volcanology and Geothermal Research, 395, 106835.

Tibaldi, A., Corti, N., De Beni, E., Bonali, F. L., Falsaperla, S., Langer, H., Neri, M., Cantarero, M., Reitano, D., & Fallati, L. (2021). Mapping and evaluating kinematics and the stress and strain field at active faults and fissures: A comparison between field and drone data at the NE rift, Mt Etna (Italy). Solid Earth, 12(4), 801-816.

Tibaldi, A., Bonali, F. L., Corti, N., Russo, E., Drymoni, K., De Beni, E., Branca, S., Neri, M., Cantarero, M. & Pasquaré Mariotto, F. (2022). Surface deformation during the 1928 fissure

eruption of Mt. Etna (Italy): Insights from field data and FEM numerical modelling. Tectonophysics, 837, 229468.

Toda, S., Stein, R. S., & Sagiya, T. (2002). Evidence from the AD 2000 Izu islands earthquake swarm that stressing rate governs seismicity. Nature, 419(6902), 58-61.

Tonkin, T. N., & Midgley, N. G. (2016). Ground-control networks for image based surface reconstruction: An investigation of optimum survey designs using UAV derived imagery and structure-from-motion photogrammetry. Remote Sensing, 8(9), 786.

Townsend, M. R., Pollard, D. D., & Smith, R. P. (2017). Mechanical models for dikes: A third school of thought. Tectonophysics, 703, 98-118.

Trexler, C. C., Morelan, A. E., Oskin, M. E., & Kreylos, O. (2018). Surface slip from the 2014 South Napa earthquake measured with structure from motion and 3-D virtual reality. Geophysical Research Letters, 45(12), 5985-5991.

Trippanera, D., Acocella, V., & Ruch, J. (2014). Dike-induced contraction along oceanic and continental divergent plate boundaries. Geophysical Research Letters, 41(20), 7098-7104.

Trippanera, D., Ruch, J., Acocella, V., & Rivalta, E. (2015a). Experiments of dike-induced deformation: insights on the long-term evolution of divergent plate boundaries. Journal of Geophysical Research: Solid Earth, 120(10), 6913-6942.

Trippanera, D., Acocella, V., Ruch, J., & Abebe, B. (2015b). Fault and graben growth along active magmatic divergent plate boundaries in Iceland and Ethiopia. Tectonics, 34(11), 2318-2348.

Trippanera, D., Ruch, J., Passone, L., & Jónsson, S. (2019). Structural mapping of dike-induced faulting in Harrat Lunayyir (Saudi Arabia) by using high resolution drone imagery. Frontiers in Earth Science, 7, 168.

Tryggvason, E. (1973). Seismicity, earthquake swarms, and plate boundaries in the Iceland region. Bulletin of the Seismological Society of America, 63(4), 1327-1348.

Tryggvason, E. (1994). Surface deformation at the Krafla volcano, North Iceland, 1982–1992. Bulletin of Volcanology, 56, 98-107.

Turner, D., Lucieer, A., & Watson, C. (2012). An automated technique for generating georectified mosaics from ultra-high resolution unmanned aerial vehicle (UAV) imagery, based on structure from motion (SfM) point clouds. Remote sensing, 4(5), 1392-1410.

Ukawa, M., & Tsukahara, H. (1996). Earthquake swarms and dike intrusions off the east coast of Izu Peninsula, central Japan. Tectonophysics, 253(3-4), 285-303.

Urbani, S., Acocella, V., Rivalta, E., & Corbi, F. (2017). Propagation and arrest of dikes under topography: Models applied to the 2014 Bardarbunga (Iceland) rifting event. Geophysical Research Letters, 44(13), 6692-6701.

Urlaub, M., Petersen, F., Gross, F., Bonforte, A., Puglisi, G., Guglielmino, F., Krastel, S., Lange, D., & Kopp, H. (2018). Gravitational collapse of Mount Etna's southeastern flank. Science Advances, 4(10), eaat9700.

Vachon, R., & Hieronymus, C. F. (2017). Effect of host-rock rheology on dyke shape, thickness and magma overpressure. Geophysical Journal International, 208(3), 1414-1429.

Vezzoli, L., Tibaldi, A., Renzulli, A., Menna, M., & Flude, S. (2008). Faulting-assisted lateral collapses and influence on shallow magma feeding system at Ollagüe volcano (Central Volcanic Zone, Chile-Bolivia Andes). Journal of Volcanology and Geothermal Research, 171(1-2), 137-159.

Villani, F., Pucci, S., Azzaro, R., Civico, R., Cinti, F. R., Pizzimenti, L., Tarabusi, G., Branca, S., Brunori, C. A., Caciagli, M., Cantarero, M., Cucci, L., D'Amico, S., De Beni, E., De Martini, P. M., Mariucci, M. T., Messina, A., Montone, P., Nappi, R., Nave, R., Pantosti, D., Ricci, T., Sapia, V., Smedile, A., Vallone, R., & Venuti, A. (2020). Surface ruptures database related to the 26 December 2018, MW 4.9 Mt. Etna earthquake, southern Italy. Scientific data, 7(1), 1-9.

Walter, T., & Schmincke, H. U. (2002). Rifting, recurrent landsliding and Miocene structural reorganization on NW-Tenerife (Canary Islands). International Journal of Earth Sciences, 91, 615-628.

Walter, T. R., & Troll, V. R. (2003). Experiments on rift zone evolution in unstable volcanic edifices. Journal of Volcanology and Geothermal Research, 127(1-2), 107-120.

Walter, T. R., Acocella, V., Neri, M., & Amelung, F. (2005a). Feedback processes between magmatic events and flank movement at Mount Etna (Italy) during the 2002–2003 eruption. Journal of Geophysical Research: Solid Earth, 110(B10).

Walter, T. R., Troll, V. R., Cailleau, B., Belousov, A., Schmincke, H. U., Amelung, F., & Vd Bogaard, P. (2005b). Rift zone reorganization through flank instability in ocean island volcanoes: an example from Tenerife, Canary Islands. Bulletin of Volcanology, 67, 281-291.

Walter, T. R., Salzer, J., Varley, N., Navarro, C., Arámbula-Mendoza, R., & Vargas-Bracamontes, D. (2018). Localized and distributed erosion triggered by the 2015 Hurricane Patricia investigated by repeated drone surveys and time lapse cameras at Volcán de Colima, Mexico. Geomorphology, 319, 186-198.

Walter, T. R., Belousov, A., Belousova, M., Kotenko, T., & Auer, A. (2020a). The 2019 eruption dynamics and morphology at Ebeko volcano monitored by unoccupied aircraft systems (UAS) and field stations. Remote Sensing, 12(12), 1961.

Walter, T. R., Jousset, P., Allahbakhshi, M., Witt, T., Gudmundsson, M. T., & Hersir, G. P. (2020b). Underwater and drone based photogrammetry reveals structural control at Geysir geothermal field in Iceland. Journal of Volcanology and Geothermal Research, 391, 106282.

Walter, T. R., Zorn, E. U., González, P. J., Sansosti, E., Muñoz, V., Shevchenko, A. V., Plank, S. M., Reale, D., & Richter, N. (2023). Late complex tensile fracturing interacts with topography at Cumbre Vieja, La Palma. Volcanica, 6(1), 1-17.

Warrick, J. A., Ritchie, A. C., Adelman, G., Adelman, K., & Limber, P. W. (2017). New techniques to measure cliff change from historical oblique aerial photographs and structure-from-motion photogrammetry. Journal of Coastal Research, 33(1), 39-55.

Wells, D. L., & Coppersmith, K. J. (1994). New empirical relationships among magnitude, rupture length, rupture width, rupture area, and surface displacement. Bulletin of the seismological Society of America, 84(4), 974-1002.

Westoby, M. J., Brasington, J., Glasser, N. F., Hambrey, M. J., & Reynolds, J. M. (2012). 'Structure-from-Motion' photogrammetry: A low-cost, effective tool for geoscience applications. Geomorphology, 179, 300-314.

White, R. S., Drew, J., Martens, H. R., Key, J., Soosalu, H., & Jakobsdóttir, S. S. (2011). Dynamics of dyke intrusion in the mid-crust of Iceland. Earth and Planetary Science Letters, 304(3-4), 300-312.

Wright, T. J., Ebinger, C., Biggs, J., Ayele, A., Yirgu, G., Keir, D., & Stork, A. (2006). Magma-maintained rift segmentation at continental rupture in the 2005 Afar dyking episode. Nature, 442(7100), 291-294.

Xu, W., Jónsson, S., Corbi, F., & Rivalta, E. (2016). Graben formation and dike arrest during the 2009 Harrat Lunayyir dike intrusion in Saudi Arabia: Insights from InSAR, stress calculations and analog experiments. Journal of Geophysical Research: Solid Earth, 121(4), 2837-2851.

Xu, X., Aiken, C. L., & Nielsen, K. C. (1999). Real time and the virtual outcrop improve geological field mapping. Eos, Transactions American Geophysical Union, 80(29), 317-324.

Yew, C. H., & Weng, X. (1997). Mechanics of Hydraulic Fracturing, Houston, Texas.

Zhao, J., Wallgrün, J. O., LaFemina, P. C., Normandeau, J., & Klippel, A. (2019). Harnessing the power of immersive virtual reality-visualization and analysis of 3D earth science data sets. Geo-spatial Information Science, 22(4), 237-250.